UNIVERSITÀ
DEGLI STUDI
DI PADOVA

Head Office: Università degli Studi di Padova

Department of Civil, Environmental and Architectural Engineering

Ph.D. COURSE IN SCIENCES OF CIVIL, ENVIRONMENTAL AND ARCHITECTURAL ENGINEERING

SERIES XXXII (32°)

Title: AN EXPERIMENTAL STUDY ON THE CORRELATION BETWEEN RESIDUAL PRESTRESS FORCE IN PRE-TENSIONED AND POST-TENSIONED CONCRETE BEAMS AND NON-DESTRUCTIVE TESTS

Thesis written with the financial contribution of Studio Franchetti srl

Coordinator: Ch.mo Prof. Marco Marani

Supervisor: Ch.mo Prof. Carlo Pellegrino

Co-Supervisor: Eng. Paolo Franchetti, PhD

Co-Supervisor: Eng. Flora Faleschini, PhD

Ph.D. student : Michele Frizzarin

Title: AN EXPERIMENTAL STUDY ON THE CORRELATION BETWEEN RESIDUAL PRESTRESS FORCE IN PRE-TENSIONED AND POST-TENSIONED CONCRETE BEAMS AND NON-DESTRUCTIVE TESTS.

Abstract:

The research activity described in this thesis was begun with the aim of investigating the possibilities of applying non-destructive techniques to develop a methodology to assess the presence of damage and the loss in prestressing on prestressed concrete (PRC) beams.

The work began with the investigation, in literature, of the methods utilized at present for the assessment of damage in prestressed beams and prestressing cable. Among others, the thesis focused on vibration-based and acoustoelastic techniques, and in particular on the following properties: variations of the fundamental frequency and mode shapes, damping ratio, velocity and attenuation of the ultrasonic signal. Such properties have been rarely analyzed together in literature; moreover, the literature analysis carried out until today showed how further efforts need to be paid to enhance the feasibility of the application of such methods in practice.

A wide assessment of the results obtained in literature for vibration based assessment of prestressing losses was carried out. Based on these results, an experimental campaign was set up in the laboratory for Construction Materials Tests of the University of Padova. The tests were carried out on 6 PRC beams, both with bonded and un-bonded tendons, in order to study the effects of the variation of specific parameters on the response of the beams. The three pre-tensioned beams had identical geometrical properties, but with different level of prestressing. The three post-tensioned beams had the peculiarity to allow the prestressing force to be applied manually in laboratory conditions, with the possibility to obtain a wider range of prestressing levels. Moreover, every post-tensioned beam had different cable eccentricity. Static tests were performed until the failure of the beams, and for every load step nondestructive tests were carried out: dynamic free vibration tests and ultrasonic tests.

From vibration tests dynamic characteristics were extracted: fundamental frequency, modal damping, mode shapes. The variation of these parameters with respect to damage level and prestressing level was studied. Moreover, also the dependence of ultrasonic parameters, like wave velocity and energy, on damage and prestressing level was emphasized.

Particular attention was paid to dissipation phenomena, like modal damping parameters and ultrasonic energy dissipation, which appeared to be extremely sensitive to the formation

of cracks and damage. The depth of the study led to the conclusion that there exists an unequivocal relationship between the presence and the entity of the damage and the appearance of such dissipation phenomena.

Finally, the effect of the change in the degree of prestressing on nondestructive parameters PRC beams was studied. A method was proposed that make use of only non-destructive tests in order to assess the residual prestressing level of a PRC beam. This methodology could enhance and improve the techniques normally used for the damage detection, enabling a more detailed assessment of the condition of the structure with limited amount of data.

Titolo: UNO STUDIO SPERIMENTALE SULLA CORRELAZIONE TRA LA FORZA DI PRECOMPRESSIONE RESIDUA IN TRAVI IN CALCESTRUZZO ARMATO PRETESE E POST-TESE E PROVE NON DISTRUTTIVE.

Sommario:

L'attività di ricerca descritta in questa tesi è stata avviata con l'obiettivo di studiare le possibilità di applicare tecniche non distruttive valutare la presenza di danno e la perdita di precompressione in travi in calcestruzzo armato precompresso (CAP).

Il lavoro è iniziato con l'indagine, in letteratura, dei metodi attualmente utilizzati per la valutazione del danno nelle travi precompresse e nei cavi di precompressione. Tra le tecniche applicabili, la tesi si è concentrata su quelle basate sui metodi vibrazionali e acusto-elastiche, in particolare sullo studio delle seguenti proprietà: variazioni delle frequenze fondamentali e delle forme modali, rapporto di smorzamento, velocità e attenuazione del segnale ultrasonico. Tali proprietà sono state raramente analizzate congiuntamente in letteratura; inoltre, lo studio di letteratura ha mostrato come siano ancora necessari ulteriori sforzi per migliorare l'applicabilità di tali metodi nella pratica.

È stata effettuata un'ampia valutazione dei risultati ottenuti negli studi di letteratura per la valutazione delle perdite di precompressione basata sullo studio delle vibrazioni. Sulla base di questi risultati, è stata avviata una campagna sperimentale nel laboratorio per le prove sui materiali da costruzione dell'Università di Padova. I test sono stati condotti su 6 travi in calcestruzzo armato precompresso, sia pretese che post-tese, al fine di studiare gli effetti della variazione di parametri specifici sulla risposta degli elementi strutturali. Le tre travi pretensione avevano proprietà geometriche identiche, ma con un diverso livello di precompressione. Le tre travi post-tese avevano la peculiarità di consentire l'applicazione manuale della forza di precompressione in condizioni di laboratorio, con la possibilità di ottenere una gamma più ampia di livelli di precompressione. Inoltre, ogni trave post-tesa aveva un'eccentricità di cavo diversa. Sono stati eseguiti test statici fino al collasso delle travi e sono stati effettuati test non distruttivi per ogni fase di carico: test dinamici impulsivi e test agli ultrasuoni.

Dai risultati delle prove vibrazionali sono state estratte le caratteristiche dinamiche, quali frequenza fondamentale, smorzamento modale, forme modali. È stata studiata la variazione di questi parametri rispetto allo stato di danno e al livello di precompressione. Inoltre, è stata enfatizzata anche la dipendenza di tali fenomeni dai parametri ultrasonici, come la velocità e l'energia delle onde trasmesse.

Particolare attenzione è stata prestata ai fenomeni dissipativi, come i parametri di smorzamento modale e la dissipazione di energia dell'onda ultrasonica, che sembrano essere

estremamente sensibile alla formazione di fessure e danneggiamenti. L'approfondimento dello studio ha portato alla conclusione che esiste una relazione inequivocabile tra la presenza e l'entità del danno e la comparsa di tali fenomeni dissipativi.

Infine, è stato studiato l'effetto del cambiamento nel grado di precompressione sui parametri non distruttivi delle travi in CAP. È stato proposto un metodo che fa utilizzo solamente di test non distruttivi al fine di valutare il livello di precompressione residuo degli elementi in calcestruzzo armato precompresso. Questa metodologia potrebbe portare un miglioramento alle tecniche normalmente utilizzate per il rilevamento del danno, consentendo una valutazione più dettagliata delle condizioni della struttura con una quantità limitata di dati.

Summary

Index of figures

1 Introduction

1.1 Background

The conservation of the enormous stock of existing buildings, bridges and other civil structures world-wide is an extremely complex issue that involves cultural, social, economic and political considerations.

The conservation related economy is currently booming world-wide and huge investments are being encouraged and made to ensure conservation by means of restoration interventions In this context, several research projects were financed aimed at identifying broadly-recognized procedures and strategies that can be applied by public and private authorities for the management of infrastructural assets (COST 345 2004; SA.MA.R.I.S. 2005; COST TU1404 2014). However, while this issue is gaining increasing social attention with time, as a consequence of structural failure events that had a great media impact ([1][2]), the sensitivity to the research required to improve and/or establish reliable intervention procedures and techniques is still inadequate. As a consequence, there is a lack of an appropriate framework of well-established theoretical schemes and technical tools for the diagnosis and design of such interventions, which would take into account the historic, functional and economic value of any asset, on which interventions are done.

In particular, at present only in specific cases, increasing attention is paid to all the activities aimed at maintaining an acceptable level of structural safety over time: it is noted that suitable interventions are essential for the reduction of costs, lengthening the life of the structures and delaying their complete restoration. Maintenance requires that at any moment it is possible to decide or, even better, to forecast and plan minimum interventions to prevent an unacceptable decrease in the level of safety, established at a given moment in the life of the structure. To this end, the most relevant physical parameters related to the safety of a structure and sensitive to faults or damages would have to be continuously observed and evaluated: this means monitoring, which is a task concerning safety and risk management.

Within these quantities, it is commonly noted that damage to a structure alters its dynamic characteristics. This change is characterized by alterations to its structural parameters (boundary conditions, mass, damping, stiffness) that involve global behavior. Therefore, while most current experimental damage detection methods (acoustic tests, sonic tests, radiography, magnetic field tests, thermal field tests, etc.) require prior knowledge of the position of damage in a given section of the structure, the analysis of the variation of dynamic characteristics can be defined a global damage detection method.

Over the past 30 years damage detection from changes in global dynamic parameters has received increasing attention from the civil, aerospace and mechanical engineering sectors.

The aerospace sector began studying the use of vibration-based damage detection during the late 1970s [3] and early 1980s with the NASA Space Shuttle project [4]. The civil engineering sector has been studying vibration-based damage assessment of bridge structures (and especially in Italy, of monuments) since the early 1980s.

Many techniques based on experimental modal analysis have been developed: they revolve around the fact that changes in physical properties cause detectable changes in modal parameters (resonance frequencies, mode shapes, modal damping), namely the eigen-properties. In practice, the problem of damage detection is usually translated into identifying and measuring, using modal analysis, which structural variations in particular have caused alterations to the measured dynamic characteristics. These most commonly-used techniques are based on linear analysis and their reliability has general recognition and the range of their applications is widely known. However, there are still some remaining factors which make vibration-based damage identification difficult to implement in practice.

In the case of civil structures, which are very complex compared to mechanical structures, for example (non-linear behavior of materials, uncertainty over real boundary conditions, considerable size, limited number of identifiable modes, high damping, etc.), it is not always possible to conduct dynamic tests which provide a complete set of measurements to allow satisfactory modal extraction.

Furthermore, mainly because of a lack of comparison with measurements on the undamaged structure, the widespread full-scale tests between the 1980s and 1990s on buildings have been unable to completely validate the efficacy of the numerous damage identification techniques proposed. The research on large civil structures, developed from 1995 onwards at the Los Alamos National Laboratory (USA), was therefore of enormous interest because, for the first time, it allowed researchers to compare the dynamic response before and after the introduction of different levels of damage [5]. Even localization methods without explicit reference to the undamaged state [6] have been proposed in the literature.

The standard modal properties also represent a form of data compression. On the basis of greater attention to directly checking test results, especially for large structures, some authors [7] have suggested a change of methodology, aimed at a direct analysis of time histories for indications of damage, even though it is more difficult to identify damage by examining response-time histories directly.

It follows that this technology has still not been formally and generally adopted by the civil engineering community and no method covering the three steps of a process of damage detection (detection, localization, quantification) has yet been identified.

1.2 Aim of the investigation

The current practice on the performance assessment of bridges, and more generally infrastructures, suffers from several deficiencies, the most-well known that of being based on visual observations of structural damage only, thus being limited on qualitative data [6] [9]. In-depth investigations are instead needed when safety and serviceability are evaluated during structures service life, and for them, it is necessary to improve and/or establish reliable procedures and techniques to carefully assess the current health condition of structures. In the field of prestressed reinforced concrete (PC) structures, this becomes even more fundamental, being the variation of prestressing level within the element an additional parameter of uncertainty [10], other than deterioration [11], variation of the external loads [12], time-dependent phenomena [13] involving material properties variation (e.g., for concrete creep and shrinkage, and steel relaxation), natural hazards occurrence [18], etc.

The knowledge of the residual prestressing force in existing PC bridges is considered one of the fundamental keys for understanding the actual health condition of the whole structure. Indeed, a substantial difference between design and current prestress force might lead to serviceability and safety impairments [22], linked to the increase of tensile stresses in concrete and possible cracking phenomena, with consequent effects on the exposure of reinforcement, and lastly leading to potential structural failure. Further, several studies highlighted discrepancies when experimental residual prestressing force has been compared with the theoretical one, as predicted applying different Codes, for PC members that were extracted from structures in service from more than 25 years [19][20]. Such deviations (typically underestimating prestress loss) might be significant even if most of the Codes are generally conservative in the estimation of prestress losses [21], which occur within the first months after the element casting and that are relatively easy to be predicted. Hence, they are associated to the above mentioned phenomena linked to materials degradation, long-term effects, and even to construction defects or structural damage, that may lead to a progressive deterioration of the prestressing level along the PC member.

Despite this, unless the bridge is instrumented at the time of construction, the existing prestress force cannot be directly estimated, at least without destructive testing of the element. This is due to the impossibility of directly accessing the prestressing cables, except for the case of external ones.

This thesis has been developed within this context , investigating the possible applications of vibration-based damage detection techniques to check the integrity, to localize and eventually quantify progressive damages artificially inflicted on six precast PC beam elements, both pre-tensioned and post-tensioned, and to predict the level of prestressing inside the beams through the use of only non-destructive tests (NDT).

For many years, at the University of Padova, a theoretical and experimental investigation was ongoing, aiming to define a practical procedure for the quality control of the production of PC hollow core floor panels [14]. Types of defects investigated include 1) imperfectly applied prestressing tension and 2) presence of cracks. With regards to the second aspect, much experimental work focused on a single panel, where dynamic investigation techniques were extensively applied before and after a controlled damaging of the specimen [15][16][17]. Prestressing tends to re-close cracks, when the cause of cracking has been eliminated, therefore this type of damage to a PC product is not usually visible. As mentioned, damage detection using localized investigation methods is not cost effective if the position of damage in a given section of the structure is unknown. For these reasons, vibration techniques are more suitable for supplying information about and the location of damages, with a limited cost.

The tests were performed under experimental conditions which were well-controlled in terms of boundary conditions and excitation sources at the Laboratory of the Department of Civil, Environmental and Architecture Engineering at the University of Padova.

The first part of the analysis concerned the application of NDT such as vibration tests and ultrasonic tests to 3 pre-tensioned beams, at 5 different damage states. Each beam had a different level of prestressing. In this phase of the research classical and already used extraction techniques were applied (modal frequencies and damping, but also ultrasonic velocity) in order to confirm the applicability of methods already used in other research campaign.

In the second part of the research, the methods were extended to 3 post-tensioned beams. Being the prestressing force regulated manually by an external jack, it had been possible to perform the NDT tests for more prestressing state. Moreover, every beam had a different cable eccentricity, being able to introduce another parameter of variability in the experimentation.

Having once detected the presence of damage, in order to situate the problem of prestressing state evaluation, a methodology that made us of only NDT experimental data was tested, discussing their applicability to PRC beams.

Borrowing the results of the previous experimental campaign, particular attention was paid to dissipation phenomena (often unconsidered in literature) and their evolution with regard to damage increase, also by direct examination of time-histories. In particular, the research focused on vibrational damping and with ultrasonic wave attenuation, and their evolution with damage and with prestressing levels.

1.3 Thesis Organization

The thesis is divided into 7 chapters which follow the implicit logical path presented in the previous section.

Chapter 2 presents a state-of-the-art literature review of the current methods in damage identification and prestress level detection in PC beams. Given the aims of this study, the author placed emphasis on damage identification methods specifically proposed for and numerically and/or experimentally applied to beam type structures.

In the following chapters, the laboratory tests on the 6 PC precast beams are described in detail.

In chapter 3, the beams construction at the Castelvetro prefabrication plant of RDB Italprefabbricati are briefly described and the experimental results of materials characterization are reported. The laboratory campaign was aimed at investigating the evolution of dynamic parameters after application of incremental load/damage levels. The experimental static set-up and progressive load tests for all 6 beams is described in detail.

Chapter 4 describes the execution of ultrasonic tests, first in the 3 pre-stressed beams, and the in the 3 post-tensioned beams. The extraction methods based on ultrasonic velocity and on signal attenuation are described, and the results are presented in form of graphs and of tomographic contour figures..

Chapter 5 describes the execution of dynamic tests: the test setup, the elaboration procedure and curve-fitting method are described. The frequency and damping extraction procedure is described, and the results are analyzed.

In chapter 6 a procedure for residual prestressing force detection is introduced, that make use of only NDT for the definition of the beams effective condition state. Moreover, some considerations are made on the use of dissipation phenomena (vibration damping, ultrasonic wave attenuation) for damage detection and localization.

The research's findings are reported in chapter 7.

1.4 Innovative features of the research

The thesis contains unpublished material, or in part, material that has recently been submitted to scientific journals or conferences by the author in a different form. Information derived from other publications is always accompanied by a reference. Most of the concepts presented and experiences reported are therefore new.

Some particularly innovative theoretical aspects of the work are as follows:

1. The use of the ultrasonic signal to calculate its energy attenuation, and the use of this parameter in correlation to damage evolution and prestressing change;
2. The combined use of ultrasonic tests and dynamic tests with the purpose of assessing the damage level and prestressing level on pre-tensioned and post-tensioned beams;
3. The combined use of ultrasonic tests and dynamic tests in order to localize damage.

1.5 Restrictions

In this study, the field of investigation has necessarily been restricted to just some of the many aspects involved because of the breadth of the research topic. In particular:

4. the thesis does not deal extensively with modal testing techniques, even though these aspects were actually developed during the experimental research;
5. damage has been modelled at local level, but not at a microscopic scale;
6. the thesis does not deal extensively with friction models;
7. the thesis does not deal with fracture mechanics.

2 Literature review

2.1 Residual prestressing force

In the field of structural damage identification, the measure of the residual prestressing force in existing prestressed concrete bridges is one of the fundamental parameters for the understanding of the real health condition of the whole structure. In fact, a substantial difference between the design and the actual prestress force can lead to serviceability and safety problems [22]. Despite this, unless the bridge is instrumented at the time of construction, the existing prestress force usually cannot be directly estimated. This is due to the impossibility of directly accessing the prestressing cables, unless they are external. In fact, although forces can be monitored by means of a hydraulic force gauge, this would only provide information of the force near the anchorage (where the sensor is usually installed).

Non-destructive tests have the advantage to rely on measuring a parameter that can be correlated with force levels. Recently, Abdel-Jaber and Glisic [23] made a comprehensive review of the available methods for monitoring prestressing forces in PC elements, identifying mainly five strategies:

a) vibration methods (based on acceleration): based on the analysis of natural frequencies as modal shapes or displacement measurements. This method has been largely discussed in literature, as it will be better detailed in Chapter 5, but it might not be effective due to several concurrent cases, e.g. insignificant changes in frequency until relatively high prestress losses;

b) impedance-based methods (based on electrical impedance): a piezoceramic material patch, that works as both an actuator and a sensor, is affixed to the PC element and an alternating electrical field is applied to it. Due to the converse piezoelectric effect, that couples electrical and mechanical response in piezoelectric materials, a deformation is induced both in the sensor and, hence, in the structure, causing an electric charge. Changes in the electrical impedance signature reflect thus the changes in the mechanical properties of the monitored structure. Such method has been shown being very promising [24], even though results are significantly affected by environmental conditions [23], thus limiting, until now, their potential exploitation in real structures;

c) acoustoelastic methods (based on wave velocity): this method, used for the assessment of many other structural and materials properties, generally provides few accuracy in assessing prestress losses, and generally its use alone does not allow to obtain reliable results [30];

d) elasto-magnetic methods (based on magnetic permeability): this technique has shown promising results to provide measurements of absolute stress within ferromagnetic materials, even if also in this case, temperature variations might influence significantly results, although they can be compensated through the use of empirical relationships derived from tests.

Additionally, elasto-magnetic are local properties, and hence distributed sensors are necessary to capture the behavior of the whole structure. In literature, such method has been applied for studying external prestressing tendons or strands in cable-stayed bridges [25], and at laboratory scale also PS beams, but sensors were embedded in the concrete before prestressing operations [26];

e) strain-based methods (based on strain): based on the assessment of concrete, or even better, steel strain evolution, which however need for instrumenting elements before concrete casting. Strain monitoring is regarded as the closest to direct monitoring of stress. Recent advances in the development of durable and stable strain sensors have led to the increasing popularity and use of strain-based methods for prestress force monitoring. If structures are instrumented with sensors during construction, either through attaching them to prestressing strands or embedding them in the concrete, long-term strain changes can be monitored. Additionally, instrumentation during construction allows for measuring strain changes during prestress force transfer, thereby enabling calculation of the initial stress in the prestressing strands. If the strain change at the location of the prestressing strands is determined, the stress change can be calculated using Hooke's law. However, this type of measurement has the limitation to require for instrumentation at construction because strain changes are relative and not absolute. Given that the strain-based methods are relatively mature both in terms of sensors and algorithms, future research could focus on pervasive implementation of strain sensors, for example, by using distributed fiber optic sensors, self-sensitive (nano-) materials, large-area electronics, and so on, and algorithms that combine mathematical/numerical models with monitoring results, to more accurately discern prestress losses from other unusual behaviors. Hence, these methods are viable for new structures but not for the existing ones and assessment purpose.

The above-described context shows that, among the four strategies applicable for the existing structures, there is no-one fully mature yet for large scale implementations in real structures, and further efforts should be paid to enhance the feasibility of their application.

- Both elasto-magnetic and impedance-based methods seem the most advanced methods currently available in this field, even though they still present some disadvantages [23] that need to be overpassed, due to the relatively young age of these techniques compared to others, such as vibration-based and acoustic ones. Impedance methods, electro-magnetic methods and strain methods show different degree of reliability, but all of them are related to local measurements; that means, for practical applications, a previous knowledge of the possible location of damage is necessary. Moreover, some of them have some limitations regarding the application (for example, the need for external strands in EM measurements) or need to be installed from the beginning with a continuous monitoring (strain methods).

- Vibration methods have the advantage to give a global information, and therefore can be used as an “early warning” procedure to detect the presence of any discrepancy from the expected behavior, If some anomaly is detected, other local or pseudo-local tests can be used to locate the damage more precisely, like for example ultrasonic tests. The latter can be applied to the concrete matrix, in order to detect ultrasonic velocity or other ultrasonic parameters that can give local information about damage and prestressing of the concrete itself.
- On the other side, vibration methods have shown controversial results, as described here below.

Accordingly, in this thesis an experimentally-based research focused on vibration-based and acoustoelastic methods has been carried out, particularly focusing on the following properties: variations of the fundamental frequency, damping ratio, attenuation of the ultrasonic signal. Such properties have been rarely analyzed in literature indeed. Results obtained with these non-destructive tests were then compared with the experimental ones, that were directly measured in PC beams with single straight post-tensioned cables, through two load cells at the tendon ends, as it will be discussed in the following chapters.

2.2 Use of vibration tests

The problem of prestress force estimation through dynamic tests is being tackled since at least 30 years [31]. The first approach to the problem is related to the well-known method of the measure of the variation in the fundamental frequency of vibration [32]. The classical formulation of the measure for the fundamental frequencies in a prestressed beam-type element, for barycentric prestressing load, is the following:

$$\omega_n^2 = -\left(\frac{n\pi}{L}\right)^2 \frac{N}{m} + \left(\frac{n\pi}{L}\right)^4 \frac{EI}{m} \quad (1)$$

Where ω_n is the nth circular frequency, N is the axial force applied to the beam, m is the mass per unit length in kg/m, L is the length of the beam and EI is the rigidity.

The formulation can be expressed, in the case of the first fundamental frequency, in the following terms:

$$f = \frac{\pi}{2L^2}\sqrt{\frac{EI}{m}\left(1 - \frac{N}{N_{cr}}\right)} \quad (2)$$

Where N_{cr} is the Critical Eulerian compressive force:

$$N_{cr} = \frac{\pi^2 EI}{L^2} \quad (3)$$

As seen from Equation (2), the variation in the fundamental frequency of the element depends on the square root of the ratio between the applied prestressing force and the Critical Eulerian force. The variation will be perceptible only for considerable variation of the force with respect to N_{cr} [33]. The same paper proposed a more detailed equation for the description of the phenomenon:

$$\omega_n^2 = \frac{n^4\pi^4}{mL^4}\left[\left(E - \frac{N}{A}\right) I + \left(E_S - \frac{N}{A_S}\right) I_S\right] \quad (4)$$

Where E_s, A_s and I_s are the Young Modulus, the section area and the inertia of the steel cable, respectively. For small values of the ratio between the inertia of the cable and the inertia of the concrete section, the second value inside the square brackets can be neglected, and the equation becomes:

$$\omega_n^2 = -\left(\frac{n\pi}{L}\right)^4 \frac{NI}{mA} + \left(\frac{n\pi}{L}\right)^4 \frac{EI}{m} \quad (5)$$

Since the first studies of it was clear that the prestressing force was affecting the fundamental frequencies of vibration not only in terms of compressing force, but also in terms of variation of the effective rigidity, as seen in [22] and in [34].

In the last two decades, several experimental campaigns were carried out in order to validate these models. The results were shown to be controversial. Unger et al. concentrated the study on modal identification without taking into account the variation of prestressing force [35]. Wang et al., in opposition with previous experimental results, stated that the variation of flexural rigidity of prestressed beams with parabolic tendons decreases with increasing prestressing force, while flexural rigidities of prestressed beams with straight tendons are not be affected by prestressing forces [36]. These consideration were again denied by Toyota et al. [37] were a comprehensive study was made taking into account the effects of temperature, and comparing the experimental values with the theoretical formulation of equation (2).

Other studies made use of time domain techniques to identify the prestressing force, without considering frequency based models [38].

Few papers addressed also on the measure of damping [37] as another parameter that changes with prestressing force, showing a general decrement of damping with prestressing force. Also in this case other studies suggested that the variation in damping was not enough strong to be perceived over the temperature and humidity effects.

2.2.1 Comparison of literature results – vibration tests

In the present paper a comparison of literature results was made, in order to highlight the difference between the conclusions obtained in each study.

Between the experimental campaigns that were analyzed, 3 of them were chosen based on the following characteristics of homogeneity:

1. Rectangular section;
2. Straight cables;
3. Information about zero-prestressing conditions;
4. Numerosity of data.

The first paper that was analyzed is the one from Saiidi et al. [22], published in 1994. In this paper a rectangular beam with length of 3,66 m and single barycentric strand was tested. The axial force as increased from 0 kN to 131.3 kN, and then back to almost 0 kN, with 14 steps in total. For every step, the fundamental frequencies and the effective rigidity were measured with the use of dynamic tests.

The second paper is the one from Noble et al. [34], published in 2015. The experimental tests were performed on 9 rectangular beams with length of 2 m and different eccentricity of the cable (from 52 mm to – 52 mm). The load was increased from 0 kN to 201.54 kN, with 11 steps in total. For every step, the fundamental frequencies were measured with the use of dynamic tests. The effective rigidity was measured through load-deflection data. Also the viscous damping was measured during dynamic tests.

The last paper is from Toyota et al. [37], published in 2017. A rectangular beam with length of 9 m and eccentric cable was subjected to a cycle of decompressing-compressing, from 490 kN to 0 kN and back to 490 kN, with 21 steps in total. For each step natural frequency and viscous damping coefficient were measured.

Besides the reason already exposed, the three papers represent the comparison between the first tests [22] and more recent results [34] [37]. On the other sides, two of the papers find a clear correlation between the level of prestressing force and the fundamental frequencies [22] [37], while the third shows controversial results [34].

In order to make the results to be comparable, they were resumed in a table and made dimensionless. In particular, the results were expressed in terms of:

1. Ratio between the applied prestressing force and the critical Eulerian force in the x axis: N/N_{cr};
2. Ratio between the measured first fundamental circular frequency and the theoretical first fundamental circular frequency at zero prestressing level, squared in the y axis: $[\omega/\omega_{0,t}]^2$.

The theoretical relationship between these two terms, from eq. (2), is the following:

$$\left(\frac{\omega_{N,t}}{\omega_{o,t}}\right)^2 = \left(1 - \frac{N}{N_{cr}}\right) \qquad (6)$$

There $\omega_{N,t}$ represents the theoretical circular frequency at level of prestressing N, and $\omega_{0,t}$ represents the same quantity at level of prestressing zero.

The results are resumed in the following table and figure.

Table 1: Fundamental frequencies vs. level of prestressing. Comparison of results

Paper	L (m)	E (N/m2)	I (m4)	m (kg/m)	N (N)	N_{cr} (N)	f_{theor} (Hz)	f_{exp} (Hz)	N/Ncr	$(\omega/\omega_0)^2$
1994 Saiidi	3,66	8,59E+09	1,73E-05	30,97	0	109804	8,13	11,41	0,00	1,000
	3,66	1,30E+10	1,73E-05	30,97	26732	166588	9,18	13,47	0,16	1,394
	3,66	1,55E+10	1,73E-05	30,97	56579	197562	9,22	14,15	0,29	1,538
	3,66	1,71E+10	1,73E-05	30,97	80865	218210	9,10	14,49	0,37	1,613
	3,66	1,91E+10	1,73E-05	30,97	120052	243699	8,63	14,72	0,49	1,664
	3,66	1,99E+10	1,73E-05	30,97	129392	254776	8,69	14,97	0,51	1,721
	3,66	2,02E+10	1,73E-05	30,97	131260	258218	8,75	15,07	0,51	1,744
	3,66	1,96E+10	1,73E-05	30,97	129882	250259	8,52	14,78	0,52	1,678
	3,66	1,86E+10	1,73E-05	30,97	90205	238214	9,44	14,72	0,38	1,664
	3,66	1,82E+10	1,73E-05	30,97	85535	232299	9,40	14,95	0,37	1,717
	3,66	1,72E+10	1,73E-05	30,97	72929	219824	9,41	14,72	0,33	1,664
	3,66	1,45E+10	1,73E-05	30,97	56592	185409	8,81	13,63	0,31	1,427
	3,66	1,24E+10	1,73E-05	30,97	36064	158415	8,59	12,89	0,23	1,276
	3,66	1,03E+10	1,73E-05	30,97	15532	131206	8,35	12,09	0,12	1,123
2015 Noble	2,0	2,69E+10	7,03E-05	72,00	150	4663388	63,62	68,00	0,00	1,000
	2,0	2,69E+10	8,41E-05	72,00	23060	5576326	69,43	67,00	0,00	0,971
	2,0	2,69E+10	1,01E-04	72,00	44530	6711331	76,07	70,00	0,01	1,060
	2,0	2,69E+10	1,21E-04	72,00	63070	8043728	83,23	71,00	0,01	1,090
	2,0	2,69E+10	1,39E-04	72,00	82340	9203406	88,98	71,00	0,01	1,090
	2,0	2,69E+10	1,53E-04	72,00	100690	10141019	93,36	69,00	0,01	1,030
	2,0	2,69E+10	1,62E-04	72,00	121040	10757869	96,09	73,00	0,01	1,152
	2,0	2,69E+10	1,93E-04	72,00	141480	12805812	104,85	68,00	0,01	1,000
	2,0	2,69E+10	1,77E-04	72,00	161640	11720155	100,17	68,00	0,01	1,000
	2,0	2,69E+10	1,88E-04	72,00	179960	12485050	103,35	69,00	0,01	1,030
	2,0	2,69E+10	1,89E-04	72,00	202420	12559072	103,57	71,00	0,02	1,090
2017 Toyota	9,0	3,42E+10	7,20E-03	576,00	0	30003597	12,68	13,5	0,00	1,000
	9,0	3,42E+10	7,20E-03	576,00	49000	30003597	12,67	13,5	0,00	1,000
	9,0	3,42E+10	7,20E-03	576,00	98000	30003597	12,66	13,3	0,00	0,971
	9,0	3,42E+10	7,20E-03	576,00	147000	30003597	12,65	13,7	0,00	1,030
	9,0	3,42E+10	7,20E-03	576,00	196000	30003597	12,64	14,3	0,01	1,122
	9,0	3,42E+10	7,20E-03	576,00	245000	30003597	12,63	14,8	0,01	1,202
	9,0	3,42E+10	7,20E-03	576,00	294000	30003597	12,62	14,9	0,01	1,218
	9,0	3,42E+10	7,20E-03	576,00	343000	30003597	12,61	14,9	0,01	1,218
	9,0	3,42E+10	7,20E-03	576,00	392000	30003597	12,60	15,0	0,01	1,235
	9,0	3,42E+10	7,20E-03	576,00	441000	30003597	12,59	15,0	0,01	1,235
	9,0	3,42E+10	7,20E-03	576,00	490000	30003597	12,58	15,1	0,02	1,251

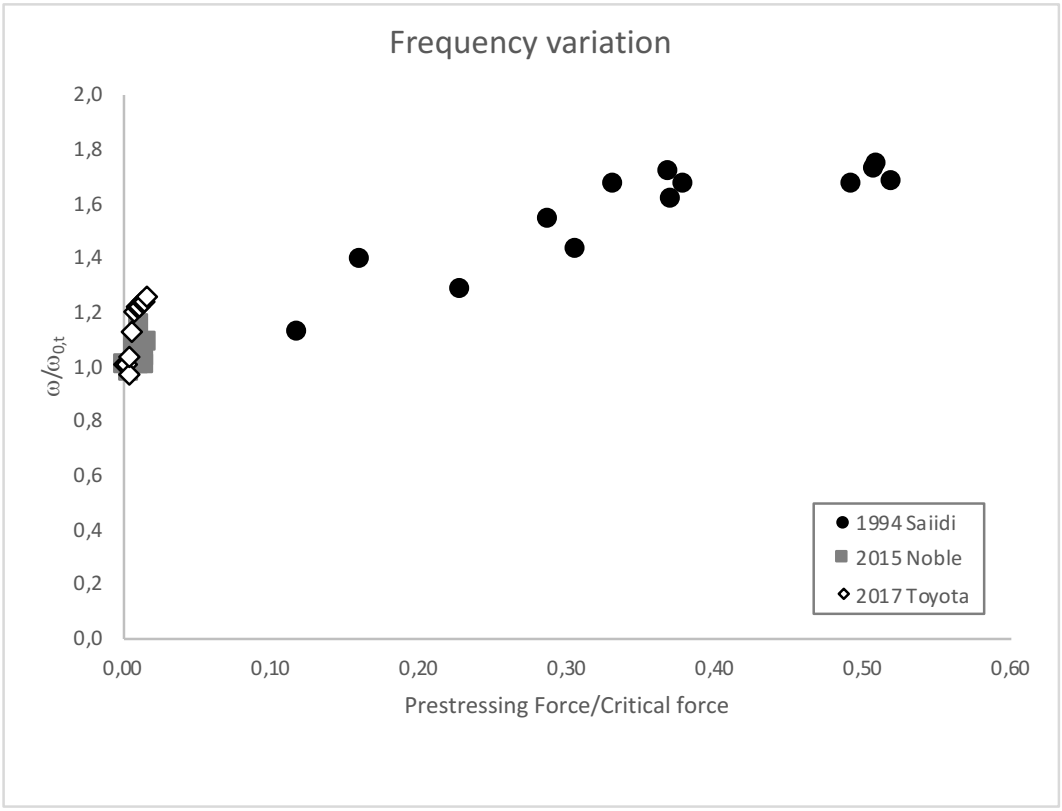

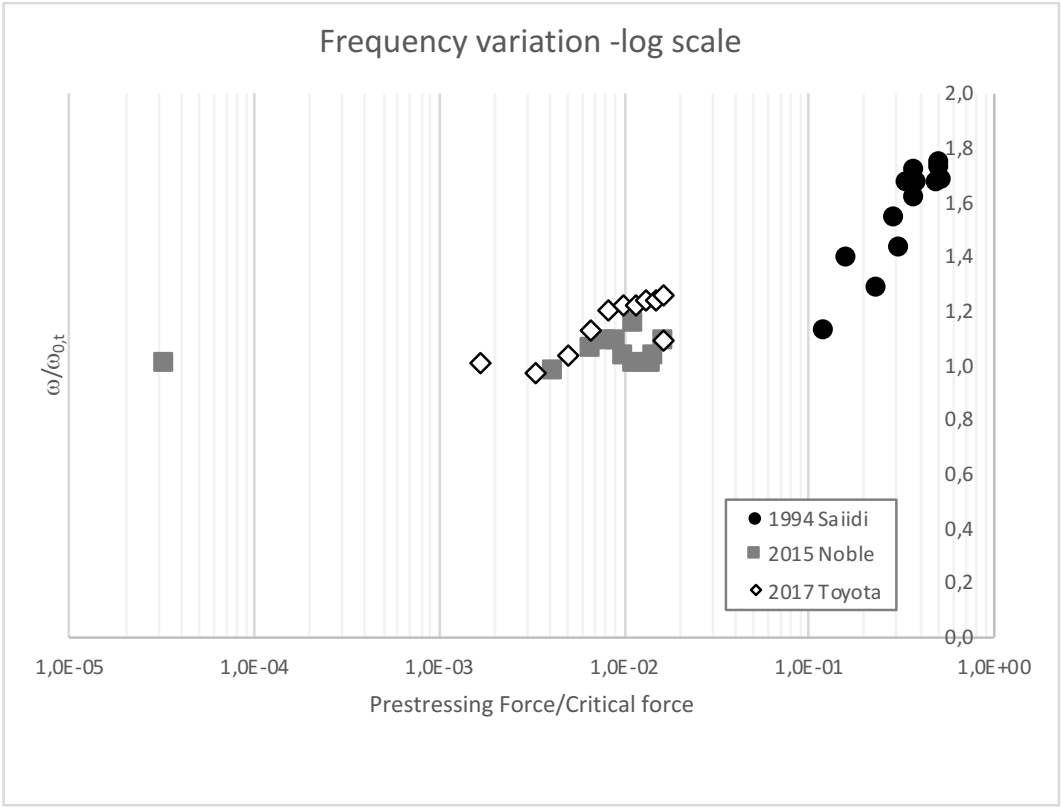

Figure 2.1: Fundamental frequencies vs. level of prestressing. Comparison of results

From the exposed results it can be deducted that:

1. The level of pre-stressing applied by Saiidi et al. was much larger, with respect to the critical value. As a result the variation in frequency is larger than in the other two cases.
2. The results between the three papers are not consistent: all the three papers find a quasi-linear dependence of the two variables, but while the two papers of Noble et al. and Toyota et al. the slope of the line is similar, in the paper from Saiidi et al. the slope is much different. Moreover, in the paper from Noble et al. the dispersion of data is more evident, in coherence with the final result of the paper.

2.2.2 Techniques of extraction of vibration parameters

In the following pages a short excursus of the main techniques of extraction utilized in the present thesis is presented, with the main characteristics and theoretical basis of the methodologies.

2.2.3 Frequency changes

The use of natural frequency as a diagnostic parameter in structural identification procedures is based on the fact that natural frequencies are sensitive indicators of structural integrity.

The method proposed in [39][3] uses the sensitivity concept and is based on the premise that the ratio of frequency changes in two modes is a function of the location of the damage only if changes in stiffness are independent of frequency and no changes in mass occur.

In particular, given an undamped system with natural frequencies and modal shapes:

$$\mathbf{M}\ddot{x} + \mathbf{K}x = \mathbf{0} \quad \Rightarrow \quad \phi_1 \ldots \phi_n \quad \omega_1 \ldots \omega_m \tag{7}$$

The damage can be modelled as a variation of the global stiffness $\Delta\mathbf{K}$ and δ are the local parameters defining the scenario of admissible damages: $\Delta\mathbf{K} = \delta_1\mathbf{K}_1 + \delta_2\mathbf{K}_2 + \ldots + \delta_n\mathbf{K}_n$ (1.)

Assuming a linear relationship d=F(δ), the changes of the *s*th natural frequency and modal shape are linked to damage with the following equation:

$$(\mathbf{K} + \Delta\mathbf{K})(\phi_s + \Delta\phi_s) = (\omega_s^2 + \Delta\omega_s^2)\mathbf{M}(\phi_s + \Delta\phi_s) \tag{8}$$

It is clear that the relationship is typically nonlinear and the problem can generally be solved by means of nonlinear optimization techniques. Since the nonlinearity of the relationship between frequency changes and stiffness changes, a direct relationship such as:

$$\Delta\omega_s \propto \delta$$

cannot exist.

Instead, left-multiplying for $(\phi_s)^T$ and ignoring the high order terms, it follows that:

$$\Delta\omega_s^2 = \frac{(\phi_s)^T \Delta\mathbf{K}\phi_s}{(\phi_s)^T \mathbf{M}\phi_s} \tag{9}$$

The frequency change ratio can be expressed by:

$$\frac{\Delta\omega_s^2}{\Delta\omega_r^2} = \frac{\dfrac{(\phi_s)^T \Delta\mathbf{K}\phi_s}{(\phi_s)^T \mathbf{M}\phi_s}}{\dfrac{(\phi_r)^T \Delta\mathbf{K}\phi_r}{(\phi_r)^T \mathbf{M}\phi_r}} \tag{10}$$

It is exclusively a function of the location of the damage.

To obtain relations between damage in individual members and changes in global vibration response, the global $\Delta\mathbf{K}$ can be broken down into individual member stiffness change matrices and member deformation $\varepsilon_i(\phi)$ (deformations of the *i*th member associated to ϕ mode shape):

$$\phi_i^T \Delta\mathbf{K}\phi_i = \varepsilon_1^T(\phi_i)\mathbf{K}_1\varepsilon_1(\phi_i) + \ldots + \varepsilon_n^T(\phi_i)\mathbf{K}_n\varepsilon_n(\phi_i) \tag{11}$$

and by hypothesizing, for example, $\Delta\mathbf{K} = \delta_i\mathbf{K}_i$, one can simply obtain [39]:

$$\frac{\Delta\omega_s^2}{\Delta\omega_r^2} = \frac{\dfrac{\varepsilon_i^T(\phi_s)\mathbf{K}_i\varepsilon_i(\phi_s)}{(\phi_s)^T \mathbf{M}\phi_s}}{\dfrac{\varepsilon_i^T(\phi_r)\mathbf{K}_i\varepsilon_i(\phi_r)}{(\phi_r)^T \mathbf{M}\phi_r}} \tag{12}$$

The predictor required for this interpretation is computed entirely from initial quantities: initial member stiffness and initial mode shapes.

In any case, to locate the defect, theoretical characteristic frequency change ratios, due to damage at selected positions, are calculated and compared with observed values.

Stubbs and Osegueda [40][41] developed a method based on the work of Cawley and Adams (1979), considering the first variation of the equation [42]:

$$\omega_s^2 = \frac{(\phi_s)^T \mathbf{K}\phi_s}{(\phi_s)^T \mathbf{M}\phi_s} \tag{13}$$

The authors showed that this method could accurately locate the damage and predict its order of magnitude by both numerical application (simply supported RC beam 10 m long, transverse section: 200 mm x 600 mm, with different damage hypotheses [40]) and by experimental

applications on a series of cantilevered aluminum beams (1 m long, transverse section: 25 mm x 12,7 mm [41]). Accidentally, the method identified additional low-level damages close to the actual damage location. The results for multiple damage location are similar to those obtained for the single damage location, but cannot precisely locate the second damage location. A method that also considers damping sensitivity matrix was introduced.

Ju and Mimovich [43] used changes in modal frequencies to locate damage occurring at sections of a beam to within 3% of the length, representing damage using the “fracture hinge” concept. The fracture hinge is a torsional spring whose rigidity depends on the fracture geometry. The frequencies of the first four flexural modes were measured before and after the introduction of cracking. The authors used frequency changes of the first four flexural modes to locate and quantify the damage in the beams. The authors were not very successful at estimating crack intensity.

Rizos [44] presented a simple method for one-dimensional structures, where the crack, in a cantilever beam, is represented by a spring that connects the two half components. The natural frequencies are related to the crack location and depth. Small cuts of between 2 and 14 mm were made along the length of steel cantilever beams. The beam was then excited at a resonance frequency and the vibration amplitude measured in many points. From the measurements of these amplitudes at two random points, the position and entity of the cracks were then calculated by the Newton-Raphson method. The error is less than 8%.

Silva and Gomes [45] applied a frequency change method to experimental data obtained from fatigue-cracked steel beams. They used a cantilever beam 600 mm long (cross-section: 18 mm x 32 mm). From 8 to 16 mm deep cracks were made along the beam, in positions ranging from the fixed end to 75 mm from the free end. The authors did not specify the direction of the cracks. In any case they succeeded in locating cracks to within 12 mm and appraising the length to within 1 mm. The best results were obtained using the first four frequencies.

Meneghetti and Maggiore [46] applied a sensitivity-based damage detection method to experimental data obtained from steel beams 600 mm long (square cross-section 15 mm x 15 mm). 0.3 mm wide cracks were carved in different beams. The authors succeeded in locating a 2 mm deep crack measuring frequencies before and after the damage occurred and plotting the local stiffness decrease curve against the crack location.

In any case, low sensitivity of frequency changes to damage makes these methods limited for practical applications. Obviously, in the case of symmetric structures, the solution is always

symmetric and therefore the damage cannot be unambiguously determined. Furthermore, a type of damage located in a different section can give rise to the same frequency change.

2.2.4 Mode shape changes

While methods based on natural frequency changes are not spatially specific, mode shape methods have this advantage. Comparison of modal shapes may be done by visually analyzing (by superposition) the shape change or by numerically quantifying the change.

Mode shape changes quantification can be obtained by computing the MAC (Modal Assurance Criterion): this [47] is a measure of the correlation between two sets of modal shapes by evaluation of the least square deviation.

$$MAC\left(\boldsymbol{\phi}_{s|P},\boldsymbol{\phi}_{r|Q}\right)=\frac{\left|\boldsymbol{\phi}_{r|Q}^{T}\boldsymbol{\phi}_{s|P}\right|^{2}}{\left(\boldsymbol{\phi}_{s|P}^{T}\boldsymbol{\phi}_{s|P}\right)\left(\boldsymbol{\phi}_{r|Q}^{T}\boldsymbol{\phi}_{r|Q}\right)} \tag{14}$$

where $\boldsymbol{\phi}_{s|P}$ is the sth eigenvector of P data set and $\boldsymbol{\phi}_{r|Q}$ is the rth eigenvector of Q data set, respectively. A MAC value close to 1 means that modes differ little, while a value close to 0 means that the modes are totally different. The MAC gives no indications on damage location.

The COMAC (COordinate Modal Assurance Criterion) is the reverse of the MAC in that it measures the correlation at each DOF averaged over the set of Correlated Mode Pairs [42]. It is expressed by the ratio between modal shapes in some location on the structure, as follows:

$$COMAC(i)=\frac{\left|\sum_{s=1}^{m}\boldsymbol{\phi}_{s|Q}(i)\boldsymbol{\phi}_{s|P}(i)\right|^{2}}{\sum_{s=1}^{m}\left(\boldsymbol{\phi}_{s|P}(i)\right)^{2}\sum_{s=1}^{m}\left(\boldsymbol{\phi}_{s|Q}(i)\right)^{2}} \tag{15}$$

where the modes from P and Q sets are paired, i is the measurement point, m the total number of correlated mode pairs, $\left(\boldsymbol{\phi}_{s|P}(i)\right)$ is the ith element of the array of P set of sth mode.

MAC and COMAC express, respectively, the global and local distance between correlated mode shapes. Therefore, their application to localization problem is quite inadequate because as damage parameters they have no physical meaning. This appears from various tests and models [49][42]. In fact, the damage is not directly connected to modal shapes, but to mode shape curvature changes. The fact that, in some cases, attractive results were obtained, is just fortuitous, because the structures in those cases are simply supported: in this restraint condition

the modes are a multiple of a half sinusoidal function, a shape that coincides with that of the curvature. Moreover, if a cantilever beam was studied and the damage was near the fixed end, the modal shapes at the free end would be greatly modified and unchanged at the fixed end. The location would therefore fail entirely. Assuming identical modal parameters and damage indexes, this method comes into the linearization methods category. Some authors used the direct local difference of the modal shapes as damage parameter, in an analogous way to the use of the COMAC and finding the same limitations.

Ko J.M. et al. [50] applied a MAC/COMAC-based identification technique to data obtained from a 2 m steel portal frame. Impulse and harmonic tests were done with both rigid and pinned nodes. The damage was simulated by removing bolts from two positions (one at the column-beam node, one at the column base). The authors showed that COMAC can be used to locate damage but not MAC.

Ren W.X. & De Roeck G. [51] proposed recently a method particularly suitable for structural damage identification on reinforced concrete beams. As this method was chosen by the author for the comparative study on experimental data obtained from laboratory tests on precast beams for different damage levels, it will be extensively described here.

For undamaged structures, the modal characteristics are described by the following expression:

$$\mathbf{K}\boldsymbol{\phi}_s = \omega_s^2 \mathbf{M}\boldsymbol{\phi}_s \quad \text{for } s=1,\ldots..,m \tag{16}$$

where **K** and **M** are the global stiffness and the mass matrices; ω_s and $\boldsymbol{\phi}_s$ are the sth circular natural frequency and the sth mode shape of the structure; m is the total number of obtained mode shapes for the undamaged structure.

Once damaged, the eigenvalue equations become:

$$\tilde{\mathbf{K}}\tilde{\boldsymbol{\phi}}_r = \tilde{\omega}_r^2 \tilde{\mathbf{M}}\tilde{\boldsymbol{\phi}}_r \quad \text{for } r=1,\ldots..,\tilde{m} \tag{17}$$

where $\tilde{\mathbf{K}}$ and $\tilde{\mathbf{M}}$ are the global stiffness and the mass matrices of the damaged structure; $\tilde{\omega}_r$ and $\tilde{\boldsymbol{\phi}}_r$ are the rth circular natural frequency and the rth mode shape of the damaged structure; $\tilde{m}$ is the total number of obtained mode shapes for the damaged structure.

The global stiffness and mass matrices are all considered symmetric and positive definite and the orthogonality conditions for the mass normalized mode shapes can be written as follows:

$$\tilde{\boldsymbol{\phi}}_s^T \tilde{\mathbf{M}} \tilde{\boldsymbol{\phi}}_r = \delta_{rs} \tag{18}$$

$$\tilde{\boldsymbol{\phi}}_s^T \tilde{\mathbf{K}} \tilde{\boldsymbol{\phi}}_r = \delta_{rs} \tilde{\omega}_r^2 \tag{19}$$

where δ_{rs}=1 if r=s and δ_{rs}=0 if $r \neq s$. Within the context of finite elements models, damage can be represented by a decrease in the stiffness of the individual finite elements. Damage identification is then carried out at the element level, assuming that the stiffness matrix of the whole element decreases uniformly. The fractional change in stiffness of ith element is expressed by the damage index δ_i:

$$\Delta \mathbf{k}_i = \left(\mathbf{k}_i - \tilde{\mathbf{k}}_i \right) = \delta_i \mathbf{k}_i \tag{20}$$

where $\mathbf{k}_i$ and $\tilde{\mathbf{k}}_i$ are the ith element stiffness matrices of the undamaged and damaged structures, respectively. $\Delta \mathbf{k}_i$ is the stiffness reduction of the ith element. A positive value of $\delta_i \in [0,1]$ will indicate a loss of element stiffness. The ith element is undamaged when δ_i=0 and the stiffness of the ith element is completely lost when δ_i=1. In this way, the damaged element stiffness matrix can be represented by:

$$\tilde{\mathbf{k}}_i = \mathbf{k}_i \left(1 - \delta_i \right) \tag{21}$$

Within the context of finite elements models, the global stiffness matrix **K** is the assemblage of each element stiffness matrix $\mathbf{k}_i$

$$\mathbf{K} = \sum_{i=1}^{n} \mathbf{k}_i \tag{22}$$

where n is the total number of finite elements. This is also true for damage structure:

$$\tilde{\mathbf{K}} = \sum_{i=1}^{n} \tilde{\mathbf{k}}_i = \sum_{i=1}^{n} \mathbf{k}_i (1 - \delta_i) \tag{23}$$

and the sth global mode shape can be written as follows:

$$\boldsymbol{\phi}_s = \sum_{i=1}^{n} \boldsymbol{\phi}_{si} \quad \text{or} \quad \tilde{\boldsymbol{\phi}}_s = \sum_{i=1}^{n} \tilde{\boldsymbol{\phi}}_{si} \tag{24}$$

Multiplying equation (2.23) for the damaged mode shape $\tilde{\boldsymbol{\phi}}_s^T$ ($s=1,\ldots\ldots,\tilde{m}$) and combining the above equations, the element damage index equations can be finally formulated:

$$\sum_{i=1}^{n} \tilde{\boldsymbol{\phi}}_{si}^T \tilde{\mathbf{k}}_i \tilde{\boldsymbol{\phi}}_{ri} = \omega_r^2 \tilde{\boldsymbol{\phi}}_s^T \tilde{\mathbf{M}} \tilde{\boldsymbol{\phi}}_r \tag{25}$$

$$\sum_{i=1}^{n} \tilde{\boldsymbol{\phi}}_{si}^T \mathbf{k}_i \tilde{\boldsymbol{\phi}}_{ri} \delta_i = \tilde{\boldsymbol{\phi}}_s^T \mathbf{K} \tilde{\boldsymbol{\phi}}_r - \tilde{\omega}_r^2 \delta_{rs} \quad (r=1,\ldots,\ \tilde{m};\ s=1,\ldots,\ \tilde{m};\ \delta_{rs}=1 \text{ if } r=s;\ \delta_{rs}=0 \text{ if } r\neq s) \tag{26}$$

These equations can be written in matrix notation ($\tilde{m}\,3\tilde{m}$ is the total number of rows; n is the total number of columns):

$$\mathbf{S}_{(\tilde{m}\times\tilde{m})\times n} \boldsymbol{\delta}_{n\times 1} = \Delta\mathbf{R}_{(\tilde{m}\times\tilde{m})\times 1} \tag{27}$$

where:

$$S_{sri} = \tilde{\boldsymbol{\phi}}_{si}^T \mathbf{k}_i \tilde{\boldsymbol{\phi}}_{ri} \tag{28}$$

$$\Delta R_{sr} = \tilde{\boldsymbol{\phi}}_s^T \mathbf{K} \tilde{\boldsymbol{\phi}}_r - \tilde{\omega}_r^2 \delta_{sr} \tag{29}$$

In order to involve not only damaged mode shapes, alternatively, multiplying equation (2.23) for the undamaged mode shape $\boldsymbol{\phi}_s^T$ ($s=1,\ldots..,m$), yields:

$$\boldsymbol{\phi}_s^T \tilde{\mathbf{K}} \tilde{\boldsymbol{\phi}}_r = \tilde{\omega}_r^2 \boldsymbol{\phi}_s^T \tilde{\mathbf{M}} \tilde{\boldsymbol{\phi}}_r \tag{30}$$

and, assuming that the mass matrix doesn't alter with damage, the following system can be written ($m\,3\tilde{m}$ is the total number of rows; n is the total number of columns):

$$\mathbf{S}_{(m\times\tilde{m})\times n} \boldsymbol{\delta}_{n\times 1} = \Delta\mathbf{R}_{(m\times\tilde{m})\times 1} \tag{31}$$

where:

$$S_{sri} = \tilde{\boldsymbol{\phi}}_{ri}^{T} \mathbf{k}_i \boldsymbol{\phi}_{si} \tag{32}$$

$$\Delta R_{sr} = \left(1 - \frac{\tilde{\omega}_r^2}{\omega_s^2}\right) \tilde{\boldsymbol{\phi}}_r^{T} \mathbf{K} \boldsymbol{\phi}_s \tag{33}$$

Theoretically, the solution for the unknown element damage indices allows the damage to be located and quantified. However, the system matrix **S** is not always square: the element damage equations may be determined, over-determined, or underdetermined depending on the number of undamaged modes *m*, damaged modes $\tilde{m}$, and element *n* chosen. When a direct inverse solution becomes impossible, other numerical algorithms can be supplemented.

2.2.5 Frequency Response Function (FRF) changes

The modal data based structural damage identification methods (SDIMs) have some shortcomings: the modal data are indirectly measured test data and could be contaminated by measurement errors as well as unavoidable modal extraction (e.g. Curve fitting) errors. Moreover, modal identification can be a time-consuming task and the completeness of modal data cannot be met in most practical cases because they often require a large number of sensors. The FRF data can be considered as alternatives to modal data because they are measured directly from structures and are free of errors such as modal extraction errors. FRF data can also provide much more damage information within a desired frequency range than modal data because the modal data are extracted mainly from a very limited number of FRF-data around resonance.

Sampaio R.P.C. et al. [52] suggest transforming methods based on mode shape changes to methods based on operational mode shapes. Basically this method is an extension of Pandey A.K. et al. [49] method to all frequencies in the measurement range and not just modal frequencies: it uses receptance FRF data rather than mode shape data.

The equation (2.41), for each location *i*:

$$\boldsymbol{\phi}_s''(i) = \frac{\boldsymbol{\phi}_s(i+1) - 2\boldsymbol{\phi}_s(i) + \boldsymbol{\phi}_s(i-1)}{h^2} \tag{34}$$

becomes:

$$\alpha''_{i,j} = \frac{\left(\alpha_{i+1,j} - 2\alpha_{i,j} + \alpha_{i-1,j}\right)}{h^2} \tag{35}$$

where $\alpha_{i,j}$ is the receptance FRF measured at location *i* for a force input at location *j*. The absolute difference between the FRF curvatures of the damaged and undamaged structure at location *i* along the chosen frequency range, is calculated, for an applied force at point *j*, by:

$$\Delta\alpha''_{i,j} = \sum_{\omega} \left| \tilde{\alpha}''(\omega)_{i,j} - \alpha''(\omega)_{i,j} \right| \tag{36}$$

Finally, one can sum up for several force locations:

$$\delta_i = \sum_j \Delta\alpha''_{i,j} \tag{37}$$

The FRF curvature method performed well in detecting and locating damage.

Maia N.M.M et al. [53] compared the previous FRF curvature method to the FRF-based mode shape method, FRF-based mode shape slope method, FRF-based mode shape curvature square method and FRF-based damage index. To avoid false damage location, at each frequency, the authors look for the location where the difference of damaged and undamaged case is maximum and they count an occurrence at that location; as they proceed along the frequency range, they simply keep summing the occurrences, not the differences themselves. It was found that the methods based on curvatures performed better.

Lee U. & Shin J. [54] proposed a frequency-domain method that requires only the frequency response function experimentally measured from the damaged structures as input data. The authors state that the method can locate and quantify many local damages at the same time. Besides, in contrast to the classical FEM, the spectral element method (SEM) is adopted because it provides extremely accurate dynamic solutions. Finally the equation system becomes:

$$\mathbf{\Phi}(\omega)_{n_{master}\ x\ n}\ \delta_{n\ x\ 1} = \mathbf{b}(\omega)_{n_{master}\ x\ 1} \tag{38}$$

where $\mathbf{\Phi}(\omega)$ and $\mathbf{b}(\omega)$ are determined only from the dynamic stiffness matrix in the intact state, the nodal force locator vector and the measured inertance FRF. n_{master} is the number of

"master" nodal d.o.f.s (where nodal force are no zero) and n is the number of finite elements to be examined for unknown damage magnitudes δ_i.

In order to make the damage identification problem well-posed n should be no lower of n_{master}: otherwise, more linear algebraic equations need to be derived.

2.2.6 Modal damping changes

This procedure of damage location is based on the use of modal damping changes. It has not been widely applied, even if, unlike some procedures already seen, it is theoretically justifiable. This parameter has been neglected by most researchers because damping cannot be obtained by finite elements analyses. Only more recently have numerical model updating techniques been found, which also consider damping changes [55][56].

Nevertheless, this seems an undue limitation because damping is extremely sensitive to damage. Viscous damping, typical of a homogeneous structure, is a material characteristic that depends neither on the geometry nor on type of vibration. The damping value is generally around 0.5% for prestressed concrete undamaged elements [57].

What is reported below is described in detail in [16][17][15]. Besides that directly derived from the equation of motion procedures, a technique was drawn up, based on the interpretation of damping changes in a damaged structure. The structural vibrating structure is divided into different elements and specific damping is associated with each element. The damaged element will show greater damping (roughly including nonlinear damping effects), so an increase of dissipation is logical for the damaged element. In the case of classically damped system, the damping ratio for the sth mode can be expressed as:

$$\xi_s = \omega_s \frac{\boldsymbol{\phi}_s^T \mathbf{C} \boldsymbol{\phi}_s}{\boldsymbol{\phi}_s^T \mathbf{K} \boldsymbol{\phi}_s} \tag{39}$$

where **C** is the proportional viscous damping matrix. More generally it can be interpreted as a ratio of dissipated energy in a cycle and the maximum potential energy of the system:

$$\xi_s = \frac{E_{visc}}{4\pi E_P} = \frac{E_{visc}}{2\pi \boldsymbol{\phi}_s^T \mathbf{K} \boldsymbol{\phi}_s} \tag{40}$$

So, for an ith element of the vibrating system, an analogous expression can be written:

$$\xi_i = \frac{E_{visc,i}}{2\pi \boldsymbol{\phi}_s^T \mathbf{K}_i \boldsymbol{\phi}_s} \tag{41}$$

where ξ_i is defined as specific damping ratio. For each mode shape, given a complete group of elements, it is necessary that:

$$E_{visc} = \sum_i E_{visc,i} \tag{42}$$

for which:

$$\xi_s = \sum_i \frac{\boldsymbol{\phi}_s^T \mathbf{K}_i \boldsymbol{\phi}_s}{\boldsymbol{\phi}_s^T \mathbf{K} \boldsymbol{\phi}_s} \xi_i \tag{43}$$

The presence of a crack in the *i*th element generally leads to the formation of a local dissipative mechanism, increasing the specific damping. Assuming that the system stiffness does not degrade, yields:

$$d_s = \Delta\xi_s = \sum_i \frac{\boldsymbol{\phi}_s^T \mathbf{K}_i \boldsymbol{\phi}_s}{\boldsymbol{\phi}_s^T \mathbf{K} \boldsymbol{\phi}_s} \delta_i \tag{44}$$

where $d_s = \Delta\xi_s$ is the global damage index and $\delta_i = \Delta\xi_i$ represents the local damage index. For the applications to case studies, the writer refers the reader to mentioned papers and theses.

2.2.7 Other extraction methods: Frequency Domain Decomposition

One of the most advanced non-parametric dynamic identification methods is the Frequency Domain Decomposition (FDD) [58]. This method is based on the assertion that the eigenvectors, which represent the modes of vibration, constitute a base, being linearly independent, and therefore any movement of the system can be represented by their linear combination. It is therefore possible to decouple the components of the various modes. In analogy, this property can be applied not only directly to the response x (t), but also to the spectral density (PSD), through a decomposition to the singular values (SVD) of the matrix that represents it at each frequency value. The advantage of this method lies in the fact that it is possible to distinguish modes at nearby frequencies. The Enhanced Frequency Domain

Decomposition (EFDD) (parametric) method substantially reconstructs the time domain signal, broken down into its main frequencies, through an inverse transformation (IDFT), after the FDD analysis has taken place. The use of a linear interpolation allows to eliminate harmonic components due to unwanted forcing, which can compromise the goodness of the results. In this way the damping ratios can also be estimated.

2.3 Use of ultrasonic tests

Ultrasonic testing is a non-destructive method applied in several fields, and it is often used in the field of structural monitoring for checking the health conditions of structural elements.

This chapter briefly describes the physical characteristics of the ultrasounds and their operating principle.

2.3.1 Generalities

The term "ultrasound" indicates various types of elastic waves (consisting of elastic vibrations) that propagate in a material. The general method of ultrasonic test consist in using one or more transmitters of elastic waves (generators) and one or more receivers (sensors), being the wave traveling ("flying") from the transmitter to the receiver passing through the investigated material [59].

In non-destructive tests the frequency range considered is between 200kHz and 20MHz and the ultrasonic beams are generated by suitable transducers that are electrically excited by transmitting vibrations to the medium and propagating in the form of waves. The shape of the beam depends on the size of the transducer and the frequency of the vibrations in the medium in question. The fundamental quantities involved in the process are described below.

2.3.2 Ultrasonic characteristics

Ultrasounds, like all wave-like phenomena, are characterized by the following physical parameters:

- Propagation speed (V): is the space covered by the wave front in the unit of time. It is directly detectable and theoretically depends on the characteristics of the medium in which the wave propagates with the following formula:

  $$E = \frac{(1+\nu)(1-2\nu)}{(1-\nu)}\rho v^2 \quad (45)$$

  Where E represents the elastic modulus of the material, ρ its density and ν is the Poisson modulus.

  For linear element, the formulation can be simplified as follows:

  $$V = \sqrt{\frac{E}{\rho}} \quad (46)$$

- Frequency (f) is the number of oscillations that occur in the unit of time and is calculated in Hz.

- Sound pressure (p) is a directly detectable fundamental parameter.
- Period (T) is the time (expressed in seconds) that uses the wave to pass from a maximum of pressure to the next.
- Wavelength (λ) represents the distance traveled by the beam in a period and at speed V. In formula:

  $$\lambda = VT \tag{47}$$

- Acoustic impedance (Z) is a parameter dependent on the characteristics of the medium and represents the resistance to the passage of the beam in the material. In formula:

  $$Z = \rho V \tag{48}$$

- Acoustic intensity (I) represents the energy that is transmitted in the unit of time through a unitary area, and normal to the surface. In formula:

  $$I = \frac{p^2}{2Z} \tag{49}$$

2.3.3 Propagation of ultrasonic waves

The propagation of ultrasonic waves depends both on the medium in which they propagate and on the way in which the wave is generated.

According to the oscillatory characteristics of the particles, the waves can be classified as follows:

- Longitudinal waves (or compression waves): they are the most used and are characterized by alternating phases of compression and expansion of the particles of the medium. In these waves the direction of vibration coincides with that of propagation and is perpendicular to the emitter plane of the probe.
- Transverse waves: they are characterized by a vibration of the particles perpendicular to the direction of motion.
- Surface waves (or Rayleigh) are obtained from the composition of longitudinal and transverse waves. These waves propagate only in the surface layer of solids and in this case the direction of vibration of the molecules is perpendicular to the surface of the element.
- Lamb (or flexural) waves are generated in small thickness materials and are subject to oscillations according to two perpendicular directions (of symmetrical compression or asymmetrical bending).

Wave propagation is characterized by attenuation, reflection, refraction, diffusion and interference phenomena.

As regards the attenuation, this involves the dissipation of energy of the ultrasonic beam as a function of the molecular movement and its transformation into heat. The attenuation is due to two phenomena: diffusion and absorption.

The phenomenon of diffusion occurs when the dimensions of the beam are smaller or similar to the wavelength and the wave front is distorted, generating attenuations of the wave along the propagation axis.

The attenuation is measured by the formula:

$$dB = 20\log\left(\frac{I_1}{I_2}\right) \tag{50}$$

Where I1 and I2 represent the signal intensities before and after attenuation.

The absorption instead is linked to the thermoelastic and hysteresis characteristics of the medium in which the propagation takes place. A wave propagating in the material involves the relative movement of particles. This movement is hindered by the viscosity that transforms some of the energy transmitted by the particles into heat. The absorption can be expressed through the following formula:

$$I_z = I_0 \cdot e^{-\alpha z} \tag{51}$$

Where I_z is the intensity of the beam as a function of the thickness z, I_0 is the intensity at the entrance of the signal and α represents the attenuation coefficient (function of the material) [60].

Refraction and reflection take place when a wave encounters a separation surface with different elastic characteristics. The amount of reflected energy is proportional to the square of the amplitude of the reflected wave [61].

Finally, the interference originates from the superposition of two or more vibrations of equal frequency (or wavelength).

The ultrasonic investigations are regulated by UNI EN 12504-4: 2005 [62] which establishes how to measure the speed of propagation of sound pulses to be reproducible.

2.3.4 Application of ultrasonic waves for damage detection and stress changes

In practical applications, ultrasonic investigations are mostly used to determine elastic characteristics of materials and the presence of cracks, voids and discontinuities also not visible from the surface. This purpose can be achieved by taking into account that the presence of a discontinuity represents, in terms of ultrasonic velocity, a deceleration (change in material characteristics). In these conditions, the preferable path of a wave between the origin and the destination can be non-straight segment, with the result of taking more time for the signal to reach the destination. If the change in material characteristics is strong (e.g. concrete vs. air) the

wave is almost totally stopped, and only the portion of the wave with longer path is received. This phenomenon causes two main effects:

- Increase of the time of flight (time for the wave to go from the generator to the receiver). As a direct consequence, decrease of the apparent speed (straight line between the two transducers, divided by the measured time of flight);
- Increase of the total amount of energy lost in the flight.

The accuracy of the measurement depends on many factors (including the density of the crossed material, humidity, presence of steel reinforcement, etc.). The pulse is emitted by piezoelectric transducers, exploiting the ability of piezoelectric crystals to contract or expand under the action of an electric field. The vibrations of this crystals produce elastic waves that are transferred to the material through the contact of the transducer with the material itself.

With regards to the measure of stress changes, many studies focused mostly on the direct measure on wires. The dependence of the change in wave velocity on stress changes has been utilized in several applications in civil engineering including measurement of residual stress [63][64].

Besides wave velocity, researchers have studied other properties of wave propagation, such as the transmitted ultrasonic energy in terms of the amplitude of the frequency peak and the area under the energy spectrum [65][66]. The relationships of these properties with load are shown for a laboratory test performed by Rizzo on a core wire. Both parameters were found to linearly decrease with increasing tensile stress for a single wire, with a significant decrease in the area under the energy spectrum.

Also in this case, the experimentations found in literature are usually limited to the direct applications to single strands. When applied to an assembled strand, the results did not show linear behavior. It should be noted that the sensing mechanism requires direct access to the ends of the strands, thereby limiting the application to shorter strands due to attenuation concerns, up to a few meters long. No investigations or site implementations of this method have been reported for direct application to concrete matrix.

3 Experimental campaign

The experimental campaign described in the present paper took place at the laboratory for Test on Construction Materials of University of Padova, in Italy.

The campaign was subdivided in two main phases, and considering in total 6 beams. The first phase is related to Beam 1, Beam 2 and Beam 3, characterized by adherent cable prestressed concrete; the second phase is related to Beam 4, Beam 5 and Beam 6, characterized by post-tensioned concrete, with cables inserted in plastic ducts. In the following pages, the 6 beams are mentioned with the numbering summarized in the following table.

The characteristics of the beams were defined based on similarity with other similar experimental campaigns found in literature. All the parameters, included shrinkage and creep, were estimated with a pre-calculation before the production of the beams.

Table 2: Nomenclature of the beams

Name	Phase	Characteristics
Beam 1	1	Pre-tensioned
Beam 2	1	Pre-tensioned
Beam 3	1	Pre-tensioned
Beam 4	2	Post-tensioned
Beam 5	2	Post-tensioned
Beam 6	2	Post-tensioned

3.1 First phase: pre-tensioned prestressed concrete

3.1.1 Geometry

The first phase was related to the test of 3 reinforced concrete rectangular beam with prestressing adherent straight cables. The beams had the following common characteristics:

3. Fixed rectangular section 200 mm (base) x 300 mm (height);
4. Length (end to end) 6000 mm;
5. Regular reinforcement: 4 longitudinal bars, diameter 8 mm, at the 4 corners of the rectangular section (concrete cover 25 mm);
6. Regular reinforcement: rectangular stirrups, diameter 8 mm, at distance of 100 mm along all the length of the beam, except for the bearing length, where the distance is brought to 50 mm in order to avoid shear failure during the static tests;

7. Prestressing reinforcement: one strand made with 7 wires, equivalent diameter 6/10", straight course. Eccentricity of the strand at 80 mm from the barycenter of the section (70 mm from the bottom of the beam).

The 3 beams owned the same characteristics, apart from the level of prestressing of the cable, that was applied before the cast of the concrete. The level of prestressing and other main characteristics of the 3 prestressed beams are listed in the following table.

Table 3: Main geometrical characteristics of Beams 1, 2 and 3

Name	Beam 1	Beam 2	Beam 3
Concrete section (mm^2)	60.000	60.000	60.000
Ordinary steel (mm^2)	201	201	201
Prestressing steel (mm^2)	139	139	139
Prestressing force* (kN)	70	140	190
Prestress on concrete* (MPa)	1,13	2,27	3,07

*At the phase 0.

In the following figure are described the main geometrical characteristics of the 3 beams belonging to the first phase. As said, the geometrical dimensions are identical for the 3 beams, being the prestressing force applied to the cable the only difference.

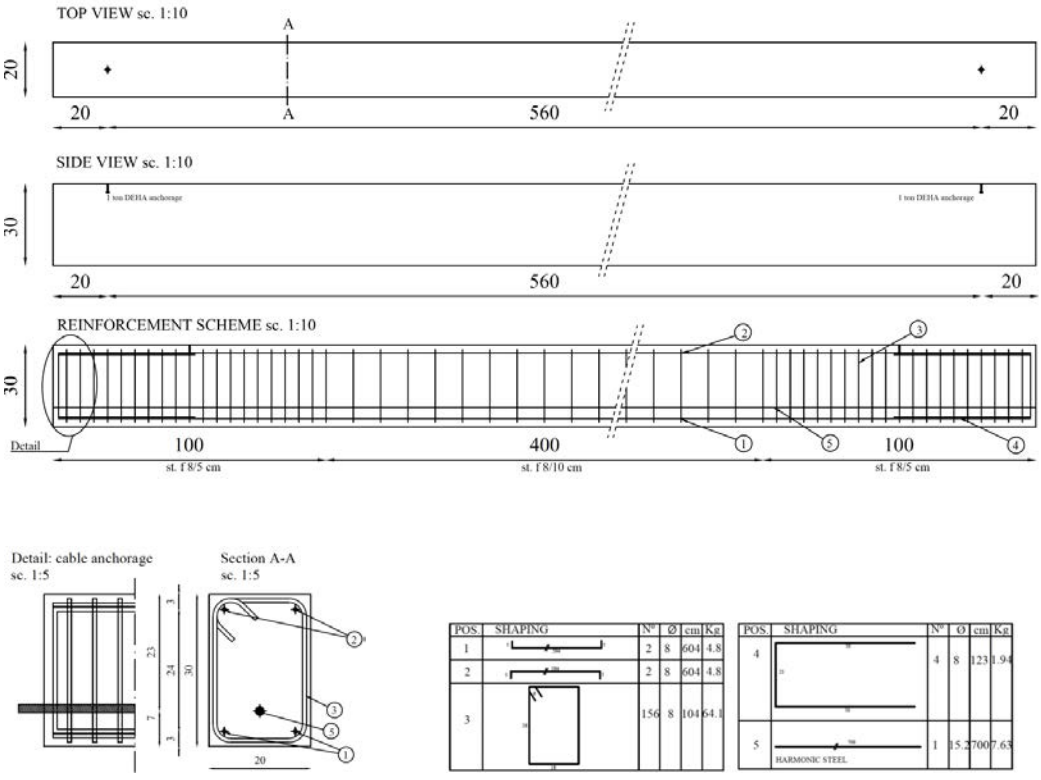

Figure 3.1: Beams 1, 2 and 3: geometrical and reinforcement dimensions (not to scale)

3.1.2 Materials

Three different materials were used to build the beams: concrete, ordinary reinforcement steel and prestressing steel.

The concrete was cast at the Castelvetro prefabrication plant of RDB Italprefabbricati. The mix design of the concrete utilized a water/cement ratio of 0,47, the use of Cement R525 S3 and 1720 kg of gravel/sand over 1 cubic meter of finite product.

The results on the compressive tests of concrete samples taken from the cast are reported in the following table.

Table 4: Concrete compressive test results

Beam reference	Curing days	R [MPa]
Beam 1	56	68.1
Beam 1	56	69.9
Beam 2	55	66.7
Beam 2	55	65.7
Beam 3	51	65.5
Beam 3	51	65.0

By taking into account the formulation given by the Italian Construction Code (§ 11.2.5 NTC 2018) a characteristic value of cylindrical strength of f_{ck} = 52 MPa is obtained.

For the reinforcement of the beam the ordinary B450C reinforcement steel was used, with a nominal yield strength of 450 MPa and a failure strength of 540 MPa.

The tensile tests performed on 3 samples of steel taken from the same production lot gave the following results, with an average resistance of 512 MPa.

Table 5: Ordinary steel tensile test results

Sample reference	Yield strength [MPa]	Failure strength [MPa]	Elongation [%]
Sample 1	509	611	9.3
Sample 2	515	615	11.5
Sample 3	513	608	9.8

For the prestressing cable, prestessing steel was used, with a nominal strength at 1% of total elongation ($fp_{(1)k}$) of 1670 MPa and a failure strength of 1860 MPa.

The tensile tests performed on 3 samples of steel taken from the same production lot gave the following results, with an average resistance of 1703 MPa.

Table 6: Prestressing steel tensile test results

Sample reference	Effective diameter [mm]	Section [mm2]	fp(1)k [MPa]	Failure strength [MPa]	Elongation [%]	Elastic modulus [MPa]
Sample 1	13.3	139.3	1703	1930	6.9	195145
Sample 2	13.4	140.5	1700	1921	5.7	199824
Sample 3	13.4	140.6	1707	1925	6.5	196444

3.1.3 Test set-up

In the present chapter the procedure of test of the first 3 beams (first phase) is presented.

The test program includes a series of load cycles (load-unload) up to the failure of each beam, with contemporary measurement of the following static parameters: longitudinal deformation, vertical displacement and vertical force applied. Between one cycle and another non-destructive measurements were taken, described in the following chapter. This chapter describes the procedure for load tests, the set up and the instrumentation used to follow the loading process up to failure.

The beams were positioned on two steel supports (with a height of 50cm each) placed at a distance of 200 mm from the end, bringing the effective length between supports being 5600 mm.

Between each steel support and the concrete surface a steel hinge was placed, with the same width of the beam (200 mm) in order to simulate the static scheme of simple supported beam. The supports were positioned in order to avoid any relative movement of the different parts, and in order to avoid any damping during vibration tests (see following chapters).

The load test was performed through a bending test in which the vertical load is induced by a hydraulic jack applied to a steel portal, and is transmitted to the beam by means of a stiff steel beam. The steel beam had a length of 2100 mm. The hydraulic jack applied a concentrated load at the center of the beam, which transmitted the load in 2 points with a distance of 900 mm from the center of the beam. At the interface between the distribution steel beam and the upper

concrete surface 20 mm thick plates were positioned, in order to distribute the concentrated load on a 150x200 mm^2 area. Other two steel hinges were added at the bottom of the distribution beam, in order to allow mutual rotation. At the points of application of the load, a mortar cast was set up in order to assure the perfect contact of the partition plate on the concrete surface. In the following picture the test set up is summarized.

The reading of the applied force is done through two load cells: one with a capacity of 30 ton connected to the automatic acquisition system and one with a capacity of 10 ton connected to the acquisition system).

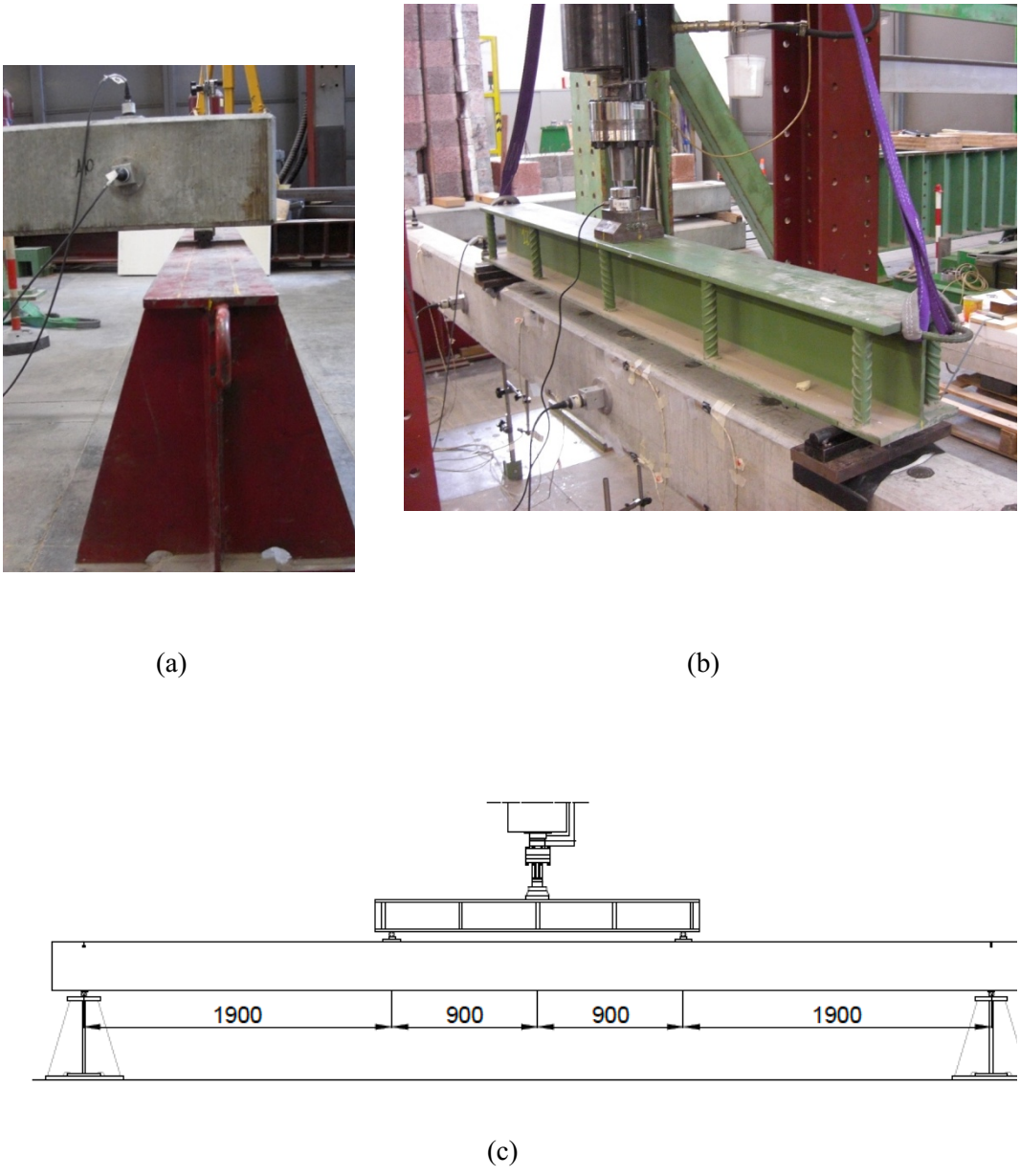

(a) (b)

(c)

Figure 3.2: (a) Bearing system; (b) load distribution beam; (c) whole system: side view

Figure 3.3: load cells utilized in the system. Upper cell with 30 ton capacity; lower cell with 10 ton capacity

Table 7: 10 ton load cell characteristics

Model	CBL 10000 (LAUMAS)
Weight [kg]	1.1
Material	Stainless steel 17-4 PH
Nominal load [kg]	10000
Combined error	≤±0.03%
Deflection at nominal load [mm]	0.4
Sensitivity	2mV/V ± 0.1%
Field of working temperature	-20°C/+70°C

In order to measure the vertical deflection due to the applied load, 5 LVDT (Linear Variable Differential Transformer) were used.

For the purpose of the test, they were fixed inside a magnetic support placed on the ground (or on the steel supports in correspondence to the two bearings). The probe of the instrument was placed in contact with the surface of the beam.

Two transducers were positioned in correspondence to the supports, one at the center of the span and two at the two points of application of the load, as schematized in the following figure. In order to measure the longitudinal deformation, 8 strain gauges were positioned along the beam in 4 couples, one at the upper side and one at the lower side of the beam, at 25 mm from

the upper and lower surface respectively. The 4 sections were identified at the center of the span, at 450 mm from the center in both direction, and at 1150 mm from one of the two bearing. The purpose of the disposition is to measure the bending deformation at the beam at significant points.

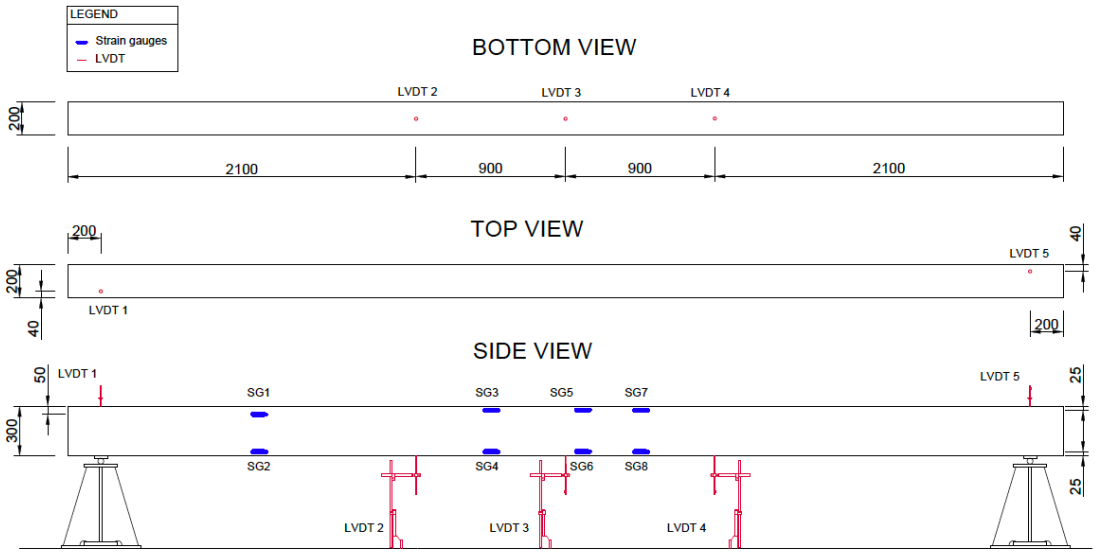

Figure 3.4: position of LVDT and strain gauges

For Beam 3, the 8 strain gauges were substituted with 8 DD1, a compact high-precision deformation transducer that converts the movement of the probe tip into an electrical signal.

(a) (b)

Figure 3.5: (a) LVDT at supports; (b) LVDT in the central part of the span

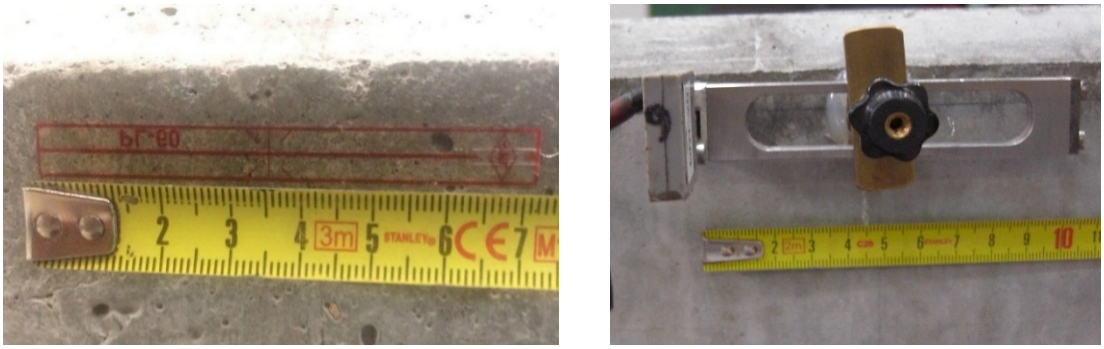

(a) (b)

Figure 3.6: (a) strain gauges; (b) DD1

The acquisition system utilized for the static test is the HBM Spider8, an electronic measuring system for PCs for electric measurement of mechanical variables such as strain, force, pressure, path, acceleration and for temperatures. It can manage all measurement tasks with S/G in quarter, half or full bridge connection.

All the signal conditioning – excitation for passive transducers and amplification, digitalization, computer interface and connection technology for a maximum of 8 channels – is combined in one. Spider8 is connected to the computer via the printer port or via an RS232 interface.

The software utilized for the data acquisition is the CATMAN DAQ Software.

Figure 3.7: Acquisition system for static tests

3.1.4 Static test procedure

For each beam several load cycles have been carried out, that consisted in incremental load with constant speed of load increase, followed by a stationary phase and then unload with constant speed of load decrease, until total unloading. In the following table the load steps for every beam of the first phase are summarized.

Table 8: Load steps for the beams 1, 2 and 3

CYCLE	BEAM 1		BEAM 2		BEAM 3	
	Load [kN]	% of max load	Load [kN]	% of max load	Load [kN]	% of max load
0	0	0,00%	0	0,00%	0	0,00%
1	20	35,54%	18,62	27,60%	25,77	36,54%
2	11,87	21,09%	26,46	39,22%	35,66	50,57%
3	18,67	33,18%	35,29	52,31%	45,76	64,89%
4	26,05	46,29%	45,13	66,90%	70,52	100,00%
5	34,61	61,51%	65,27	96,75%		
6	45,08	80,11%	67,46	100,00%		
7	56,27	100,00%				

In the phase in which the load was kept fixed, the path of the visible cracks was traced, in order to observe the evolution of the cracking pattern with the increase of load applied.

3.1.5 Beam 1: static tests results

This test concerns the beam with the lowest prestressing force, equal to 70 kN.

Table 9 and Table 10 show the maximum values of displacements and deformations obtain from the load cycles applied to the beam, through the load applied to the beam at +0,9 m and -0,9 m from the barycenter.

Table 9: Maximum displacement values for every load cycle – beam 1

Cycle	U_{max} LVDT 1 [mm]	U_{max} LVDT 2 [mm]	U_{max} LVDT 3 [mm]	U_{max} LVDT 4 [mm]	U_{max} LVDT 5 [mm]
1	-0,004297	5,199	5,454	5,809	-0,03868
3	-0,006072	9,737566	10,15981	10,52142	-0,06072
4	0,001778	14,63	15,38	15,98	-0,1124
5	0,029681	24,20182	24,93229	26,1475	-0,2416
6	-0,00129	40,59	41,83	42,94	-0,186
7	-0,1991	46,504	44,5	44,384	-0,3214

Table 10: Maximum deformation values for every load cycle – beam 1

Cycle	$\varepsilon_{1\ max}$ SG1 [mm/m]	$\varepsilon_{2\ max}$ SG2 [mm/m]	$\varepsilon_{3\ max}$ SG3 [mm/m]	$\varepsilon_{4\ max}$ SG4 [mm/m]	$\varepsilon_{5\ max}$ SG5 [mm/m]
1	-0,034	0,038	-0,119	1,065	-0,127
3	-0,054	0,060	-0,189	2,059	-0,202
4	-0,075	0,083	-0,262	3,122	-0,280
5	-0,104	0,409	-0,344	5,439	-0,362
6	-0,198	1,028	-0,418	8,237	-0,453
7	-0,251	2,176	-0,469	11,17	-0,534

The graph in Figure 3.8 shows the curve load-displacement for LVDT 3 (center of the span). As it can be seen, up to around 12 kN of applied force the graph trend is linear and no relevant event is noted. When the load increases, a slight drop in stiffness is initially evident, and once the steel yield is reached, a further reduction in the stiffness can be observed.

The graph in Figure 3.9 shows instead the absolute displacements of LVDTs n. 2, 3 and 4 with respect to the average displacements measured at the supports n. 1 and 5 (that are anyhow relatively small with respect to the n. 2, 3 and 4).

Except for the last cycle (failure step) where the instrumentation was disturbed by the excessive deformation of the beam, it is clear how with the increase of the force the increase of displacement is non-linear (larger space between consecutive steps).

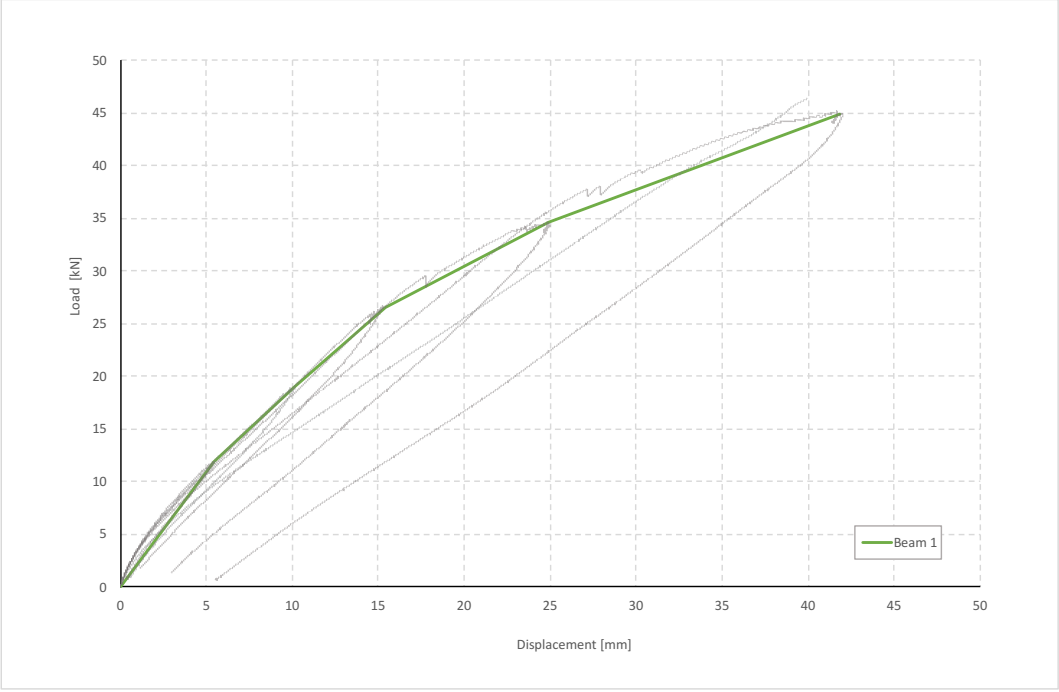

Figure 3.8: Load-displacement curve for Beam 1 – LVDT 3 (center of the beam)

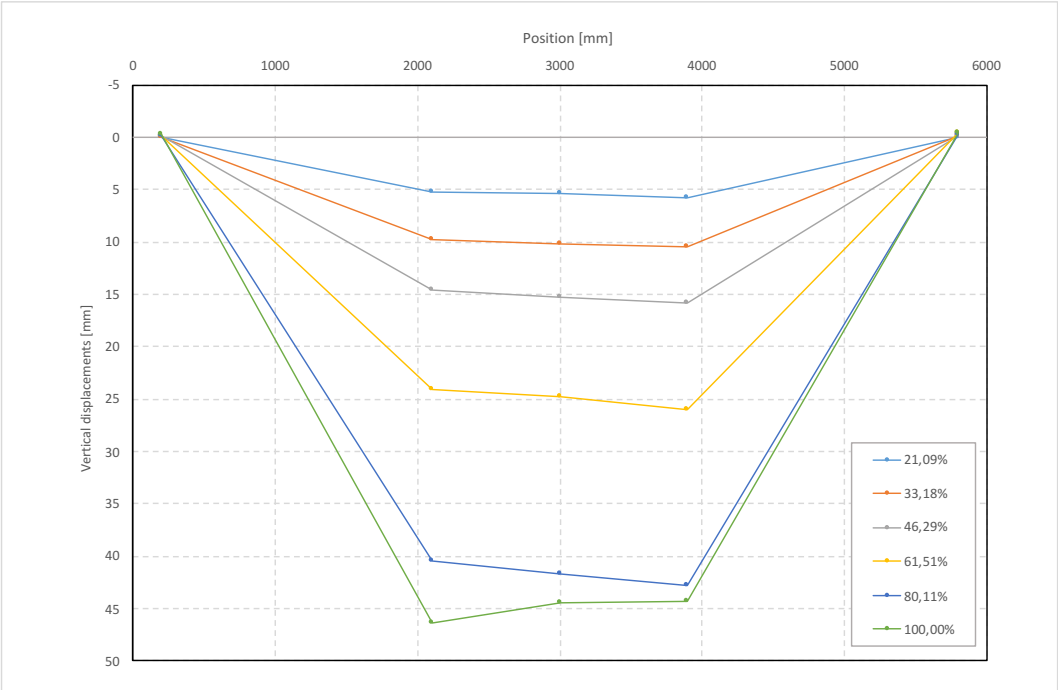

Figure 3.9: Displacement-position schemes for Beam 1

Figure 3.10: Load process of Beam 1

Depending on the position along the beam and on the load applied, the neutral axis will change accordingly. With the deformation values recorded by the strain gauges for the various load cycles it was possible to represent its variation. The results here reported already take into account the contribution of the prestressing, which was not measured since already present at the installation of the instrumentation. The contribution was then calculated theoretically.

Table 11: Neutral axis for every load cycle – beam 1

SG1-SG2	Cycle 2	Cycle 3	Cycle 4	Cycle 5	Cycle 6	Cycle 7
$\varepsilon_{c,sup}$	-0,06172	-0,08563	-0,11125	-0,17606	-0,34192	-0,51485
$\varepsilon_{c,inf}$	0,022262	0,04795	0,075165	0,437194	1,127971	2,395622
Neutral axis [mm]	220,4786	192,3135	179,0382	86,12876	69,78475	53,06893
SG3-SG4	Cycle 2	Cycle 3	Cycle 4	Cycle 5	Cycle 6	Cycle 7
$\varepsilon_{c,sup}$	-0,28439	-0,46044	-0,64694	-0,96928	-1,32979	-1,67996
$\varepsilon_{c,inf}$	1,186302	2,286398	3,462768	6,01974	9,105147	12,33617
Neutral axis [mm]	58,01156	50,28754	47,22502	41,60596	38,23095	35,95779
SG5-SG6	Cycle 2	Cycle 3	Cycle 4	Cycle 5	Cycle 6	Cycle 7
$\varepsilon_{c,sup}$	-0,25146	-0,39882	-0,55341	-0,83943	-1,09952	-1,3167
$\varepsilon_{c,inf}$	0,718112	1,43874	2,204795	4,367353	6,129471	7,556912
Neutral axis [mm]	77,80583	65,11148	60,19206	48,36554	45,62971	44,51505
SG7-SG8	Cycle 2	Cycle 3	Cycle 4	Cycle 5	Cycle 6	Cycle 7
$\varepsilon_{c,sup}$	-0,26892	-0,44274	-0,63513	-0,93188	-1,27819	-1,69866
$\varepsilon_{c,inf}$	0,922192	1,876591	2,964808	5,007622	7,315417	10,68166
Neutral axis [mm]	67,73105	57,26754	52,92831	47,06856	44,62125	41,162

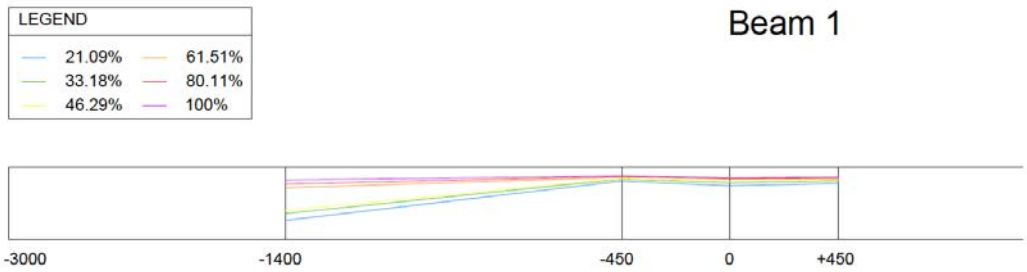

Figure 3.11: Graphical representation of neutral axis variation in the measured sections - Beam 1

A higher deformation and a higher position of the neutral axis are observed for central strain gauges. Moreover, the neutral axis position is nearer to the upper edge for higher load rate.

The variation of the neutral axis position is consistent with the theoretical results. In particular, for low amounts of external force, the neutral axis is low, and its position goes upward with the increase of the load. This is due to the presence of the prestressing load and moment, which contribution tends to keep down the neutral axis.

The next figure shows the cracking state when the increase of the load. As it can be seen, the beam already presented a crack pattern before the beginning of the load tests. This phenomenon was detected only at the two side faces. For this reason, the crack pattern was recorded but it was assumed that its presence doesn't give contribution to the flexural behavior of the beam in the following load steps.

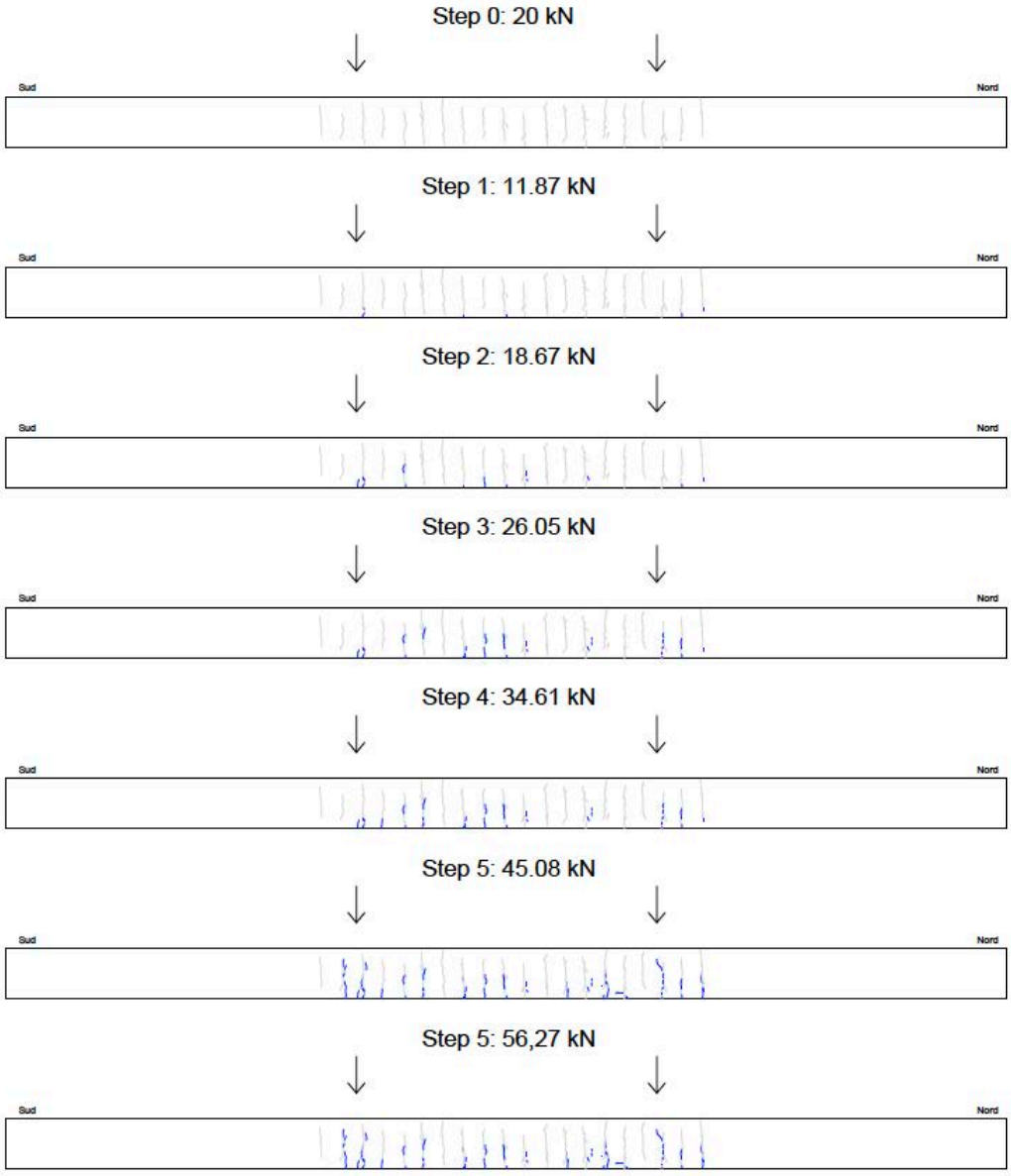

Figure 3.12: Evolution of crack pattern - Beam 1

3.1.6 Beam 2: static tests results

This test concerns the beam with the prestressing force equal to 140 kN.

Table 12 and Table 13 show the maximum values of displacements and deformations obtain from the load cycles applied to the beam, through the load applied to the beam at +0,9 m and -0,9 m from the barycenter.

Table 12: Maximum displacement values for every load cycle – beam 2

Cycle	U_{max} LVDT 1 [mm]	U_{max} LVDT 2 [mm]	U_{max} LVDT 3 [mm]	U_{max} LVDT 4 [mm]	U_{max} LVDT 5 [mm]
1	-0,107	3,646	3,676	3,867	-0,22537
2	-0,154	6,361	6,274	6,474	-0,26839
3	-0,21	14,26	14,99	15,37	-0,45316
4	-0,197	23,47	24,47	25,43	-0,637
5	-0,113	-	-	-	-1,331
6	-0,106	-	-	-	-1,249

Table 13: Maximum deformation values for every load cycle – beam 2

Cycle	$\varepsilon_{1\ max}$ SG1 [mm/m]	$\varepsilon_{2\ max}$ SG2 [mm/m]	$\varepsilon_{3\ max}$ SG3 [mm/m]	$\varepsilon_{4\ max}$ SG4 [mm/m]
1	-0,063	0,063	-0,135	0,120
2	-0,082	0,088	-0,230	0,931
3	-0,107	0,120	-0,388	2,342
4	-0,137	0,223	-0,502	3,803
5	-0,261	1,196	-0,737	12,395
6	-0,237	0,999	-0,660	9,053

Cycle	$\varepsilon_{5\ max}$ SG5 [mm/m]	$\varepsilon_{6\ max}$ SG6 [mm/m]	$\varepsilon_{7\ max}$ SG7 [mm/m]	$\varepsilon_{8\ max}$ SG8 [mm/m]
1	-0,150	0,115	-0,142	0,142
2	-0,271	1,273	-0,233	0,955
3	-0,465	4,816	-0,375	2,221
4	-0,607	6,581	-0,493	3,674
5	-0,961	18,570	-0,812	14,784
6	-0,852	15,879	-0,713	11,456

The graph in Figure 3.13 shows the curve load-displacement for LVDT 3 (center of the span). As it can be seen, up to around 27 kN of applied force the graph trend is linear and no relevant event is noted. When the load increases, a slight drop in stiffness is initially evident, and once the steel yield is reached, a further reduction in the stiffness can be observed.

The graph in Figure 3.14 shows instead the absolute displacements of LVDTs n. 2, 3 and 4 with respect to the average displacements measured at the supports n. 1 and 5 (that are anyhow relatively small with respect to the n. 2, 3 and 4). Except for the last cycle (failure step) where the instrumentation was disturbed by the excessive deformation of the beam, it is clear how with the increase of the force the increase of displacement is non-linear (larger space between consecutive steps).

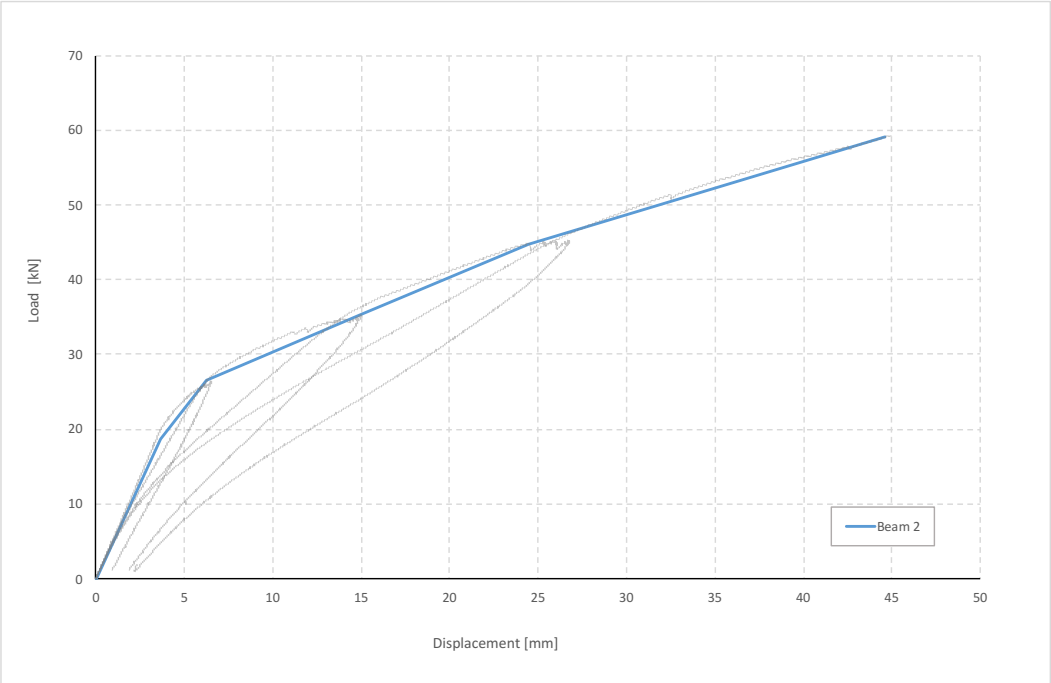

Figure 3.13: Load-displacement curve for Beam 2 – LVDT 3 (center of the beam)

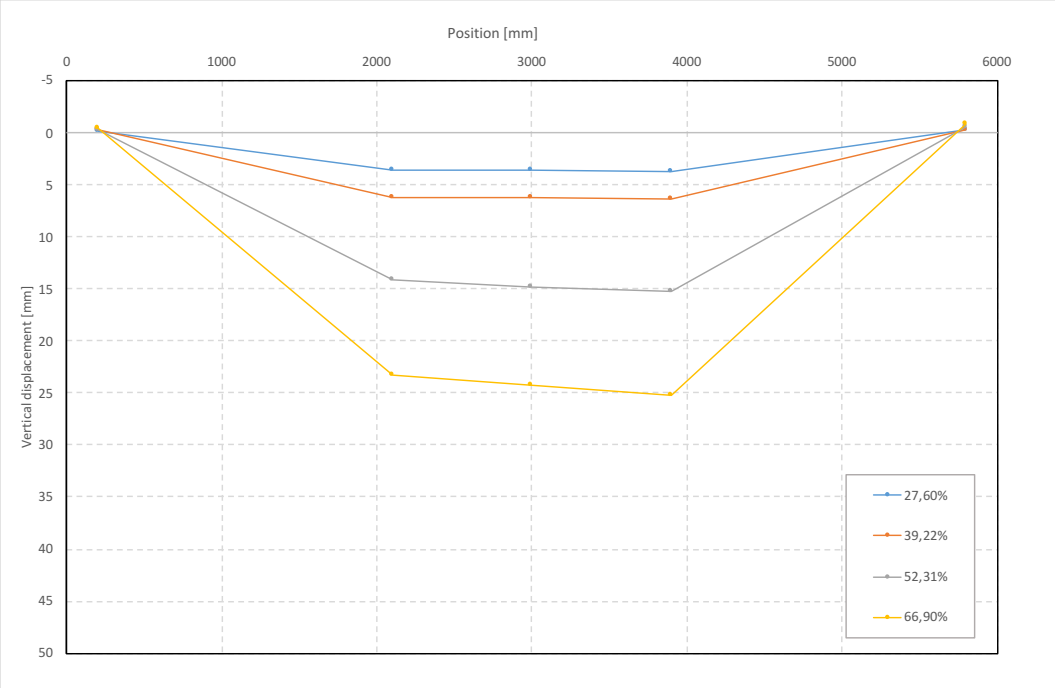

Figure 3.14: Displacement-position schemes for Beam 2

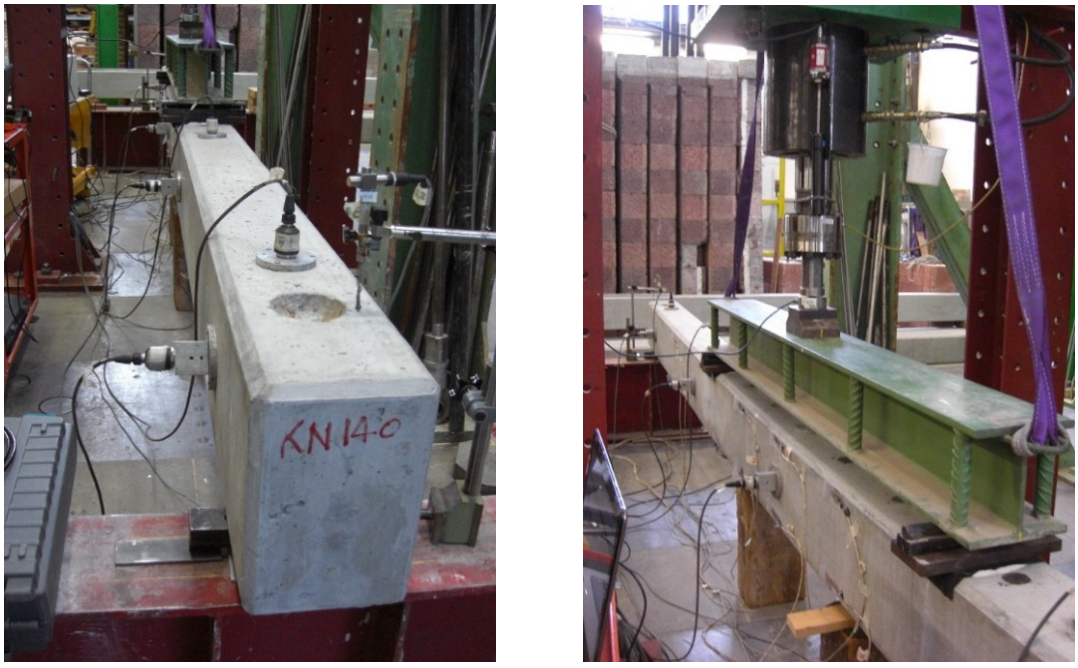

Figure 3.15: Load process of Beam 2

Depending on the position along the beam and on the load applied, the neutral axis will change accordingly. With the deformation values recorded by the strain gauges for the various load cycles it was possible to represent its variation. The results here reported already take into account the contribution of the prestressing, which was not measured since already present at the installation of the instrumentation. The contribution was then calculated theoretically.

Table 14: Neutral axis for every load cycle – beam 2

SG1-SG2	Cycle 1	Cycle 2	Cycle 3	Cycle 4	Cycle 5	Cycle 6
$\varepsilon_{c,sup}$	-0,09799	-0,12665	-0,16459	-0,22445	-0,59218	-0,51889
$\varepsilon_{c,inf}$	-0,00797	0,021904	0,060379	0,178129	1,272731	1,050631
Neutral axis [mm]	326,5479	255,7675	219,4836	167,2585	95,26092	99,18132
SG3-SG4	Cycle 1	Cycle 2	Cycle 3	Cycle 4	Cycle 5	Cycle 6
$\varepsilon_{c,sup}$	-0,19323	-0,3786	-0,69371	-0,96492	-2,08296	-1,66451
$\varepsilon_{c,inf}$	0,085809	0,987791	2,555417	4,173737	13,64803	9,964282
Neutral axis [mm]	207,7443	83,12377	64,05229	56,33284	39,72345	42,94112
SG5-SG6	Cycle 1	Cycle 2	Cycle 3	Cycle 4	Cycle 5	Cycle 6
$\varepsilon_{c,sup}$	-0,21075	-0,4594	-1,02695	-1,35986	-2,94784	-2,55961
$\varepsilon_{c,inf}$	0,083338	1,369158	5,285985	7,241324	20,46432	17,49312
Neutral axis [mm]	214,9851	75,3704	48,80212	47,43054	37,77317	38,29316
SG7-SG8	Cycle 1	Cycle 2	Cycle 3	Cycle 4	Cycle 5	Cycle 6
$\varepsilon_{c,sup}$	-0,20368	-0,38435	-0,66746	-0,94224	-2,4046	-1,96284
$\varepsilon_{c,inf}$	0,110658	1,0143	2,421106	4,031167	16,284	12,61318
Neutral axis [mm]	194,3908	82,44097	64,83177	56,83691	38,6	40,39863

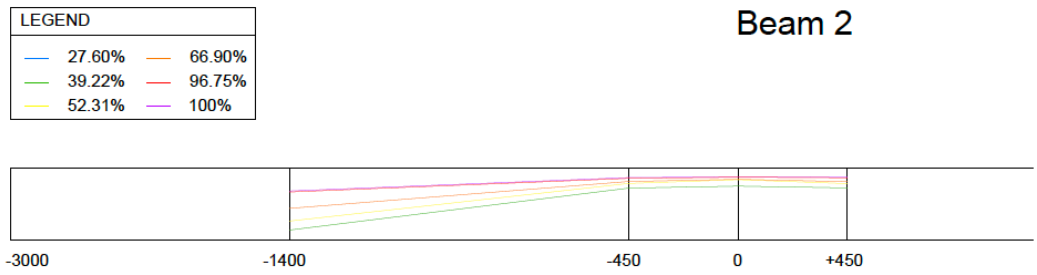

Figure 3.16: Graphical representation of neutral axis variation in the measured sections - Beam 2

A higher deformation and a higher position of the neutral axis are observed for central strain gauges. Moreover, the neutral axis position is nearer to the upper edge for higher load rate.

The variation of the neutral axis position is consistent with the theoretical results. In particular, for low amounts of external force, the neutral axis is low, and its position goes upward with the increase of the load. This is due to the presence of the prestressing load and moment, which contribution tends to keep down the neutral axis.

The next figure shows the cracking state when the increase of the load. As it can be seen, the beam already presented a crack pattern before the beginning of the load tests. This phenomenon was detected only at the two side faces. For this reason, the crack pattern was recorded but it was assumed that its presence doesn't give contribution to the flexural behavior of the beam in the following load steps.

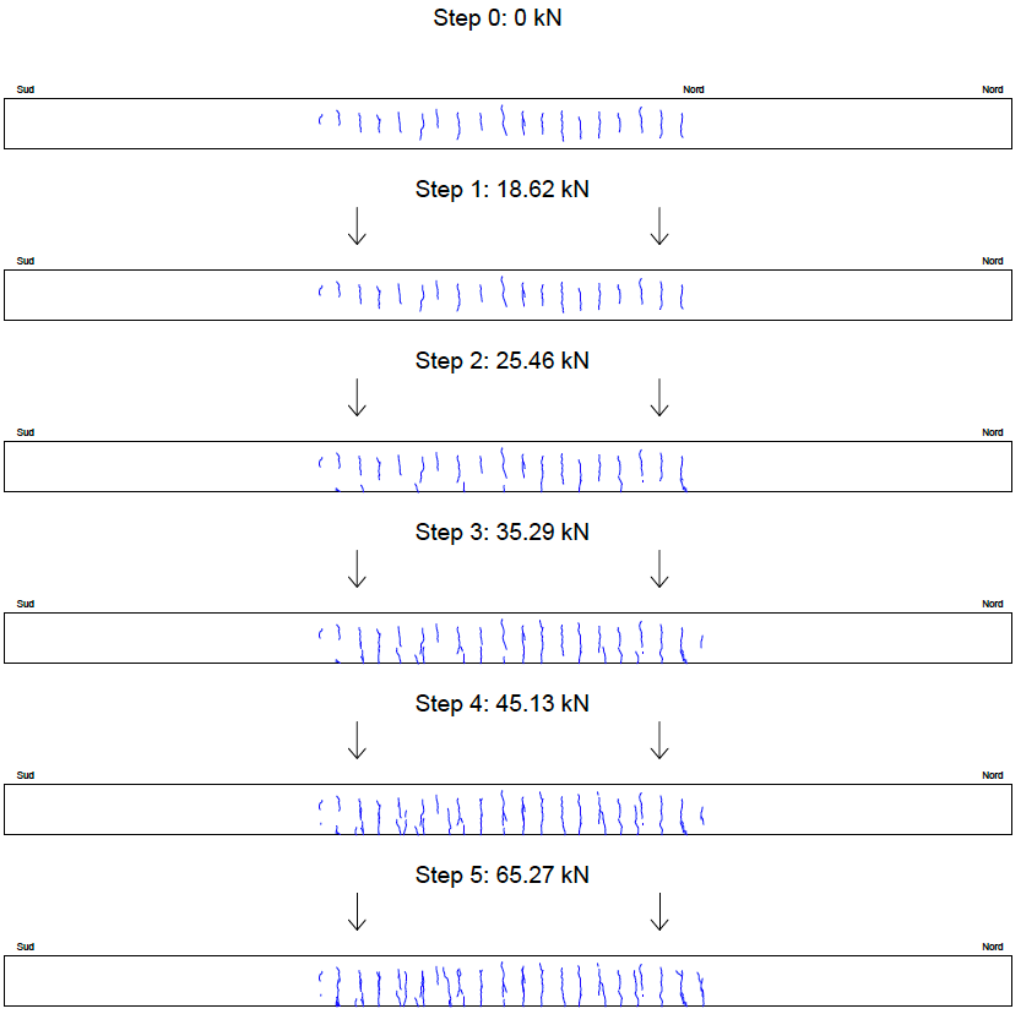

Figure 3.17: Evolution of crack pattern - Beam 2

3.1.7 Beam 3: static tests results

This test concerns the beam with the highest prestressing force, equal to 190 kN.

Table 15 and Table 16 show the maximum values of displacements and deformations obtain from the load cycles applied to the beam, through the load applied to the beam at +0,9 m and -0,9 m from the barycenter.

Table 15: Maximum displacement values for every load cycle – beam 3

Cycle	U_{max} LVDT 1 [mm]	U_{max} LVDT 2 [mm]	U_{max} LVDT 3 [mm]	U_{max} LVDT 4 [mm]	U_{max} LVDT 5 [mm]
1	0,174	4,688	4,688	4,828	-0,059
2	0	8,271875	8,378125	8,63125	-0,15873
3	0	17,8687	18,1844	18,54063	-0,19
4	0	-	-	-	-0,295

Table 16: Maximum deformation values for every load cycle – beam 3

Cycle	$\varepsilon_{1\ max}$ SG1 [mm/m]	$\varepsilon_{2\ max}$ SG2 [mm/m]	$\varepsilon_{3\ max}$ SG3 [mm/m]	$\varepsilon_{4\ max}$ SG4 [mm/m]
1	-0,380	-0,130	-0,200	-0,080
2	1,618	0,130	0,220	0,130
3	-0,388	-0,138	-0,208	-0,088
4	1,505	0,017	0,107	0,017

Cycle	$\varepsilon_{5\ max}$ SG5 [mm/m]	$\varepsilon_{6\ max}$ SG6 [mm/m]	$\varepsilon_{7\ max}$ SG7 [mm/m]	$\varepsilon_{8\ max}$ SG8 [mm/m]
1	-0,380	-0,130	-0,200	-0,080
2	1,618	0,130	0,220	0,130
3	-0,388	-0,138	-0,208	-0,088
4	1,505	0,017	0,107	0,017

The graph in Figure 3.18 shows the curve load-displacement for LVDT 3 (center of the span). As it can be seen, up to around 27 kN of applied force the graph trend is linear and no relevant event is noted. When the load increases, a slight drop in stiffness is initially evident, and once the steel yield is reached, a further reduction in the stiffness can be observed.

The graph in Figure 3.19 shows instead the absolute displacements of LVDTs n. 2, 3 and 4 with respect to the average displacements measured at the supports n. 1 and 5 (that are anyhow relatively small with respect to the n. 2, 3 and 4).

Except for the last cycle (failure step) where the instrumentation was disturbed by the excessive deformation of the beam, it is clear how with the increase of the force the increase of displacement is non-linear (larger space between consecutive steps).

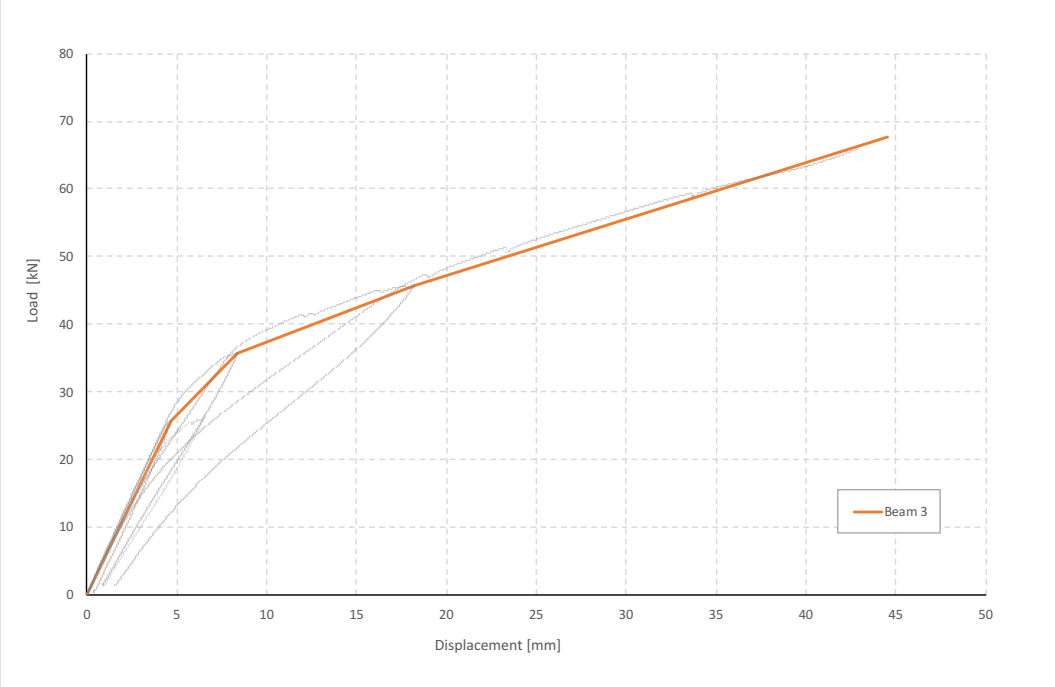

Figure 3.18: Load-displacement curve for Beam 3 – LVDT 3 (center of the beam)

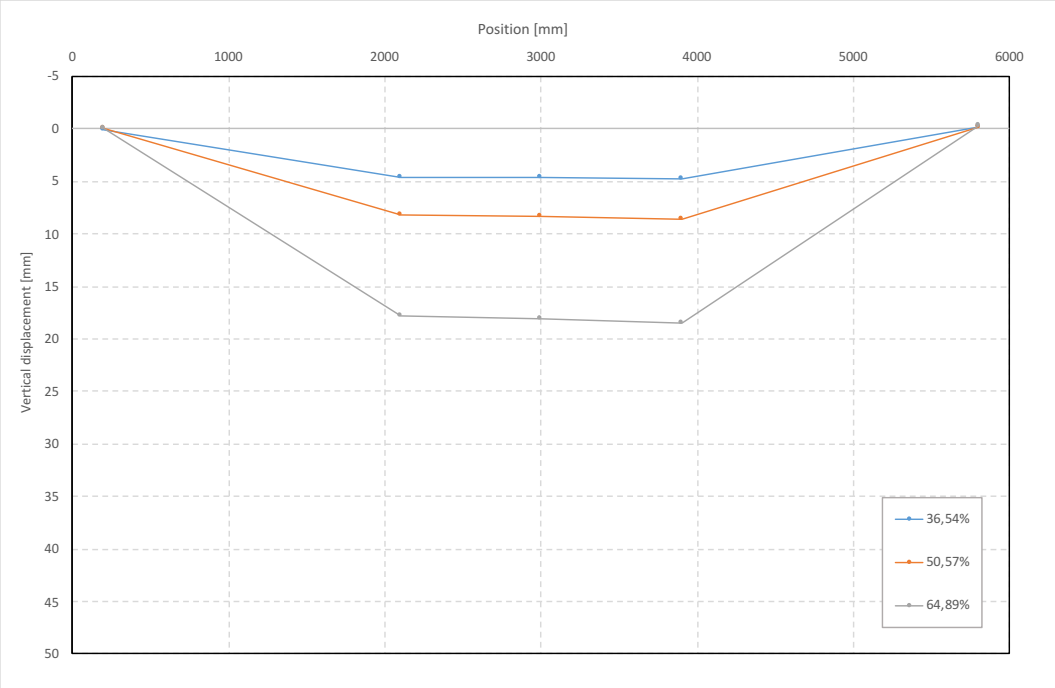

Figure 3.19: Displacement-position schemes for Beam 3

Figure 3.20: Load process of Beam 3

Depending on the position along the beam and on the load applied, the neutral axis will change accordingly. With the deformation values recorded by the strain gauges for the various load cycles it was possible to represent its variation. The results here reported already take into account the contribution of the prestressing, which was not measured since already present at the installation of the instrumentation. The contribution was then calculated theoretically.

Table 17: Neutral axis for every load cycle – beam 3

SG1-SG2	Cycle 1	Cycle 2	Cycle 3	Cycle 4
$\varepsilon_{c,sup}$	-0,36153	-0,15117	-0,19797	-0,44941
$\varepsilon_{c,inf}$	-0,66571	0,029925	0,069525	0,708965
Neutral axis [mm]	-356,551	250,4252	222,0254	116,3893
SG3-SG4	Cycle 1	Cycle 2	Cycle 3	Cycle 4
$\varepsilon_{c,sup}$	-0,98609	-0,45632	-0,76165	-1,78337
$\varepsilon_{c,inf}$	-0,86707	1,052653	1,771294	7,471014
Neutral axis [mm]	2485,36	90,72172	90,20959	57,81173
SG5-SG6	Cycle 1	Cycle 2	Cycle 3	Cycle 4
$\varepsilon_{c,sup}$	-0,17971	-0,50326	-0,90171	-2,65864
$\varepsilon_{c,inf}$	0,158219	1,253832	3,332782	17,89267
Neutral axis [mm]	159,5412	85,92461	63,88308	38,80983
SG7-SG8	Cycle 1	Cycle 2	Cycle 3	Cycle 4
$\varepsilon_{c,sup}$	-0,12761	-0,41353	-0,65081	-1,35875
$\varepsilon_{c,inf}$	0,057654	0,941974	2,025654	7,019394
Neutral axis [mm]	206,6421	91,52303	72,94845	48,6535

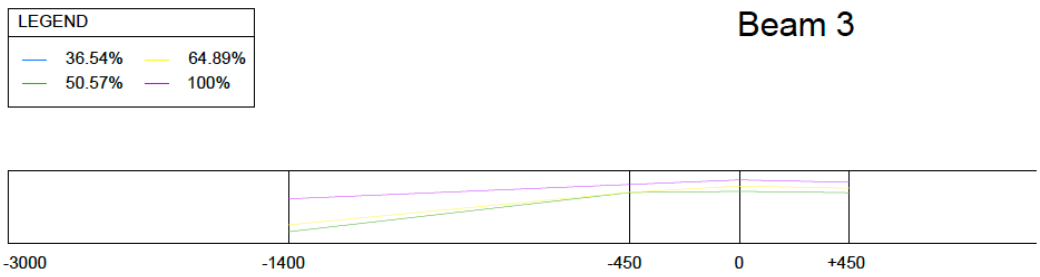

Figure 3.21: Graphical representation of neutral axis variation in the measured sections - Beam 3

A higher deformation and a higher position of the neutral axis are observed for central strain gauges. Moreover, the neutral axis position is nearer to the upper edge for higher load rate.

The variation of the neutral axis position is consistent with the theoretical results. In particular, for low amounts of external force, the neutral axis is low, and its position goes upward with the increase of the load. This is due to the presence of the prestressing load and moment, which contribution tends to keep down the neutral axis.

The next figure shows the cracking state when the increase of the load. As it can be seen, the beam already presented a crack pattern before the beginning of the load tests, probably due to shrinkage issues.

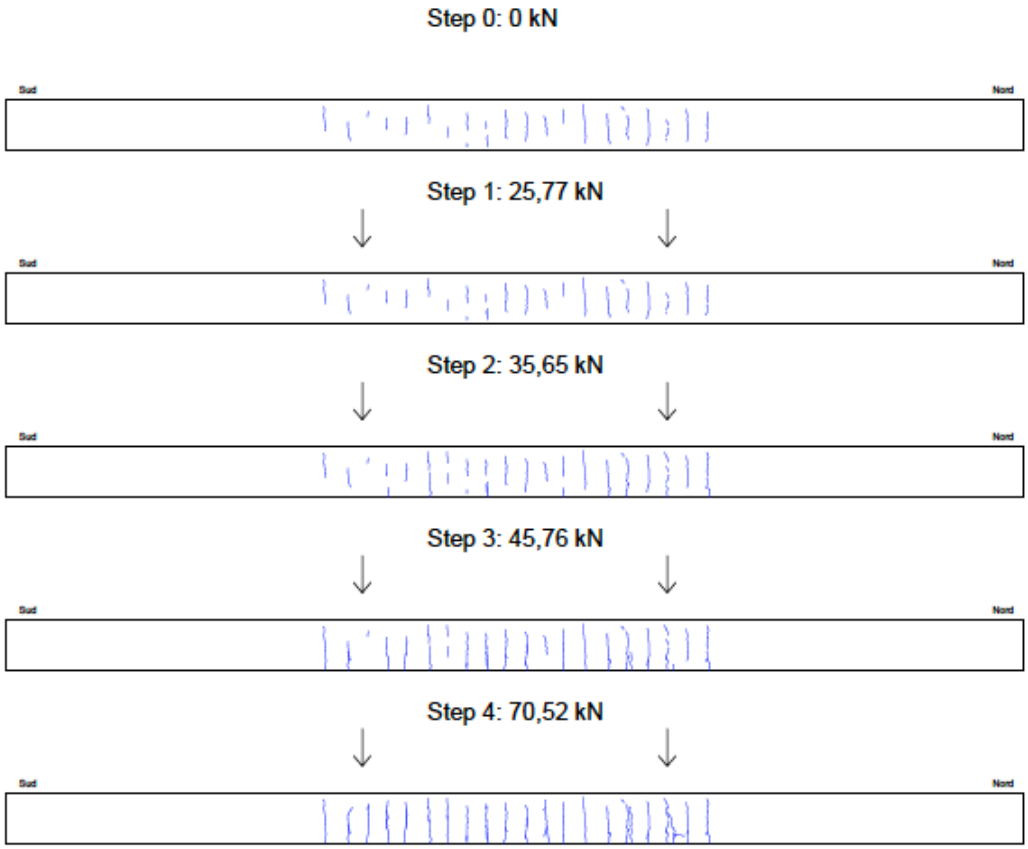

Figure 3.22: Evolution of crack pattern - Beam 3

3.1.8 Comparison of static results

In the following pages are compared the results of static quantities for the Beam 1, Beam 2 and Beam 3. The results are also compared to the theoretical values of solicitations and deformations obtained from analytical models.

The purpose is to assess the accuracy of the analytical models with respect to the experimental results, and to verify the variation on mechanical quantities with the increase on prestressing.

In Figure 3.23 the Ultimate Moment-Prestressing force relationship is shown. The prestressing force is expressed as a percentage of the maximum force that can be applied to the cable (190 kN in this case). It is seen how the experimental resistant moment values are close to the theoretical ones calculated for the three different prestressing forces.

In Figure 3.24, Figure 3.25 and Figure 3.26 the Load-Displacement graphs are plotted with reference to the mid-span point and to the 2 load application points (at -0,9 and +0,9 from the center) for the three beams. The graphs emphasize the difference in static behavior between the 3 beams.

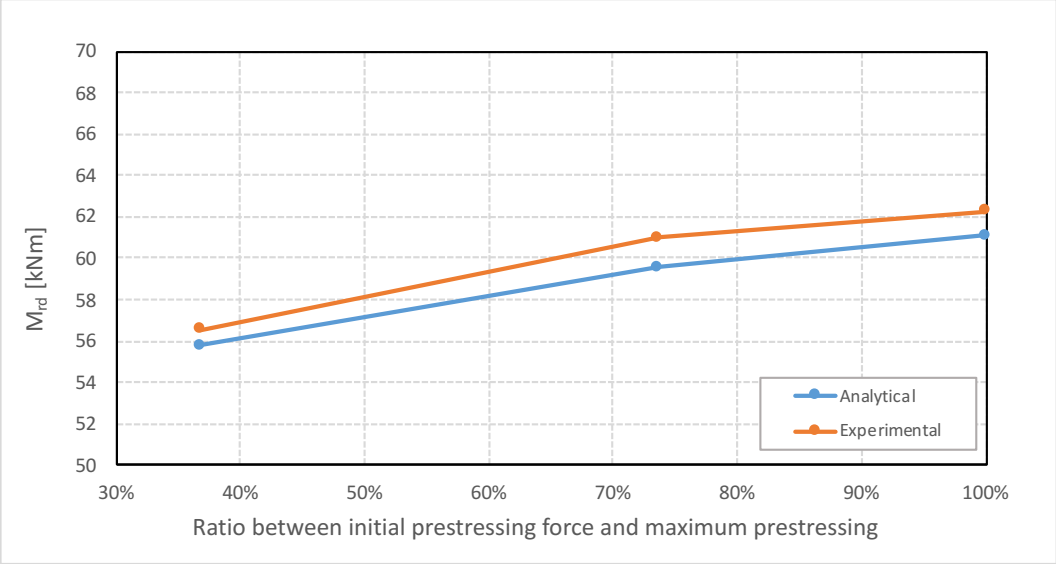

Figure 3.23: Comparison between resisting moments with respect to the applied prestressing force: analytical results vs experimental results

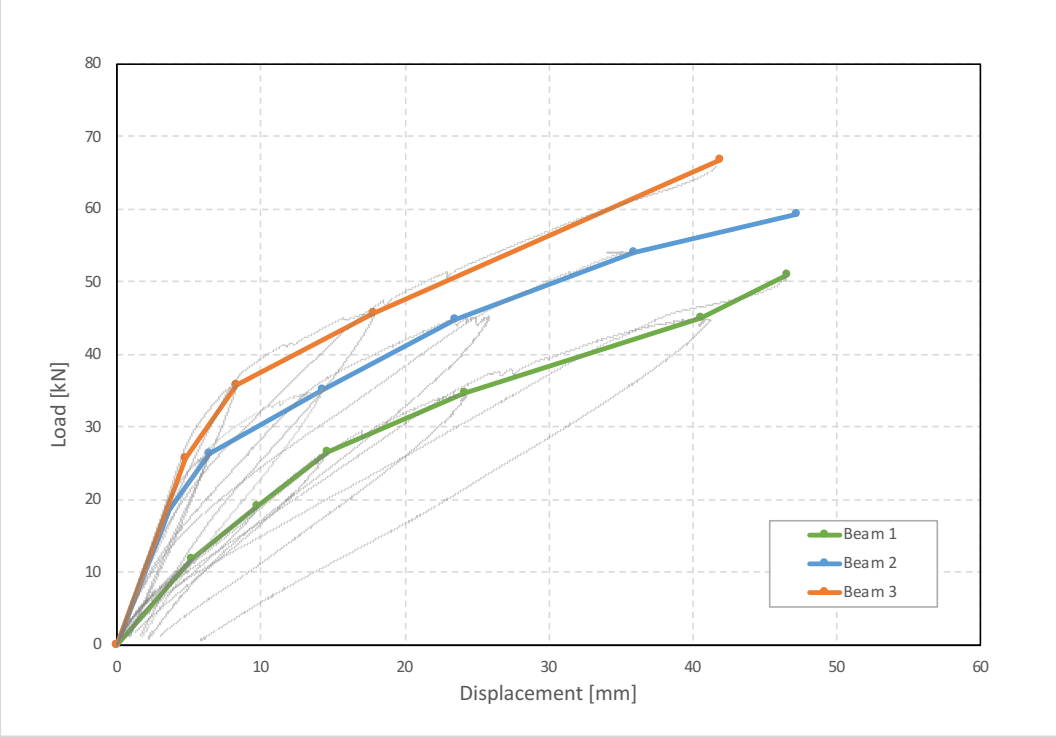

Figure 3.24: Load-displacement graph for the 3 beams: LVDT 2 (-0.9 m from mid-span)

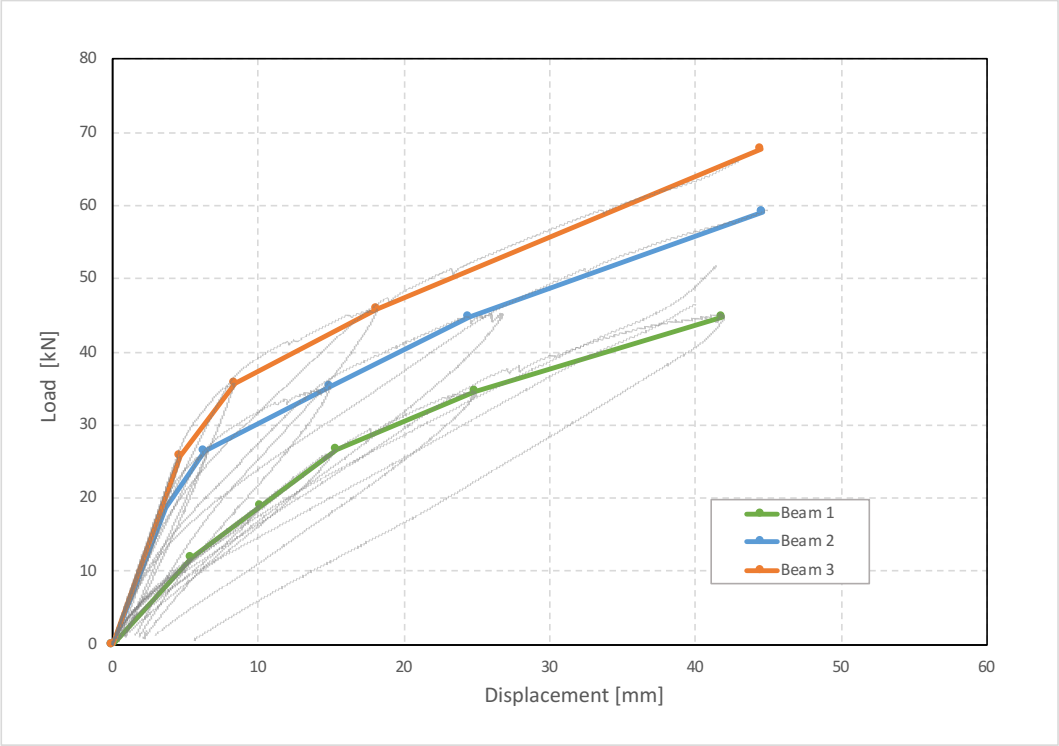

Figure 3.25: Load-displacement graph for the 3 beams: LVDT 4 (+0.9 m from mid-span)

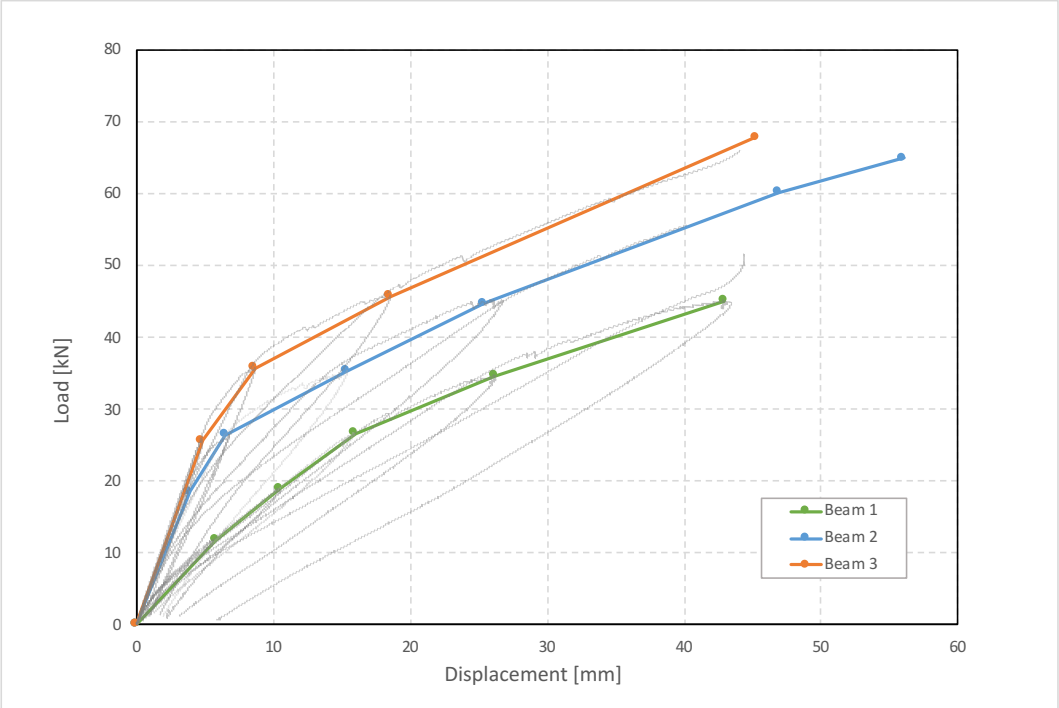

Figure 3.26: Load-displacement graph for the 3 beams: LVDT 3 (mid-span)

All three graphs show roughly the same trends for the individual beams: the segment with the initial slope represents the entirely reactive section state (elastic behavior of the materials)

for low load levels. Once the tensile strength of the concrete has been exceeded, the cracking process begins with a consequent reduction in flexural stiffness.

By comparing the behavior of the 3 beams, it is shown how the entity of the prestressing force affects by one side the entity of the cracking moment (the higher the prestressing force, the higher the cracking moment) and by the other side the transition from entirely reagent section to cracked section: for higher levels of prestressing the transition appears to be faster, while for lower levels of prestressing the transition is more gradual and less distinguishable.

If seen in terms of stiffness, the results show how, as expected, greater values are obtained with higher levels of prestressing. In the post-cracking phase, the values are instead relatively similar.

The stiffness variation can be visualized in the diagrams shown below, with stiffness defined as the average slope between the maximum values of every load cycle, in the diagram Load-Displacements.

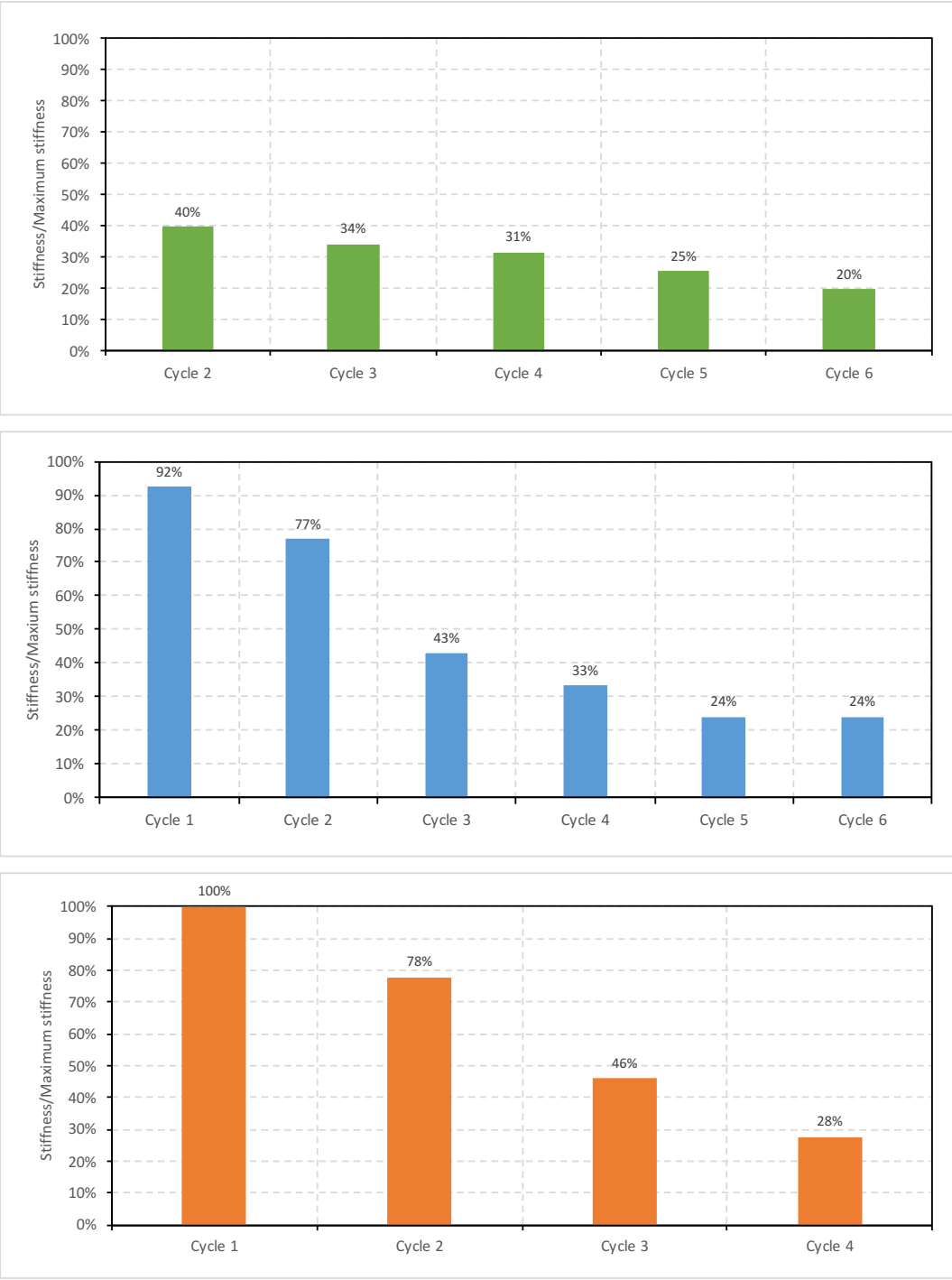

Figure 3.27: Stiffness variation for Beam 1, Beam 2 and Beam 3

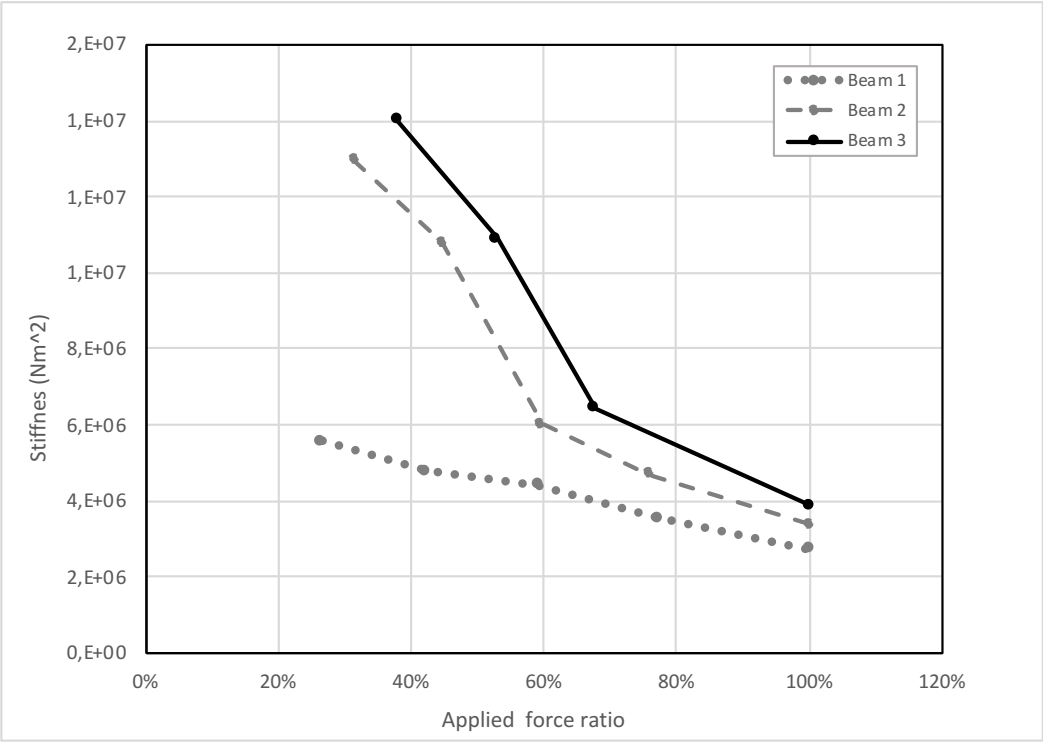

Figure 3.28: Stiffness variation for Beam 1, Beam 2 and Beam 3: comparison

Figure 3.29 shows the Moment-Bending diagram which compares experimental data collected by the instrumentation and the analytical results, calculated as follows.

In order to compare the experimental and theoretical model, both of them were depurated of the quantities corresponding to theoretical self-weight and initial prestressing curvature, which could not be measured in the tests. The value of the experimental curvature is the calculated as the ratio between the deformation in the compressed concrete and the depth of the neutral axis.

For the theoretical determination, the moments of inertia are calculated in the initial state, in which the behavior of the materials is still elastic, and in the cracked state, after the reaching of the tensile strength of the concrete.

The curvatures related to the two states are calculated as the ratio between the bending moment (deriving from the applied load, self-weight and prestressing) and the product of the elastic modulus for the moment of inertia at different stages.

In order to take into account the tension-stiffening effect, the calculations are made with reference to the indications contained in Eurocode 2. The average curvature value is calculated by the following formula [68]:

$$\frac{1}{rm} = \frac{1}{r_{II}} \cdot \zeta + (1 - \zeta) \cdot \frac{1}{r_I} \qquad (52)$$

Where:

$\frac{1}{r_I}$ identifies the curvature relative to the non-cracked state;

$\frac{1}{r_{II}}$ identifies the curvature relative to the cracked state;

ζ is a coefficient that takes into account the "tension stiffening", calculated as:

$$\zeta = 1 - \beta_1\beta_2\left(\frac{M_{cr}}{M_a}\right)^2 \qquad (53)$$

In which β_1 and β_2 are two coefficients related respectively to the type of reinforcement bar used and to the influence of the duration of the load application.

M_{cr} is the moment of first cracking and M_a is the bending moment due to external loads.

The graph shows that for low stress values the theoretical and analytical results follow the same trend. Once the cracking of the section is reached, the experimental flexional behavior appears to change with the prestressing force. This variation is not present in the theoretical results, since the model that was used does not take into account the prestressing force into the formulation.

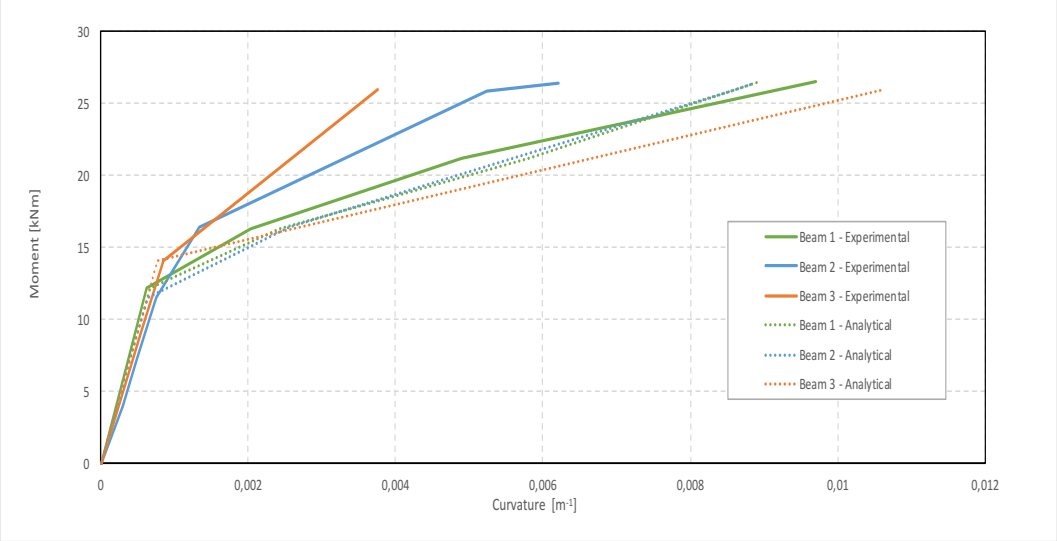

Figure 3.29: Moment-curvature diagram for the 3 beams: comparison between experimental results and analytical results

3.2 Second phase: post-tensioned prestressed concrete

3.2.1 Geometry

The second phase was related to the test of the other 3 reinforced concrete rectangular beam with prestressing straight cables inserted in plastic ducts The beams had the following common characteristics:

8. Fixed rectangular section 200 mm (base) x 300 mm (height);
9. Length (end to end) 6000 mm;
10. Regular reinforcement: 4 longitudinal bars, diameter 8 mm, at the 4 corners of the rectangular section (concrete cover 25 mm);
11. Regular reinforcement: rectangular stirrups, diameter 8 mm, at distance of 100 mm along all the length of the beam, except for the bearing length, where the distance is brought to 50 mm in order to avoid shear failure during the static tests;
12. Prestressing reinforcement: one strand made with 7 wires, equivalent diameter 6/10", straight course, inserts in a plastic duct without adherence. Moreover, a threaded anchoring system at the ends of the beam is installed.

The chosen configuration does not represent exactly the situation in real post-tensioned bridges, since in the latter case the cables are grouted. However, the aim of this work is not focused on the study of prestressing parameters. Instead, the prestressing force, which is the main variable involved in the study, is similar for laboratory conditions and real condition, where prestressing force is assumed to be applied in correspondence to the anchorage, and no friction resistance is considered for the grouting.

The 3 beams owned the same characteristics, apart from the eccentricity of the strand from the barycenter of the section. The eccentricity (from the barycenter and from the bottom of the beam) and other main characteristics of the 3 post-tensioned prestressed beams are listed in the following table.

Table 18: Main geometrical characteristics of Beams 4, 5 and 6

Name	Beam 4	Beam 5	Beam 6
Concrete section (mm^2)	60.000	60.000	60.000
Ordinary steel (mm^2)	201	201	201
Prestressing steel (mm^2)	139	139	139
Eccentricity from barycenter (mm)	0	40	80
Eccentricity from bottom (mm)	150	110	70
Prestress on concrete (MPa)	0-2,67	0-2,67	0-2,67

In the following figure are described the main geometrical characteristics of the 3 beams belonging to the second phase. As said, the geometrical dimensions are identical for the 3 beams, being the eccentricity of the strand the only difference.

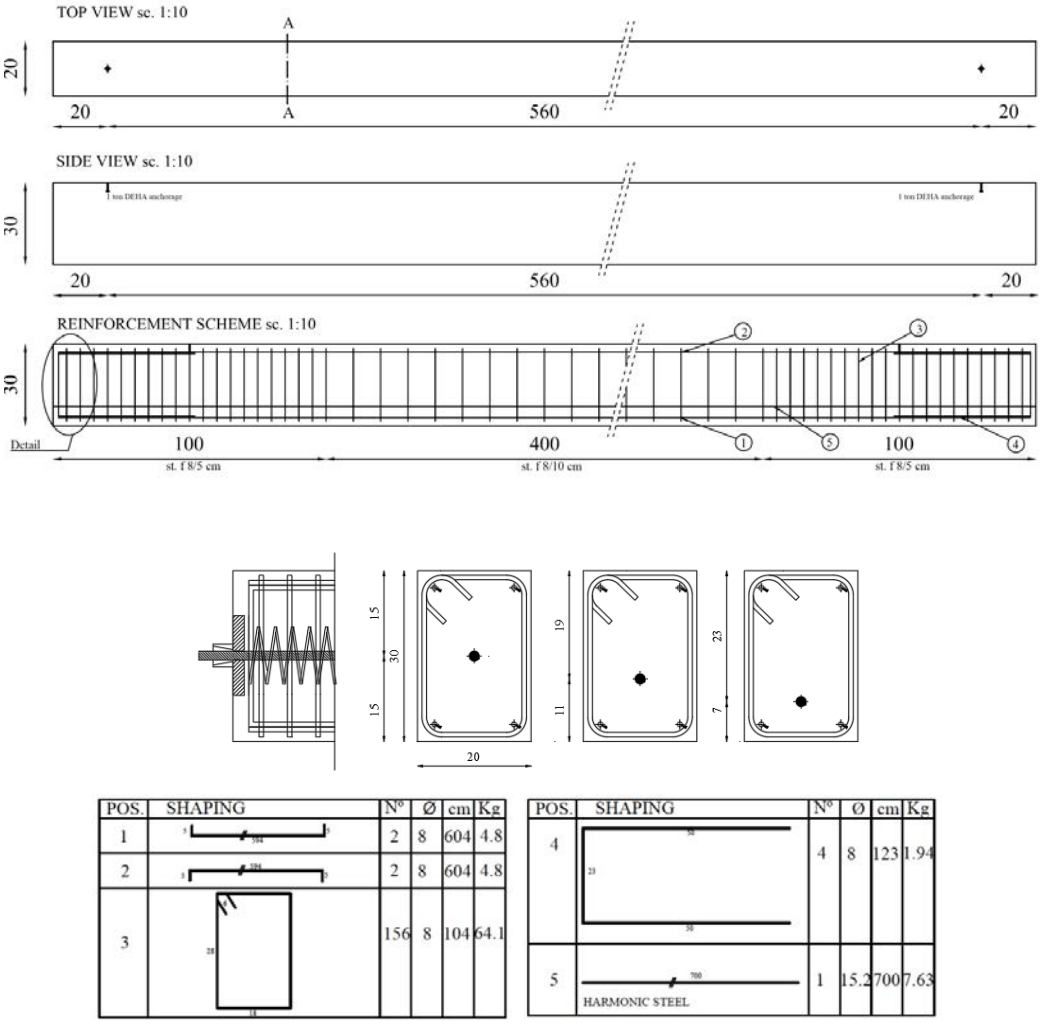

Figure 3.30: Beams 4, 5 and 6: geometrical and reinforcement dimensions (not to scale)

3.2.2 Materials

Three different materials were used to build the beams: concrete, ordinary reinforcement steel and prestressing steel.

The concrete was cast at the Castelvetro prefabrication plant of RDB Italprefabbricati. The mix design of the concrete utilized a water/cement ratio of 0,47, the use of Cement R525 S3 and 1720 kg of gravel/sand over 1 cubic meter of finite product.

The results on the compressive tests of concrete samples taken from the cast are reported in the following table.

Table 19: Concrete compressive test results

Beam reference	Curing days	R [MPa]
Beam 4	49	59.6
Beam 4	49	65.3
Beam 5	48	61.5
Beam 5	48	67.4
Beam 6	44	69.9
Beam 6	44	64.1

By taking into account the formulation given by the Italian Construction Code (§ 11.2.5 NTC 2018) a characteristic value of cylindrical strength of f_{ck} = 54 MPa is obtained.

For the reinforcement of the beam the ordinary B450C reinforcement steel was used, with a nominal yield strength of 450 MPa and a failure strength of 540 MPa.

The tensile tests performed on 3 samples of steel taken from the same production lot gave the following results, with an average resistance of 512 MPa.

Table 20: Ordinary steel tensile test results

Sample reference	Yield strength [MPa]	Failure strength [MPa]	Elongation [%]
Sample 1	509	611	9.3
Sample 2	515	615	11.5
Sample 3	513	608	9.8

For the prestressing cable, prestressing steel was used, with a nominal strength at 1% of total elongation ($fp_{(1)k}$) of 1670 MPa and a failure strength of 1860 MPa.

The tensile tests performed on 3 samples of steel taken from the same production lot gave the following results, with an average resistance of 1703 MPa.

Table 21: Prestressing steel tensile test results

Sample reference	Effective diameter [mm]	Section [mm^2]	$fp_{(1)k}$ [MPa]	Failure strength [MPa]	Elongation [%]	Elastic modulus [MPa]
Sample 1	13.3	139.3	1703	1930	6.9	195145
Sample 2	13.4	140.5	1700	1921	5.7	199824
Sample 3	13.4	140.6	1707	1925	6.5	196444

3.2.3 Test set-up

In the present chapter the procedure of test of the 3 beams of second phase is presented.

The test program includes a series of load cycles (load-unload) up to the failure of each beam, with contemporary measurement of the following static parameters: longitudinal deformation, vertical displacement and vertical force applied. Between one cycle and another non-destructive measurements were taken, applying various levels of prestressing, described in the following chapter. This chapter describes the procedure for load tests, the set up and the instrumentation used to follow the loading process up to failure.

The beams were positioned on two steel supports (with a height of 60cm each) placed at a distance of 200 mm from the end, bringing the effective length between supports being 5600 mm.

Between each steel support and the concrete surface a steel hinge was placed, with the same width of the beam (200 mm) in order to simulate the static scheme of simple supported beam. The supports were positioned in order to avoid any relative movement of the different parts, and in order to avoid any damping during vibration tests (see following chapters).

The load test was performed through a bending test in which the vertical concentrated load is induced by a hydraulic jack at a quarter of the effective length of the beam. At the interface between the hydraulic jack and the upper concrete surface 20 mm thick plates were positioned, in order to distribute the concentrated load on a 150x200 mm^2 area. At the points of application of the load, a mortar cast was set up in order to assure the perfect contact of the partition plate on the concrete surface.

The prestressing force was applied to the beam tensioning the strand with a hydraulic hollow jack, positioned at one end of the beam. The strand was locked with wedges, and at the interface between the hydraulic jack and the concrete surface 20 mm thick plates were positioned, in order to distribute the concentrated load on a 200x200 mm^2 area. In the following picture the test set up is summarized.

The reading of the applied vertical force is done through a load cell with a capacity of 30 ton connected to the acquisition system, while the prestressing force was measured with two load cells with a capacity of 60 ton installed at the ends of the beam.

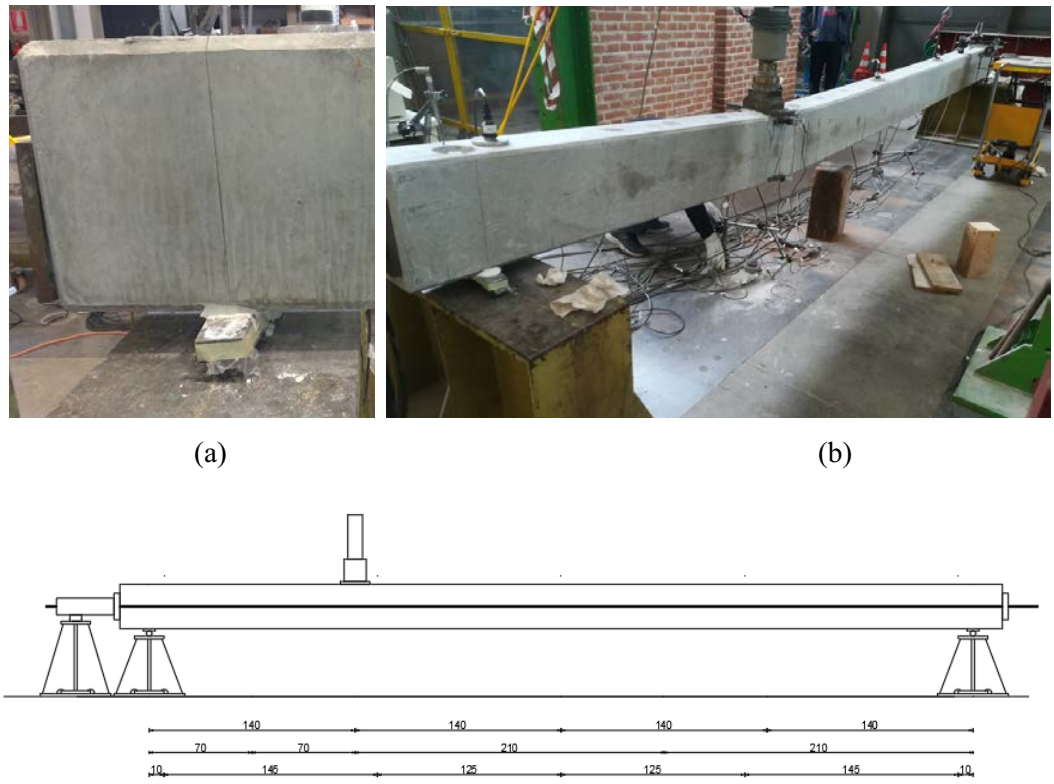

(a) (b)

(c)

Figure 3.31: (a) Bearing system; (b) Point load; (c) whole system: side view

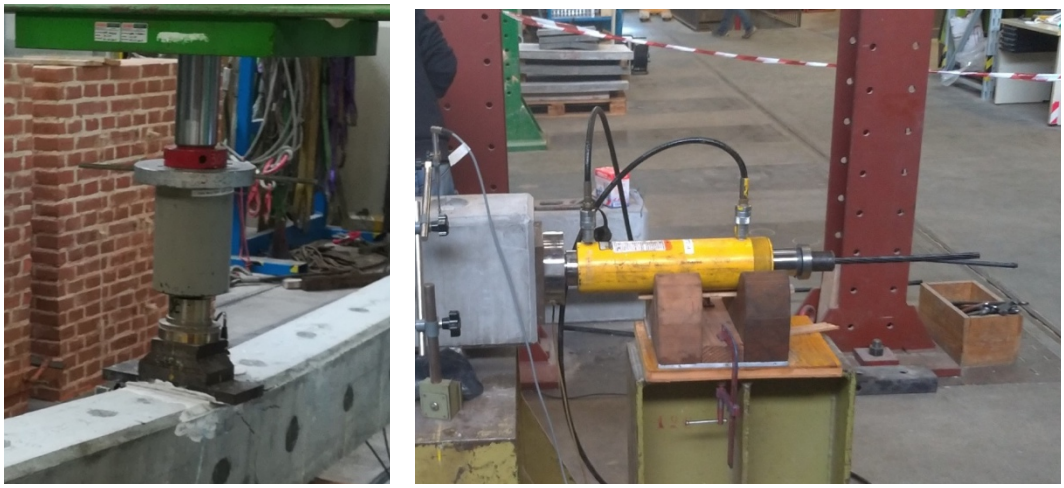

(a) (b)

Figure 3.32: (a) Cell with 30 ton capacity (vertical load); (b) cell with 60 ton capacity (prestressing force)

Table 22: 60 ton load cell characteristics

Model	CL 60000 (LAUMAS)
Weight [kg]	5.4
Material	Stainless steel 17-4 PH
Nominal load [kg]	60000
Combined error	≤±0.05%
Deflection at nominal load [mm]	0.3
Sensitivity	2mV/V ± 0.3%
Field of working temperature	-20°C/+70°C

In order to measure the vertical deflection due to the applied load, 5 LVDT (Linear Variable Differential Transformer) were used.

For the purpose of the test, they were fixed inside a magnetic support placed on the ground (or on the steel supports in correspondence to the two bearings). The probe of the instrument was placed in contact with the surface of the beam.

Two transducers were positioned in correspondence to the supports, one in correspondence of the vertical load (1/4 of the span) and two at the two halfway points between the load and the supports, as schematized in the following figure.

In order to measure the longitudinal deformation, 8 DD1 were positioned along the beam in 4 couples, one at the upper side and one at the lower side of the beam, at 25 mm from the upper and lower surface respectively. The 4 couples were positioned in this way: two in correspondence of the vertical load (one for each side of the beam) and two at the two halfway points between the load and the supports. The purpose of the disposition is to measure the bending deformation at the beam at significant points.

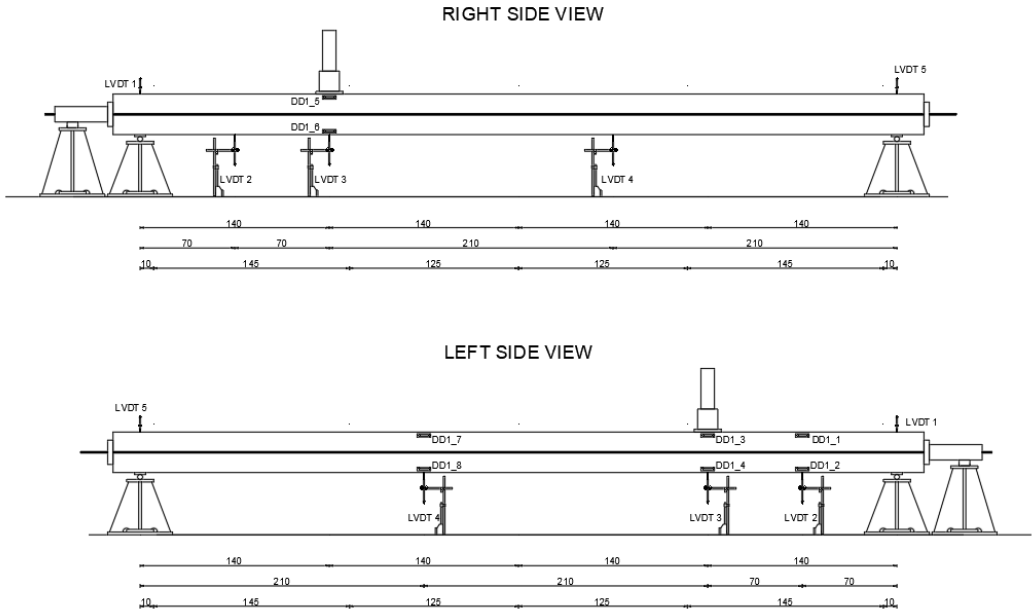

Figure 3.33: position of LVDT and DD1

In annex are listed the technical characteristics of the instrumentation used for static tests:

- LVDT: 50 mm and 20 mm;
- DD1.

The acquisition system utilized for the static test is the HBM Spider8, an electronic measuring system for PCs for electric measurement of mechanical variables such as strain, force, pressure, path, acceleration and for temperatures. It can manage all measurement tasks with S/G in quarter, half or full bridge connection.

All the signal conditioning – excitation for passive transducers and amplification, digitalization, computer interface and connection technology for a maximum of 8 channels – is combined in one housing. Spider8 is connected to the computer via the printer port or via an RS232 interface.

The software utilized for the data acquisition is the CATMAN DAQ Software.

3.2.4 Static test procedure

For each beam a test procedure composed by 5 phases was followed, as exposed in Figure 3.34:

- The first phase consisted in a cycle of increase of prestressing force, in 5 prestressing levels: 0 kN (no prestressing), 47,5 kN, 95 kN, 130 kN and 160 kN. No vertical load was applied in this phase. For every prestressing level, a set of non-destructive tests was performed (ultrasonic and dynamic tests, described in the following chapter);

- The second phase consisted in a static vertical load test, until the first cracking of the beam, with prestressing set at zero. No non-destructive test was performed;
- In the third phase the same procedure of the first phase was repeated, with the cracked beam: 5 prestressing levels with NDT at every level;
- In the fourth phase a static vertical load was applied, until failure of the beam. During the load, subdivided in sub-steps, the prestressing level was adjusted from the maximum level (160 kN) until zero, as shown in Figure 3.34;
- In the fifth phase the same procedure of the first and third phases was repeated, with the failed beam: 5 prestressing levels with NDT at every level.

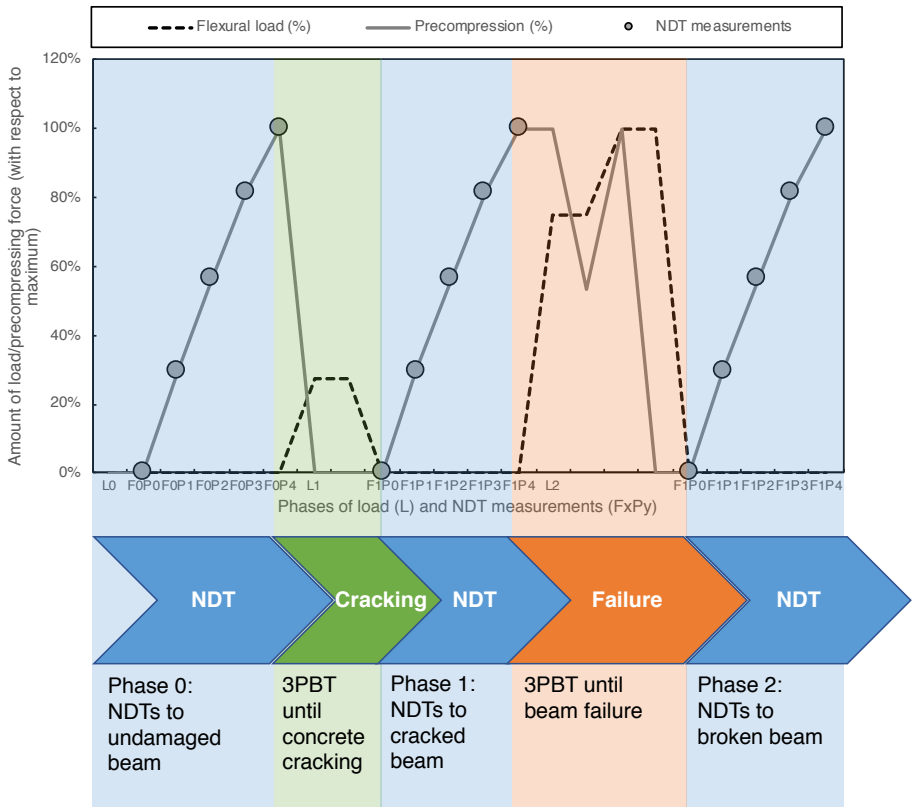

Figure 3.34 – Test procedure for post-tensioned beams.

In Table 23 the load sub-steps of the fourth phase (static load until failure) for every beam are summarized. All the values refer to a prestressing force of 160 kN.

Table 23: Load steps for the beams 4, 5 and 6 for phase 4 (static load until failure)

STEPS	BEAM 4		BEAM 5		BEAM 6	
	Load [kN]	% of max load	Load [kN]	% of max load	Load [kN]	% of max load
4.0	0	0,00%	0	0,00%	0	0,00%
4.1	22,97	47,11%	11,23	31,14%	15,10	26,86%
4.2	38,51	78,99%	33,33	71,12%	30,20	53,73%
4.3	48,51	100,00%	39,60	75,45%	49,16	87,45%
4.4			51,09	100,00%	55,23	98,25%
4.5					56,21	100,00%

In the phase in which the load was kept fixed, the path of the visible cracks was traced, in order to observe the evolution of the cracking pattern with the increase of load applied.

3.2.5 Beam 4: static tests results

This test concerns the beam with an eccentricity of the strand from the barycenter of the section equal to zero (150 mm from bottom of the beam).

Table 9 and

Table 25 show the maximum values of displacements and deformations obtain from the vertical load cycles applied to the beam, the prestressing force was equal to 160 kN.

Table 24: Maximum displacement values for every load cycle – beam 4

Cycle	U_{max} LVDT 1 [mm]	U_{max} LVDT 2 [mm]	U_{max} LVDT 3 [mm]	U_{max} LVDT 4 [mm]	U_{max} LVDT 5 [mm]
1	-0,090	3,022	5,564	4,914	0,020
2	-0,100	8,242	16,054	13,414	-0,020
3	0,080	26,142	55,744	36,274	-0,010

Table 25: Maximum deformation values for every load cycle – beam 4

Cycle	$\varepsilon_{1\,max}$ DD1_1 [mm/m]	$\varepsilon_{2\,max}$ DD1_2 [mm/m]	$\varepsilon_{3\,max}$ DD1_3 [mm/m]	$\varepsilon_{4\,max}$ DD1_4 [mm/m]
1	-0,07	0,08	-0,18	1,93
2	-0,13	0,14	-0,32	9,73
3	-0,17	0,15	0,21	28,2

Cycle	$\varepsilon_{5\,max}$ DD1_5 [mm/m]	$\varepsilon_{6\,max}$ DD1_6 [mm/m]	$\varepsilon_{7\,max}$ DD1_7 [mm/m]	$\varepsilon_{8\,max}$ DD1_8 [mm/m]
1	-0,28	2	-0,09	0,17
2	-0,73	12	-0,18	0,55
3	-1,21	30	-0,21	0,68

The graph in Figure 3.35 shows the curve load-displacement for LVDT 3 (at the vertical load). As it can be seen, up to around 23 kN of applied force the graph trend is linear and no relevant event is noted. When the load increases, a slight drop in stiffness is initially evident, and once the steel yield is reached, a further reduction in the stiffness can be observed.

The graph in Figure 3.36 shows instead the absolute displacements of LVDTs n. 2, 3 and 4 with respect to the average displacements measured at the supports n. 1 and 5 (that are anyhow relatively small with respect to the n. 2, 3 and 4).

It is clear how with the increase of the force the increase of displacement is non-linear (larger space between consecutive steps).

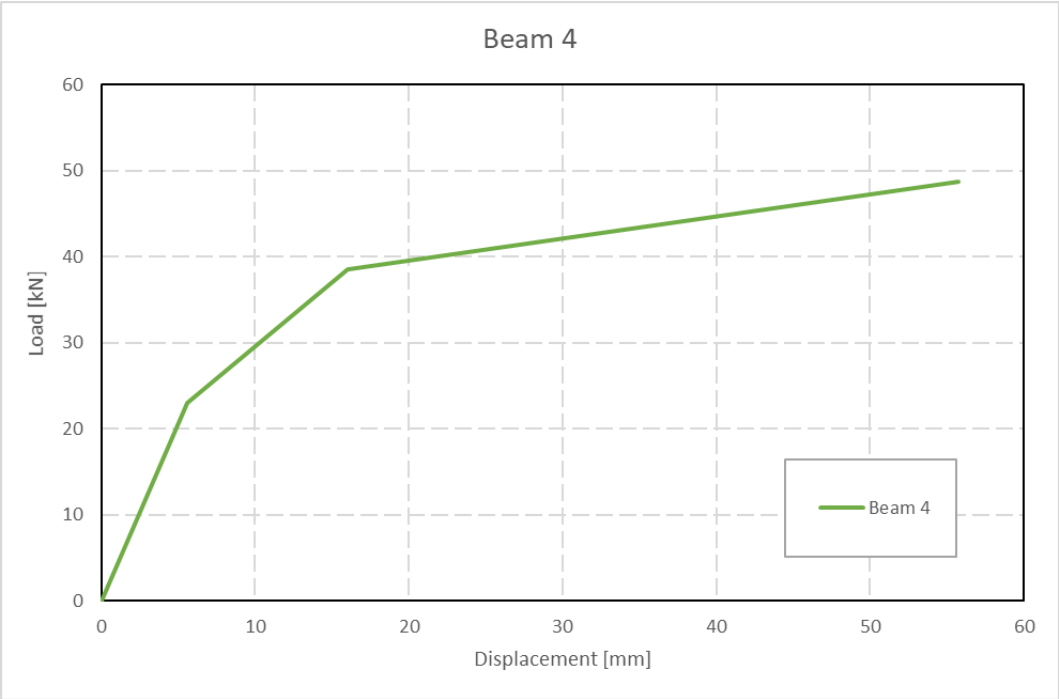

Figure 3.35 - Load-displacement curve for Beam 4 – LVDT 3 (at the vertical load)

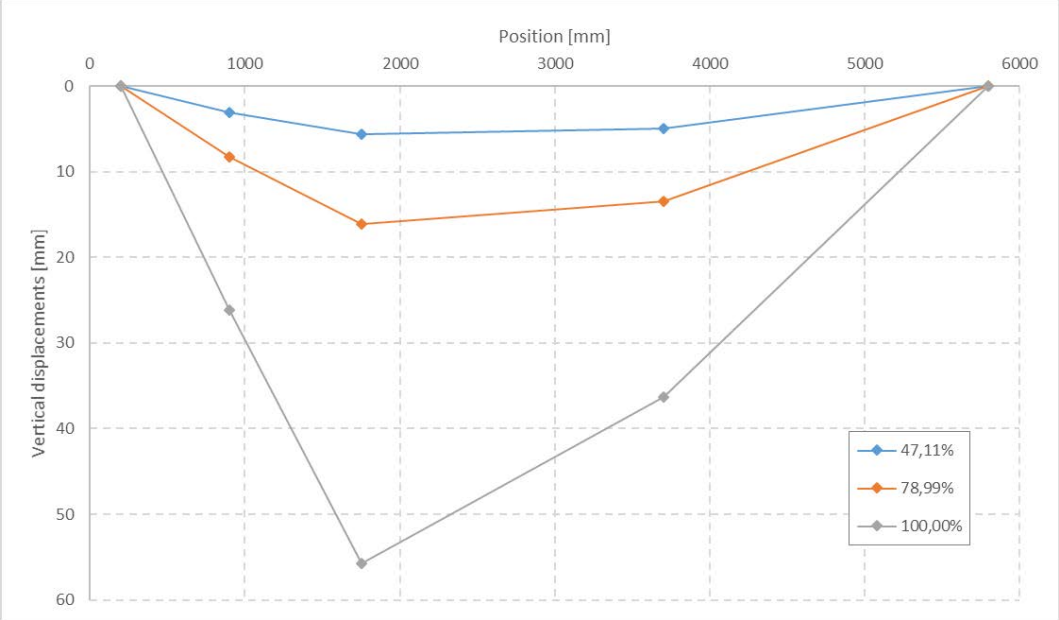

Figure 3.36 - Displacement-position schemes for Beam 4

Depending on the position along the beam and on the load applied, the neutral axis will change accordingly. With the deformation values recorded by the DD1 for the various load cycles it was possible to represent its variation.

Table 26: Neutral axis for every load cycle – beam 4

DD1_1- DD1_2	Cycle 1	Cycle 2	Cycle 3
$\varepsilon_{c,sup}$	-0.007	-0.013	-0.017
$\varepsilon_{c,inf}$	0.008	0.014	0.015
Neutral axis [mm]	141.67	145.37	157.81
DD1_3- DD1_4	Cycle 1	Cycle 2	Cycle 3
$\varepsilon_{c,sup}$	-0.018	-0.032	0.021
$\varepsilon_{c,inf}$	0.193	0.973	2.823
DD1_5- DD1_6	Cycle 1	Cycle 2	Cycle 3
$\varepsilon_{c,sup}$	-0.028	-0.073	-0.121
$\varepsilon_{c,inf}$	0.200	1.200	3.000
Neutral axis [mm]	51.01	36.15	28.91
DD1_7- DD1_8	Cycle 1	Cycle 2	Cycle 3
$\varepsilon_{c,sup}$	-0.009	-0.018	-0.021
$\varepsilon_{c,inf}$	0.017	0.055	0.068
Neutral axis [mm]	111.54	86.64	83.99

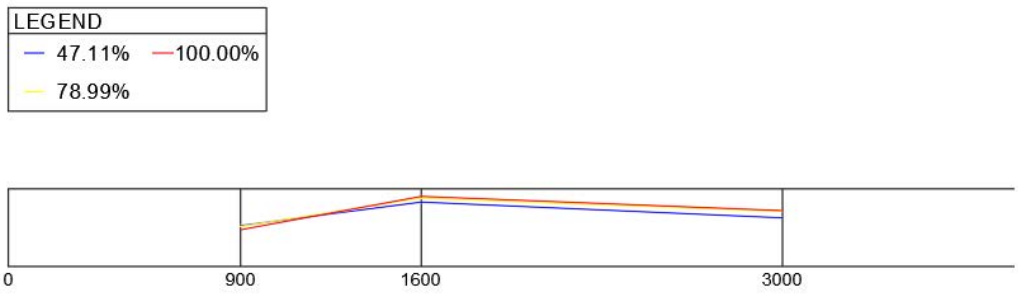

Figure 3.37 - Graphical representation of neutral axis variation in the measured sections - Beam 4

A higher deformation and a higher position of the neutral axis are observed for central DD1. However, large variations in the position of the neutral axis are not noticed when the load varies.

Figure 3.38 shows the cracking state when the increase of the load. As it can be seen, the beam already presented a crack pattern before the beginning of the load tests, probably due to shrinkage issues.

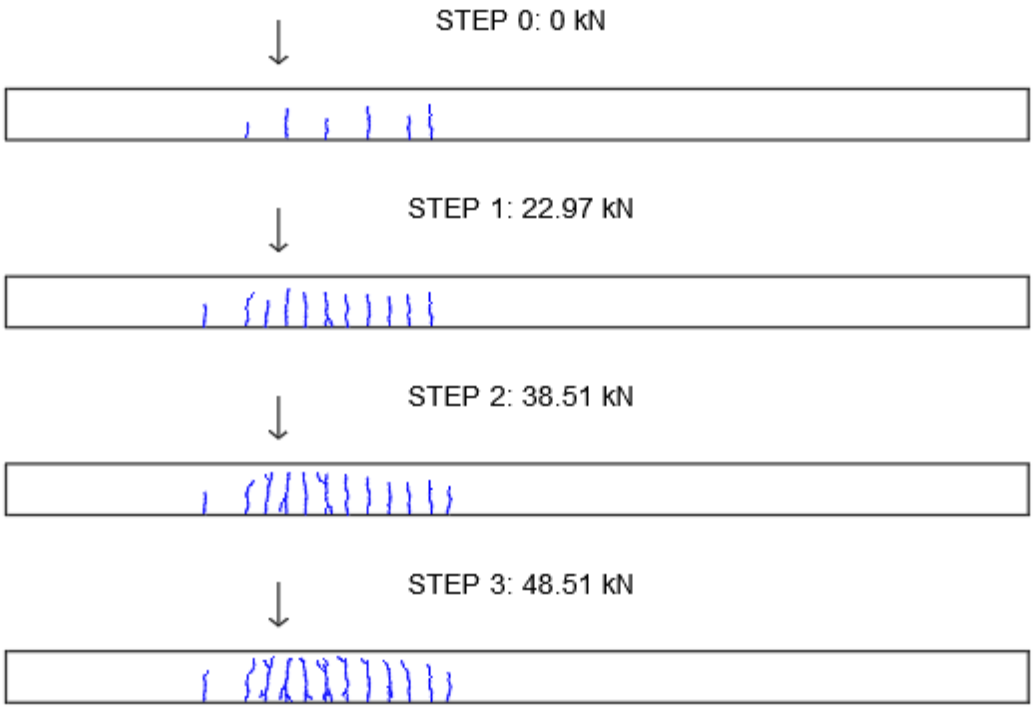

Figure 3.38 - Evolution of crack pattern - Beam 4

3.2.6 Beam 5: static tests results

This test concerns the beam with an eccentricity of the strand from the barycenter of the section equal to 40 mm (110 mm from bottom of the beam).

Table 27 and Table 28 show the maximum values of displacements and deformations obtain from the vertical load cycles applied to the beam, the prestressing force was equal to 160 kN.

Table 27: Maximum displacement values for every load cycle – beam 5

Cycle	U_{max} LVDT 1 [mm]	U_{max} LVDT 2 [mm]	U_{max} LVDT 3 [mm]	U_{max} LVDT 4 [mm]	U_{max} LVDT 5 [mm]
1	-0,130	0,930	1,580	1,540	-0,040
2	-0,340	4,920	9,410	8,040	-0,130
3	-0,350	6,870	13,260	10,940	-0,130
4	-0,521				-0,170

Table 28: Maximum deformation values for every load cycle – beam 5

Cycle	$\varepsilon_{1\,max}$ DD1_1 [mm/m]	$\varepsilon_{2\,max}$ DD1_2 [mm/m]	$\varepsilon_{3\,max}$ DD1_3 [mm/m]	$\varepsilon_{4\,max}$ DD1_4 [mm/m]
1	-0,03	0,05	-0,08	0,09
2	-0,10	0,18	-0,33	0,52
3	-0,12	0,21	-0,56	2,70
4	-0,16	0,29	-1,22	

Cycle	$\varepsilon_{5\,max}$ DD1_5 [mm/m]	$\varepsilon_{6\,max}$ DD1_6 [mm/m]	$\varepsilon_{7\,max}$ DD1_7 [mm/m]	$\varepsilon_{8\,max}$ DD1_8 [mm/m]
1	-0,08	0,00	-0,05	0,03
2	-0,27	0,00	-0,16	0,07
3	-0,36	3,00	-0,18	0,08
4			-0,28	0,08

The graph in Figure 3.39 shows the curve load-displacement for LVDT 3 (at the vertical load). As it can be seen, up to around 12 kN of applied force the graph trend is linear and no relevant event is noted. When the load increases, a slight drop in stiffness is initially evident, and once the steel yield is reached, a further reduction in the stiffness can be observed. In this case no data are available for the last cycle (failure step) where the instrumentation was disturbed by the excessive deformation of the beam.

It is clear how with the increase of the force the increase of displacement is non-linear (larger space between consecutive steps).

The graph in Figure 3.40 shows instead the absolute displacements of LVDTs n. 2, 3 and 4 with respect to the average displacements measured at the supports n. 1 and 5 (that are anyhow relatively small with respect to the n. 2, 3 and 4). We note that the greater displacements occur at the point of application of the vertical load.

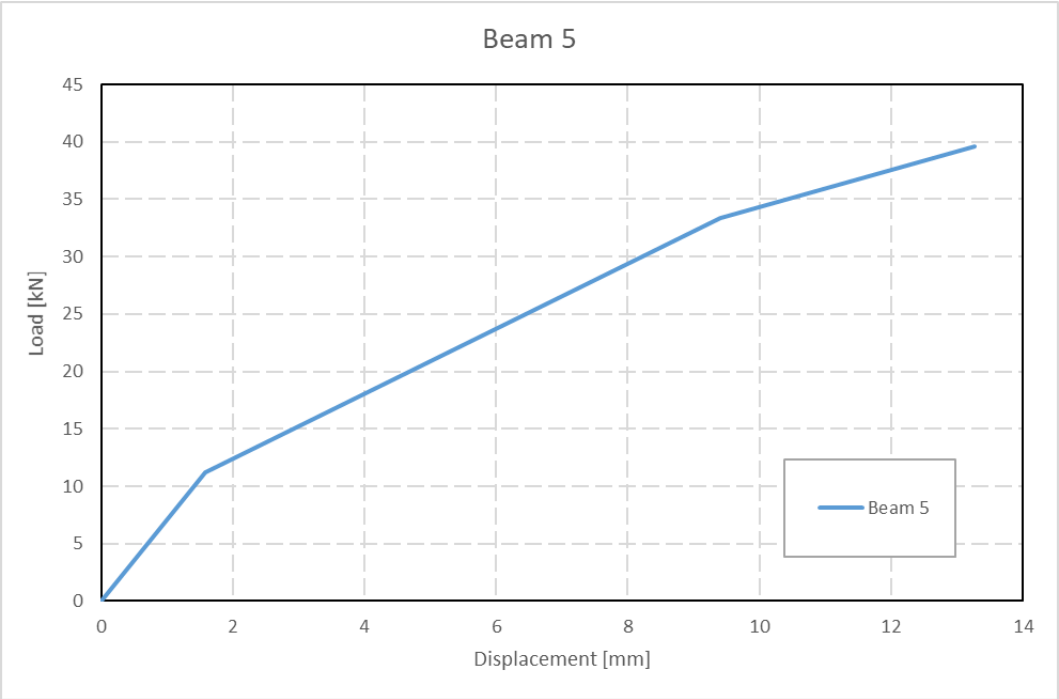

Figure 3.39 - Load-displacement curve for Beam 5 – LVDT 3 (at the vertical load)

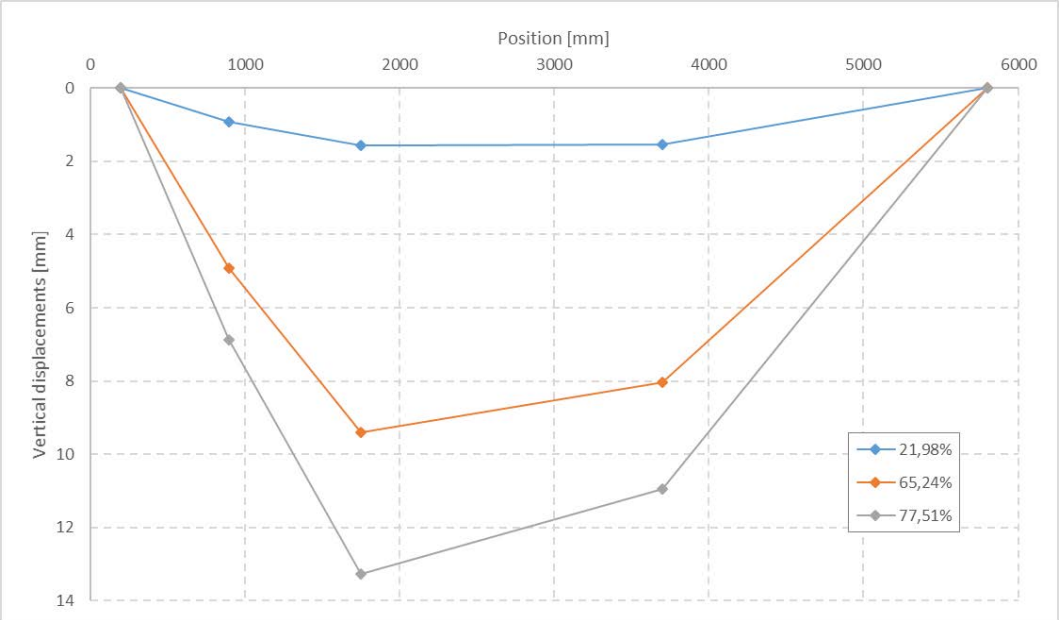

Figure 3.40 - Displacement-position schemes for Beam 5

Depending on the position along the beam and on the load applied, the neutral axis will change accordingly. With the deformation values recorded by the DD1 for the various load cycles (Table 29) it was possible to represent its variation.

Table 29: Neutral axis for every load cycle – beam 5

DD1_1- DD1_2	Cycle 1	Cycle 2	Cycle 3	Cycle 4
$\varepsilon_{c,sup}$	-0,003	-0,010	-0,012	-0,016
$\varepsilon_{c,inf}$	0,005	0,018	0,021	0,029
Neutral axis [mm]	118,75	114,29	115,91	113,89
DD1_3- DD1_4	Cycle 1	Cycle 2	Cycle 3	Cycle 4
$\varepsilon_{c,sup}$	-0,008	-0,033	-0,056	-0,122
$\varepsilon_{c,inf}$	0,009	0,052	0,270	-
DD1_5- DD1_6	Cycle 1	Cycle 2	Cycle 3	Cycle 4
$\varepsilon_{c,sup}$	-0,008	-0,027	-0,036	-
$\varepsilon_{c,inf}$	0,000	0,000	0,300	-
Neutral axis [mm]	142,65	122,06	59,87	-
DD1_7- DD1_8	Cycle 1	Cycle 2	Cycle 3	Cycle 4
$\varepsilon_{c,sup}$	-0,005	-0,016	-0,018	-0,028
$\varepsilon_{c,inf}$	0,003	0,007	0,008	0,008
Neutral axis [mm]	181,25	198,91	198,08	219,44

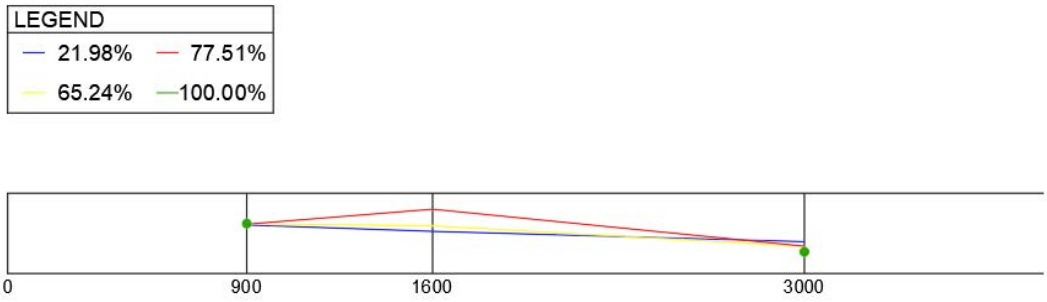

Figure 3.41 - Graphical representation of neutral axis variation in the measured sections - Beam 5

Figure 3.41 shows the positions of neutral axis when the increase of the load. A higher deformation and a higher position of the neutral axis are observed for central DD1 during the third step (77,51% of the maximum load). The last step measurements of neutral axis in central position are not available.

Figure 3.42 shows the cracking state when the increase of the load. As it can be seen, the beam already presented a crack pattern before the beginning of the load tests, probably due to shrinkage issues.

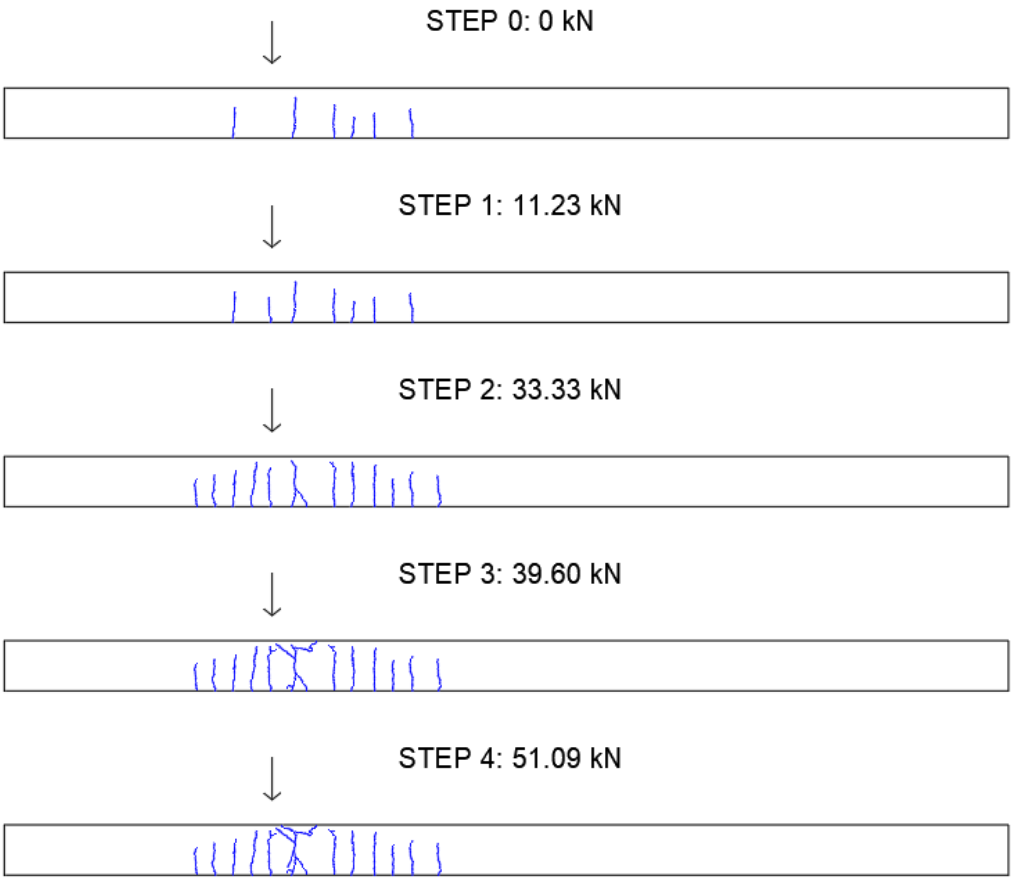

Figure 3.42 - Evolution of crack pattern - Beam 5

3.2.7 Beam 6: static tests results

This test concerns the beam with an eccentricity of the strand from the barycenter of the section equal to 80 mm (70 mm from bottom of the beam).

Table 30 and Table 31 show the maximum values of displacements and deformations obtain from the vertical load cycles applied to the beam, the prestressing force was equal to 160 kN.

Table 30: Maximum displacement values for every load cycle – beam 6

Cycle	U_{max} LVDT 1 [mm]	U_{max} LVDT 2 [mm]	U_{max} LVDT 3 [mm]	U_{max} LVDT 4 [mm]	U_{max} LVDT 5 [mm]
1	-0,18	1,270	2,200	2,040	0,01
2	-0,33	3,200	5,900	5,150	-0,01
3	-0,43	7,468	14,385	11,923	-0,12
4	-0,58	13,118	25,395	19,203	-0,21
5	-0,60	15,818	31,115		-0,26

Table 31: Maximum deformation values for every load cycle – beam 6

Cycle	$\varepsilon_{1\,max}$ DD1_1 [mm/m]	$\varepsilon_{2\,max}$ DD1_2 [mm/m]	$\varepsilon_{3\,max}$ DD1_3 [mm/m]	$\varepsilon_{4\,max}$ DD1_4 [mm/m]
1	-0,05	0,06	-0,10	0,10
2	-0,09	0,11	-0,22	0,20
3	-0,16	0,18	-0,54	2,75
4	-0,18	0,19	-0,64	7,6
5	-0,19	0,21	-1,19	29,62

Cycle	$\varepsilon_{5\,max}$ DD1_5 [mm/m]	$\varepsilon_{6\,max}$ DD1_6 [mm/m]	$\varepsilon_{7\,max}$ DD1_7 [mm/m]	$\varepsilon_{8\,max}$ DD1_8 [mm/m]
1	-0,10	1,00	-0,05	0,05
2	-0,24	1,00	-0,10	0,12
3	-0,62	3,00	-0,18	0,19
4	-0,8	8,00	-0,21	0,21
5	-0,83	15,00	-0,20	0,22

The graph in Figure 3.43 shows the curve load-displacement for LVDT 3 (at the vertical load). As it can be seen, up to around 15 kN of applied force the graph trend is linear and no relevant event is noted. When the load increases, a slight drop in stiffness is initially evident, and once the steel yield is reached, a further reduction in the stiffness can be observed.

It is clear how with the increase of the force the increase of displacement is non-linear (larger space between consecutive steps).

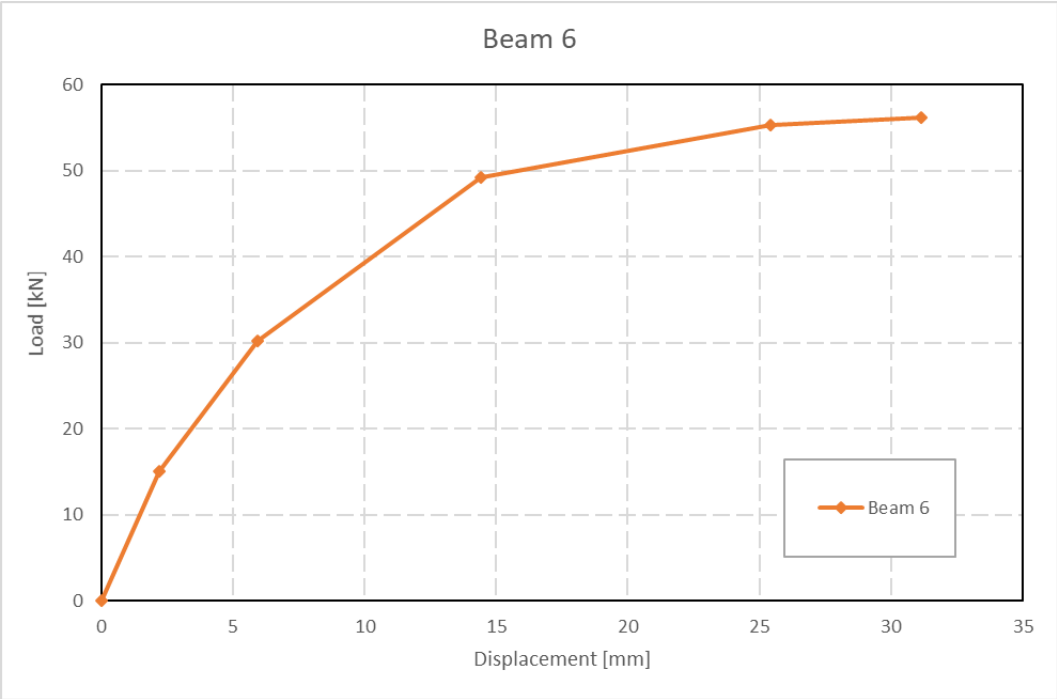

Figure 3.43 - Load-displacement curve for Beam 6 – LVDT 3 (at the vertical load)

The graph in Figure 3.44 shows instead the absolute displacements of LVDTs n. 2, 3 and 4 with respect to the average displacements measured at the supports n. 1 and 5 (that are anyhow relatively small with respect to the n. 2, 3 and 4). We note that the greater displacements occur at the point of application of the vertical load. In this case no data are available from LVDT n. 4 (position 3,7 m) for the last cycle (failure step) where the instrumentation was disturbed by the excessive deformation of the beam.

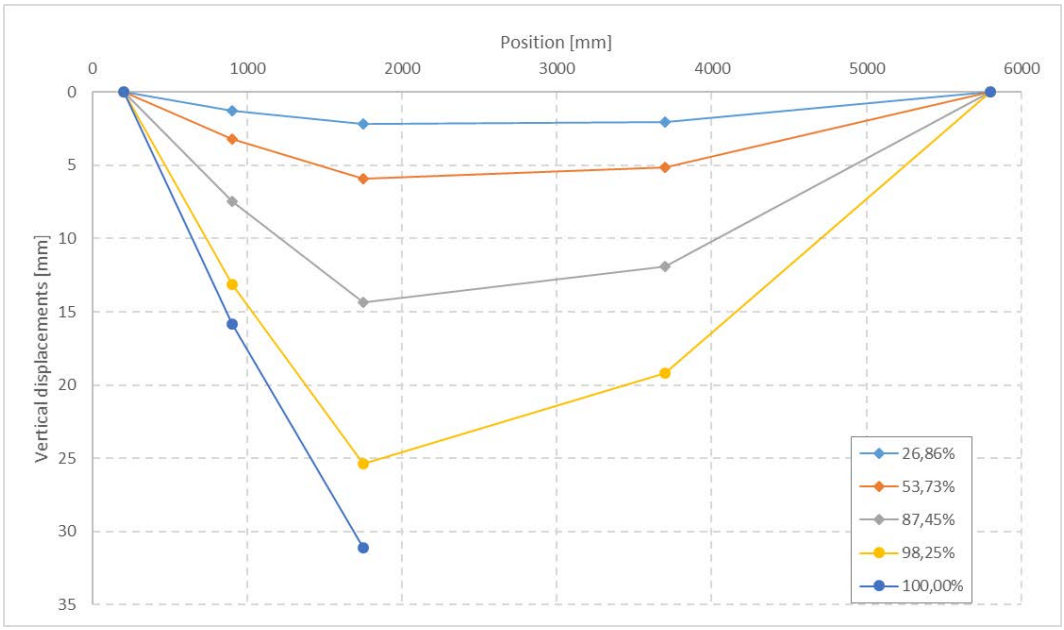

Figure 3.44 - Displacement-position schemes for Beam 6

Depending on the position along the beam and on the load applied, the neutral axis will change accordingly. With the deformation values recorded by the DD1 for the various load cycles (Table 32) it was possible to represent its variation.

Table 32: Neutral axis for every load cycle – beam 6

DD1_1- DD1_2	Cycle 1	Cycle 2	Cycle 3	Cycle 4	Cycle 5
$\varepsilon_{c,sup}$	-0,005	-0,009	-0,016	-0,018	-0,019
$\varepsilon_{c,inf}$	0,006	0,011	0,018	0,019	0,021
Neutral axis [mm]	138,64	137,50	142,65	146,62	143,75
DD1_3- DD1_4	Cycle 1	Cycle 2	Cycle 3	Cycle 4	Cycle 5
$\varepsilon_{c,sup}$	-0,010	-0,022	-0,054	-0,064	-0,119
$\varepsilon_{c,inf}$	0,010	0,020	0,275	0,760	2,962
DD1_5- DD1_6	Cycle 1	Cycle 2	Cycle 3	Cycle 4	Cycle 5
$\varepsilon_{c,sup}$	-0,010	-0,024	-0,062	-0,080	-0,083
$\varepsilon_{c,inf}$	0,100	0,100	0,300	0,800	1,500
Neutral axis [mm]	98,86	114,67	66,93	46,07	36,38
DD1_7- DD1_8	Cycle 1	Cycle 2	Cycle 3	Cycle 4	Cycle 5
$\varepsilon_{c,sup}$	-0,005	-0,010	-0,018	-0,021	-0,020
$\varepsilon_{c,inf}$	0,005	0,012	0,019	0,021	0,022
Neutral axis [mm]	150,00	138,64	146,62	150,00	144,05

Figure 3.45 shows the variation of the position of neutral axis during load cycles. A higher deformation and a higher position of the neutral axis are observed for central DD1 during load increment.

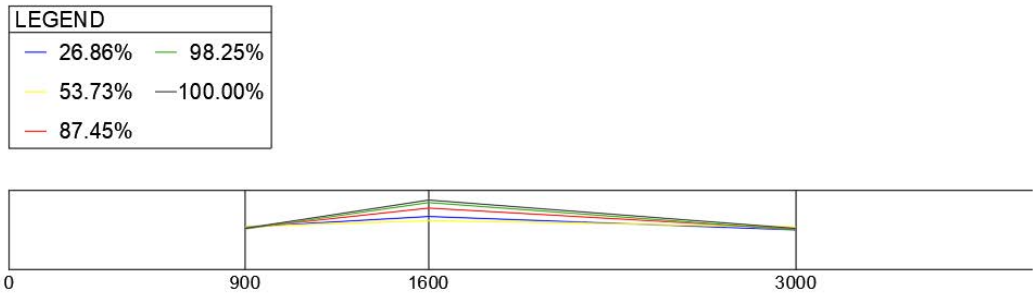

Figure 3.45 - Graphical representation of neutral axis variation in the measured sections - Beam 6

Figure 3.46 shows the cracking state when the increase of the load. As it can be seen, the beam already presented a crack pattern before the beginning of the load tests, probably due to shrinkage issues.

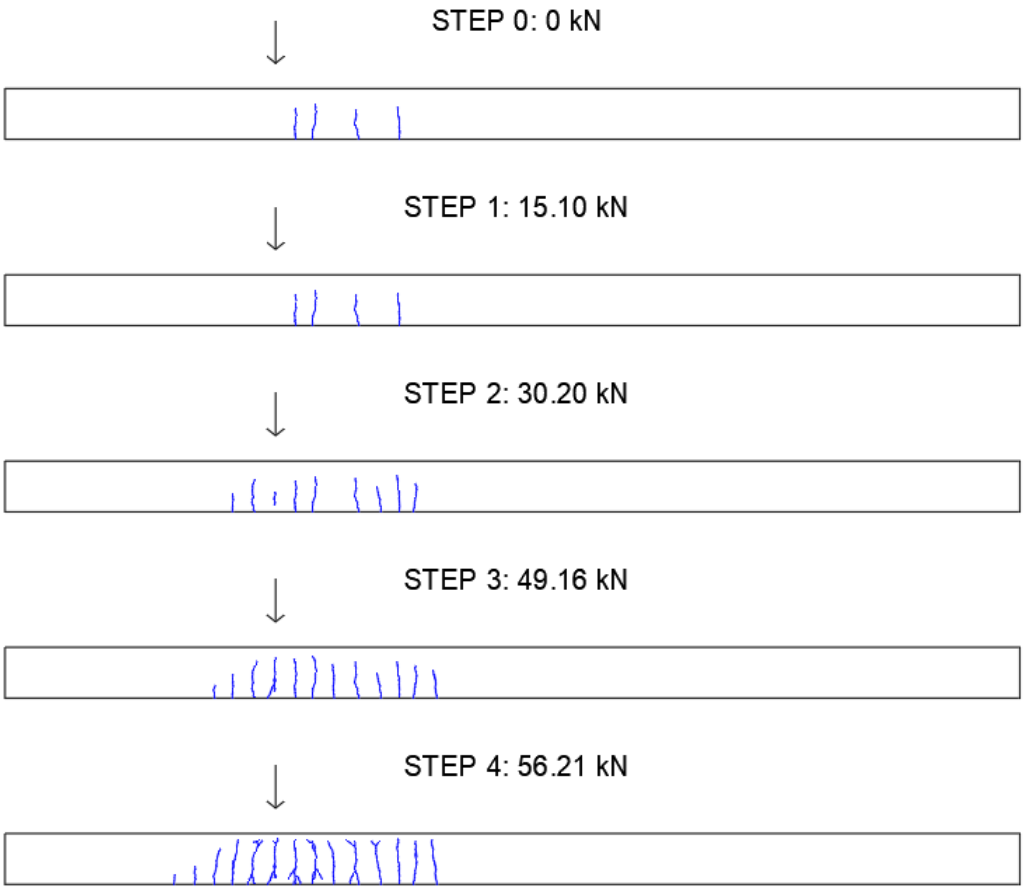

Figure 3.46 - Evolution of crack pattern - Beam 6

3.2.8 Comparison of static results

Static results are discussed here in terms of load vs. displacements and stiffness vs. applied load. All the results presented here are referred to the ultimate load phase (phase 4 in § 3.2.4). As expected, the ultimate load for the three beams is affected by the cable eccentricity: while Beam 1 (with centered cable) reached a maximum load of 40 kN before failure, Beam 2 recorded an ultimate load of 45 kN. Beam 3, with maximum eccentricity (80 mm) reached a value of 55 kN. Figure 3.47 shows the diagram load-displacements; in this plot the ultimate load is not reached due to the default of displacement sensors near failure state.

Moreover, As seen from , the absolute value of stiffness is slightly different between the three beams, probably due to the contribution of the eccentricity of the cable which, despite being non-adherent, seems to give a contribution to the global stiffness of the section.

shows also how the eccentricity of the cable does not seem to affect the change in stiffness of the beams during the load process, especially in the first phases of load. This aspect can be seen from the slopes of the curves in the figure, which values appear to be similar. Slightly different behaviors appear in the last phases of load: in this part of the test a significant portion

of the beams was cracked, and the presence of an eccentric cable helped to restrain the propagation of cracks. This can be seen for example in Beam 3, that tends to hold an higher value of stiffness with respect to linear trend, at least until the threshold of load of almost 50 kN, beyond which the beam quickly reached the failure condition.

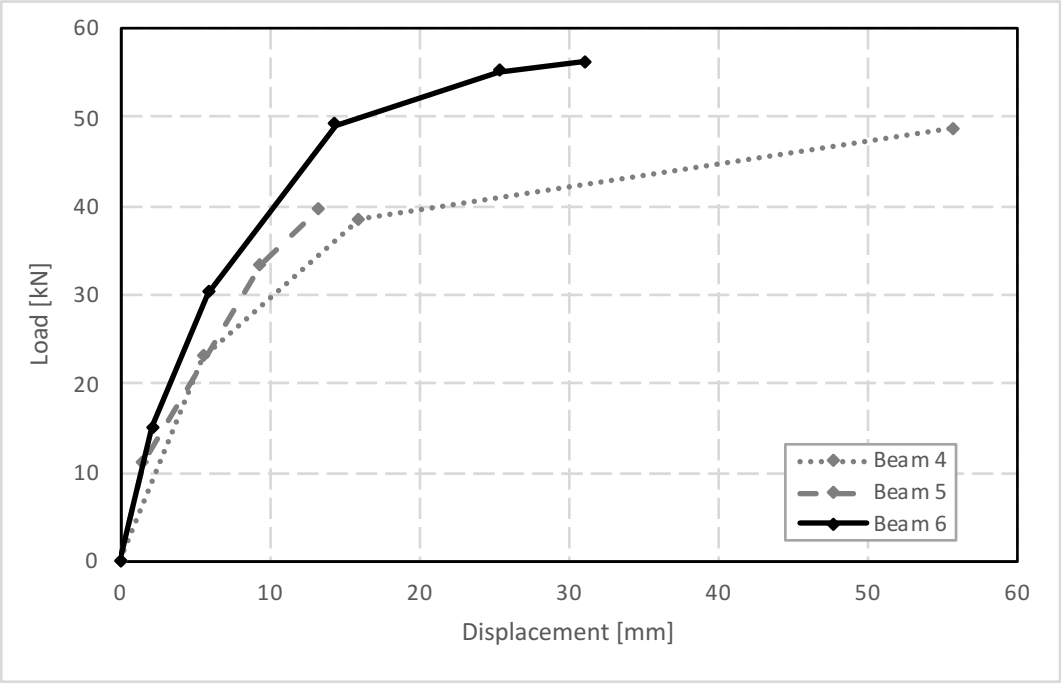

Figure 3.47 – Load-displacements of post-tensioned beams

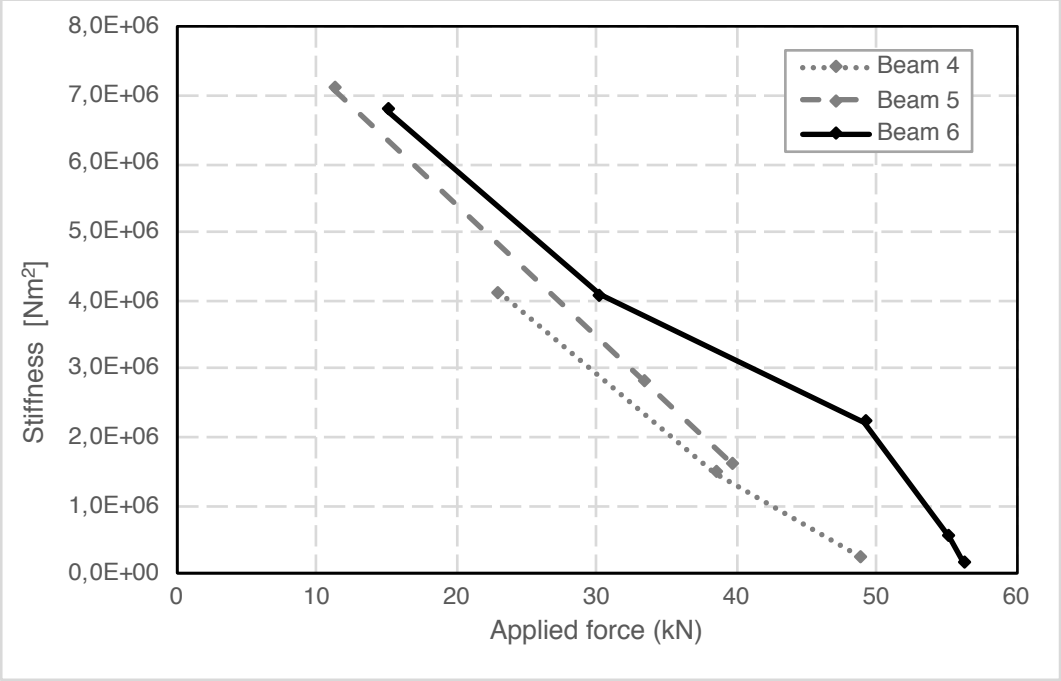

Figure 3.48 – Evolution of stiffness of post-tensioned beams: comparison

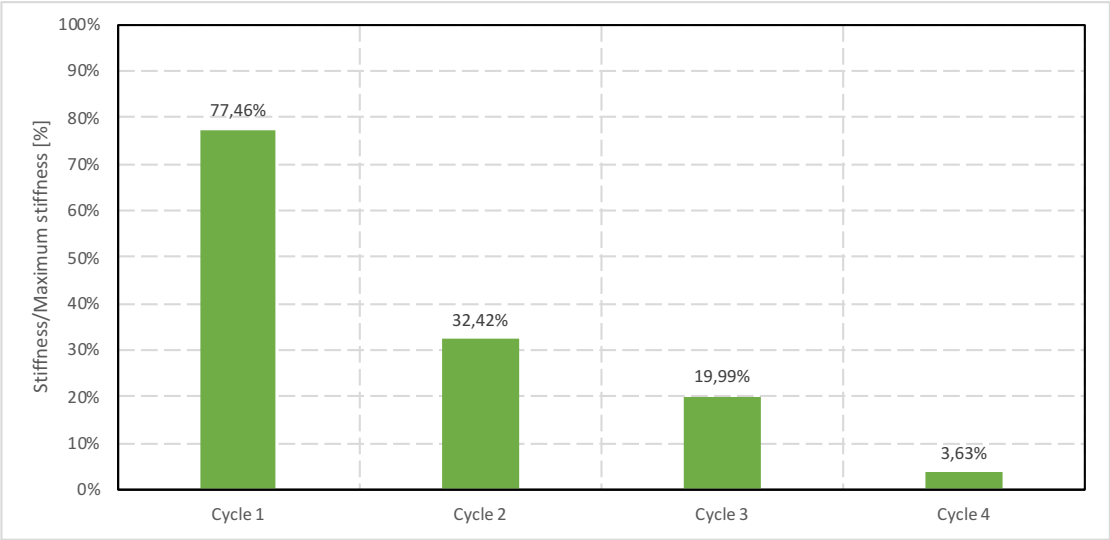

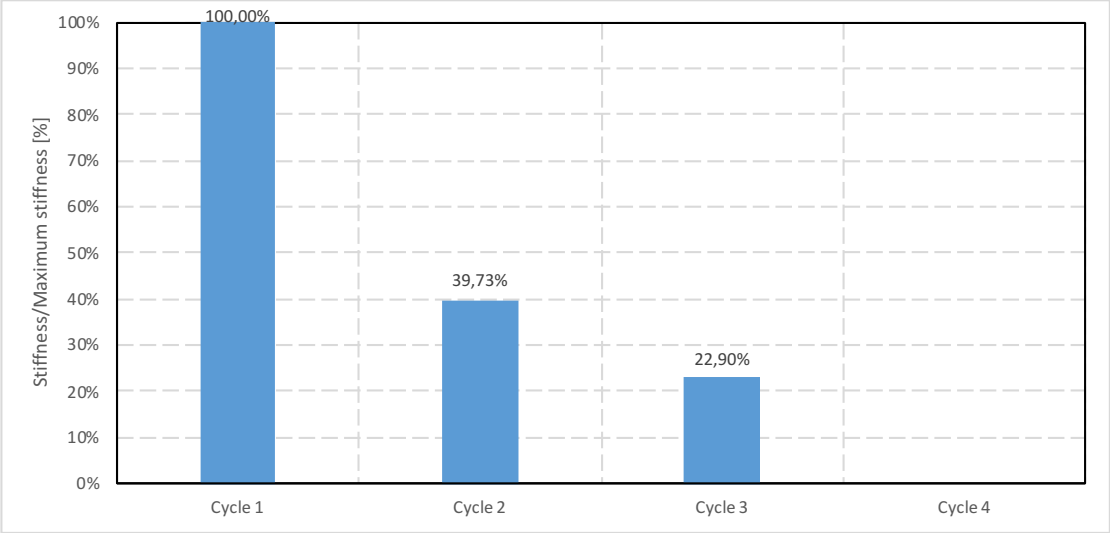

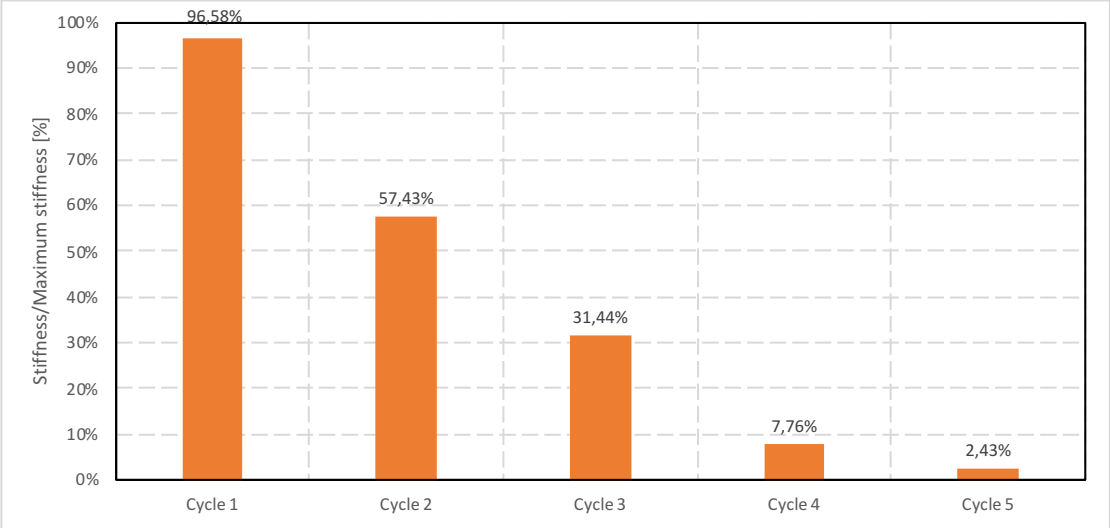

Figure 3.49: Stiffness variation for Beam 4, Beam 5 and Beam 6

4 Ultrasonic tests

4.1 Instrumentation

The tools used for the tests were the following:

- Transducers: emitter probes that produce ultrasonic pulses, exploiting the piezoelectric properties, with a predetermined frequency that, recorded by the receiving probe, allow to measure the time of flight and the wave propagation speed, thus allowing to identify, theoretically, damaged areas;
- Fluids: mainly consisting of an aqueous solution, or mineral oils with variable viscosity depending on the required use, to guarantee an adequate acoustic impedance at the surface of the material, since the ultrasounds are strongly attenuated by the air. In order to avoid the formation of air bubbles, it is necessary to check that the fluid is well adherent to the surface of the medium (the surface tension of the fluid must be lower or equal to that of the fluid / specimen bonds) . Another verification concerns the chemical interfacing to exclude possible corrosion, formation of deposits or chemical reactions during the test. Usually one chooses fluids that are easily removable and disposable in the environment at the end of the test.
- Acquisition software (PunditLink).

When the probe is reflected and returns to the transmitter probe, an electrical signal will be produced which, appropriately amplified and filtered, can be displayed on the monitor.

The acquisition device provided the transit time between the two probes, signal attenuation and speed.

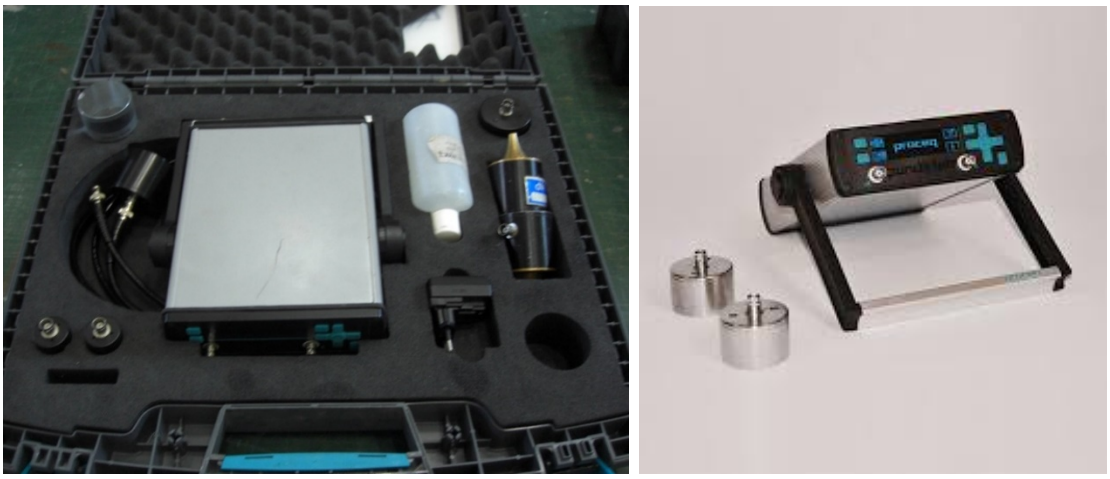

Figure 4.1: Ultrasonic tests: instrumentation

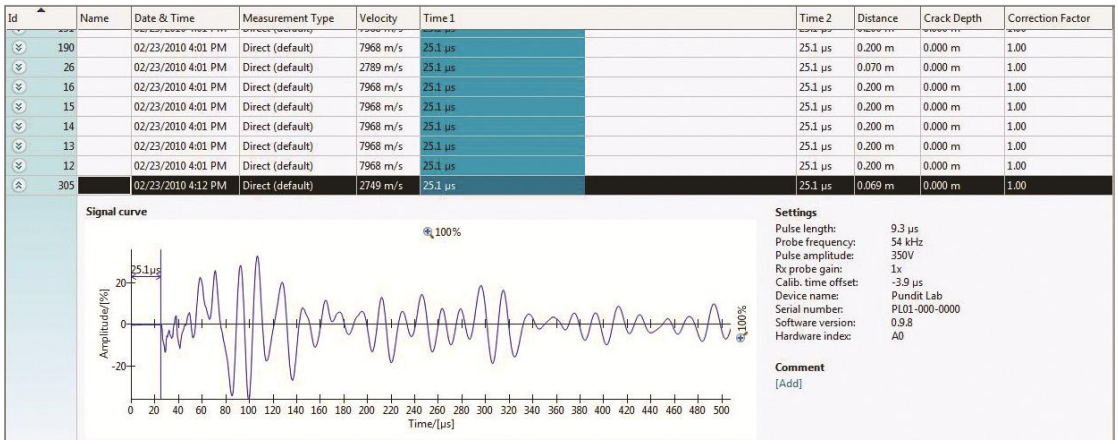

Figure 4.2: PunditLink acquisition software

4.2 Pre-stressed beams

4.2.1 Test configuration

Following is a diagram of the instrumentation for pre-tensioned beams: the measurement points were 9 in the upper face and 9 in the lower one. For each position in the upper face, three measurements were taken, one direct and two inclined, with the purpose to obtain a grid of values and a "tomographic" view of the results.

In order to obtain a "contour" representation of the results, the following steps were taken:

- First, the results in terms of velocity were stored in a matrix *m,n* where *m* was the number of ultrasonic paths for every load step (27 for pre-tensioned beams), and *n* is the number of load steps (5);

- Then, a grid was defined, with 17 points in the longitudinal directions (corresponding to the 9 points of measure plus the 8 mid-points) and 3 points in vertical directions (upper surface of the beam, barycenter, and lower surface);
- For every point of the 17x3 grid, a value of velocity was assigned, equal to the average of the values of velocity pertaining to this point, based on which paths were starting, ending or passing through it.

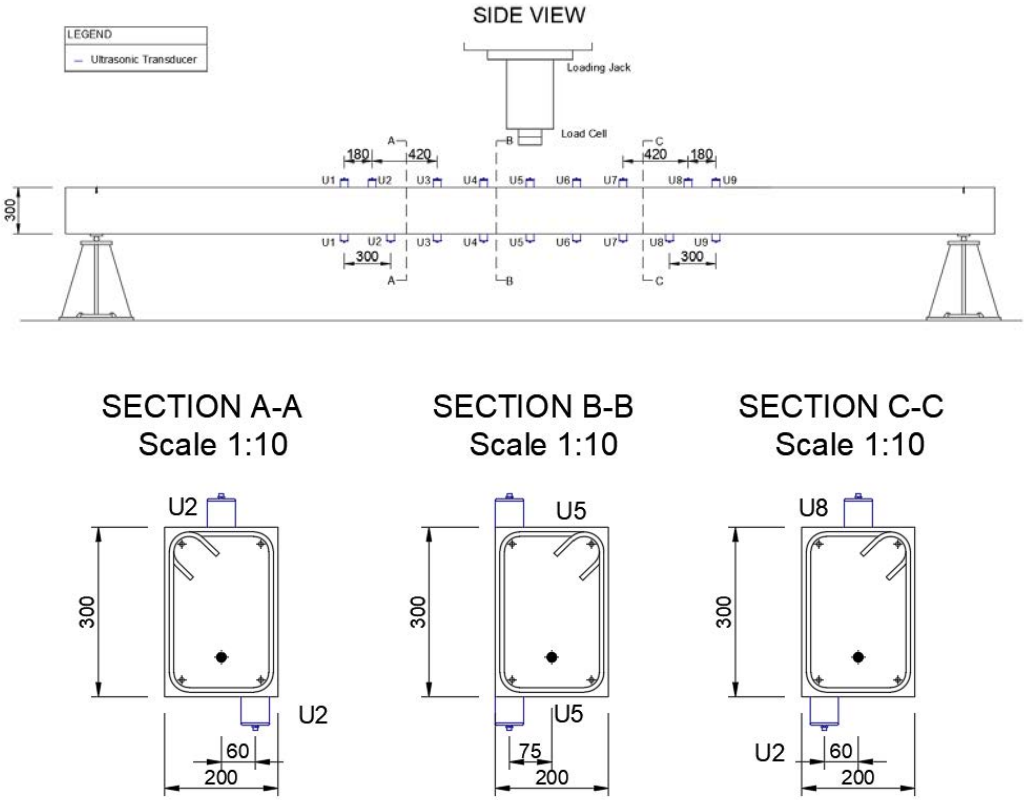

Figure 4.3 Sensor setup: pre-tensioned beams

Ultrasonic tests, such as dynamics, are performed for each load cycle. The results obtained are now reported in terms of speed.

4.2.2 Beam 1

The following pictures represent the mapping of the speed obtained by the interpolation of the 27 different measured paths (3 paths for every one of the 9 transmitting positions).

The colors in the legend represent the crack pattern for every load step: the cracks are drawn with the respective color in the corresponding picture.

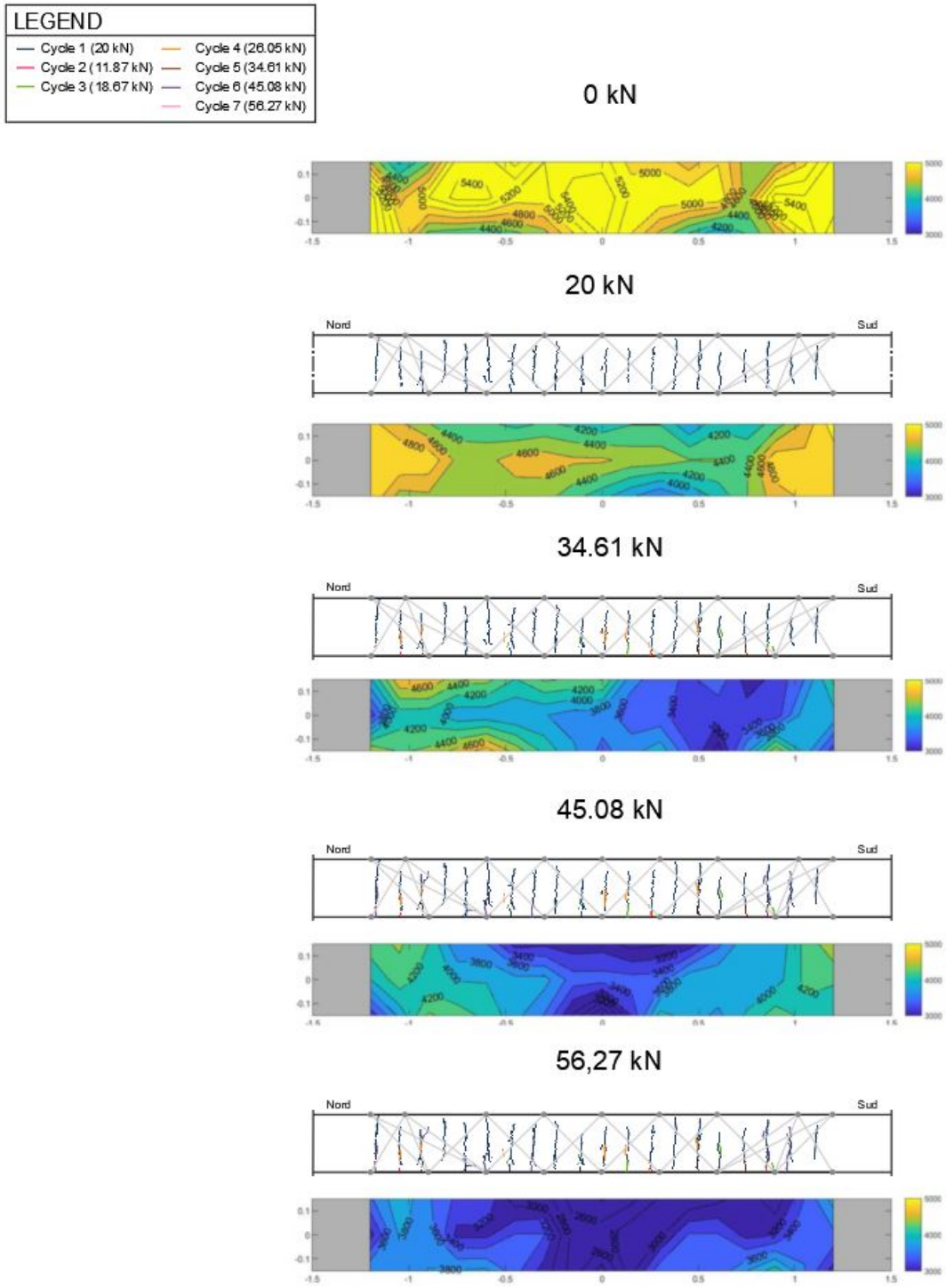

Figure 4.4. Speed mapping for the various load cycles

By comparing the speed mapping with the visual crack pattern it is observed a variation in speed consistent with the formation of the cracks and their position with respect to the inclined trajectory.

The difference in the results for vertical and inclined paths is shown in the following pictures.

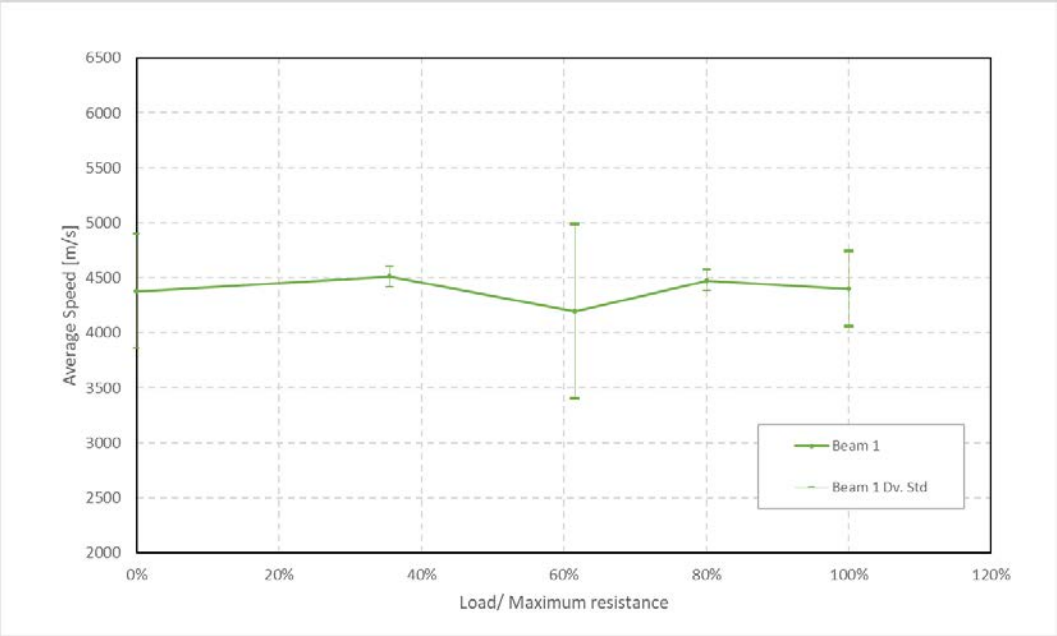

Figure 4.5. Variation of the average speed and its standard deviation for the various cycles along the vertical paths

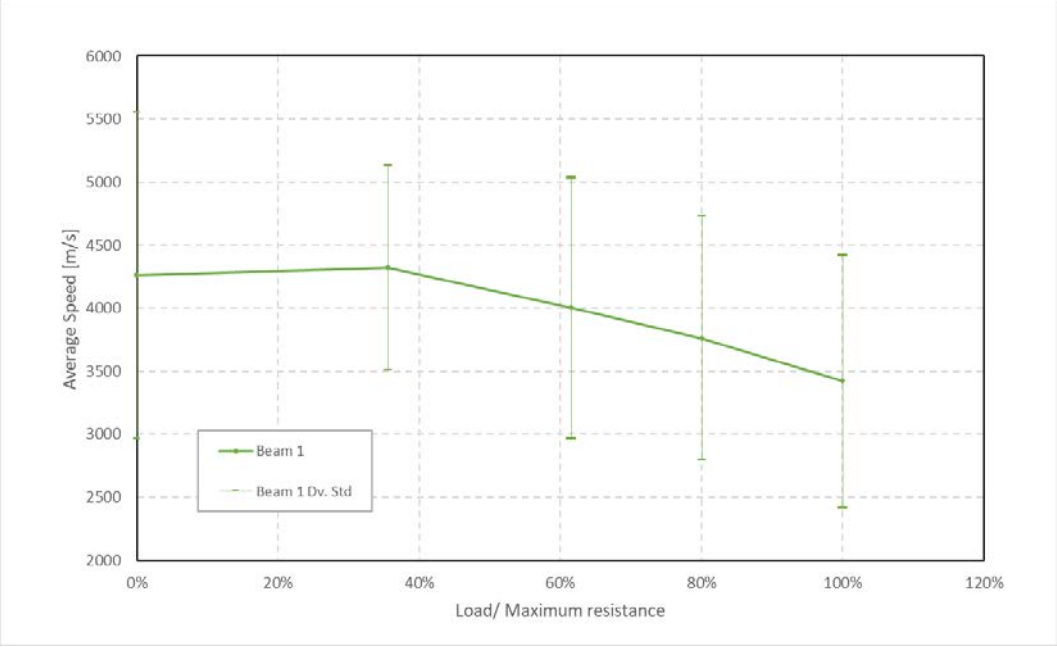

Figure 4.6. Variation of average speed and its standard deviation for the various cycles along the inclined paths

From the graphs in the previous pictures it is observed, that inclined paths have higher sensitivity to the increase of damage with respect to vertical paths. This is probably due to the fact that vertical paths rarely cross bending (vertical) cracks, and are mole likely to travel in uncracked concrete even in presence of cracks. The former have a variability between 4800m/s and 3400m/s, while the latter fluctuate around 4500m/s.

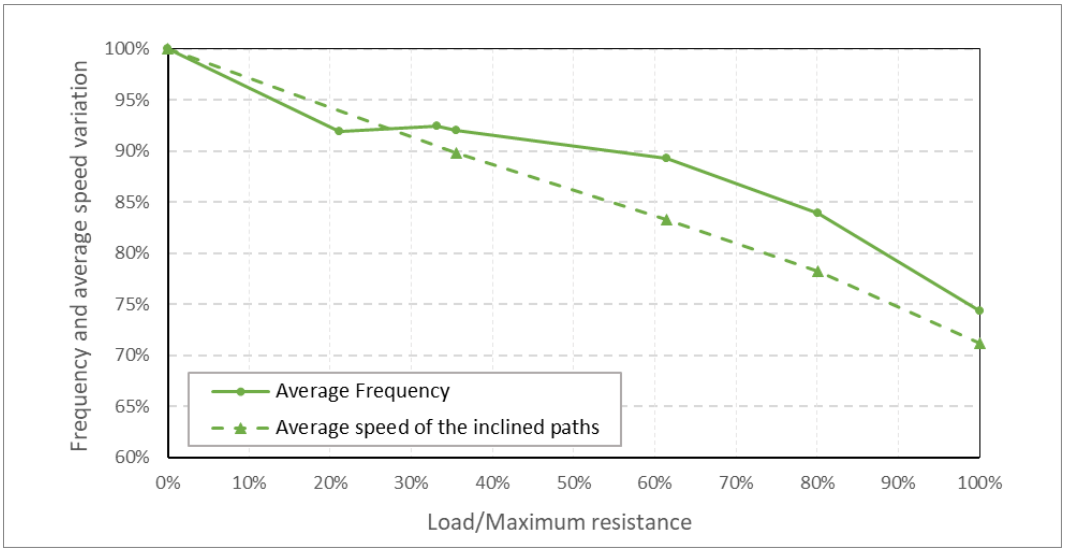

Figure 4.7. Comparison of average frequencies and speeds depending on the load.

In Figure 4.7 the variation in vibration frequency and average ultrasonic speed were compared for inclined paths. It is observed that the average vibration frequency and the average ultrasonic speed relative to the inclined paths have similar tendency.

4.2.3 Beam 2

The following pictures represent the mapping of the speed obtained by the interpolation of the 27 different measured paths (3 paths for every one of the 9 transmitting positions).

The colors in the legend represent the crack pattern for every load step: the cracks are drawn with the respective color in the corresponding picture.

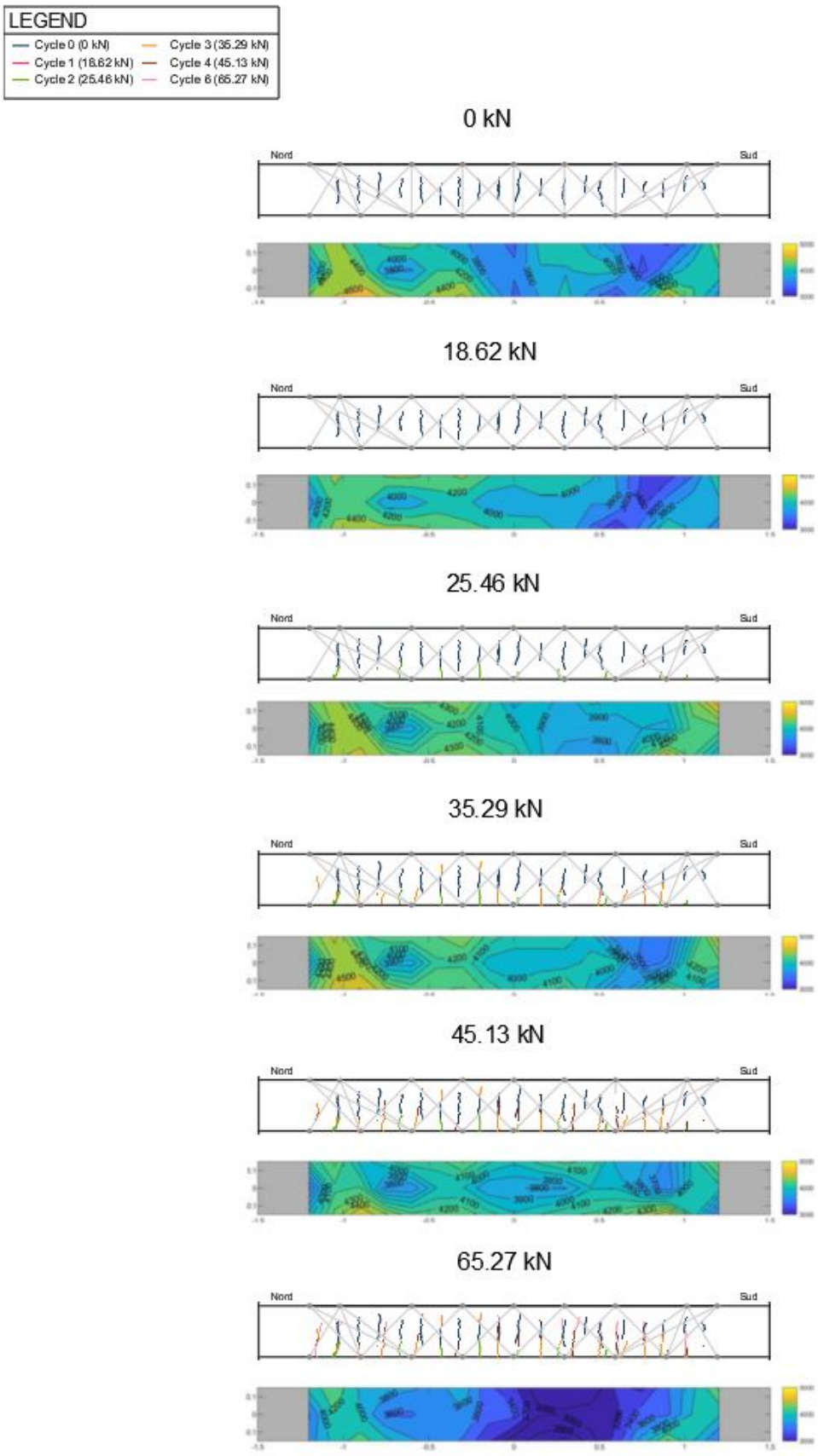

Figure 4.8. Speed mapping for the various load cycles

By comparing the speed mapping with the visual crack pattern it is observed a variation in speed consistent with the formation of the cracks and their position with respect to the inclined trajectory.

The difference in the results for vertical and inclined paths is shown in the following pictures.

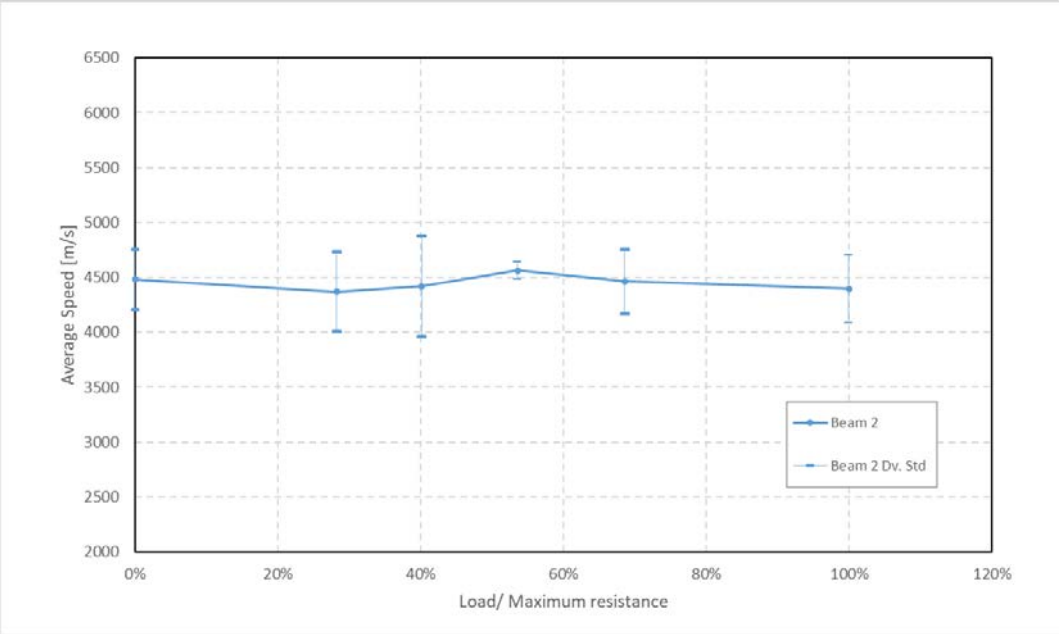

Figure 4.9. Variation of the average speed and its standard deviation for the various cycles along the vertical paths

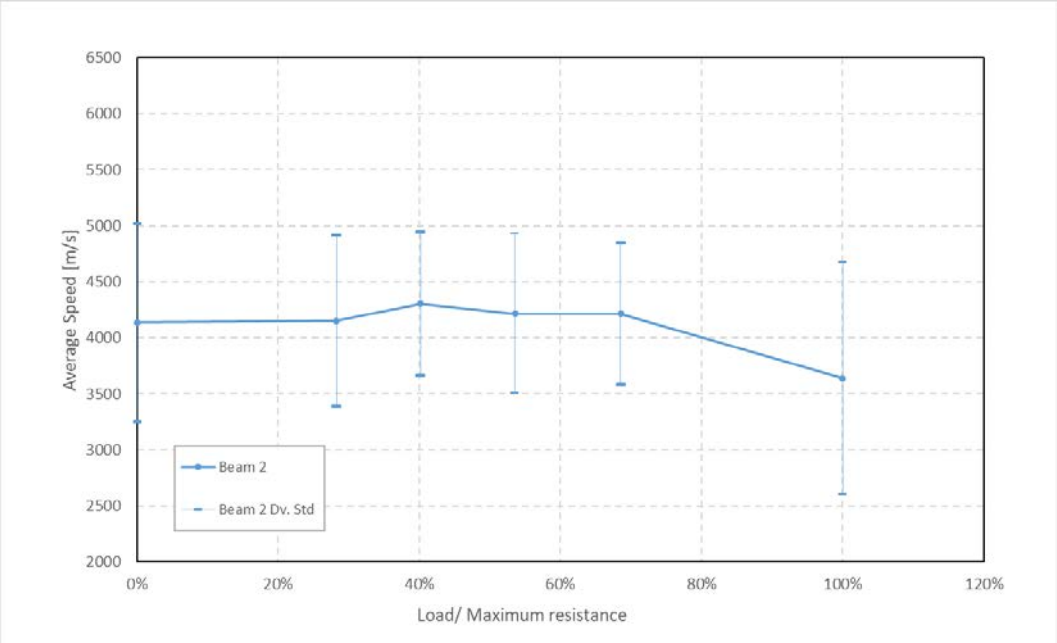

Figure 4.10. Variation of average speed and its standard deviation for the various cycles along the inclined paths

From the graphs in the previous pictures it is observed, that inclined paths have higher sensitivity to the increase of damage with respect to vertical paths. This is probably due to the fact that vertical paths rarely cross bending (vertical) cracks, and are mole likely to travel in uncracked concrete even in presence of cracks. The former have a variability between 4400m/s and 3600m/s, while the latter fluctuate around 4500m/s.

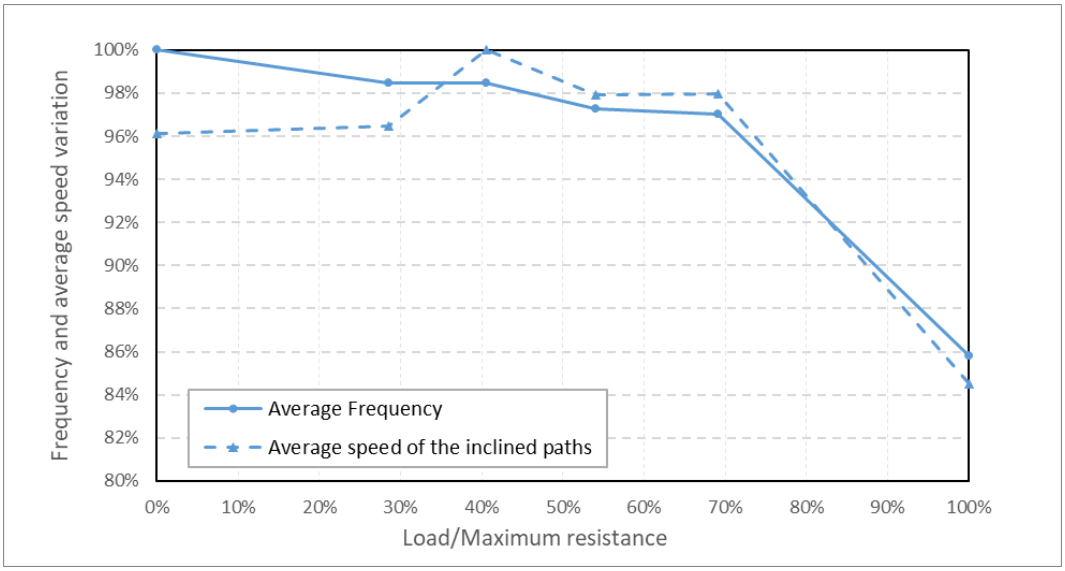

Figure 4.11. Comparison of average frequencies and speeds depending on the load.

Also in this case, it is observed that the average vibrational frequency and the average ultrasonic speed relative to the inclined paths have similar tendency.

4.2.4 Beam 3

The following pictures represent the mapping of the speed obtained by the interpolation of the 27 different measured paths (3 paths for every one of the 9 transmitting positions).

The colors in the legend represent the crack pattern for every load step: the cracks are drawn with the respective color in the corresponding picture.

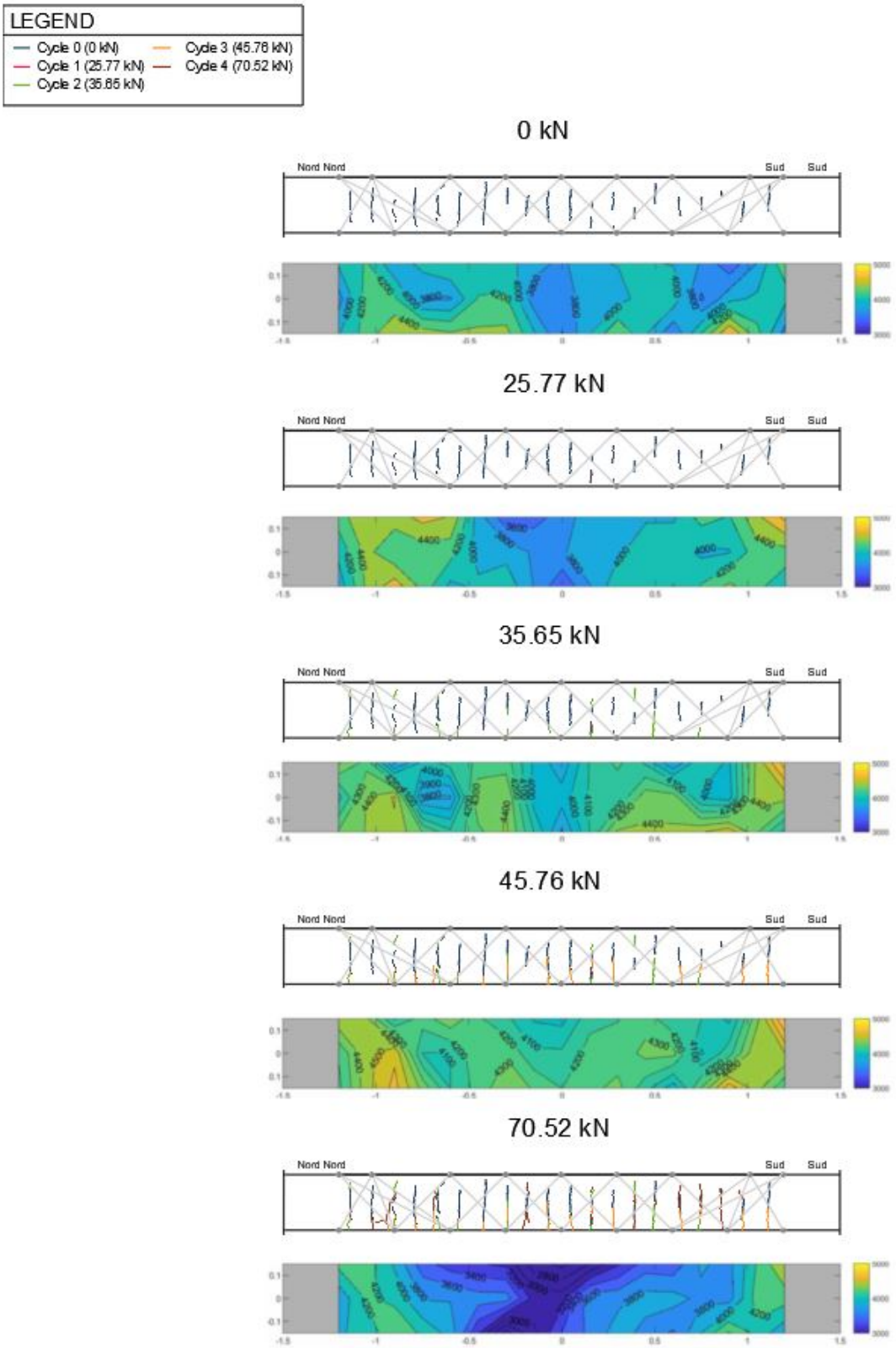

Figure 4.12. Speed mapping for the various load cycles

By comparing the speed mapping with the visual crack pattern it is observed a variation in speed consistent with the formation of the cracks and their position with respect to the inclined trajectory.

The difference in the results for vertical and inclined paths is shown in the following pictures.

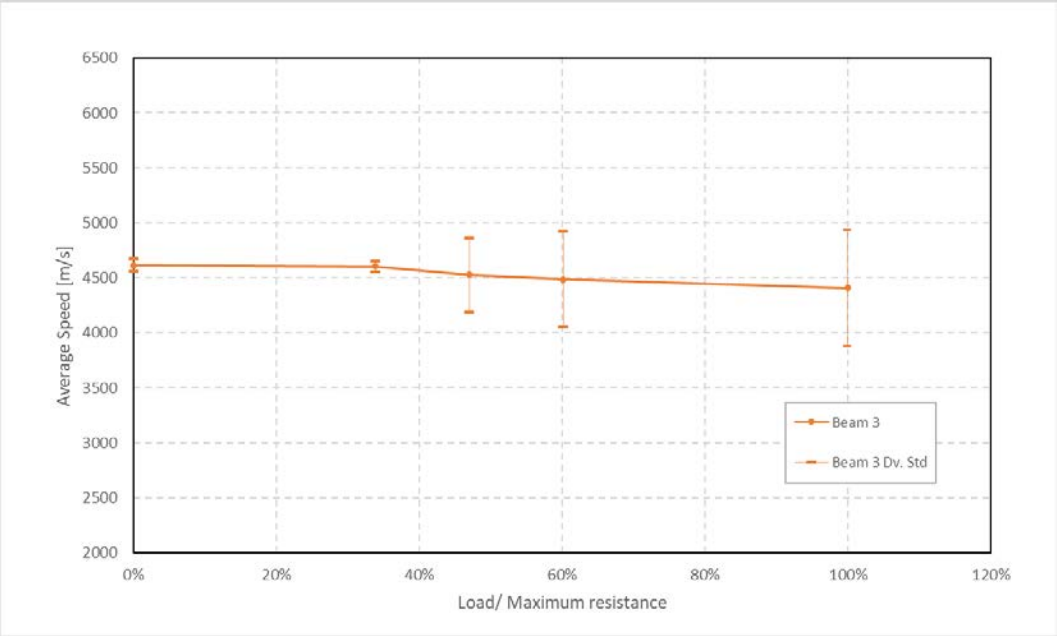

Figure 4.13. Variation of the average speed and its standard deviation for the various cycles along the vertical paths

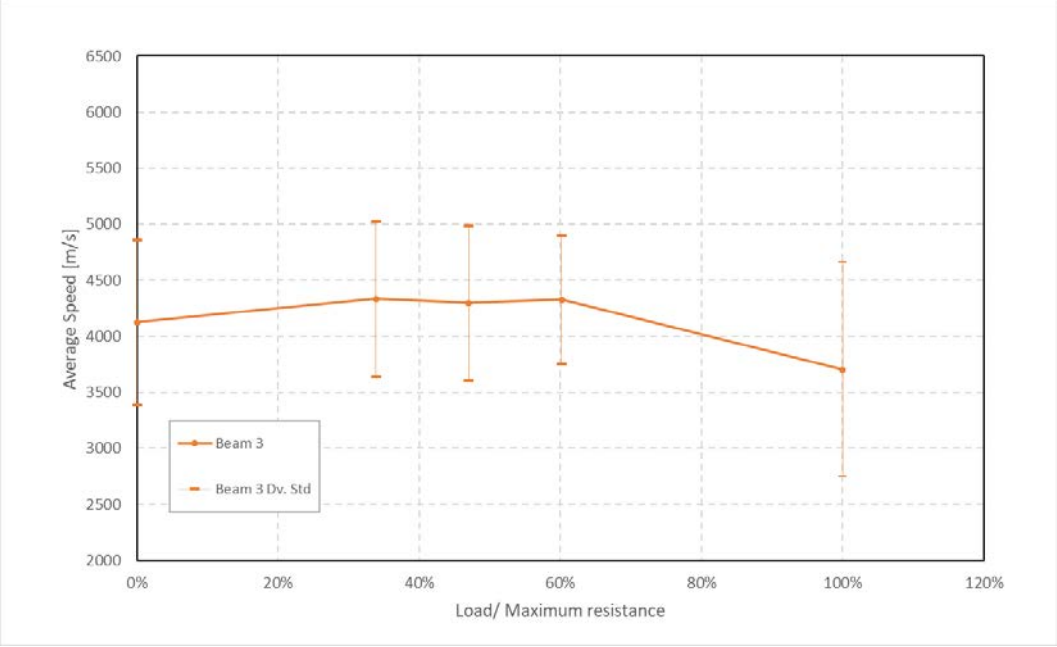

Figure 4.14. Variation of average speed and its standard deviation for the various cycles along the inclined paths

From the graphs in the previous pictures it is observed, that inclined paths have higher sensitivity to the increase of damage with respect to vertical paths. This is probably due to the fact that vertical paths rarely cross bending (vertical) cracks, and are mole likely to travel in uncracked concrete even in presence of cracks. The former have a variability between 4300m/s and 3600m/s, while the latter fluctuate around 4500m/s.

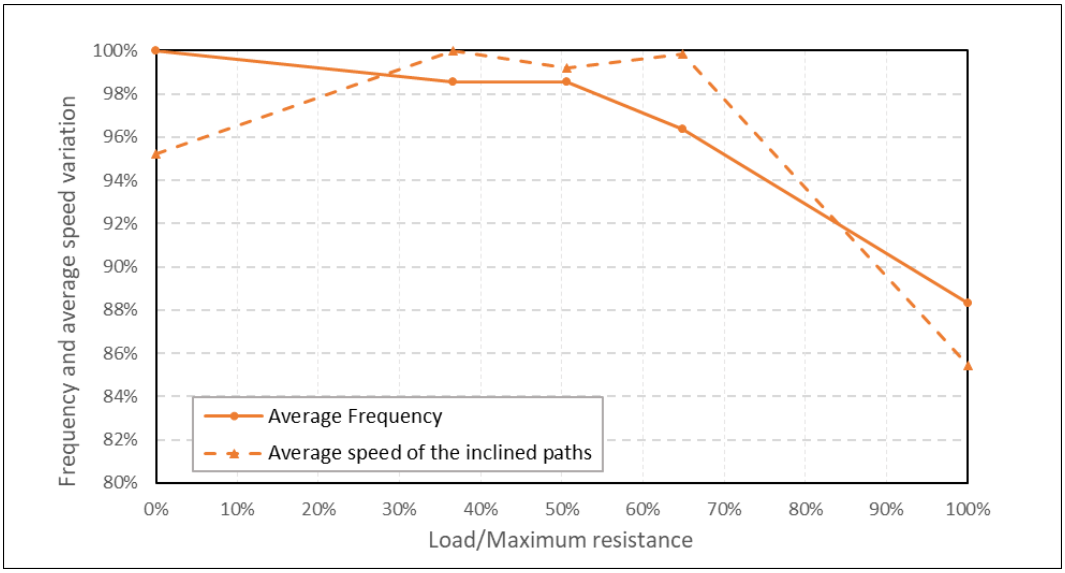

Figure 4.15. Comparison of average frequencies and speeds depending on the load.

Also in this case, it is observed that the average vibrational frequency and the average ultrasonic speed relative to the inclined paths have similar tendency.

4.2.5 Result comparison: beam 1, 2 and 3

In the following graphs the behavior of the three beams with the increase of the damage is studied. The first two figures show the average speeds depending on the load level, until failure.

As already observed previously, the average speeds of the vertical paths oscillate around 4500m/s, without considerable variation in speed as the damage increases. Moreover, no variation was observed in vertical velocity with the change in prestressing level.

On the contrary, the velocities on inclined paths start from a very similar initial value for all the three beams, but with the increase in damage a decrease in speed is observed, with a sharp drop in speed at failure state. Moreover, lower speeds were recorded for lower level of prestressing (the lower the prestressing value, the lower the measured speed). However, it can be observed that the inclined paths have a greater statistical dispersion than the vertical ones.

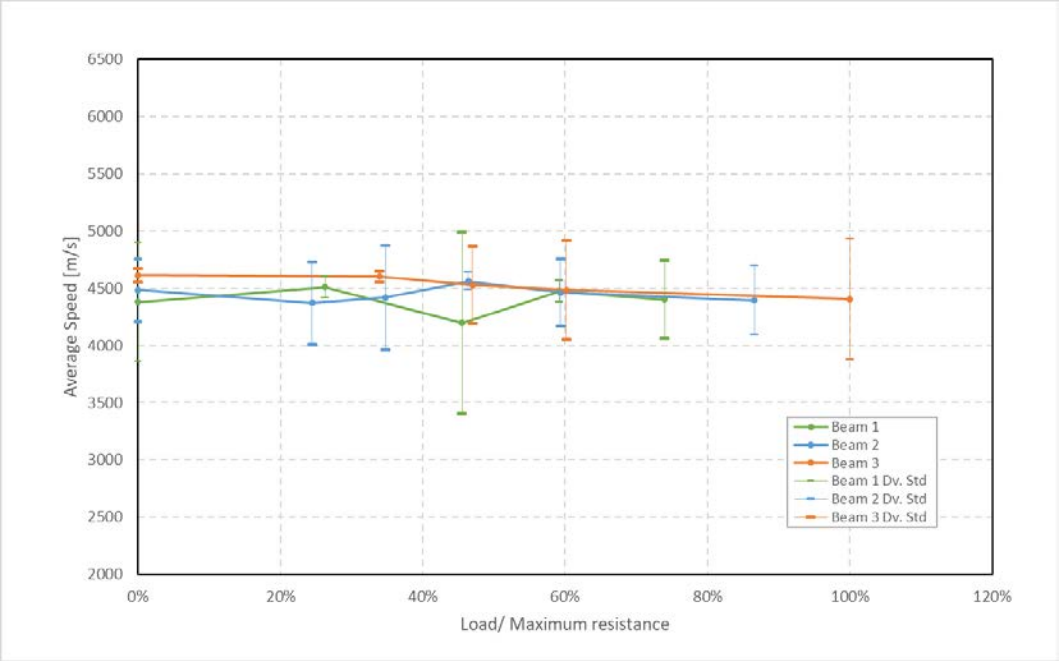

Figure 4.16. Comparison of the variation of the average speed and of its standard deviation for the load cycles along the vertical paths

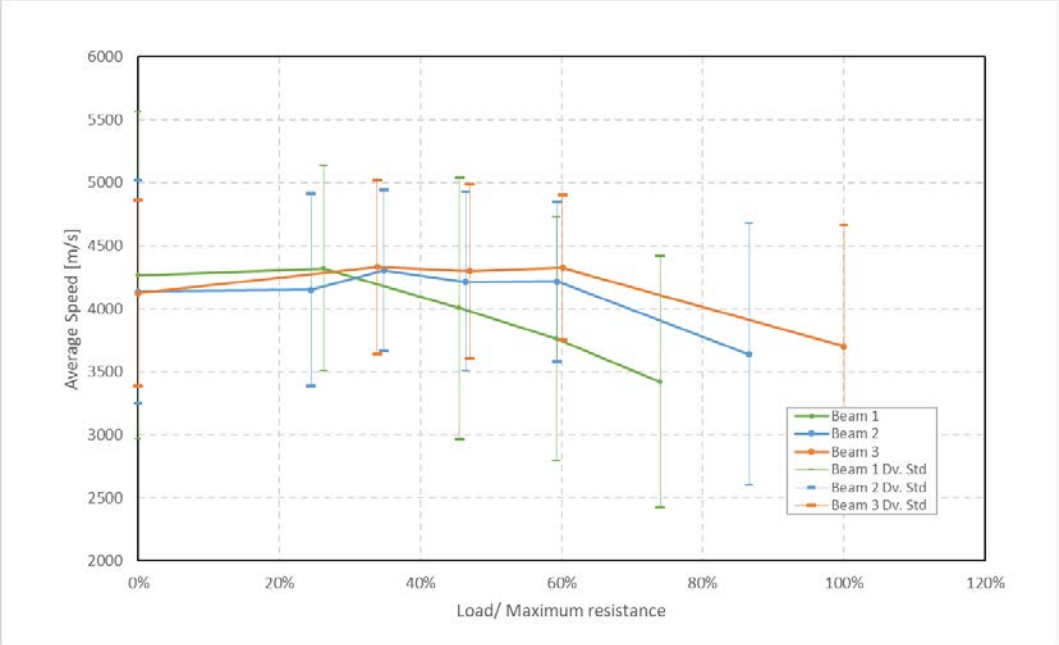

Figure 4.17. Comparison of the variation of the average speed and of its standard deviation for the load cycles along the inclined paths

4.3 Post-tensioned beams

4.3.1 Test configuration

Following is a diagram of the instrumentation for post-tensioned beams: the measurement points were subdivided in 2 groups:

- In the first group, the ultrasonic signals are transmitted in the vertical direction (upper face-lower face of the beam, indicated as "Y" in the following pages) with 7 points of transmission in the upper face and 7 receiving points in the lower face. For each position in the upper face, three measurements were taken, one direct and two inclined, with the purpose to obtain a grid of values and a "tomographic" view of the results;
- In the second group, the ultrasonic signals are transmitted in horizontal (transversal) direction (east face – west face, indicated as "X" in the following pages) with 7 points of transmission in the east face and 7 receiving points in the west face, and the same scheme of measurements.

In order to obtain a "contour" representation of the results, the following steps were taken:

- First, the results in terms of velocity were stored in a matrix *m,n* where *m* was the number of ultrasonic paths for every load step (19 for horizontal paths and 16 for vertical paths, since in this last case 1 point of the grid was occupied by the point of application of the load), and *n* is the number of load steps (3) multiplied by the number of prestressing levels (5);
- Then, a grid was defined, with 13 points in the longitudinal directions (corresponding to the 7 points of measure plus the 6 mid-points) and 3 points in vertical directions (upper surface of the beam, barycenter, and lower surface). For horizontal case the 3 points are taken in transversal direction (east surface, barycenter, west surface).
- For every point of the 13x3 grid, a value of velocity was assigned, equal to the average of the values of velocity pertaining to this point, based on which paths were starting, ending or passing through it.

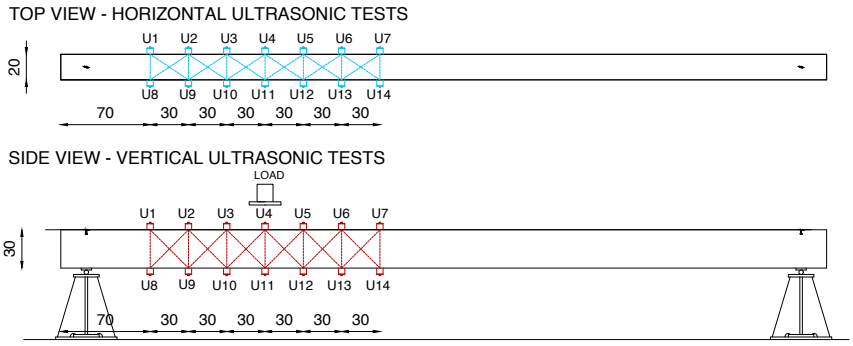

Figure 4.18. Sensor setup: post-tensioned beams

Ultrasonic tests, such as dynamics, are performed for each load and prestressing cycle. The results obtained are now reported in terms of speed. The result are analyzed first for the signal transmitted in the vertical direction (Y), then for the horizontal one (X).

4.3.2 Beam 4 – vertical signal

The following pictures represent the averaging of the 16 different measured paths in vertical direction, subdivided in straight and inclined paths, in terms of speed.

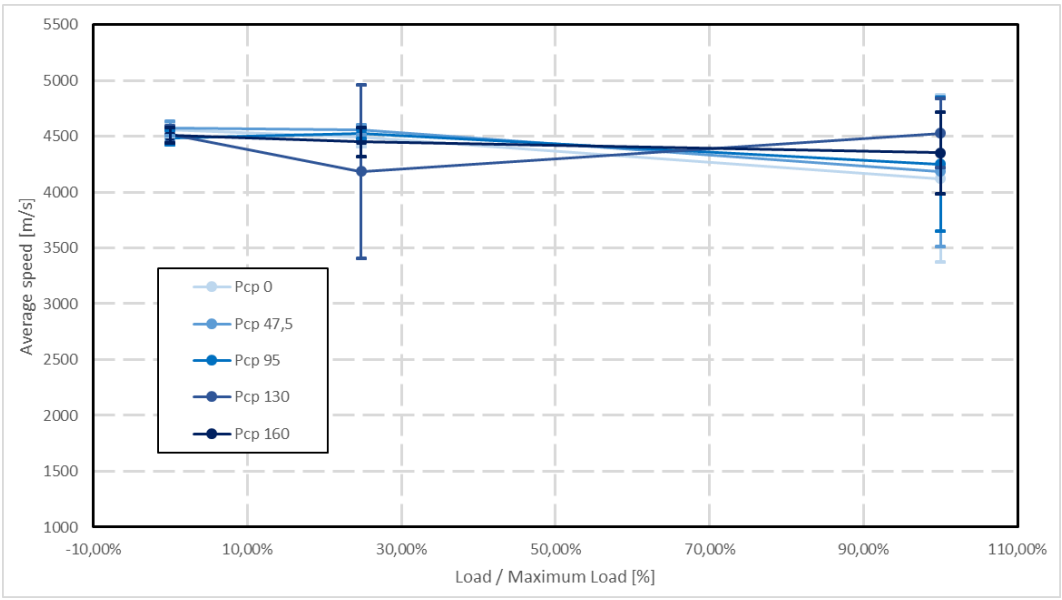

Figure 4.19. Beam 4. Variation of the average speed and its standard deviation for the various cycles along the straight vertical paths for different prestressed force levels

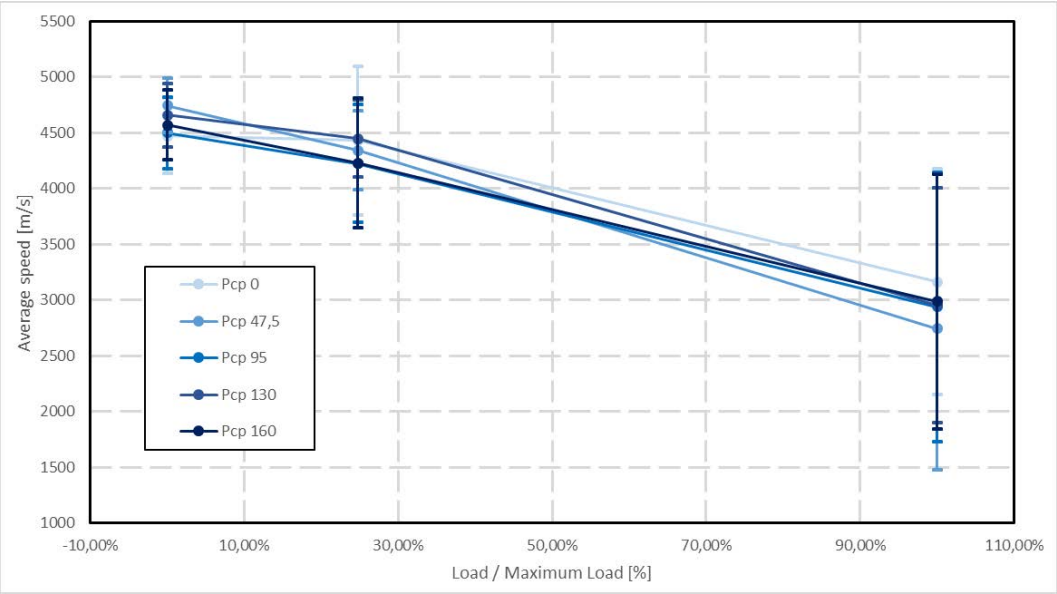

Figure 4.20. Beam 4. Variation of the average speed and its standard deviation for the various cycles along the inclined vertical paths for different prestressed force levels

From the graphs in the previous pictures it is observed, that inclined paths have higher sensitivity to the increase of damage with respect to vertical paths. This is probably due to the fact that vertical paths rarely cross bending (vertical) cracks, and are more likely to travel in uncracked concrete even in presence of cracks. The former have a variability between 4800m/s and 2700m/s, while the latter fluctuate around 4500m/s.

Furthermore, the variation of speed is similar for all prestressed forces.

The following pictures represent the tomographic mapping of the speed obtained by the interpolation of the 16 different measured paths, compared with visual survey of crack pattern.

By comparing the speed mapping with the visual crack pattern it is observed a variation in speed consistent with the formation of the cracks and their position with respect to the trajectories.

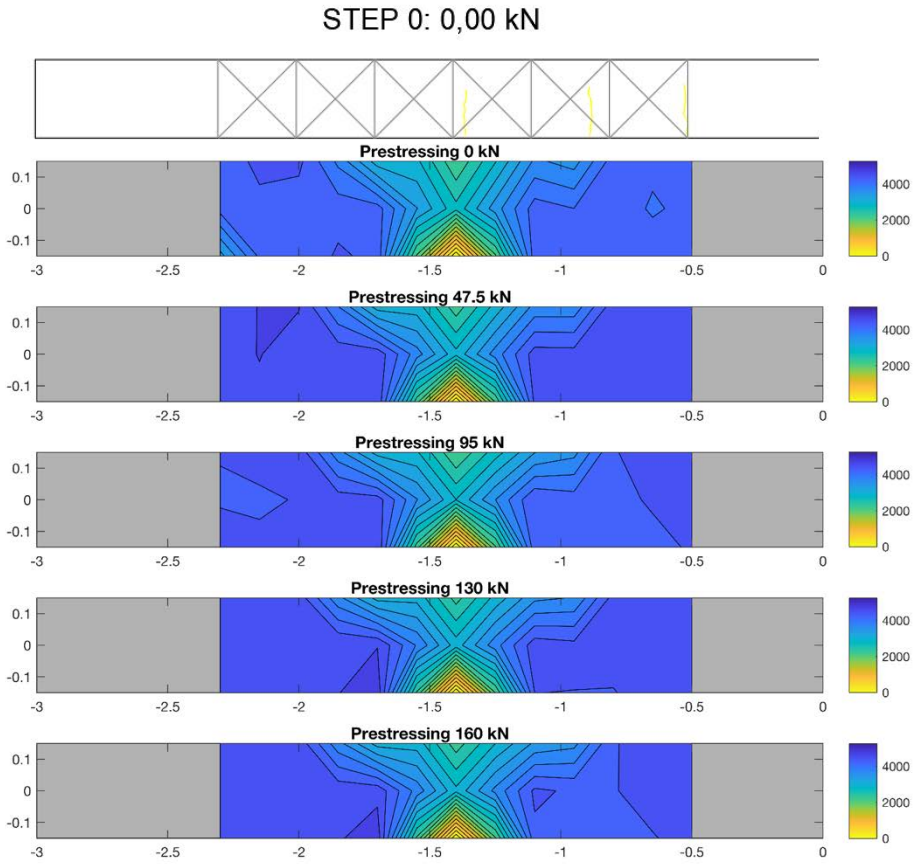

Figure 4.21. Beam 4. Tomographic ultrasonic speed for different prestressed force levels. Undamaged state

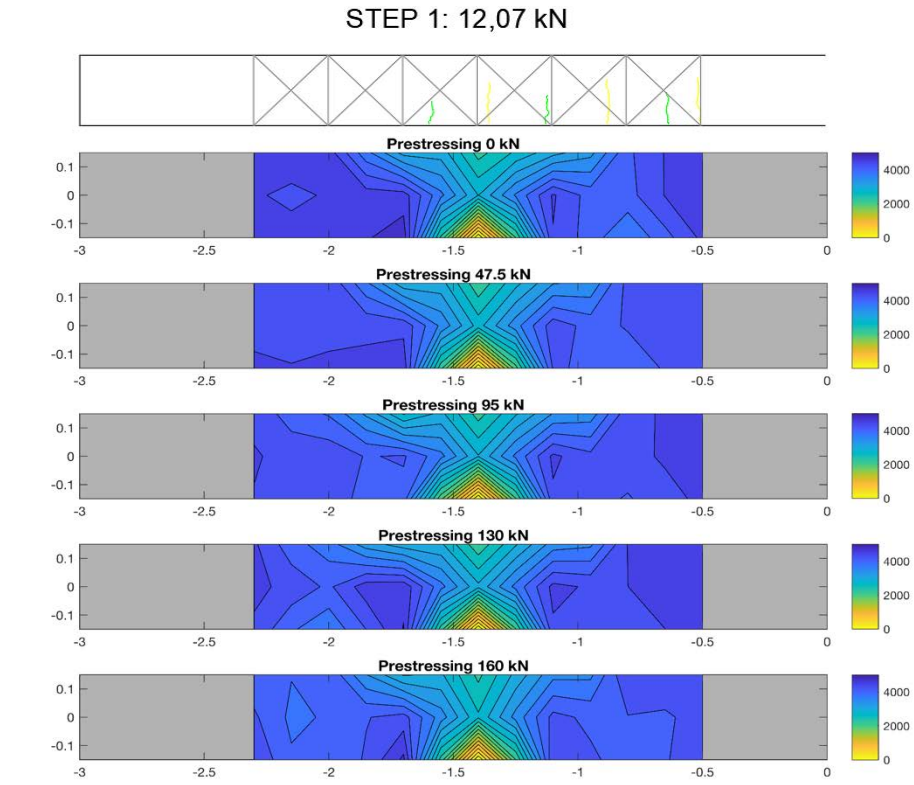

Figure 4.22. Beam 4. Tomographic ultrasonic speed for different prestressed force levels. Cracked state

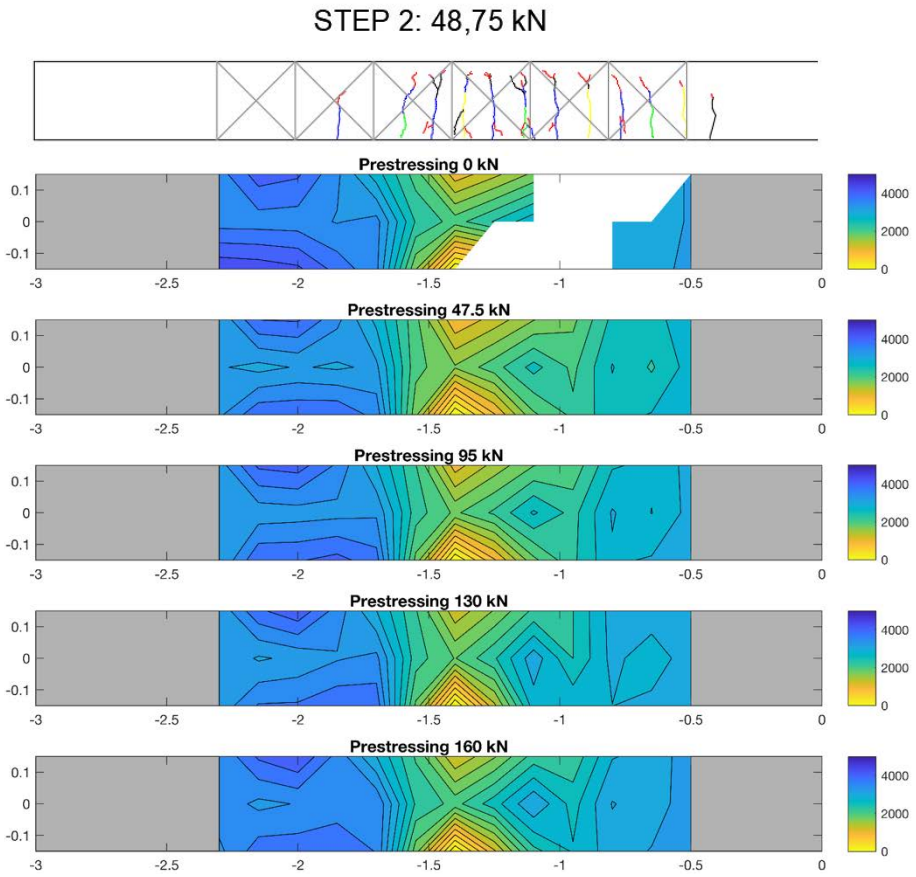

Figure 4.23. Beam 4. Tomographic ultrasonic speed for different prestressed force levels. Failure state

4.3.3 Beam 4 – horizontal signal

The following pictures represent the averaging of the 19 different measured paths in horizontal direction, subdivided in straight and inclined paths, in terms of speed.

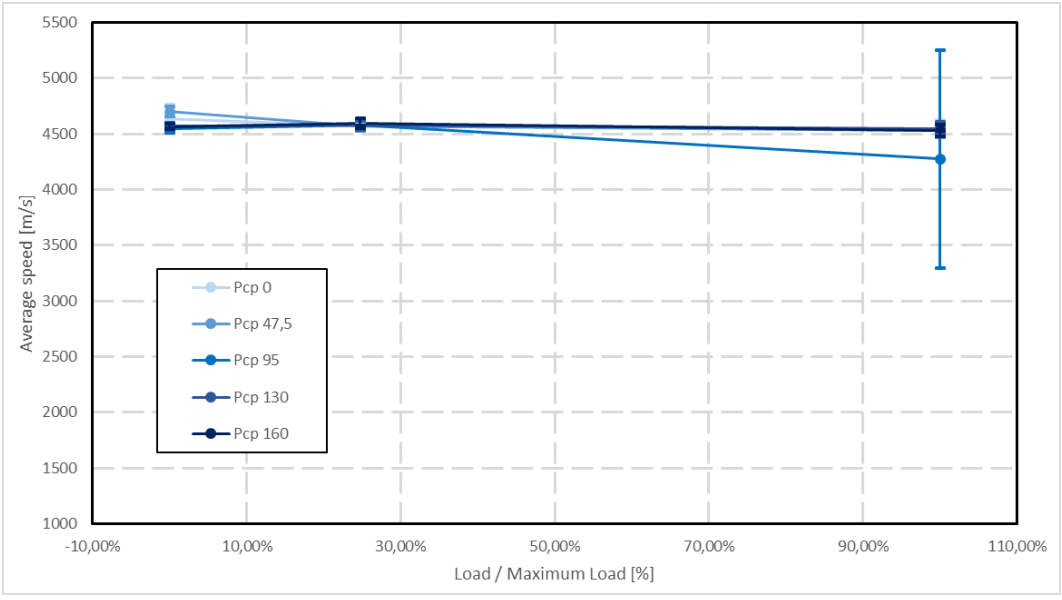

Figure 4.24. Beam 4. Variation of the average speed and its standard deviation for the various cycles along the straight horizontal paths for different prestressed force levels

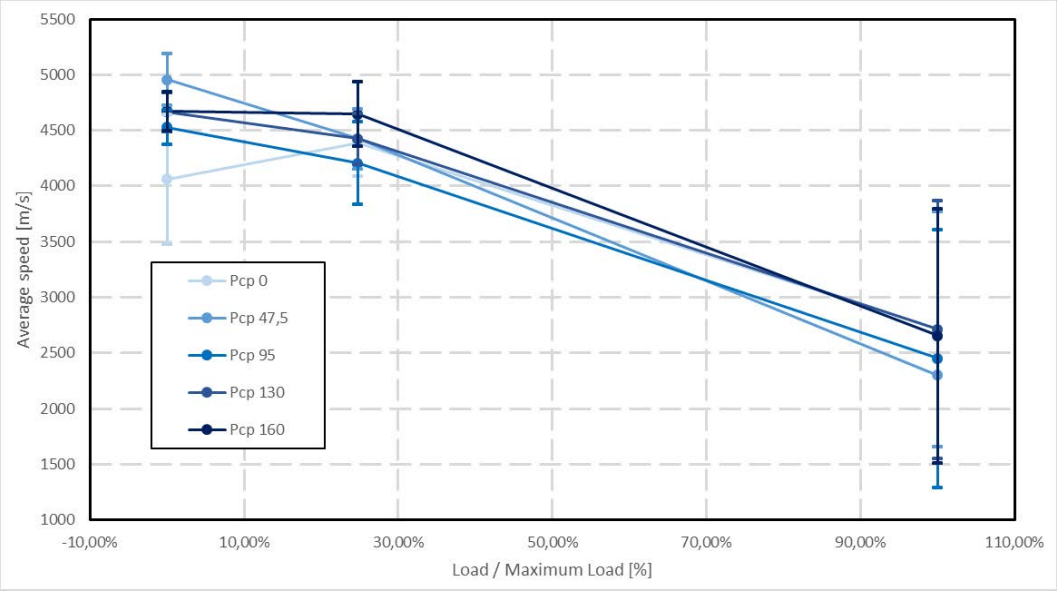

Figure 4.25. Beam 4. Variation of the average speed and its standard deviation for the various cycles along the inclined horizontal paths for different prestressed force levels

As seen for the ultrasonic signals transmitted horizontally also in this case it is observed, that inclined paths have higher sensitivity to the increase of damage with respect to vertical paths. The former have a variability between 5000m/s and 2300m/s, while the latter fluctuate around 4600m/s.

Furthermore, the variation of speed is similar for all prestressing forces.

The following pictures represent the tomographic mapping of the speed obtained by the interpolation of the 19 different measured paths, compared with visual survey of crack pattern.

By comparing the speed mapping with the visual crack pattern it is observed a variation in speed consistent with the formation of the cracks and their position with respect to the trajectories, mostly in the most cracked phase. The speed values are more homogeneous than the correspondent vertical speeds.

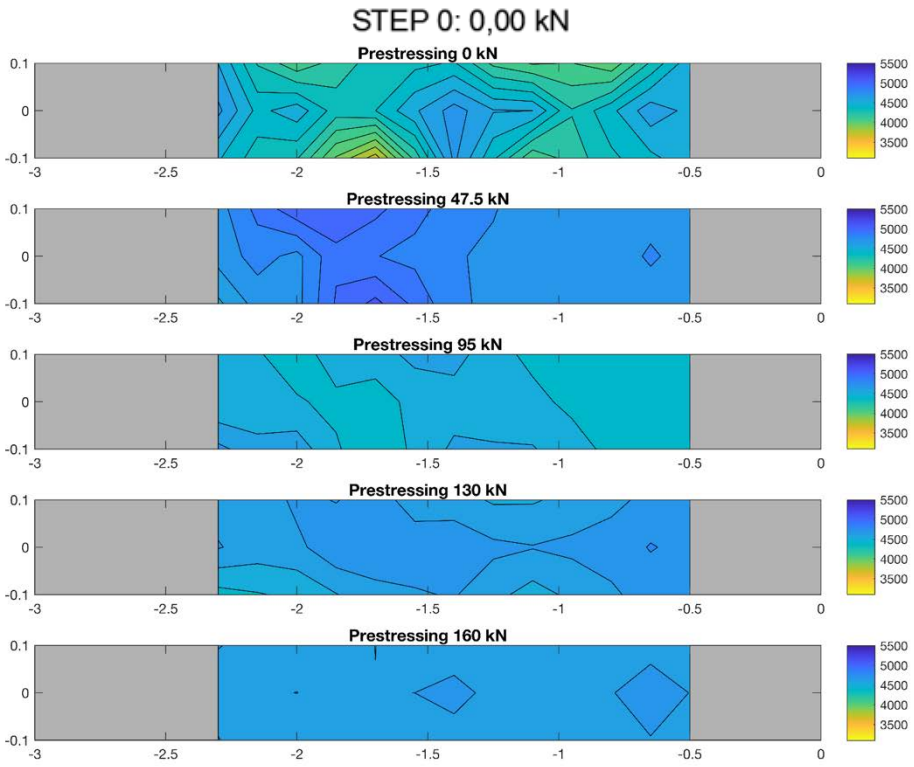

Figure 4.26. Beam 4. Tomographic ultrasonic speed for different prestressed force levels. Undamaged state

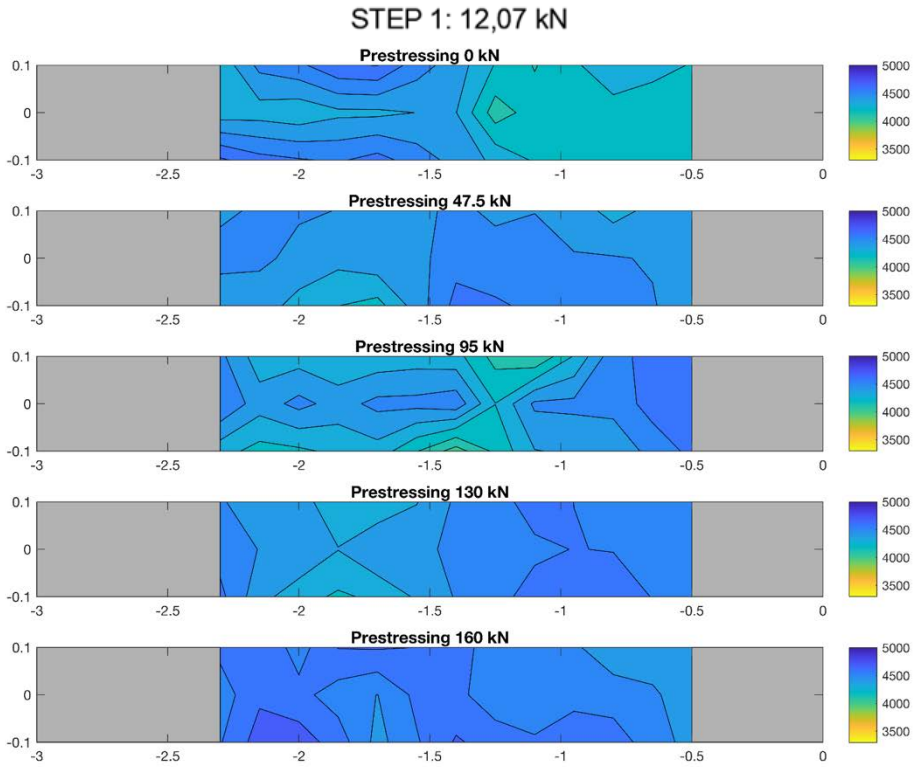

Figure 4.27. Beam 4. Tomographic ultrasonic speed for different prestressed force levels. Cracked state

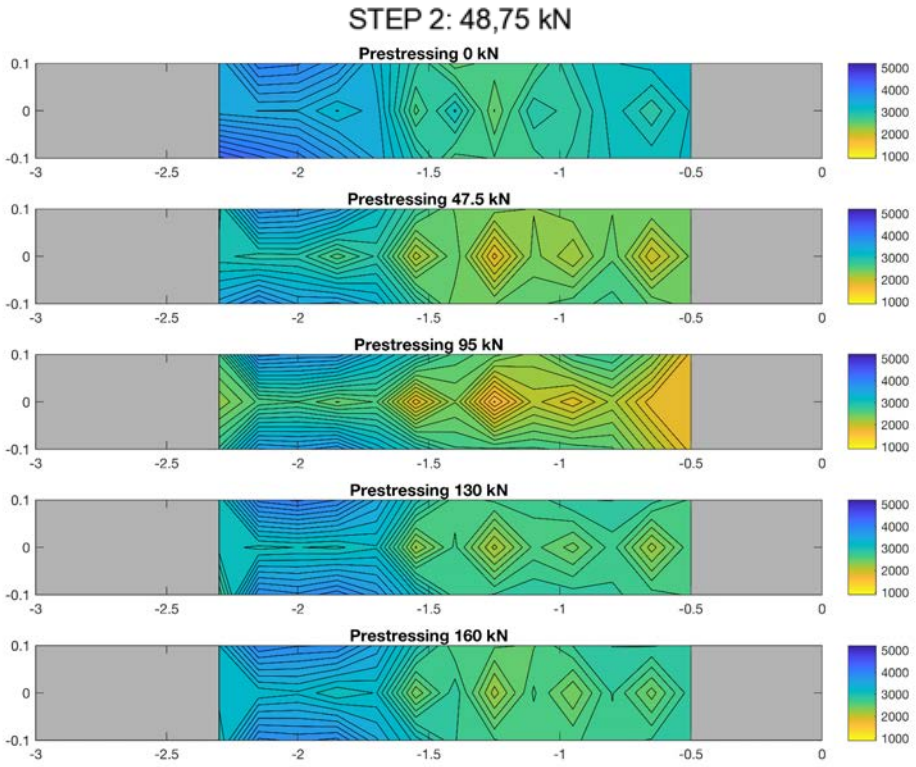

Figure 4.28. Beam 4. Tomographic ultrasonic speed for different prestressed force levels. Failure state

4.3.4 Beam 5 – vertical signal

The following pictures represent the averaging of the 16 different measured paths in vertical direction, subdivided in straight and inclined paths, in terms of speed.

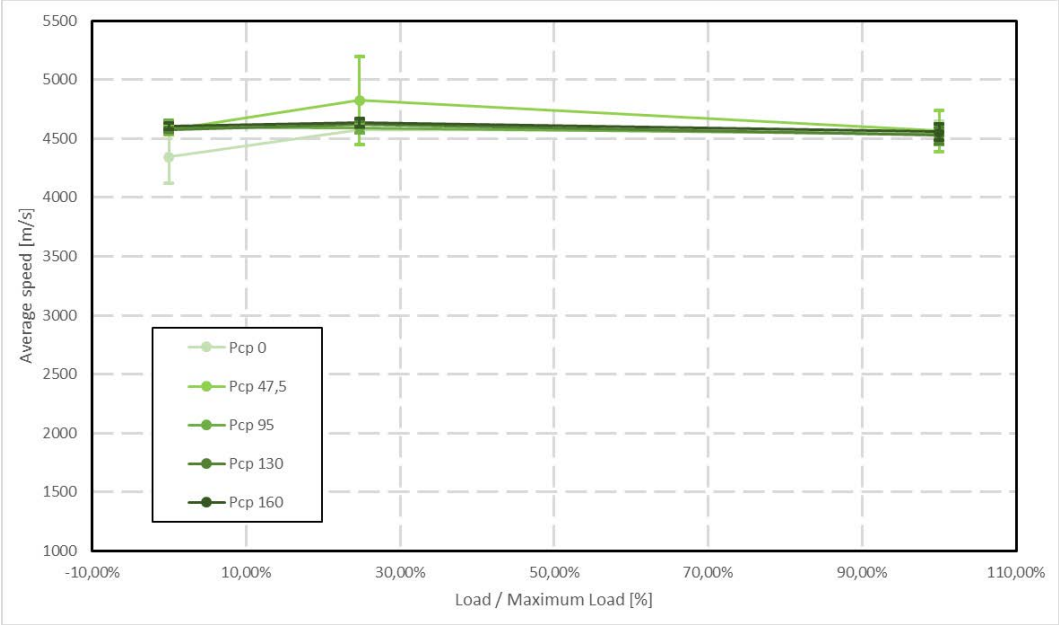

Figure 4.29. Beam 5. Variation of the average speed and its standard deviation for the various cycles along the straight vertical paths for different prestressed force levels

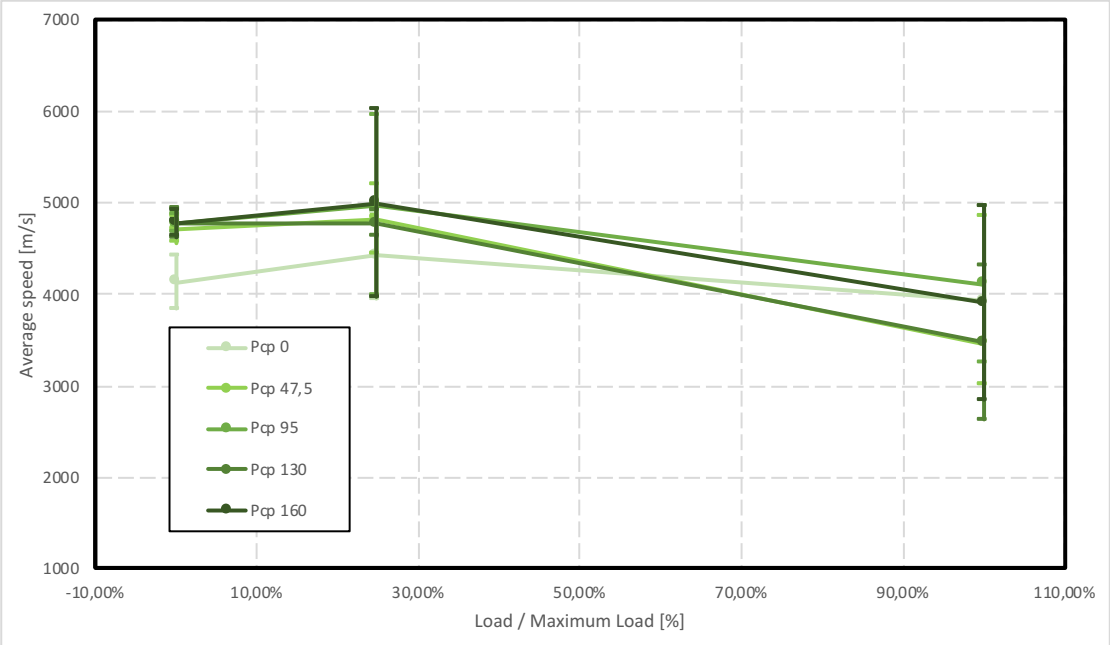

Figure 4.30. Beam 5. Variation of the average speed and its standard deviation for the various cycles along the inclined vertical paths for different prestressed force levels

From the graphs in the previous pictures it is observed, that inclined paths have higher sensitivity to the increase of damage with respect to vertical paths. This is probably due to the fact that vertical paths rarely cross bending (straight) cracks, and are more likely to travel in uncracked concrete even in presence of cracks. The former have a variability between 4800m/s and 2700m/s, while the latter fluctuate around 4500m/s.

Furthermore, the variation of speed is similar for all prestressed forces.

The following pictures represent the tomographic mapping of the speed obtained by the interpolation of the 16 different measured paths, compared with visual survey of crack pattern.

By comparing the speed mapping with the visual crack pattern it is observed a variation in speed consistent with the formation of the cracks and their position with respect to the trajectories, even if many point of measure didn't give reliable results due to the disturbance of the signal.

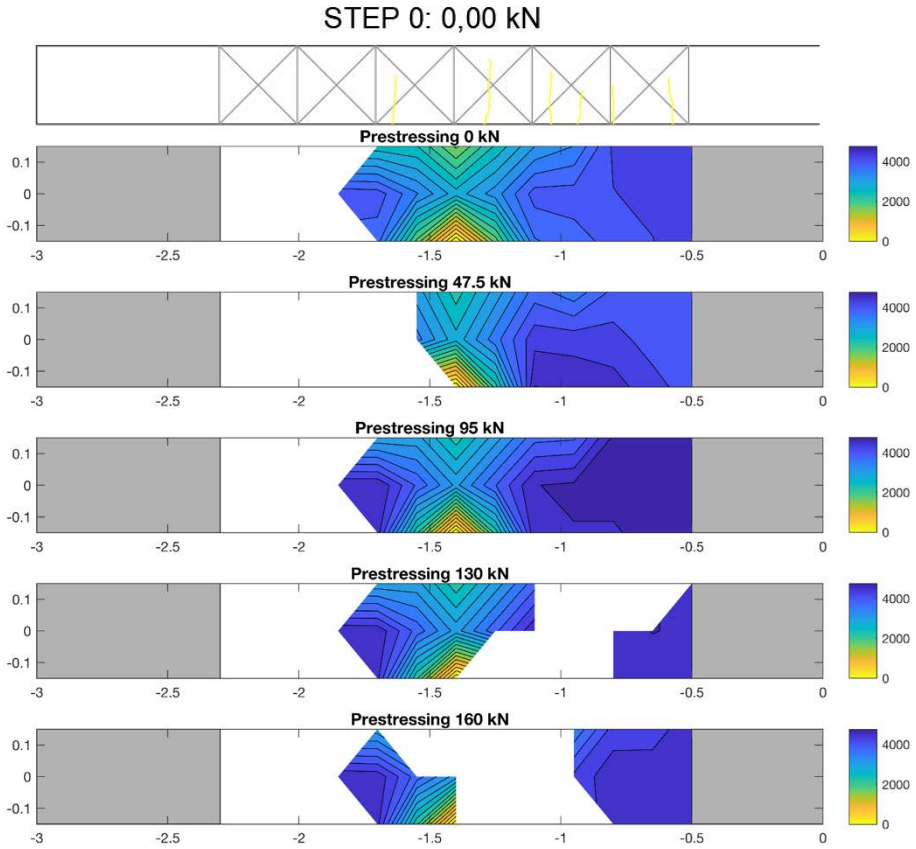

Figure 4.31. Beam 5. Tomographic ultrasonic speed for different prestressed force levels. Undamaged state

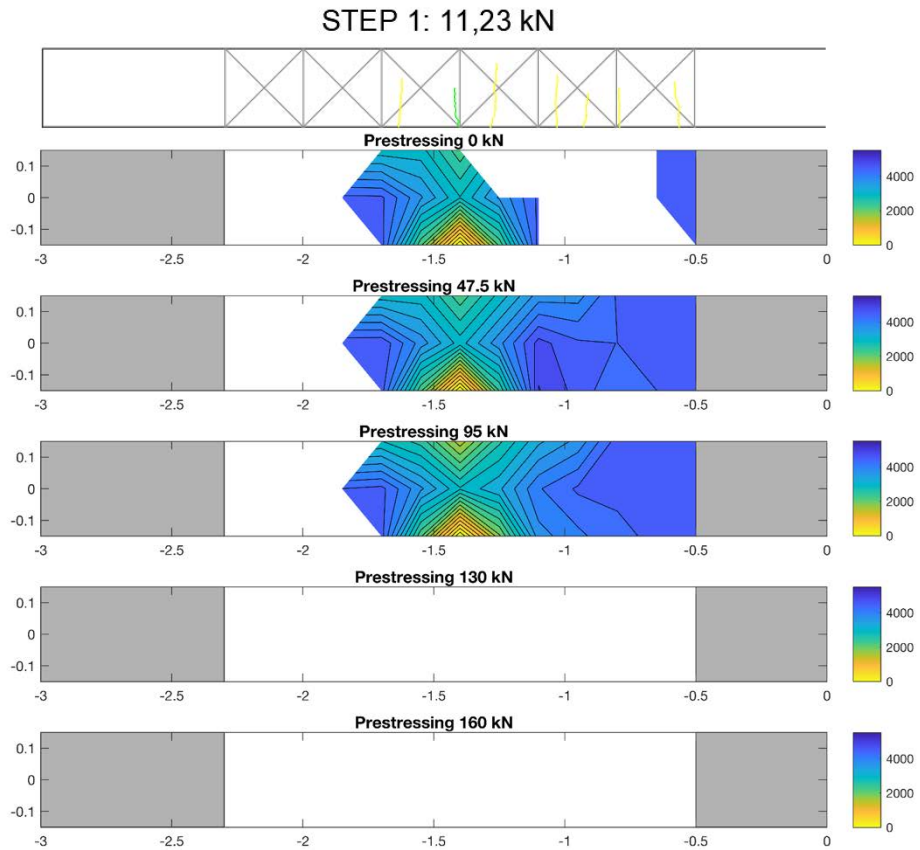

Figure 4.32. Beam 5. Tomographic ultrasonic speed for different prestressed force levels. Cracked state

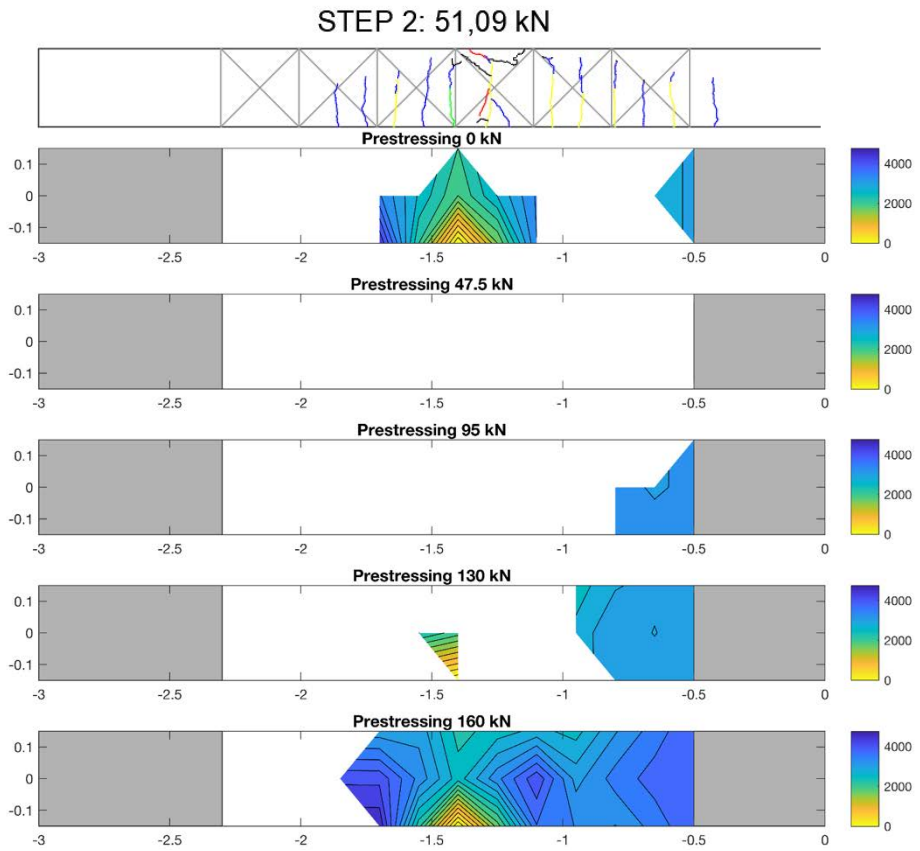

Figure 4.33. Beam 5. Tomographic ultrasonic speed for different prestressed force levels. Failure state

4.3.5 Beam 5 – horizontal signal

The following pictures represent the averaging of the 19 different measured paths in horizontal direction, subdivided in straight and inclined paths, in terms of speed.

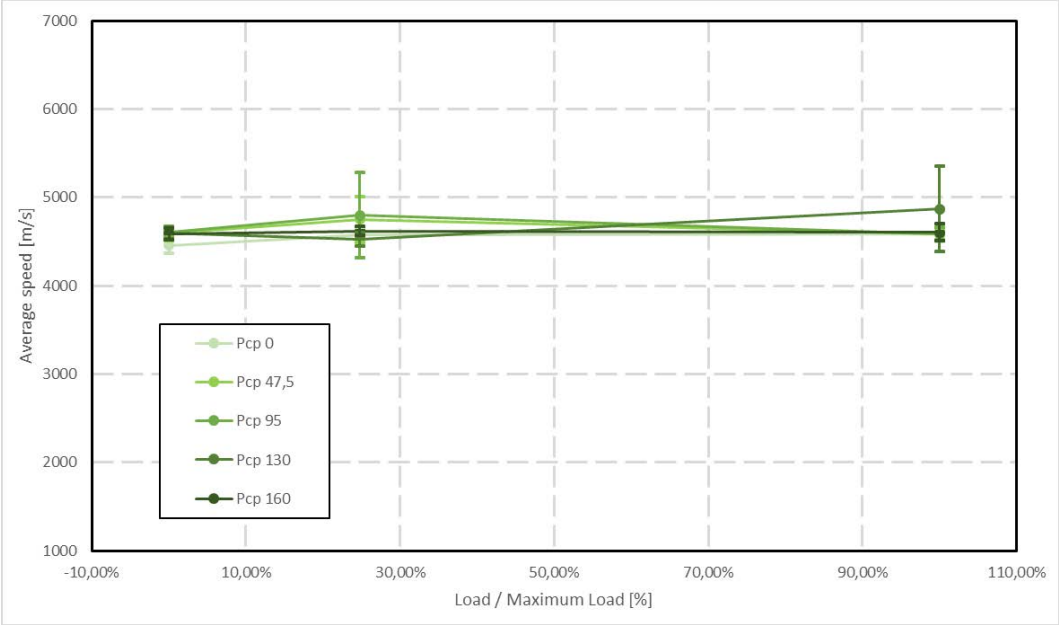

Figure 4.34. Beam 5. Variation of the average speed and its standard deviation for the various cycles along the straight horizontal paths for different prestressed force levels

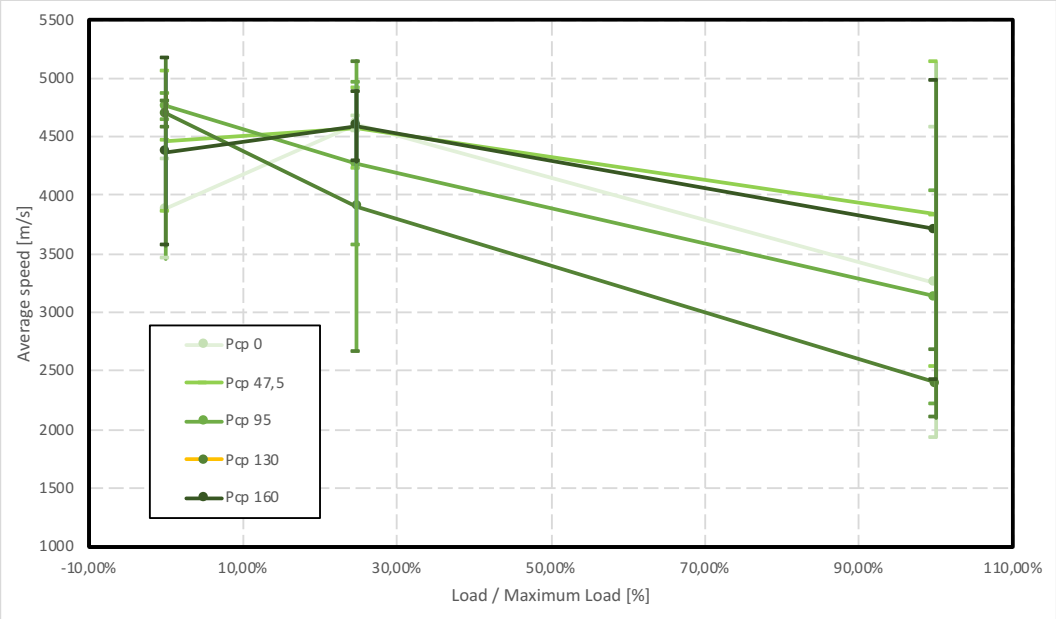

Figure 4.35. Beam 5. Variation of the average speed and its standard deviation for the various cycles along the inclined horizontal paths for different prestressed force levels

As seen for the ultrasonic signals transmitted horizontally also in this case it is observed, that inclined paths have higher sensitivity to the increase of damage with respect to vertical paths. The former have a variability between 5000m/s and 2300m/s, while the latter fluctuate around 4600m/s.

Furthermore, the variation of speed is similar for all prestressed forces.

The following pictures represent the tomographic mapping of the speed obtained by the interpolation of the 19 different measured paths, compared with visual survey of crack pattern.

By comparing the speed mapping with the visual crack pattern it is observed a variation in speed consistent with the formation of the cracks and their position with respect to the trajectories, even if many point of measure didn't give reliable results due to the disturbance of the signal.

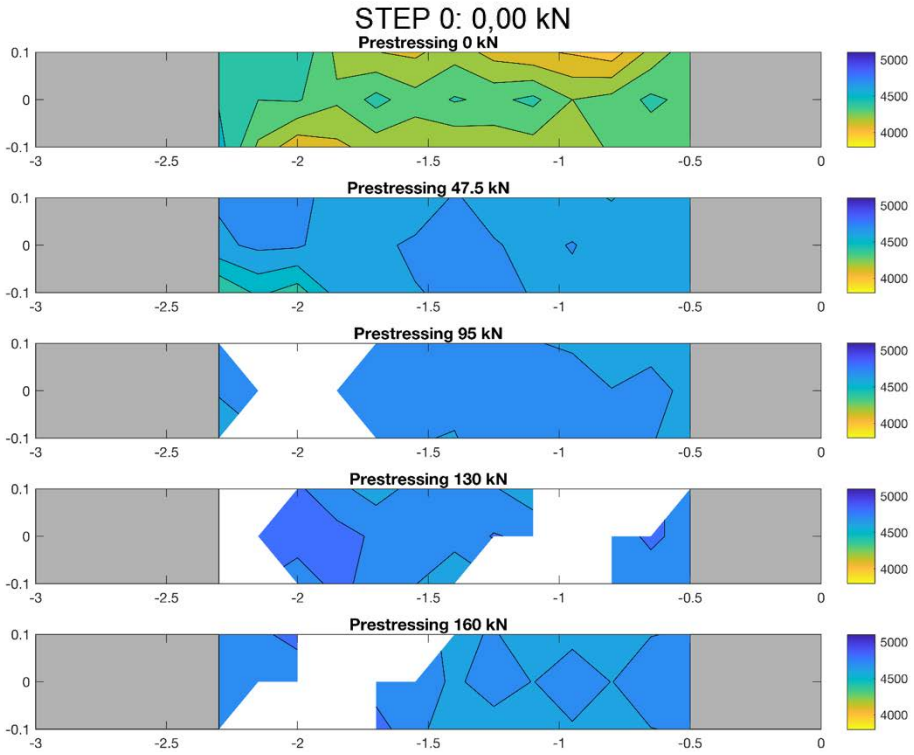

Figure 4.36. Beam 5. Tomographic ultrasonic speed for different prestressed force levels. Undamaged state

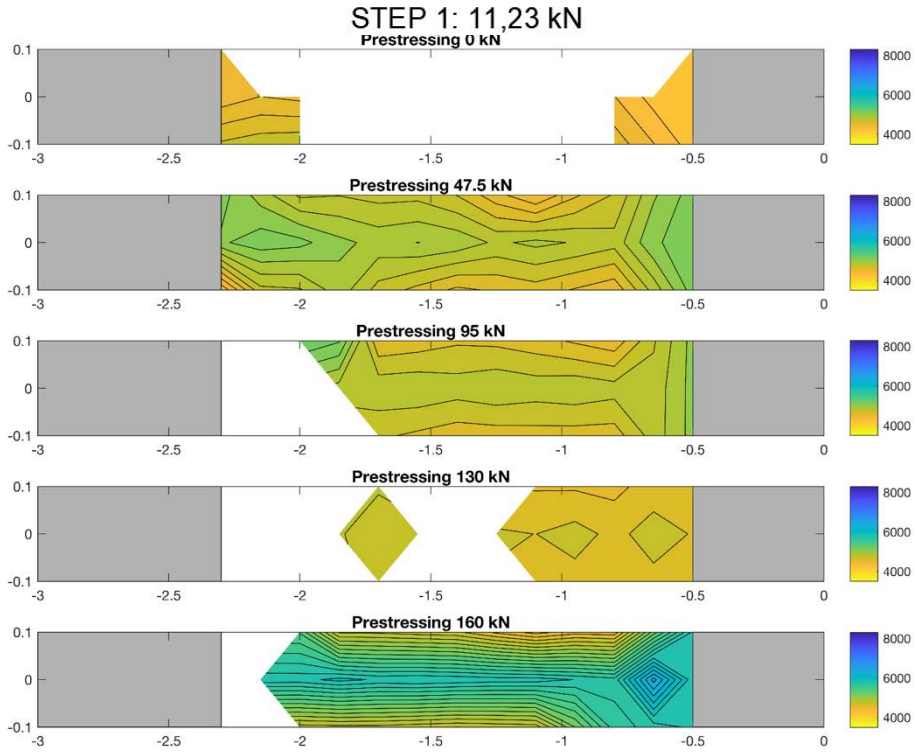

Figure 4.37. Beam 5. Tomographic ultrasonic speed for different prestressed force levels. Cracked state

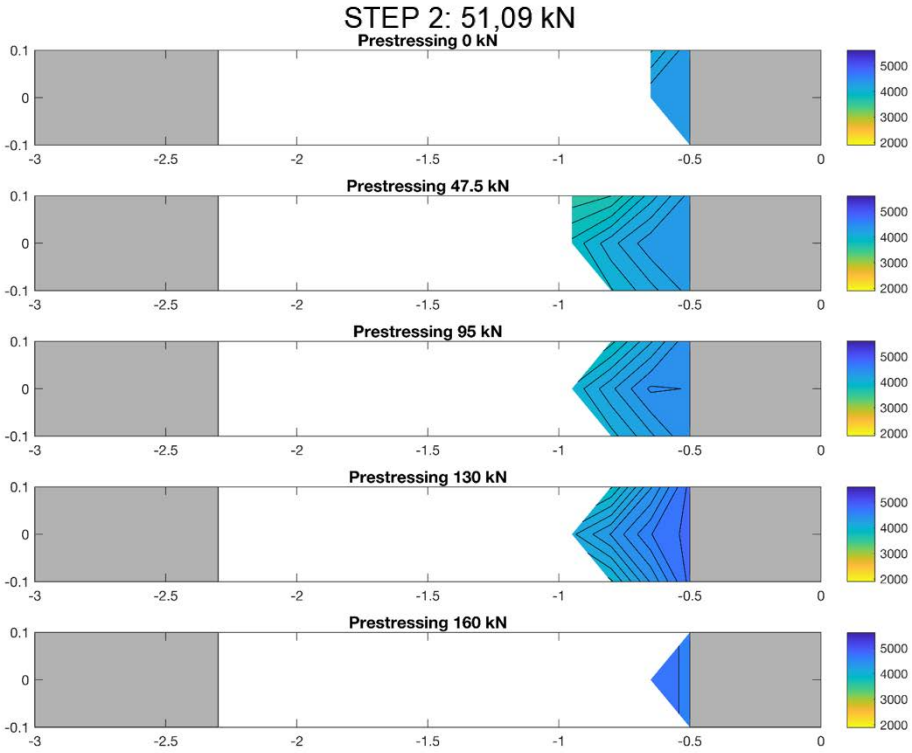

Figure 4.38. Beam 5. Tomographic ultrasonic speed for different prestressed force levels. Failure state

4.3.6 Beam 6 – vertical signal

The following pictures represent the averaging of the 16 different measured paths in vertical direction, subdivided in straight and inclined paths, in terms of speed.

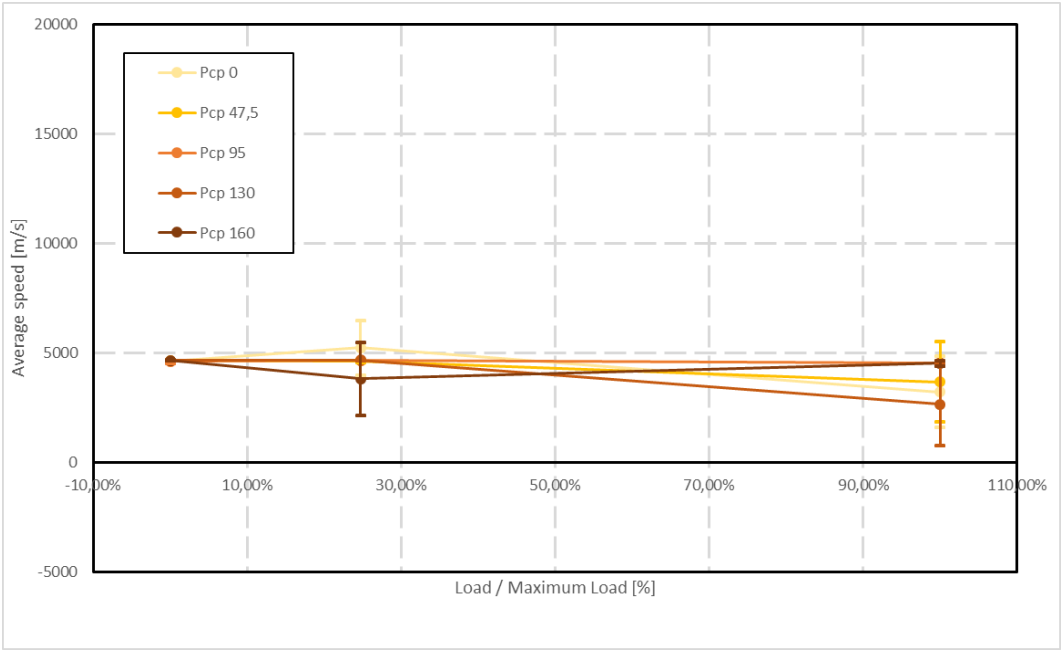

Figure 4.39. Beam 6. Variation of the average speed and its standard deviation for the various cycles along the straight vertical paths for different prestressed force levels

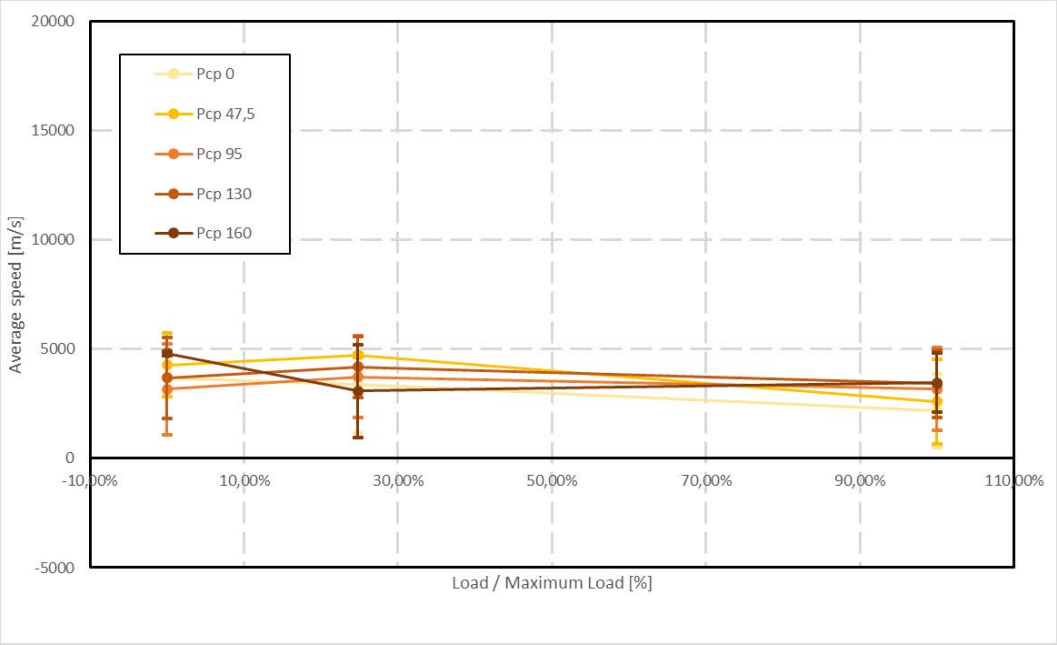

Figure 4.40. Beam 6. Variation of the average speed and its standard deviation for the various cycles along the inclined vertical paths for different prestressed force levels

From the graphs in the previous pictures it is observed no clear dependence of average speed from level of damage, both in straight and inclined paths. Both fluctuate around 4500m/s.

Furthermore, the variation of speed is similar for all prestressed forces.

The following pictures represent the tomographic mapping of the speed obtained by the interpolation of the 16 different measured paths, compared with visual survey of crack pattern.

By comparing the speed mapping with the visual crack pattern it is observed a variation in speed consistent with the formation of the cracks and their position with respect to the trajectories, even if many point of measure didn't give reliable results due to the disturbance of the signal.

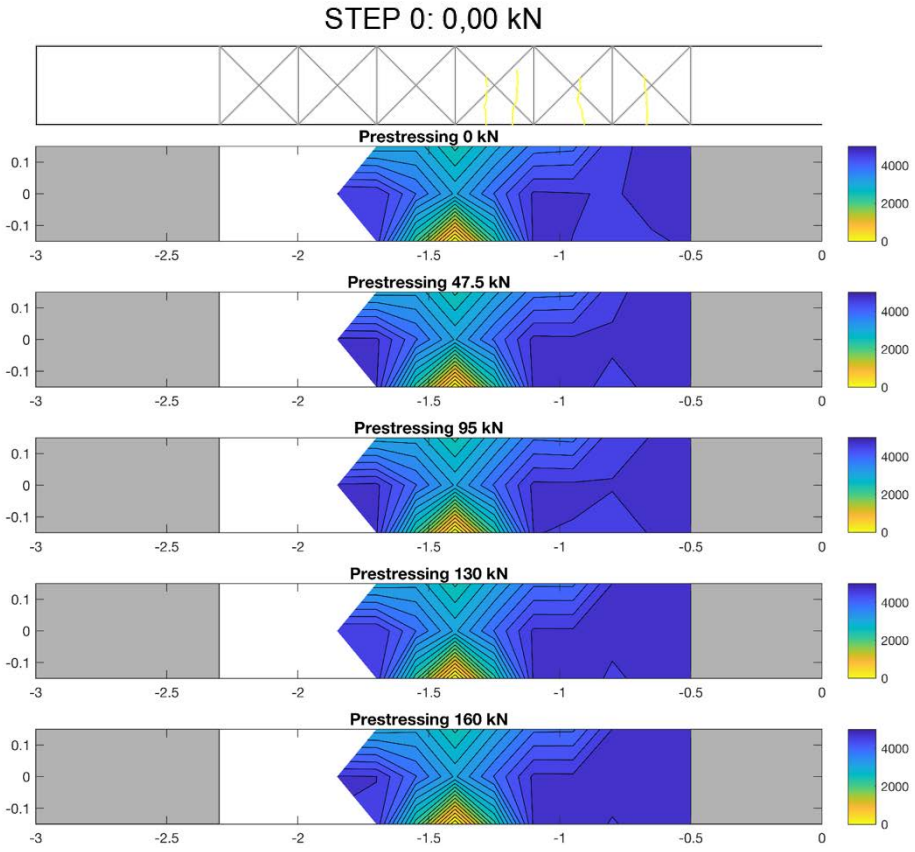

Figure 4.41. Beam 6. Tomographic ultrasonic speed for different prestressed force levels. Undamaged state

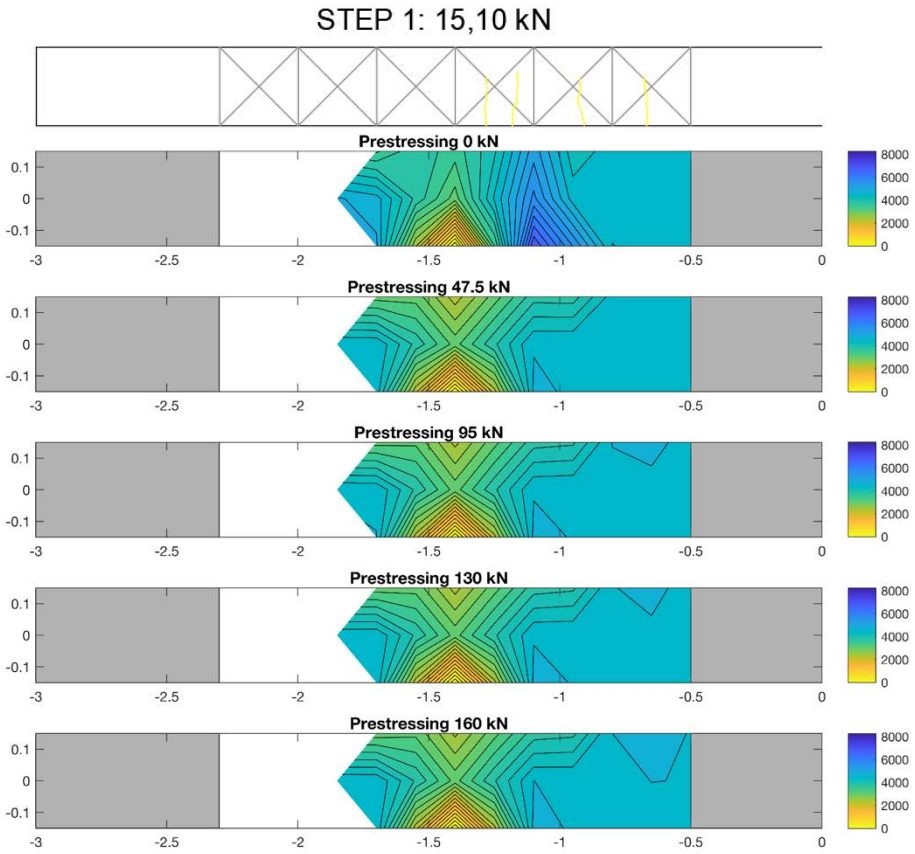

Figure 4.42. Beam 6. Tomographic ultrasonic speed for different prestressed force levels. Cracked state

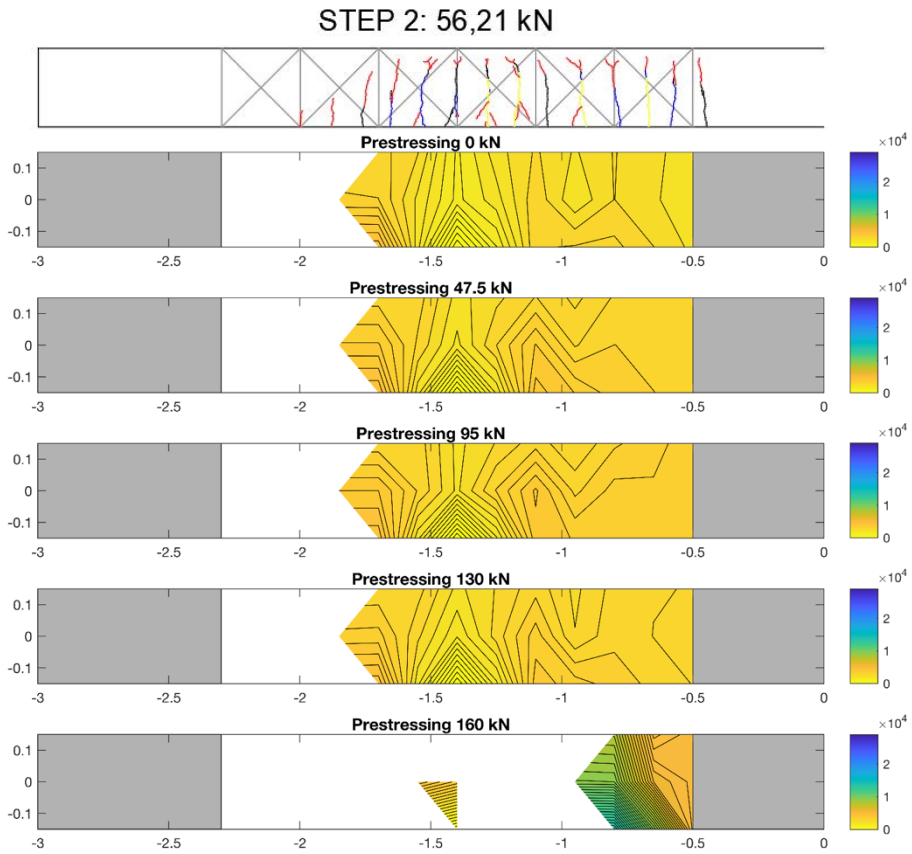

Figure 4.43. Beam 6. Tomographic ultrasonic speed for different prestressed force levels. Failure state

4.3.7 Beam 6 – horizontal signal

The following pictures represent the averaging of the 19 different measured paths in vertical direction, subdivided in straight and inclined paths, in terms of speed.

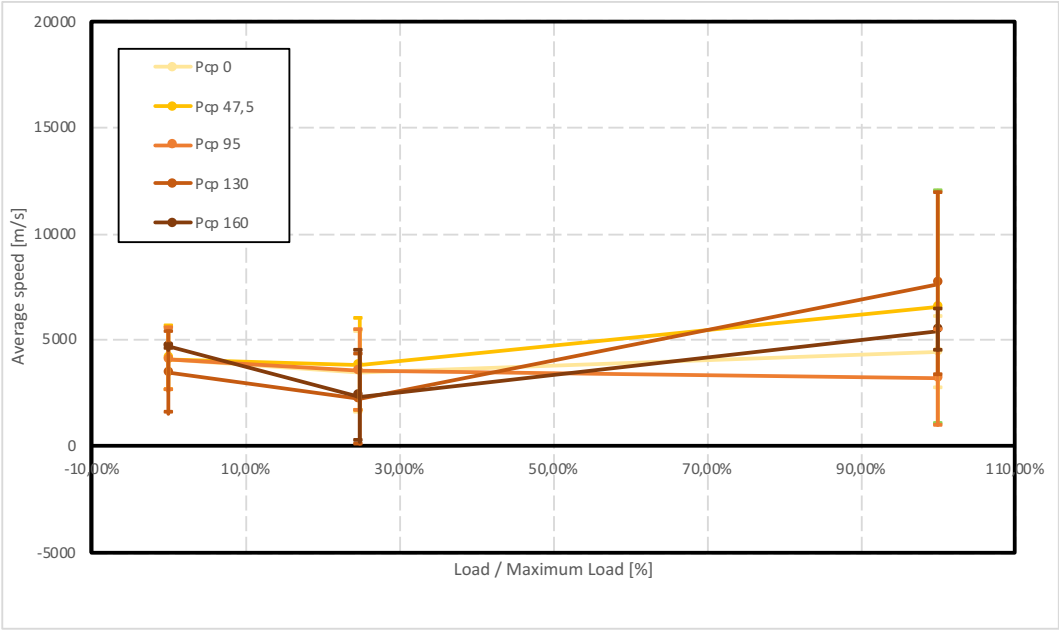

Figure 4.44. Beam 6. Variation of the average speed and its standard deviation for the various cycles along the straight horizontal paths for different prestressed force levels

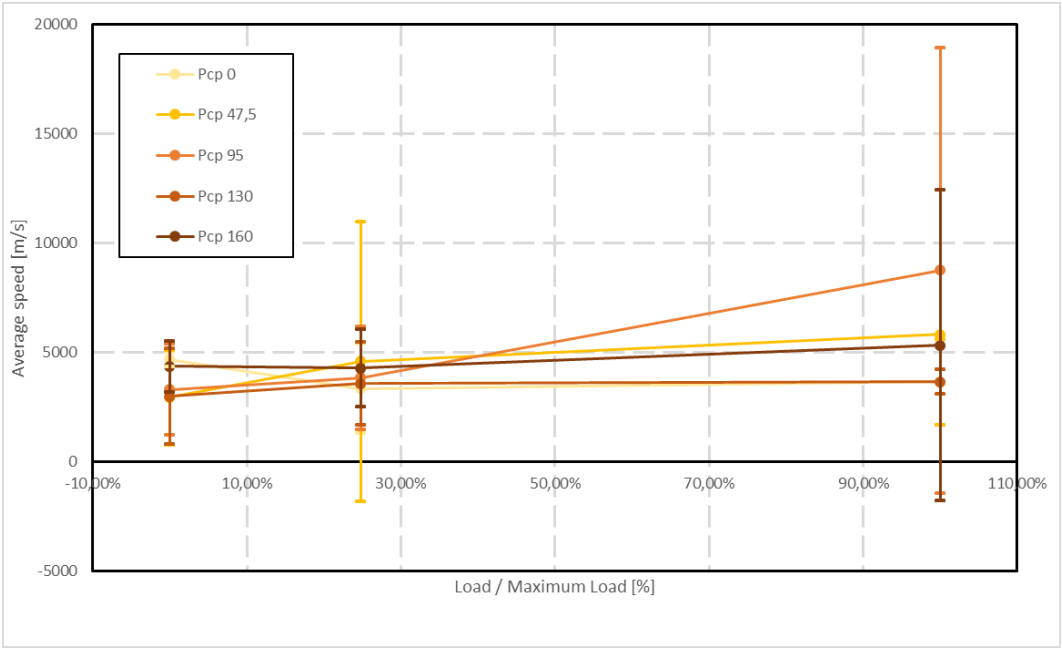

Figure 4.45. Beam 6. Variation of the average speed and its standard deviation for the various cycles along the inclined horizontal paths for different prestressed force levels

From the graphs in the previous pictures it is observed no clear dependence of average speed from level of damage, both in straight and inclined paths. Both fluctuate around 4500m/s.

Furthermore, the variation of speed is similar for all prestressed forces.

The following pictures represent the tomographic mapping of the speed obtained by the interpolation of the 19 different measured paths, compared with visual survey of crack pattern.

By comparing the speed mapping with the visual crack pattern it is observed a variation in speed consistent with the formation of the cracks and their position with respect to the trajectories, even if many point of measure didn't give reliable results due to the disturbance of the signal.

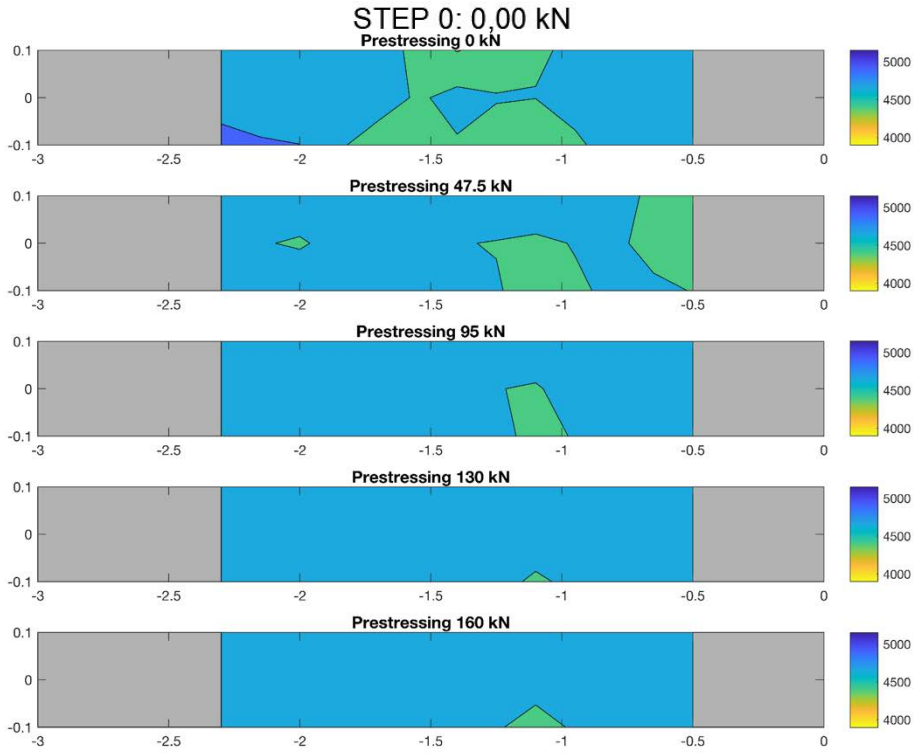

Figure 4.46. Beam 6. Tomographic ultrasonic speed for different prestressed force levels. Undamaged state

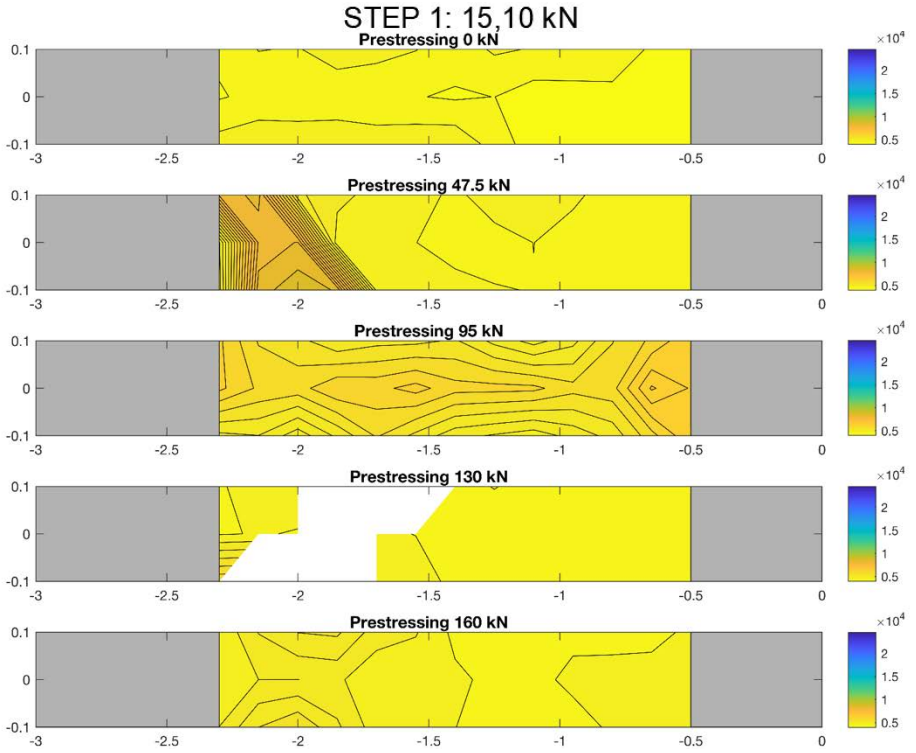

Figure 4.47. Beam 6. Tomographic ultrasonic speed for different prestressed force levels. Cracked state

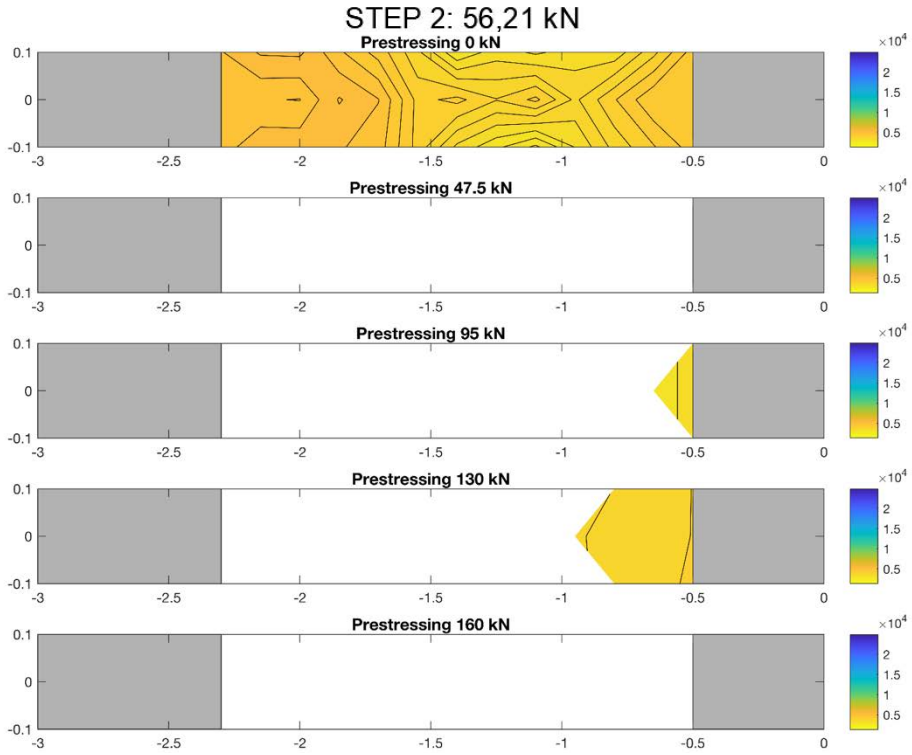

Figure 4.48. Beam 6. Tomographic ultrasonic speed for different prestressed force levels. Failure state

4.3.8 Use of velocity: conclusions

In general, from the plots of ultrasonic velocity it can be observed that the inclined paths have a velocity that depends on damage, while straight velocity (perpendicular to the axis of the beam oscillates around constant value also with the increase of damage. However, it can be observed that the inclined paths have a greater statistical dispersion than the vertical ones.

No clear dependence was observed with respect to prestressing level.

4.3.9 Use of energy attenuation

As shown, even though it is possible to identify a general decrease of velocity with the increase of damage (mostly for inclined paths), for the highest levels of vertical applied load, the ultrasonic signal suffers for a great signal disturbance. Accordingly, it was not possible to calculate the signal velocity at each location of the beam, revealing a further limitation of this method.

Although results obtained analyzing directly ultrasonic pulse velocity results were not encouraging, another parameter was investigated, that is the attenuation of the ultrasonic signal. This specific parameter was measured through the evaluation of the area underlying the Power Spectral Density (PSD) of the ultrasonic signal, measured in time. This calculation ensures to

find a result for those signals that suffer from disturb too, where the time of flight of the signal (and therefore velocity) are difficult to be assessed clearly. An example of time and frequency domain of ultrasonic signal is shown in Figure 4.49.

Results of such analysis are presented for Beam 4, Beam 5 and Beam 6 in the figures from page 136 to page 148. The pictures show first the results in average, and then in shape of tomographic contour plot, as done for the velocity.

In general, even if many times average results don't show any clear dependence on damage, results show good correlation with damage. Compared to the contour plots derived with the analysis of velocities only, attenuation plots give a quite detailed view not only on the presence of the damage, but also of the location of cracks. Finally, also in this case, the role of prestressing force in the closure of cracks is visible in the reduction of the signal attenuation.

The results are reported for Beam 4, Beam 5 and Beam 6. The attenuation calculation was not possible for beams 1, 2 and 3 because it was not recorded the whole signal, but only a part in order to measure time of flight and therefore velocity.

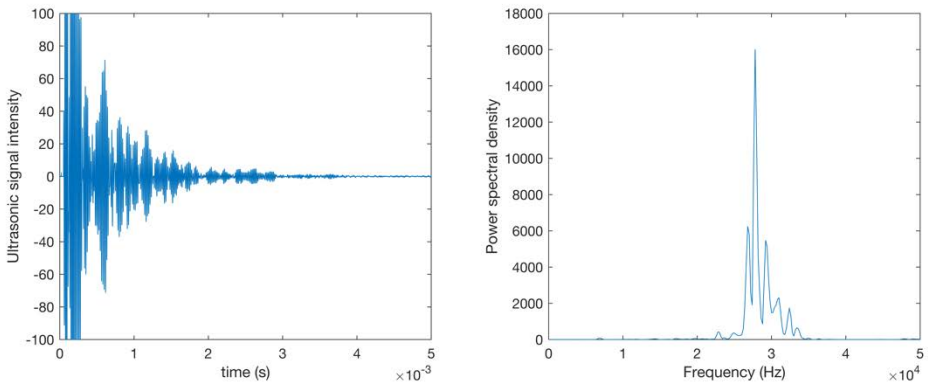

Figure 4.49. Example of time and frequency domain of ultrasonic signal

4.3.10 Beam 4 – Energy attenuation

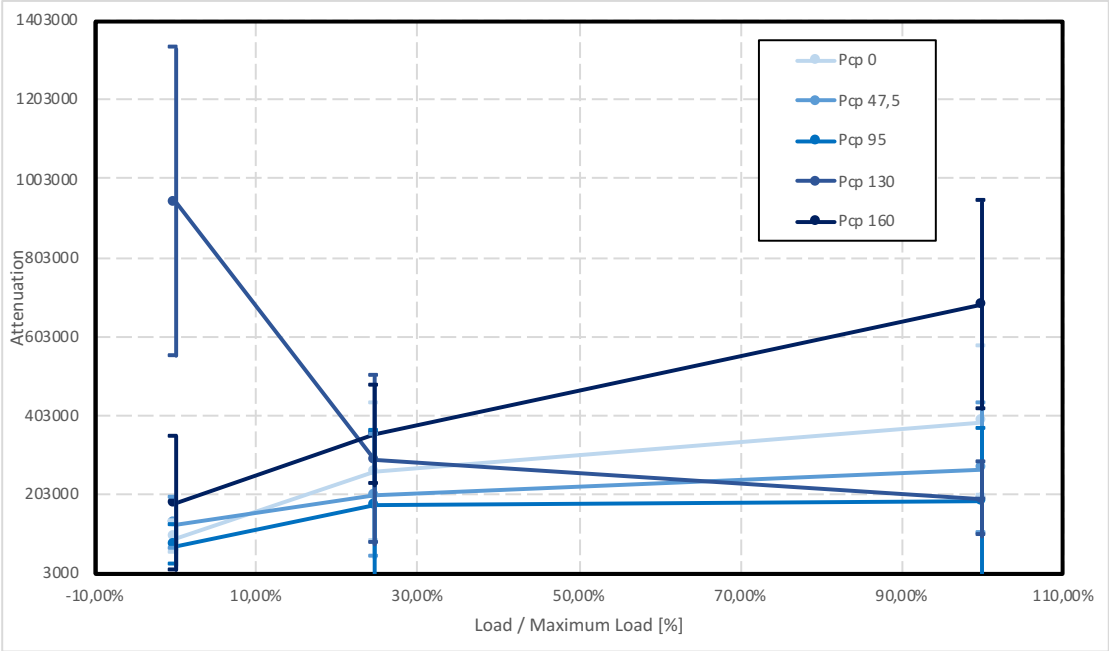

Figure 4.50. Beam 4. Variation of attenuation of the energy of the signal and its standard deviation for the various cycles along the straight paths for different prestressed force. Y direction.

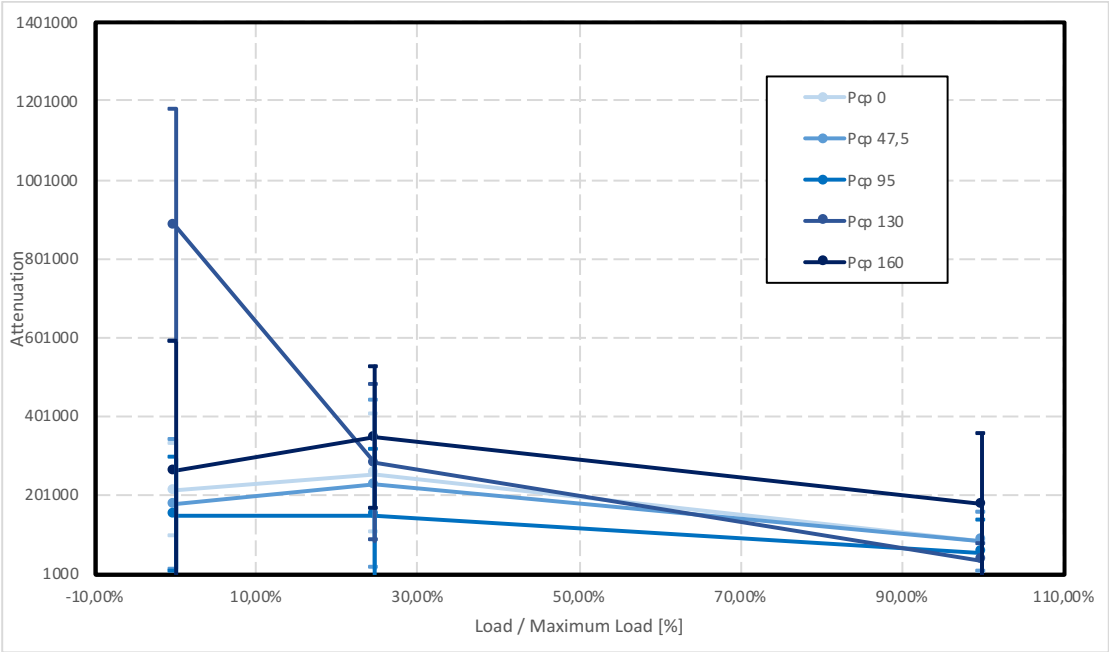

Figure 4.51. Beam 4. Variation of attenuation of the energy of the signal and its standard deviation for the various cycles along the inclined paths for different prestressed force. Y direction.

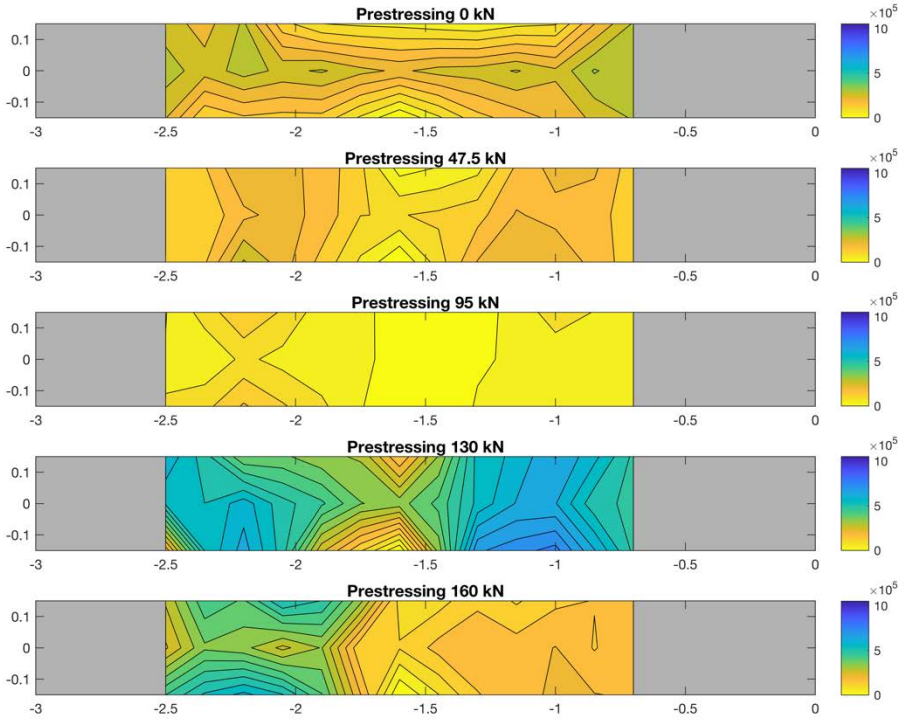

Figure 4.52. Beam 4. Attenuation in Y direction. Undamaged state

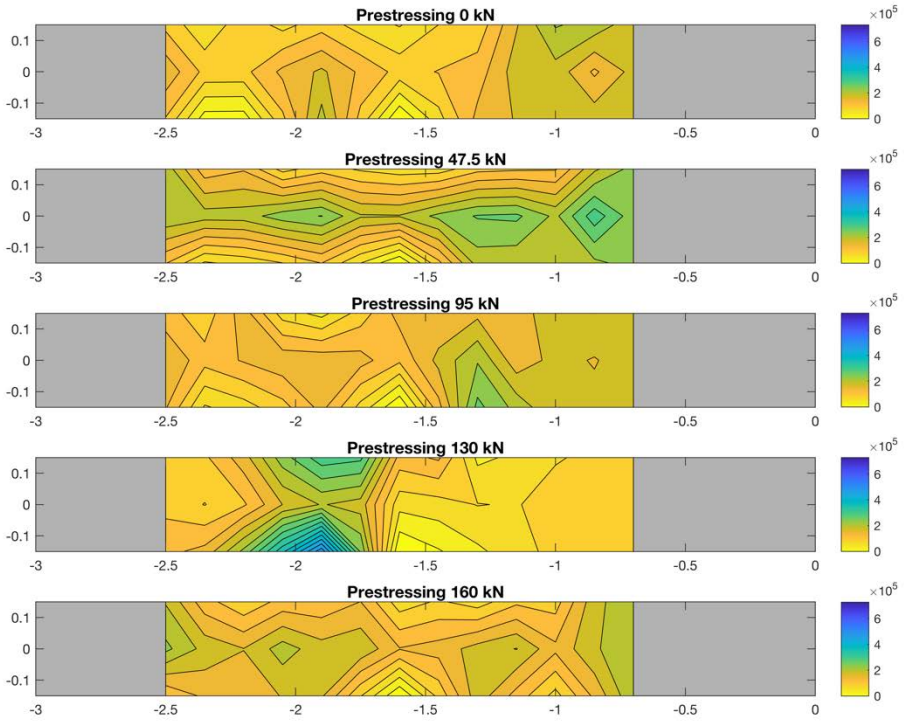

Figure 4.53. Beam 4. Attenuation in Y direction. Cracked state.

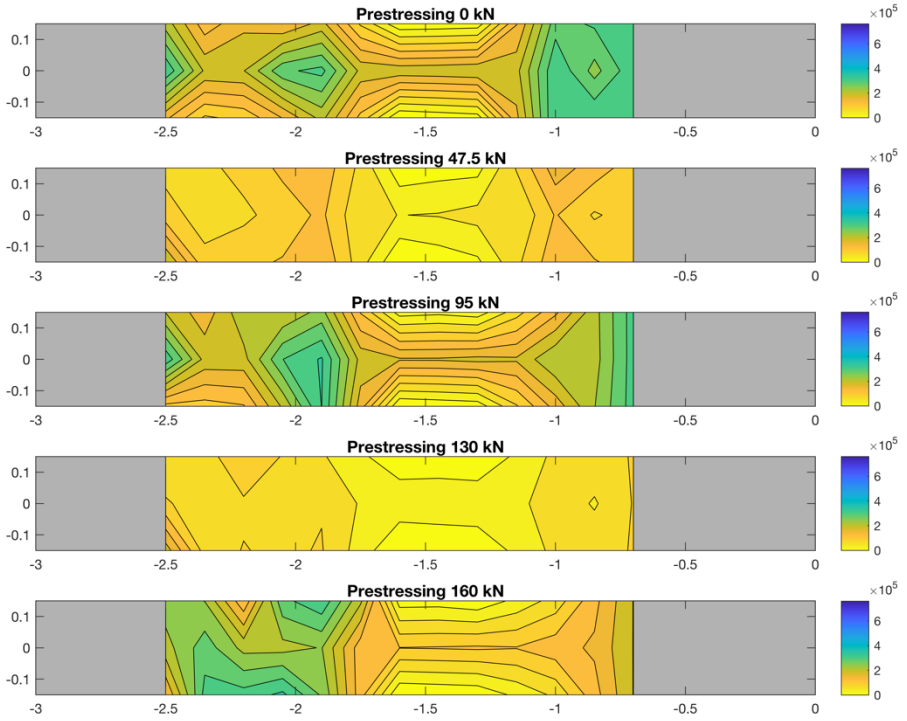

Figure 4.54. Beam 4. Attenuation in Y direction. Failure state.

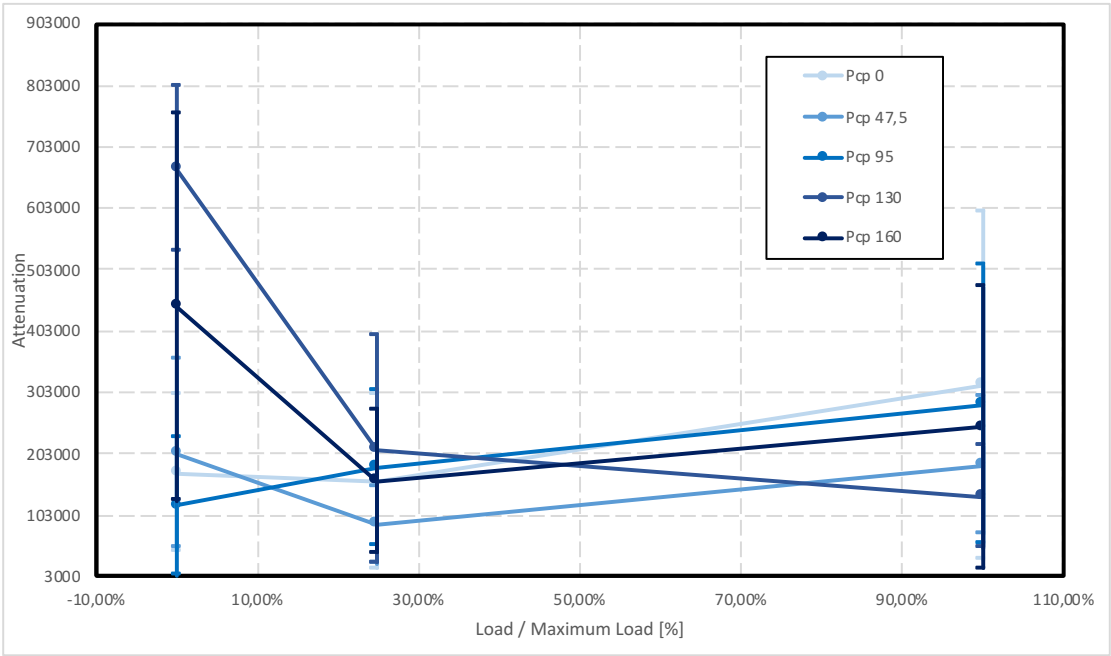

Figure 4.55. Beam 4. Variation of attenuation of the energy of the signal and its standard deviation for the various cycles along the straight paths for different prestressed force. X direction.

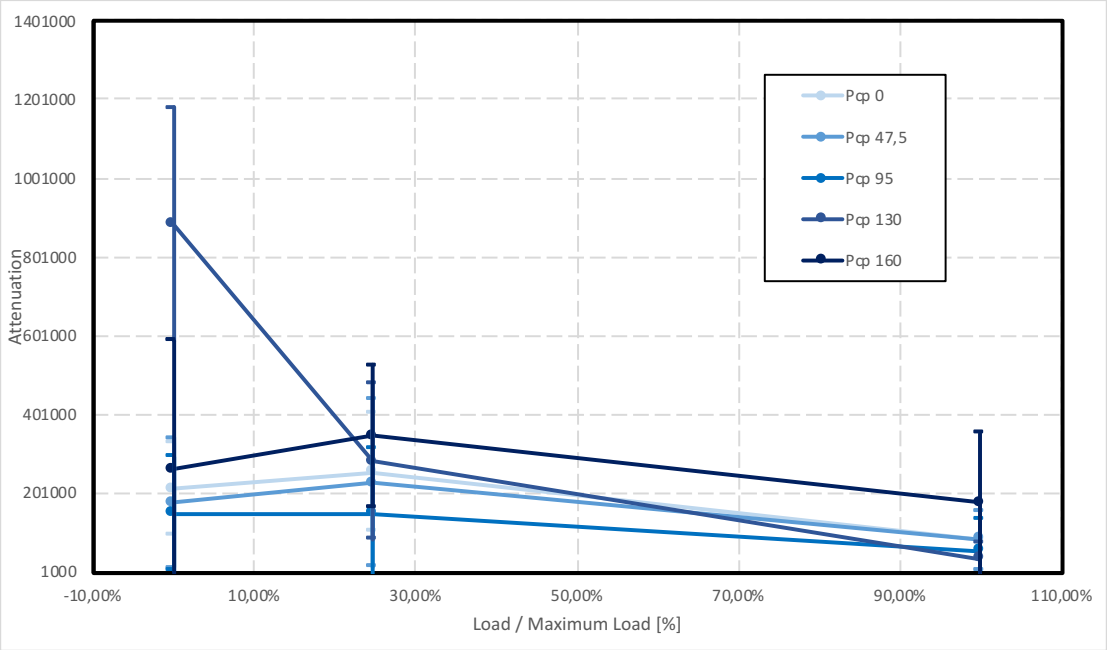

Figure 4.56. Beam 4. Variation of attenuation of the energy of the signal and its standard deviation for the various cycles along the inclined paths for different prestressed force. X direction.

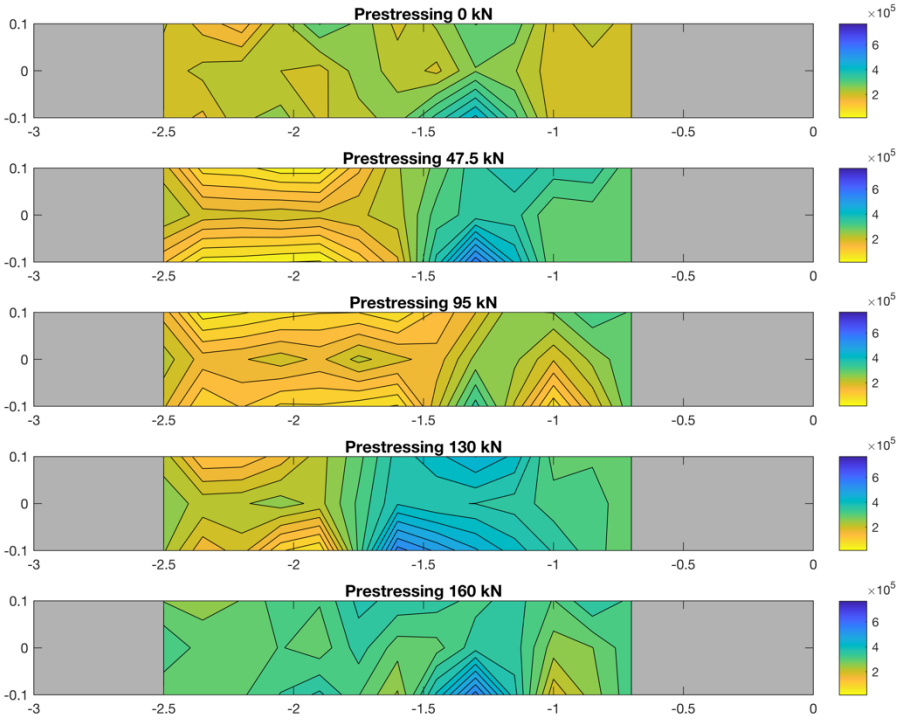

Figure 4.57. Beam 4. Attenuation in X direction. Cracked state.

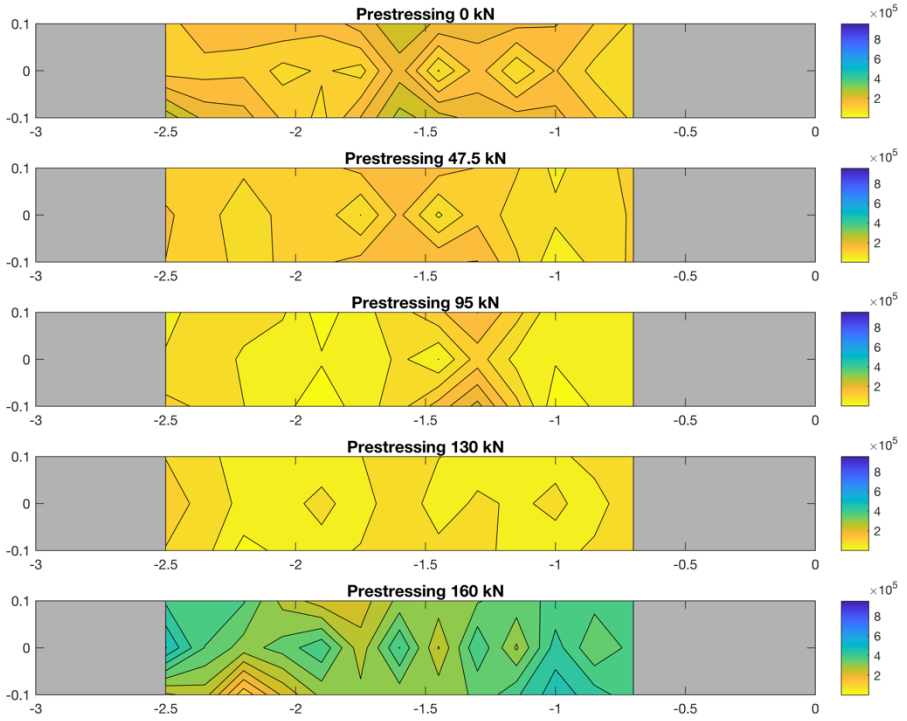

Figure 4.58. Beam 4. Attenuation in X direction. Failure state.

4.3.11 Beam 5 – Energy attenuation

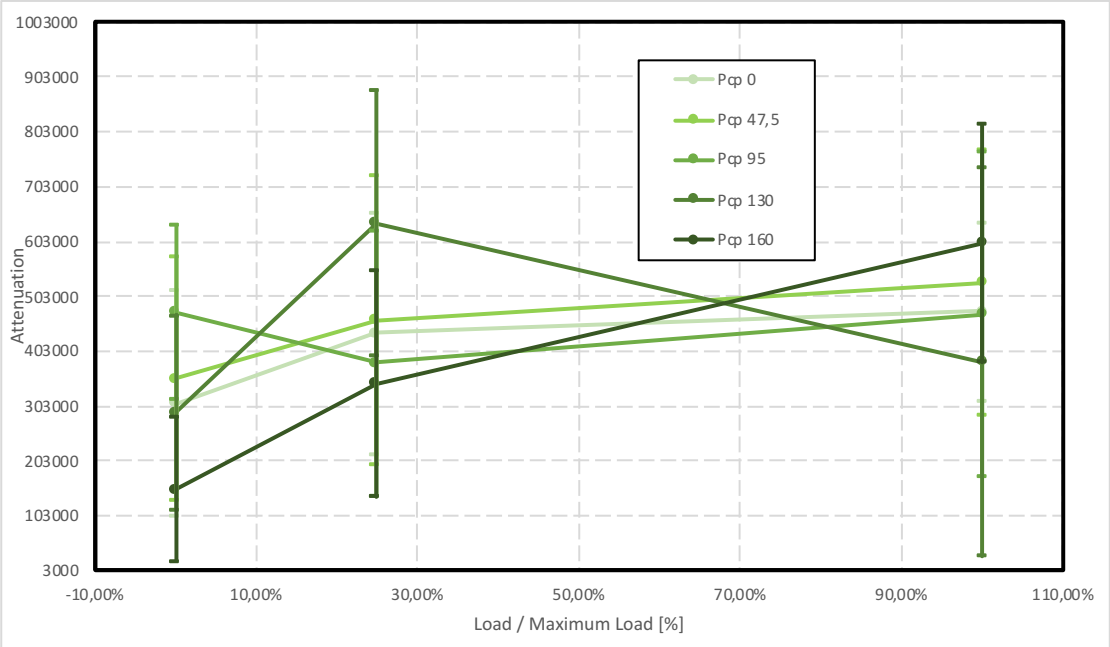

Figure 4.59. Beam 5. Variation of attenuation of the energy of the signal and its standard deviation for the various cycles along the straight paths for different prestressed force. Y direction.

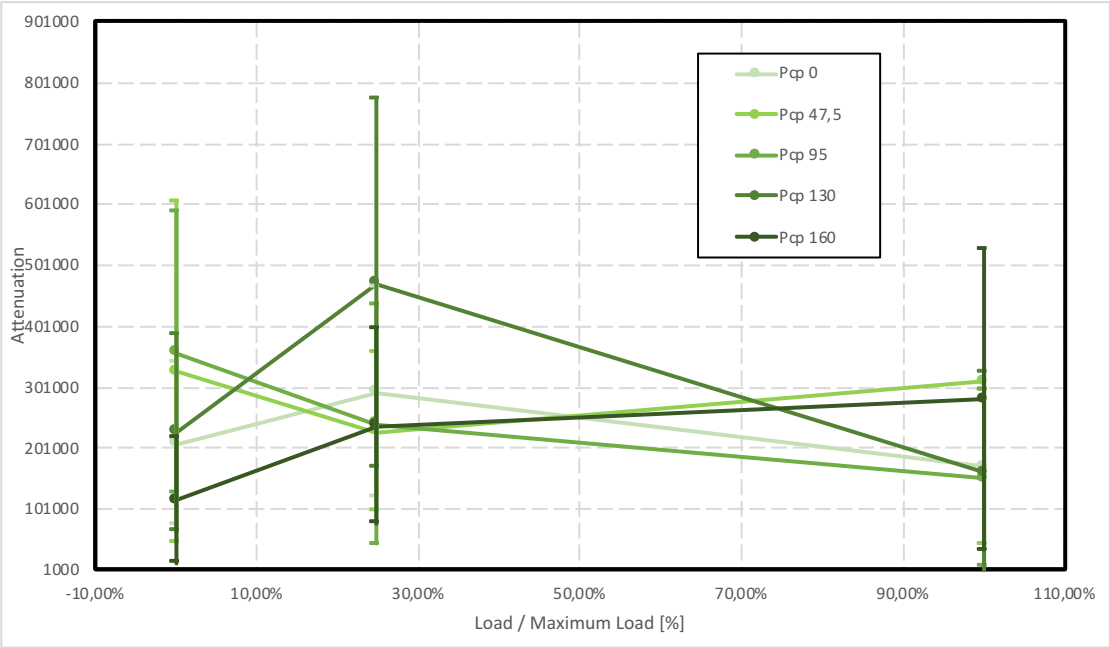

Figure 4.60. Beam 5. Variation of attenuation of the energy of the signal and its standard deviation for the various cycles along the inclined paths for different prestressed force. Y direction.

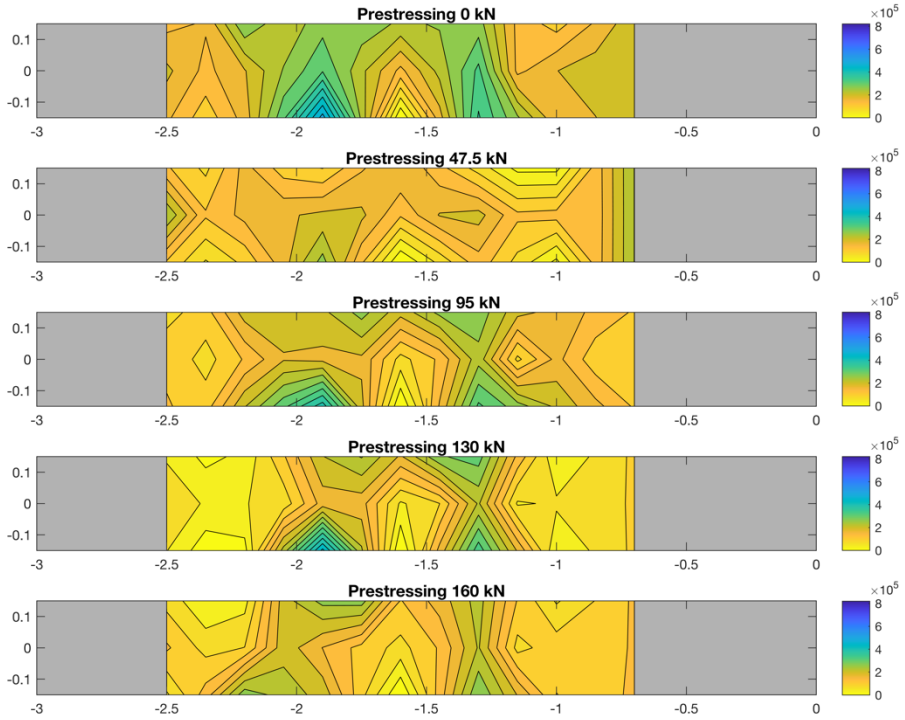

Figure 4.61. Beam 5. Attenuation in Y direction. Failure state.

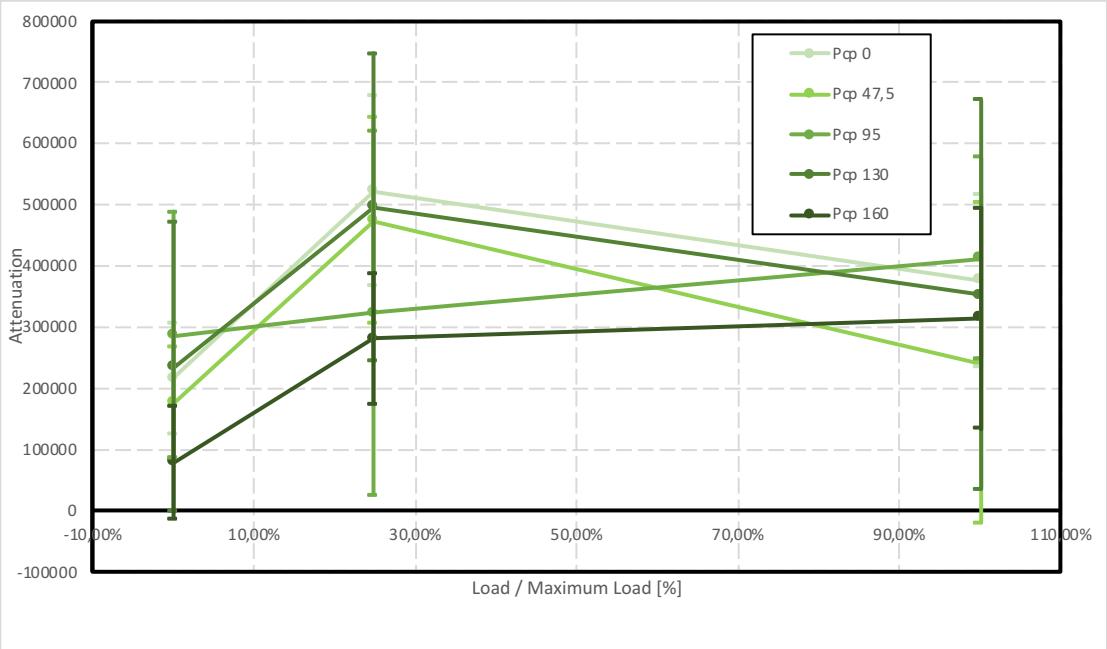

Figure 4.62. Beam 5. Variation of attenuation of the energy of the signal and its standard deviation for the various cycles along the straight paths for different prestressed force. X direction.

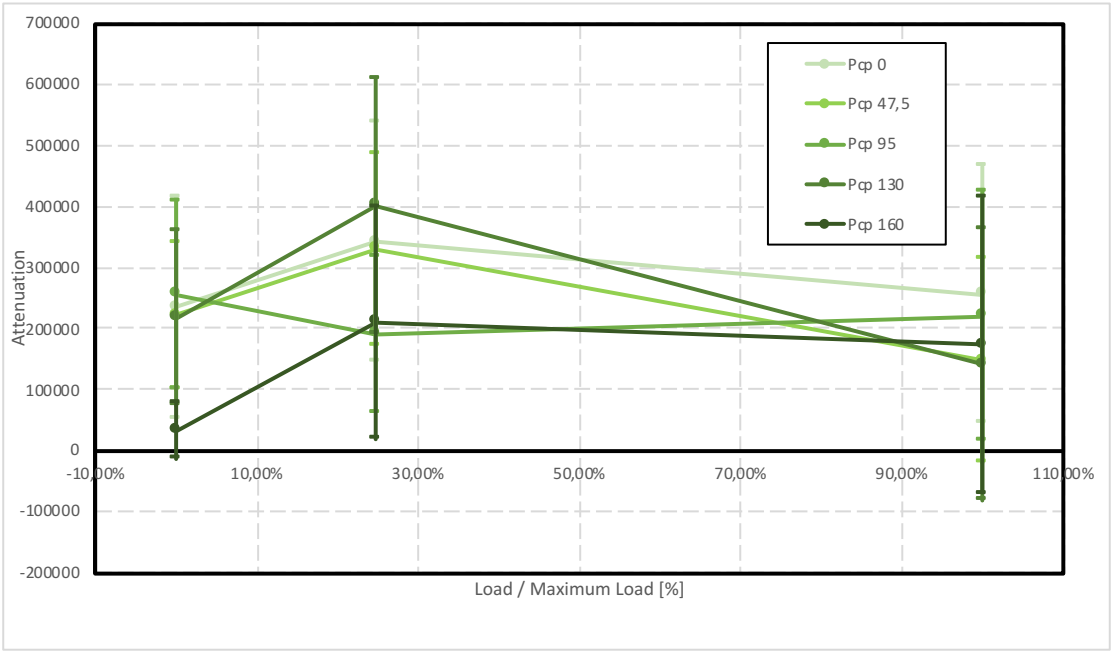

Figure 4.63. Beam 5. Variation of attenuation of the energy of the signal and its standard deviation for the various cycles along the inclined paths for different prestressed force. X direction.

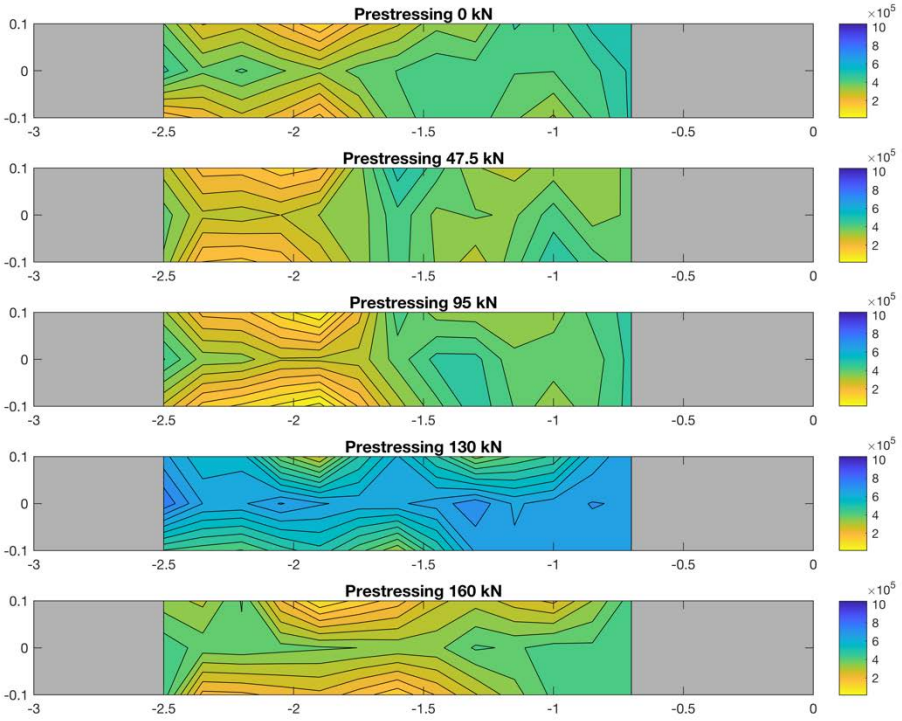

Figure 4.64. Beam 5. Attenuation in X direction. Cracked state.

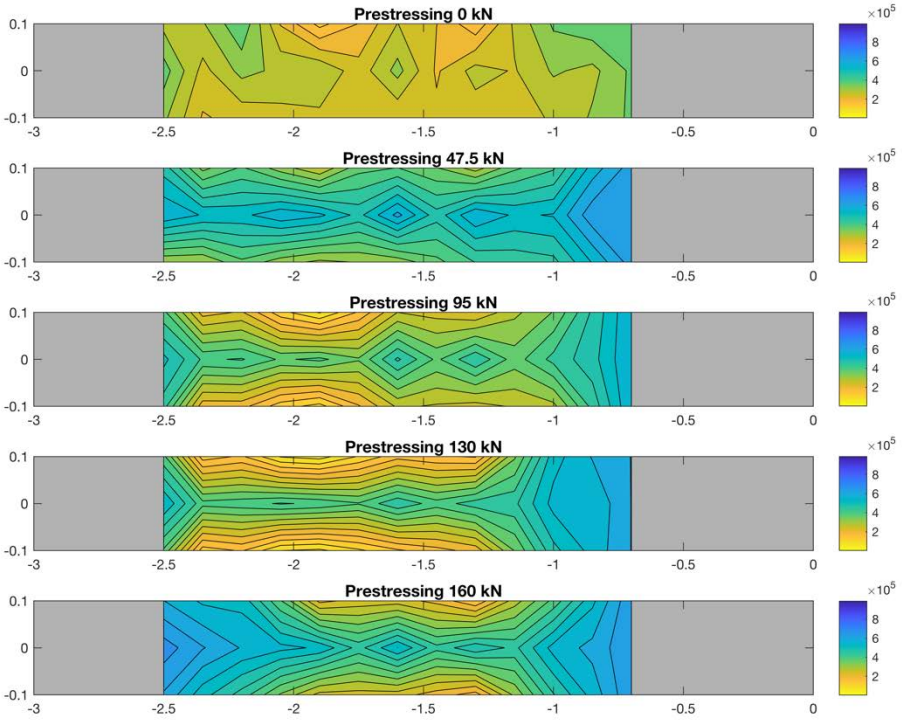

Figure 4.65. Beam 5. Attenuation in X direction. Failure state.

4.3.12 Beam 6 – Energy attenuation

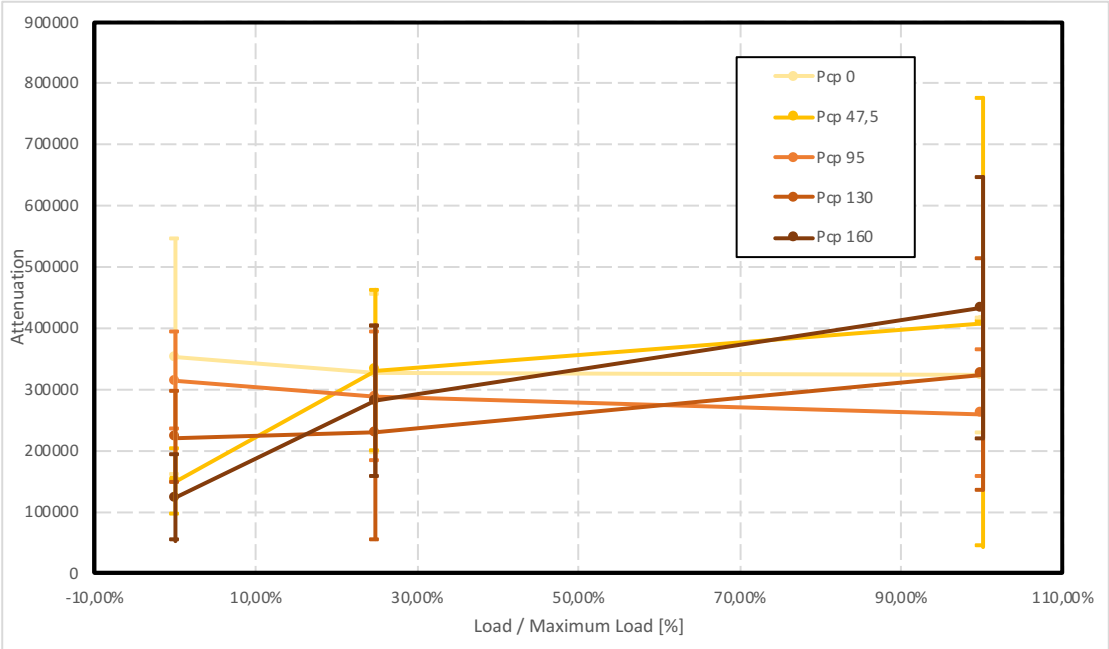

Figure 4.66. Beam 6. Variation of attenuation of the energy of the signal and its standard deviation for the various cycles along the straight paths for different prestressed force. Y direction.

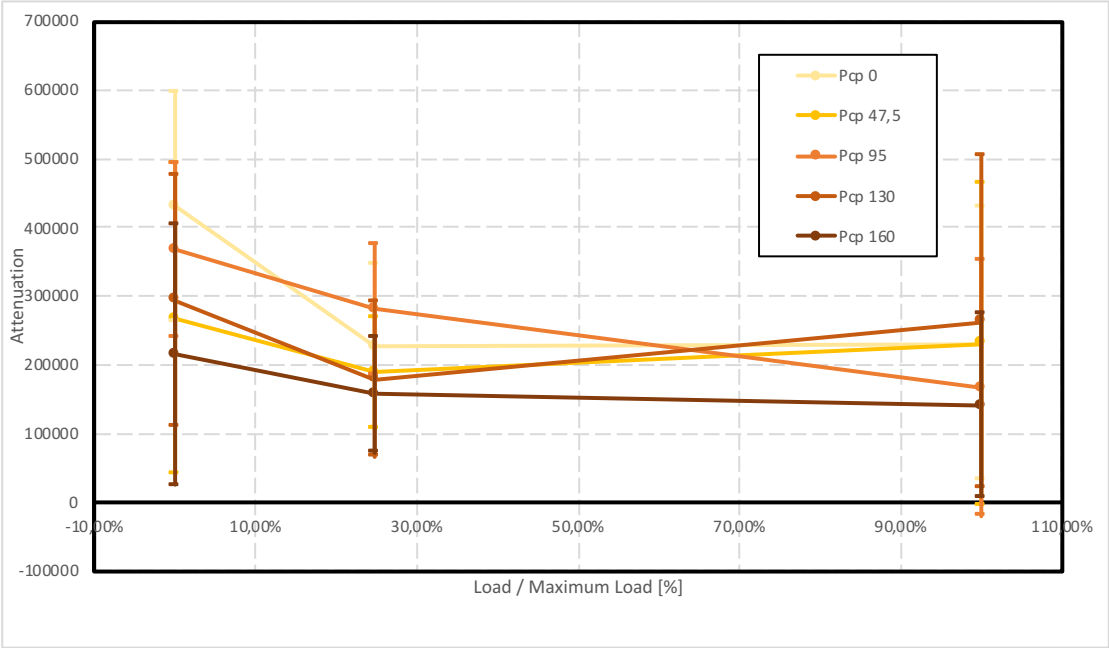

Figure 4.67. Beam 6. Variation of attenuation of the energy of the signal and its standard deviation for the various cycles along the inclined paths for different prestressed force. Y direction.

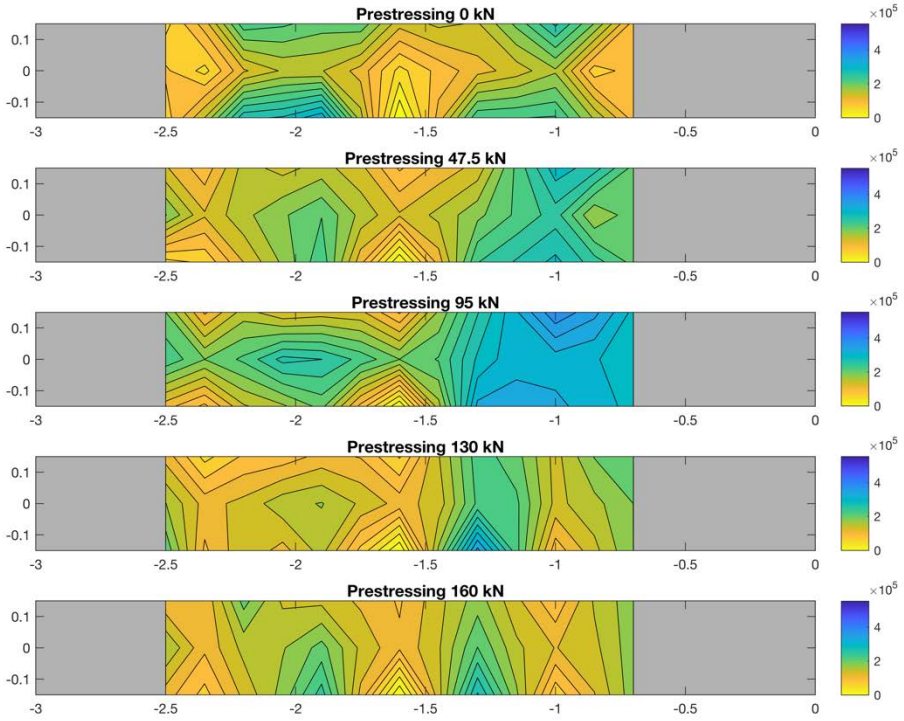

Figure 4.68. Beam 6. Attenuation in Y direction. Cracked state.

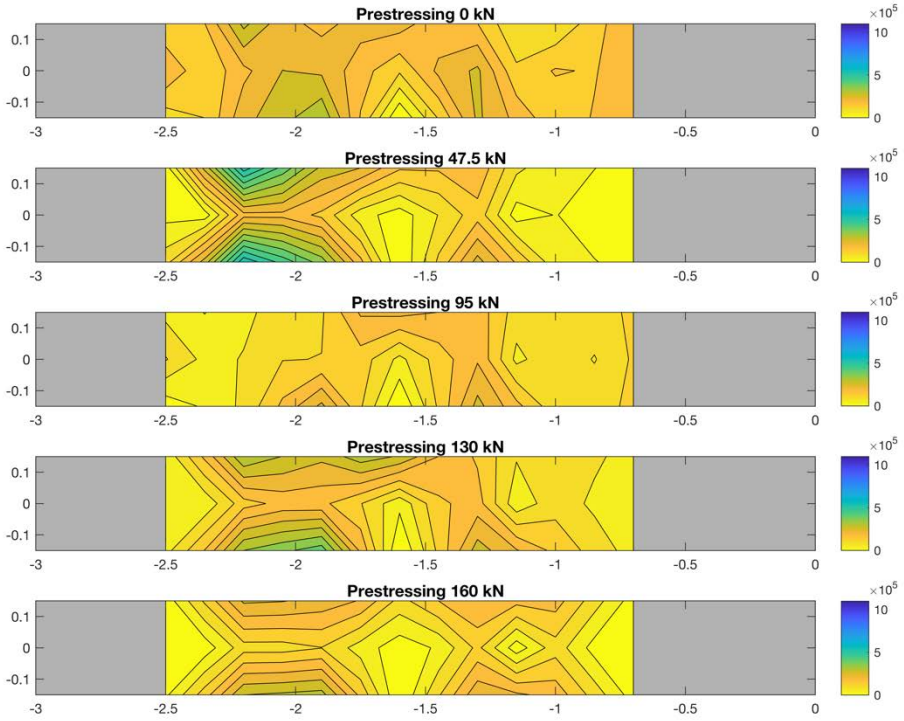

Figure 4.69. Beam 6. Attenuation in Y direction. Failure state.

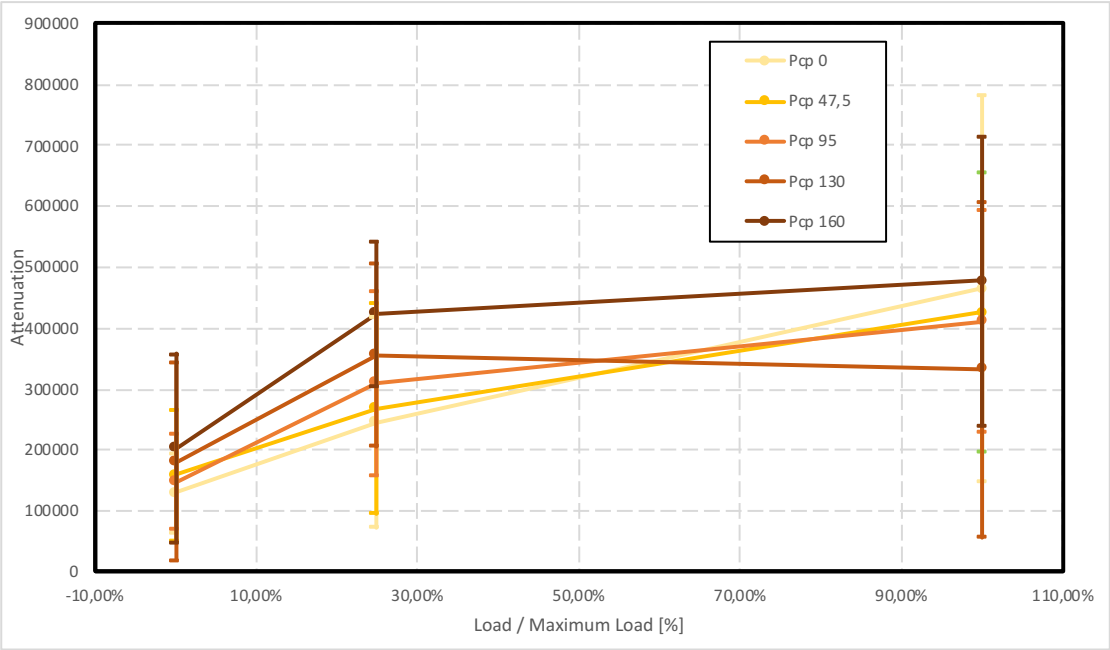

Figure 4.70. Beam 6. Variation of attenuation of the energy of the signal and its standard deviation for the various cycles along the straight paths for different prestressed force. X direction.

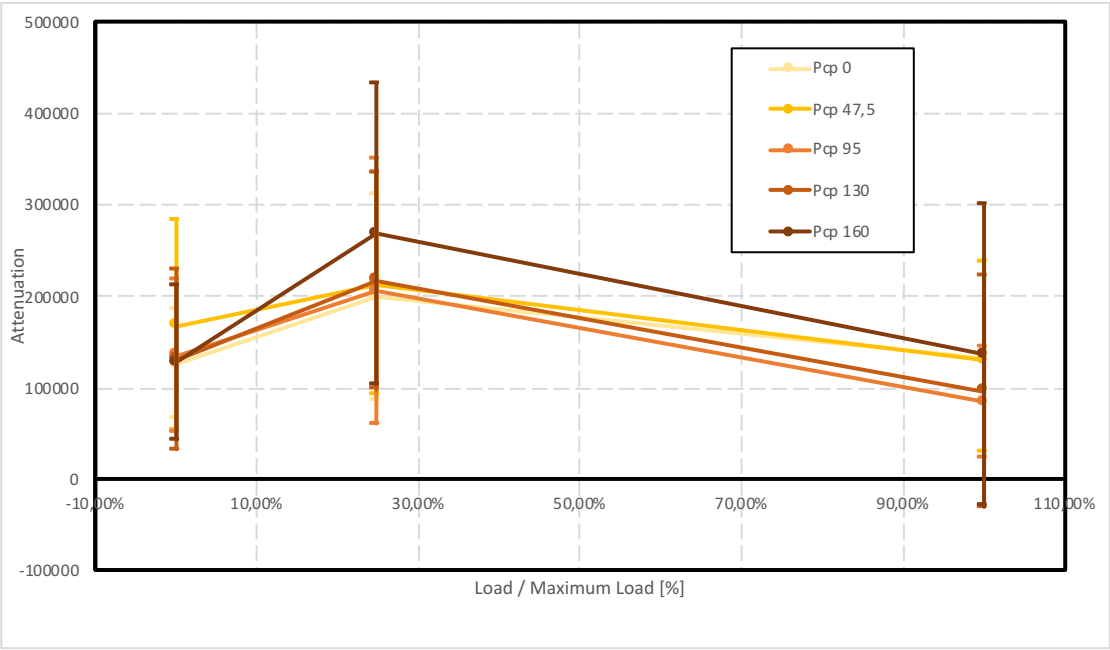

Figure 4.71. Beam 6. Variation of attenuation of the energy of the signal and its standard deviation for the various cycles along the inclined paths for different prestressed force. X direction.

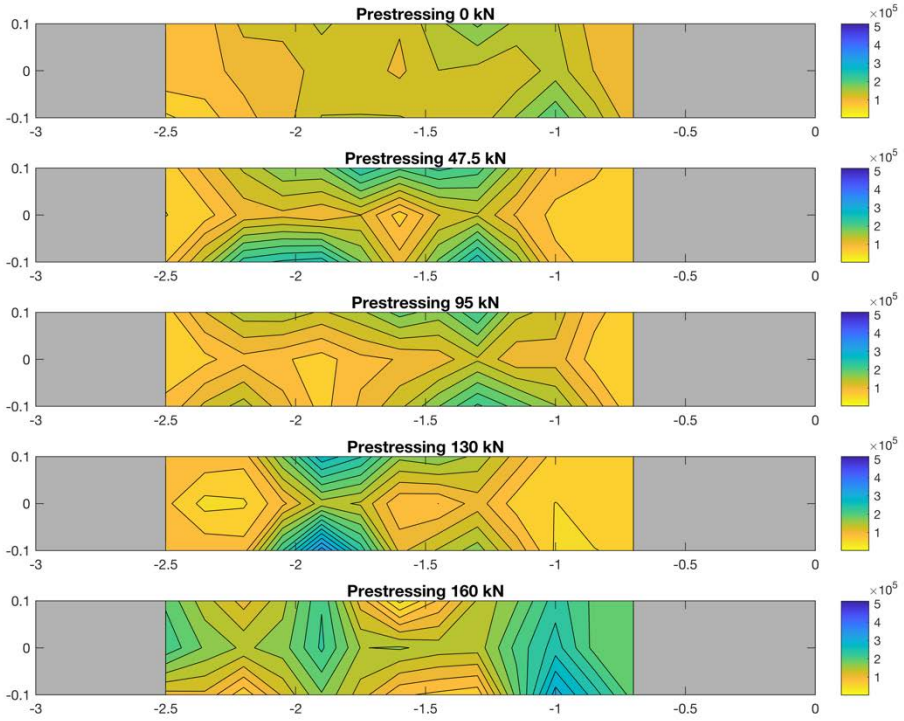

Figure 4.72. Beam 6. Attenuation in X direction. Undamaged state.

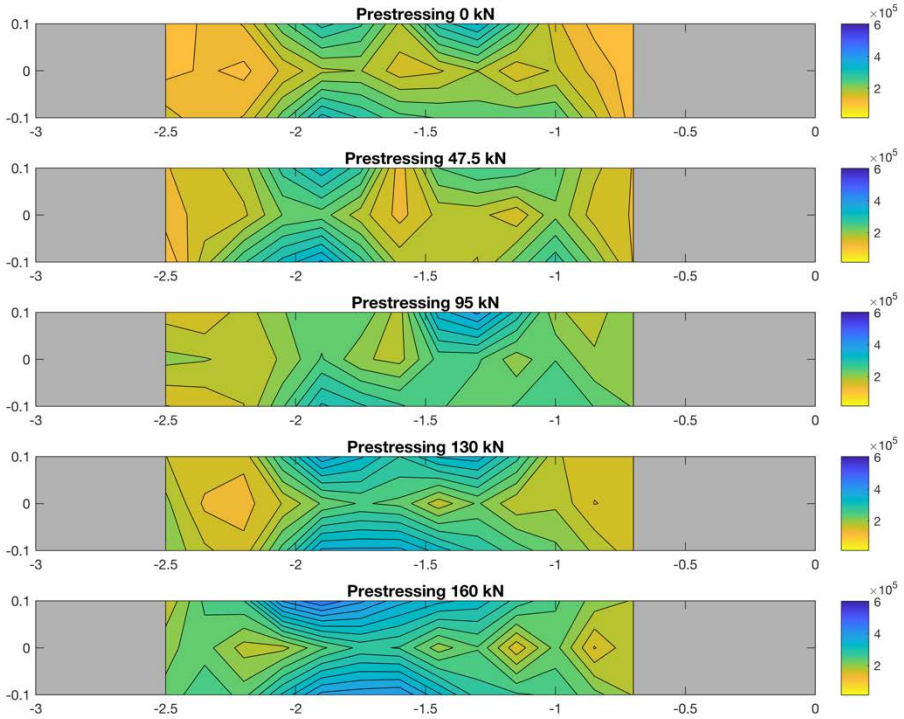

Figure 4.73. Beam 6. Attenuation in X direction. Cracked state.

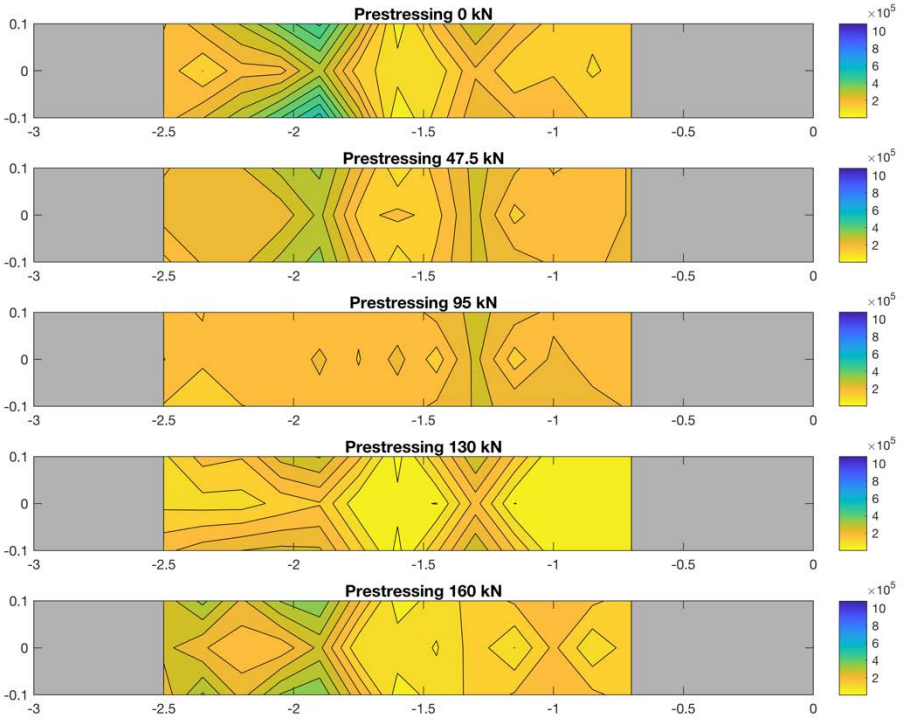

Figure 4.74. Beam 6. Attenuation in X direction. Failure state.

5 Dynamic tests

5.1 Instrumentation

The tools used in the experimental campaign are the following:

- 1 Instrumented hammer. The tip of the hammer contains a quartz force sensor with integrated microelectronic amplifier that transforms the impact force into an electrical signal (it can be of three different stiffness influencing the signal frequency). For the performed tests a PCB hammer was used, in particular the model PCB-086D20.

- 10 Accelerometers. They are transducers containing a piezoelectric crystal. When the body of the accelerometer is subject to vibration, the mass opposes itself by inertia and compresses the crystal generating charges which are converted into a potential difference measurable through a special circuit. The accelerometers used are from Piezoeletronics PCB. For the connection of test instruments coaxial cables are usually used as they guarantee high reliability and good anti-noise qualities.

- PXI: PC based platform able to offer a high performance distribution solution for measurement and automation systems. It consists of a chassis, inside which the hardware is installed. For the performed tests, a NI PXI-1042Q hardware was used, that consists in a system controller (usually housed in the first slot on the left of the chassis, it contains all the hardware components necessary for the management of the instrument and a series of peripherals for interfacing with other PXI embedded devices, model 8102) and, finally, the peripheral modules. The signal display function is guaranteed and managed independently by an acquisition software installed in the PXI. The acquisition phase starts after the equipment is assembled and, at the end of each test, the data is saved in ASCII format, to be elaborated offline.

Figure 5.1 Impulse hammer used for dynamic tests

Figure 5.2 Piezoelectric accelerometers

Figure 5.3 PXI

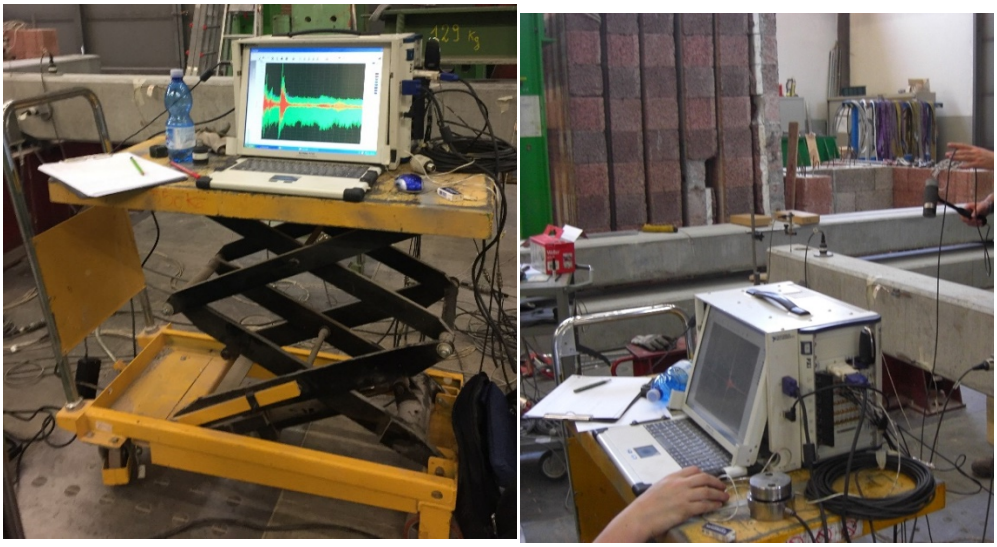

Figure 5.4 Full dynamic acquisition system

5.2 Pre-stressed beams

5.2.1 Test set-up

The set-up of the 3 pre-stressed beams consisted in 10 accelerometers (5 in the upper face, with vertical direction and 5 in the side face, transversal direction).

The input force was an impulse signal generated by the instrumented hammer, with a force transducer installed inside. The impact force was applied at nine points along the beam, as can be seen from Figure 5.5. Nine data sets were collected for each load cycle, for a total of 450 time histories recorded for each beam.

The response signals went through a post-processing process. Time domain data has been converted into frequency domain data and used to obtain FRF.

For the identification of the modal parameters necessary to describe the dynamic behavior of the structure, Frequency Domain Decomposition (FDD) and Power Spectral Density (PSD) were used.

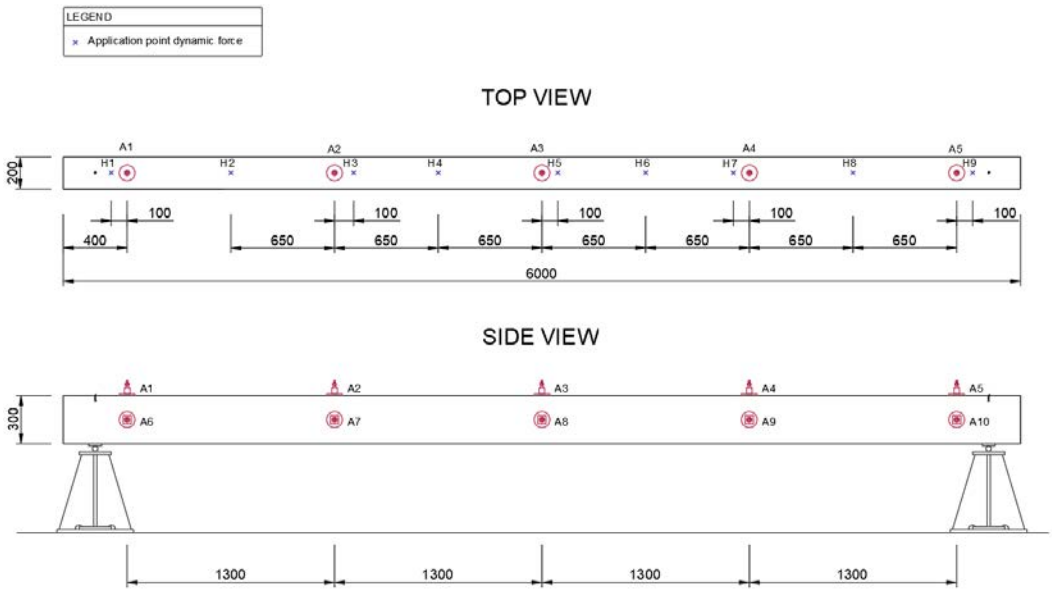

Figure 5.5 Prestressed beams: sensor set-up

5.2.2 Beam 1

For each dynamic force applied to the beam, a data set is obtained containing all the responses of the accelerometers and of the hammer. An example of recorded time history is reported below, correspondent to the hammer at the center of the span.

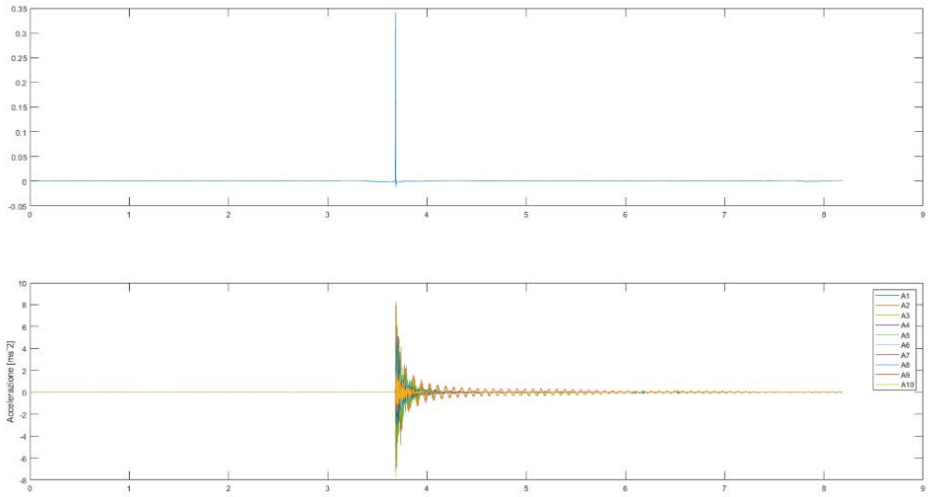

Figure 5.6 Beam 1: example of time-history

The calculation of natural frequencies is then made for the most significant impulse points (H4, H5 and H6).

The peaks of the FDD (Frequency Domain Decomposition) have been highlighted in correspondence with the first mode of vibration with the use of the Peak-Picking technique.

For the first three cycles, failing to identify the frequencies using the FDD, reference was made to the PSD (Power Spectral Density) for the A2, A3 and A4 accelerometers positioned at the center line and halfway between the center line and the load application points.

The following table shows the values of the frequencies for the various cycles which were then inserted into a graph: as expected, the frequency decreases with increasing damage, due to the presence of cracks that cause a loss in stiffness. It can be noted also as the variations in frequency are smaller in the first stages of load, where the development of cracking is small; as the load increases, the cracked part of the beam is bigger, and the decrease in frequency is more significant.

Table 33: Natural frequency values for the first mode for the points of application H4, H5 and H6.

Cycle	H5		H4		H6	
	Natural frequency [Hz]	% Decrement with respect to initial value	Natural frequency [Hz]	% Decrement with respect to initial value	Natural frequency [Hz]	% Decrement with respect to initial value
0	16,85	100,00%	16,85	100,00%	16,91	100,00%
1	15,5	91,99%	15,5	91,99%	15,565	92,05%
2	15,5	91,99%	15,4	91,39%	15,63	92,43%
3	15,5	91,99%	15,63	92,76%	15,63	92,43%
4	15,14	89,85%	15,01	89,08%	15,01	88,76%
5	14,16	84,04%	14,16	84,04%	14,16	83,74%
6	12,45	73,89%	12,57	74,60%	12,57	74,33%

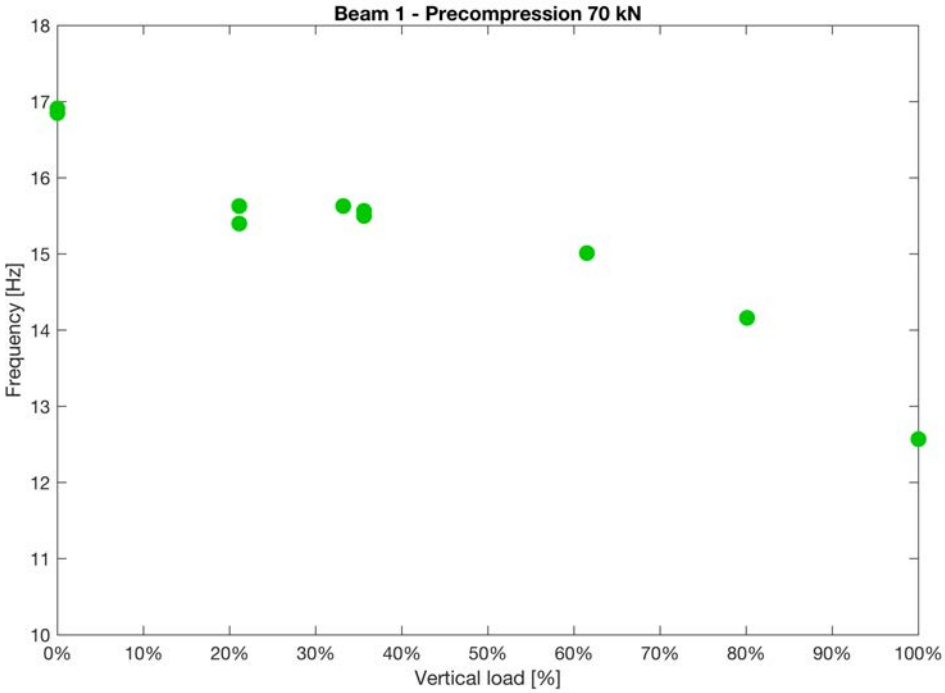

Figure 5.7 Frequency variation as function of the ratio between the applied load and the maximum resistance of the beam

Knowing the frequency values, a fitting procedure was developed in order to identify the damping ratio based on time histories. The procedure involved the following steps:

1. Windowing of the raw signal of the single accelerometer, in order to select only the post-impulse free decay of vibration (Figure 5.8);
2. Filtering of the signal: application of a lowpass digital filter in order to isolate the first frequency of vibration. A Butterworth filter was applied to the signals [67], with the order of the filter as low as possible, in order not to influence the time history;
3. Peak picking of the time history, in order to build a time series of the maximum amplitudes of the original signal;
4. Fitting of the peaks with an exponential function of the shape:

$$f(t) = A_0 e^{-\xi \omega t} \qquad (54)$$

The fitting algorithm was developed in Matlab ® environment, with the parameters A_0 (initial amplitude) and ξ (damping ratio) unknown.

The results, in term of variation of damping ratio, are summarized in the following table and figures. The presented values represent the average of the 3 vertical accelerometers A2, A3 and A4. As expected, the damping ratio increases with the increase of damage.

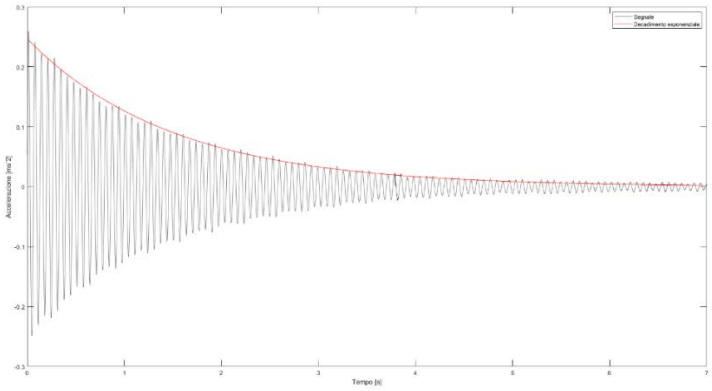

Figure 5.8 Example of free decay of vibration: beam 1. In red: fitted decay curve

Table 34: Beam 1: identified damping ratios

Cycle	Natural frequency [Hz]	Initial amplitude	ω [rad/s]	Damping ratio ξ [%]
0	16,720	0,064	105,055	0,435
1	15,750	0,797	98,960	0,605
2	15,500	1,298	97,389	0,647
3	15,140	2,071	95,127	0,741
4	14,400	0,997	90,478	0,765
5	12,700	0,630	78,226	1,225

It was observed that, since the energy of the hammer was different for every phase, the amplitude of the motion can be very different between the cycles. This effect can influence the measure of damping, being the variation in the damping not only depending to the evolution of damage but also to the amplitude variation. To minimize this disturbance, for pre-tensioned beams, signals with amplitudes with orders of magnitude different from the average were neglected. For post-tensioned beams, the tests were performed with the help of a device that allows the hammer to hit with the same energy for every blow.

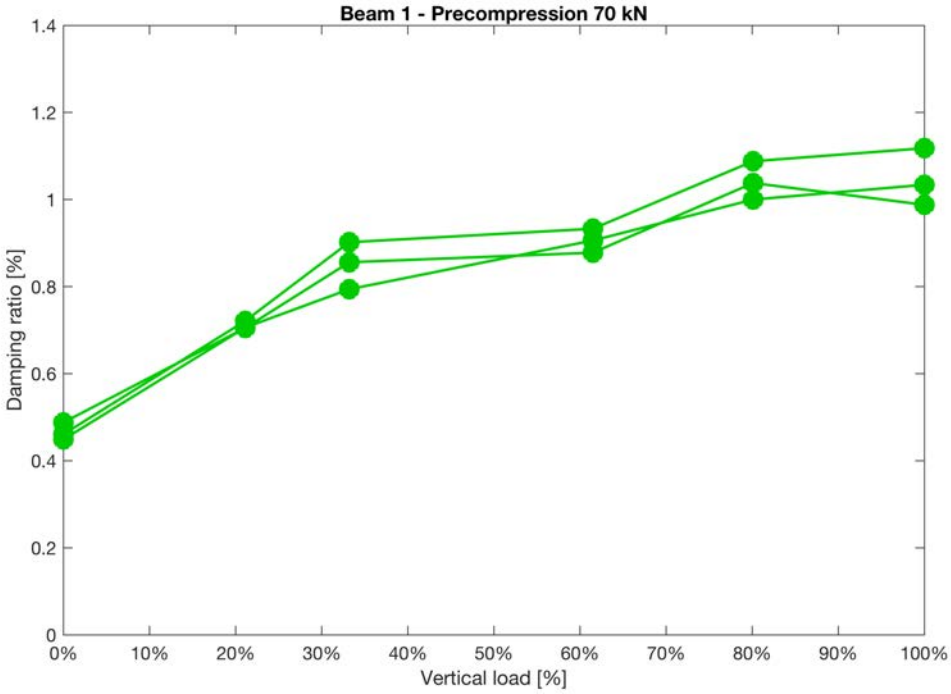

Figure 5.9 Beam 1: variation of damping ratio with increase of damage: channel 2, 3 and 4

5.2.3 Beam 2

As for Beam 2, for each dynamic force applied to the beam, a data set is obtained containing all the responses of the accelerometers and of the hammer. An example of recorded time history is reported below, correspondent to the hammer at the center of the span.

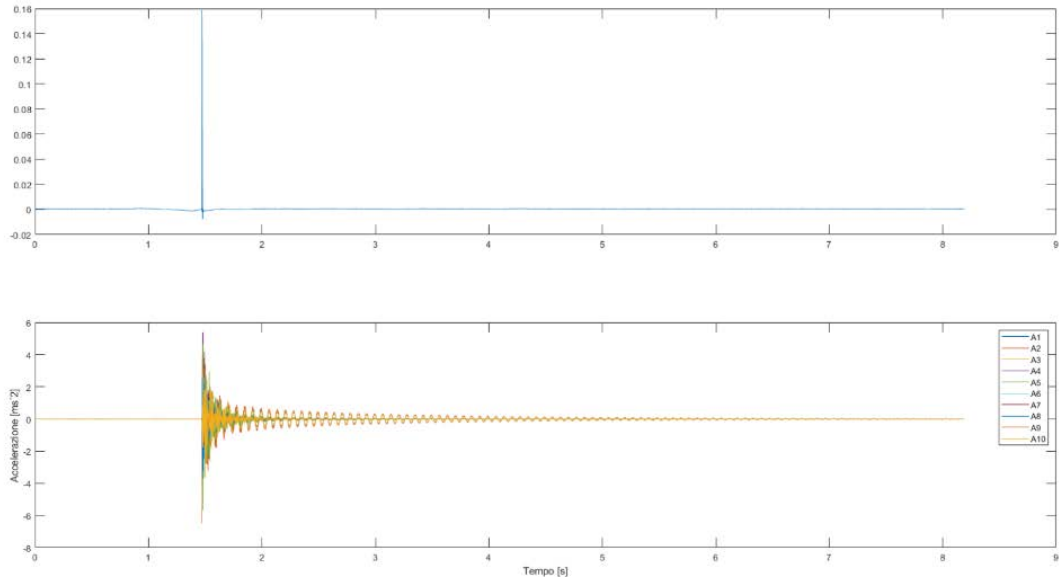

Figure 5.10 Beam 2: example of time-history

The calculation of natural frequencies is then made for the most significant impulse points (H4, H5 and H6).

The peaks of the FDD (Frequency Domain Decomposition) have been highlighted in correspondence with the first mode of vibration with the use of the Peak-Picking technique.

The following table shows the values of the frequencies for the various cycles which were then inserted into a graph: as expected, the frequency decreases with increasing damage, due to the presence of cracks that cause a loss in stiffness. It can be noted also as the variations in frequency are smaller in the first stages of load, where the development of cracking is small; as the load increases, the cracked part of the beam is bigger, and the decrease in frequency is more significant. Moreover, with respect to Beam 1, the part of the graph with stable value of frequency seems to extend for a larger part of the load history; this is probably related to the higher level of prestressing of Beam 2, that helps to keep the cracks close for a higher values of load.

Table 35: Natural frequency values for the first mode for the points of application H4, H5 and H6.

Cycle	H5		H4		H6	
	Natural frequency [Hz]	% Decrement with respect to initial value	Natural frequency [Hz]	% Decrement with respect to initial value	Natural frequency [Hz]	% Decrement with respect to initial value
0	16,36	97,09%	16,36	97,09%	16,36	96,75%
1	16,11	95,61%	16,11	95,61%	16,11	95,27%
2	16,11	95,61%	16,11	95,61%	16,11	95,27%
3	15,87	94,18%	15,87	94,18%	15,99	94,56%
4	15,87	94,18%	15,87	94,18%	15,87	93,85%
5	14,04	83,32%	14,04	83,32%	14,04	83,03%

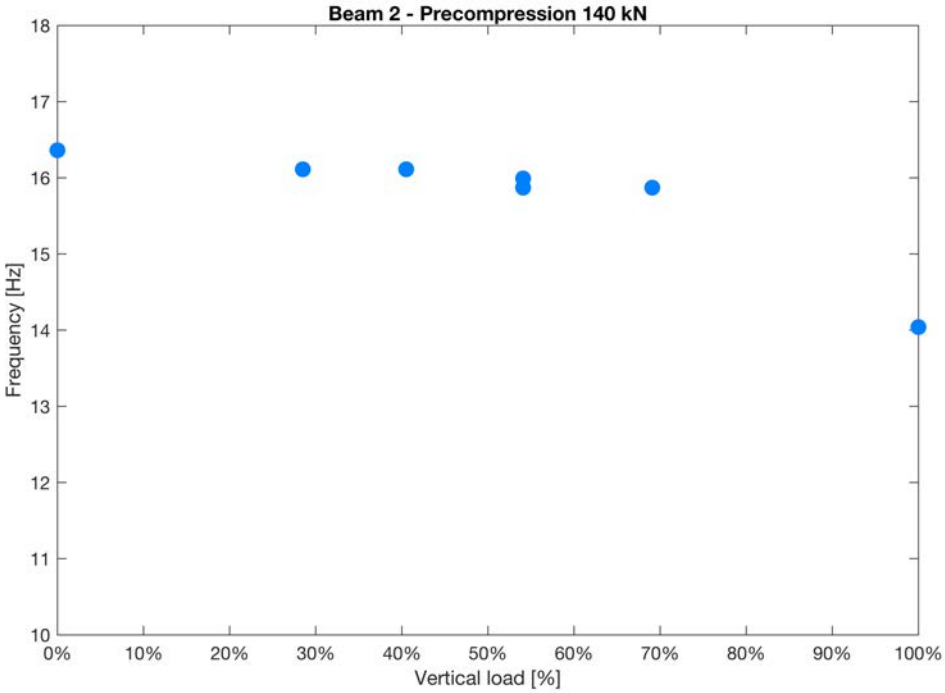

Figure 5.11 Frequency variation as function of the ratio between the applied load and the maximum resistance of the beam

Knowing the frequency values, a fitting procedure was developed in order to identify the damping ratio based on time histories. The procedure involved the same steps already described for Beam 1.

The results, in term of variation of damping ratio, are summarized in the following table e figure. As expected, the damping ratio increases with the increase of damage.

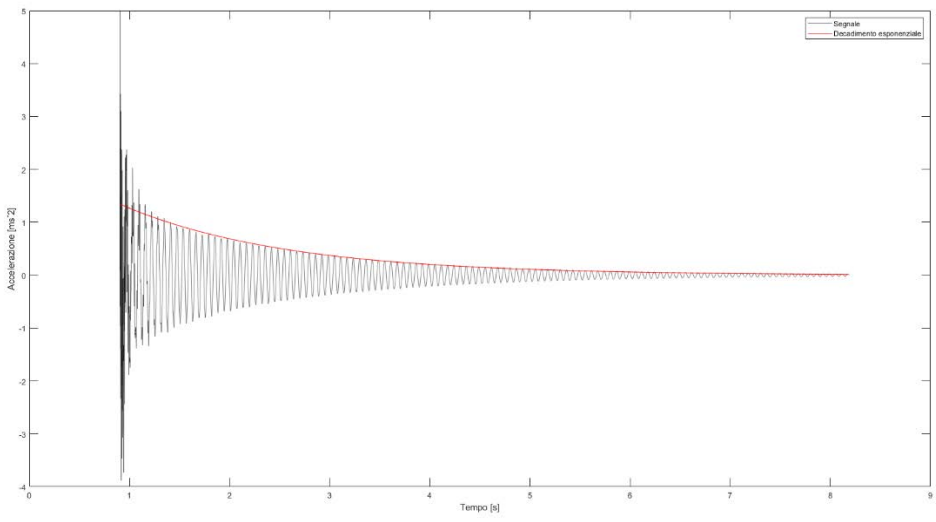

Figure 5.12 Example of free decay of vibration: beam 2. In red: fitted decay curve

Table 36: Beam 2: identified damping ratios

Cycle	Natural frequency [Hz]	Initial amplitude	ω [rad/s]	Damping ratio ξ
0	16,360	1,239	102,793	0,430
1	16,110	2,773	101,222	0,091
2	16,110	2,006	101,222	0,900
3	15,870	2,332	99,714	0,811
4	15,870	1,157	99,714	0,704
5	14,040	2,653	88,216	1,034

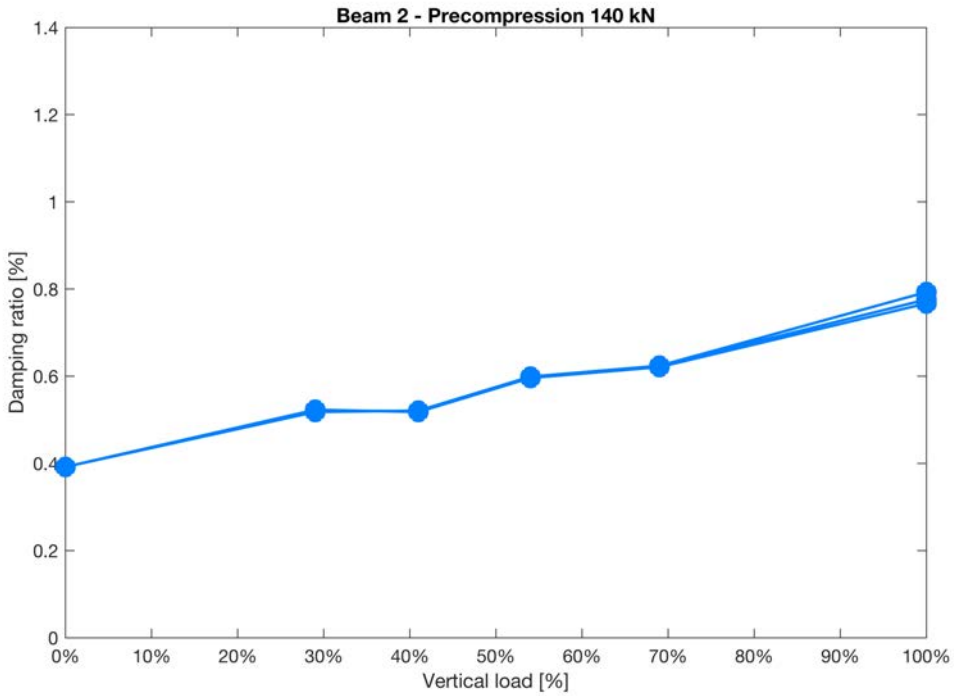

Figure 5.13 Beam 2: variation of damping ratio with increase of damage: channel 2, 3 and 4

5.2.4 Beam 3

As for Beam 1 and 2, for each dynamic force applied to the beam, a data set is obtained containing all the responses of the accelerometers and of the hammer. An example of recorded time history is reported below, correspondent to the hammer at the center of the span.

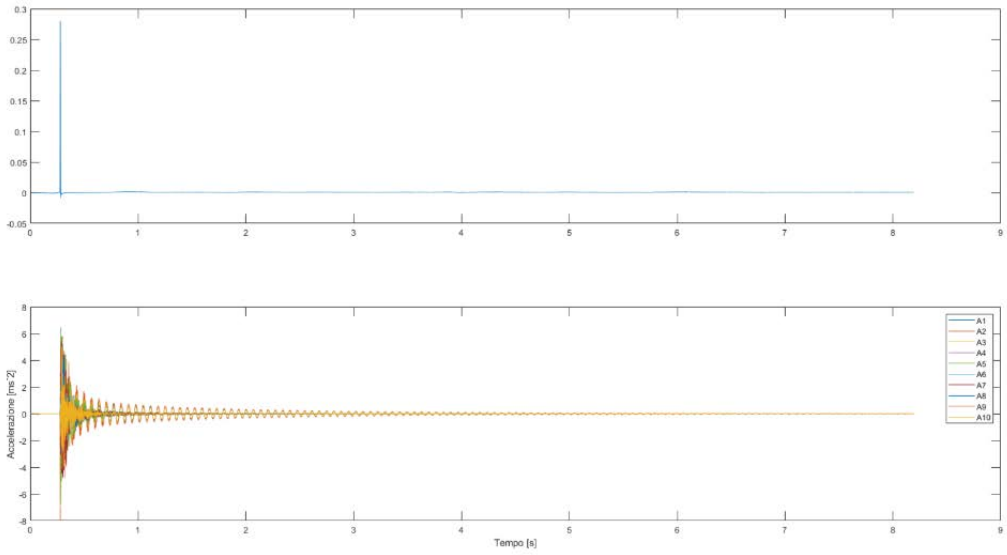

Figure 5.14 Beam 3: example of time-history

The calculation of natural frequencies is then made for the most significant impulse points (H4, H5 and H6).

The peaks of the FDD (Frequency Domain Decomposition) have been highlighted in correspondence with the first mode of vibration with the use of the Peak-Picking technique.

The following table shows the values of the frequencies for the various cycles which were then inserted into a graph: as expected, the frequency decreases with increasing damage, due to the presence of cracks that cause a loss in stiffness. It can be noted also as the variations in frequency are smaller in the first stages of load, where the development of cracking is small; as the load increases, the cracked part of the beam is bigger, and the decrease in frequency is more significant. Moreover, as for Beam 2, the part of the graph with stable value of frequency seems to extend for a larger part of the load history; this is probably related to the higher level of prestressing of Beam 2 and Beam 3 with respect to Beam 1, that helps to keep the cracks close for a higher values of load.

Table 37: Natural frequency values for the first mode for the points of application H4, H5 and H6.

Cycle	H5		H4		H6	
	Natural frequency [Hz]	% Decrement with respect to initial value	Natural frequency [Hz]	% Decrement with respect to initial value	Natural frequency [Hz]	% Decrement with respect to initial value
0	16,72	99,23%	16,72	99,23%	16,72	98,88%
1	16,48	97,80%	16,48	97,80%	16,48	97,46%
2	16,48	97,80%	16,48	97,80%	16,48	97,46%
3	16,11	95,61%	16,11	95,61%	16,11	95,27%
4	14,77	87,66%	14,77	87,66%	14,77	87,34%

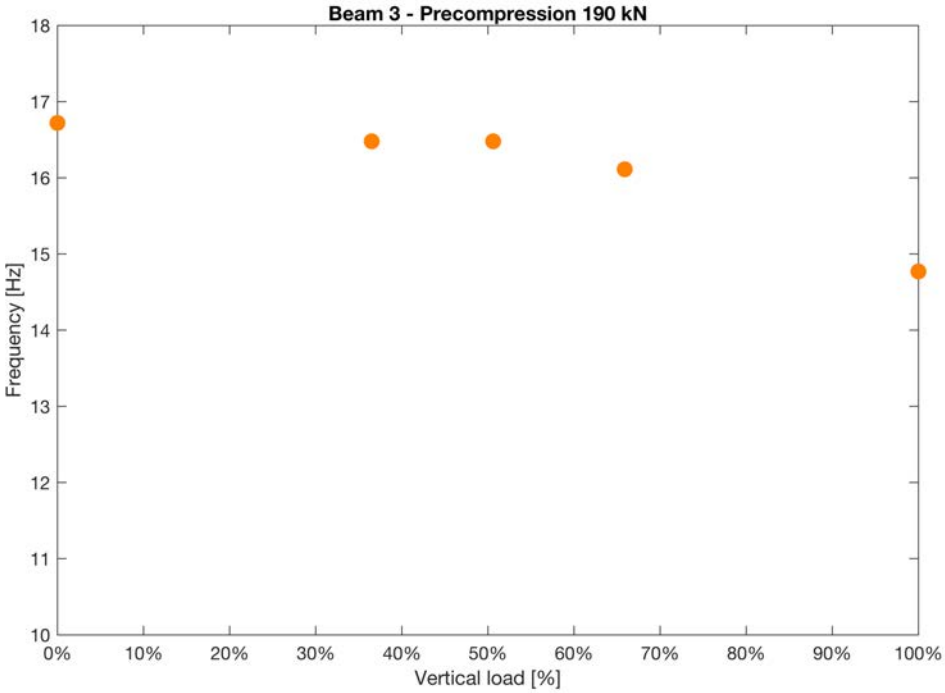

Figure 5.15 Frequency variation as function of the ratio between the applied load and the maximum resistance of the beam

Knowing the frequency values, a fitting procedure was developed in order to identify the damping ratio based on time histories. The procedure involved the same steps already described for Beam 1 and Beam 2.

The results, in term of variation of damping ratio, are summarized in the following table e figure. As expected, the damping ratio increases with the increase of damage.

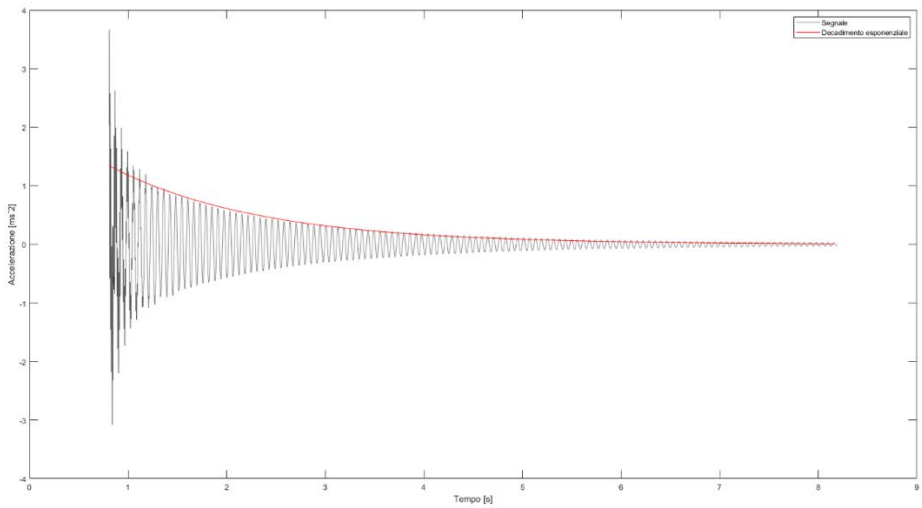

Figure 5.16 Example of free decay of vibration: beam 3. In red: fitted decay curve

Table 38: Beam 2: identified damping ratios

Cycle	Natural frequency [Hz]	Initial amplitude	ω [rad/s]	Damping ratio ξ
0	16,720	1,473	105,055	0,438
1	16,480	1,809	103,547	0,685
2	16,480	2,281	103,547	0,636
3	16,110	2,037	101,222	0,666
4	14,770	1,451	92,803	0,771

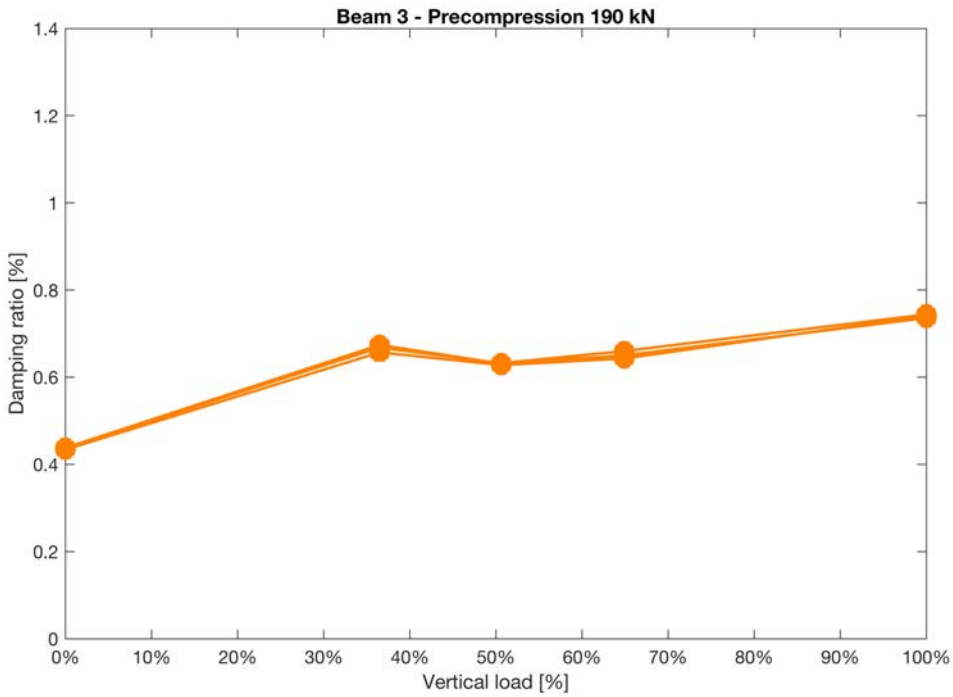

Figure 5.17 Beam 2: variation of damping ratio with increase of damage: channel 2, 3 and 4

5.2.5 Prestressed beams: comparison of results

Once the structural phases have been analyzed individually, it is possible to compare the resonance frequencies for the three beams in order to evaluate how the changes introduced in the structure have influenced the dynamic characteristics.

Figure 5.18 shows the percentage variation index of the frequency for the three beams according to the applied load for the first mode. The variation is expressed, in the figure, as the ratio between the frequency and a reference frequency, taken as the maximum recorded value:

$$I_{freq} = \frac{f}{f_{ref}} \tag{55}$$

In the initial phase of loading, the frequency decreases very slowly (probably related to the small amount of damage introduced); as the load increases, the first beam has a greater percentage of change, probably due to the lower initial prestressing force. In the last load cycle the frequency change is considerable for all the three beams.

Figure 5.19 shows a damping variation index with the increase of the load. Also in this case, the variation is expressed, in the figure, as the ratio between the damping and a reference damping, taken as the maximum recorded value:

$$I_{damping} = \frac{\xi}{\xi_{ref}} \tag{56}$$

As seen previously, the three beams follow a growing trend.

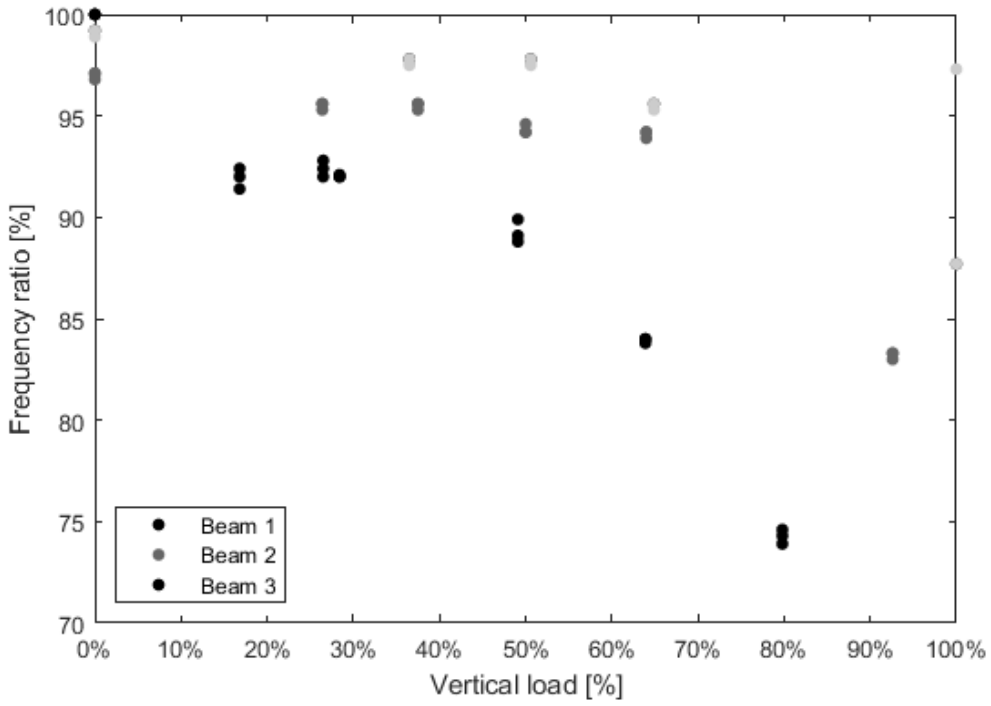

Figure 5.18 Prestressed beams: variation of frequency, first mode

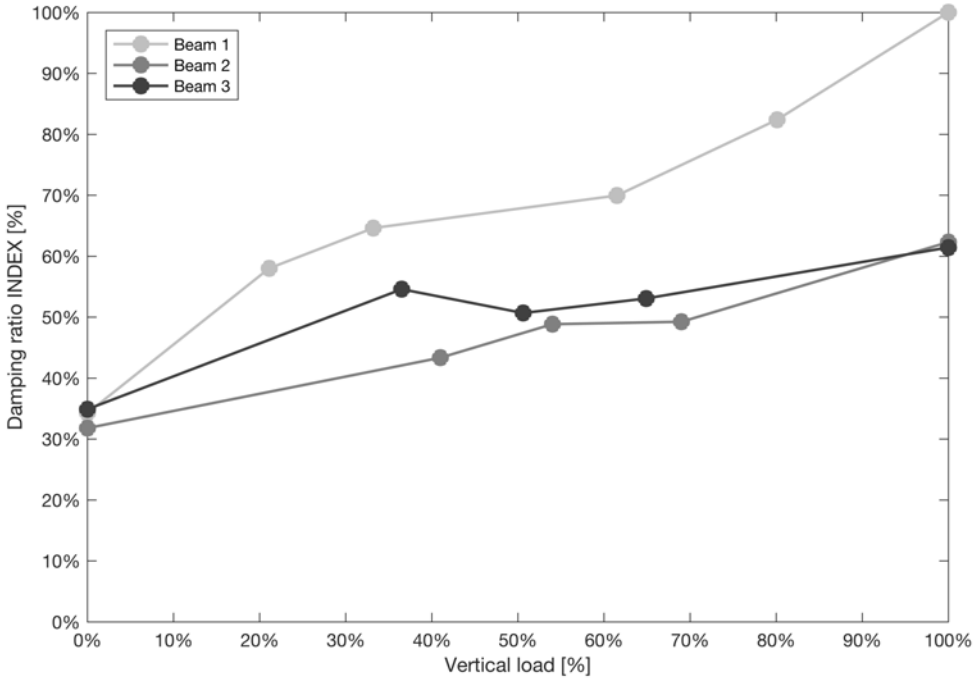

Figure 5.19 Prestressed beams: variation of damping ratio – first mode

5.3 Post-tensioned beams

5.3.1 Test set-up

The set-up of the 3 post-tensioned beams consisted in 10 accelerometers (5 in the upper face, with vertical direction and 5 in the side face, transversal direction).

The input force was an impulse signal generated by the instrumented hammer, with a force transducer installed inside. The impact force was applied at 7 points along the beam, as can be seen from Figure 5.20Figure 5.5. Seven data sets were collected for each load and prestressing cycle, for a total of 1050 time histories recorded for each beam.

The response signals went through a post-processing process. Time domain data has been converted into frequency domain data and used to obtain FRF.

For the identification of the modal parameters necessary to describe the dynamic behavior of the structure, Frequency Domain Decomposition (FDD) and Power Spectral Density (PSD) were used.

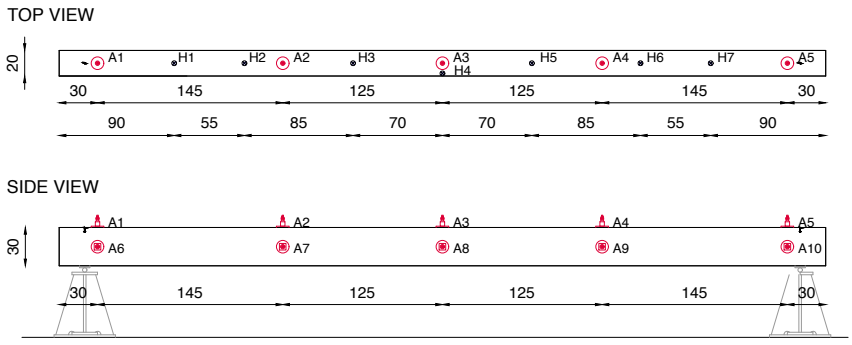

Figure 5.20 Post-tensioned beams: sensor set-up

5.3.2 Beam 4

For each dynamic force applied to the beam, a data set is obtained containing all the responses of the accelerometers and of the hammer, as for the pre-stressed beams.

The calculation of natural frequencies is then made for the most significant impulse points (H4, H5 and H6).

The peaks of the FDD (Frequency Domain Decomposition) have been highlighted in correspondence with the first mode of vibration with the use of the Peak-Picking technique.

The following table shows the mean values of the frequencies for the various cycles which were then inserted into a graph: as expected, the frequency decreases with increasing damage, due to the presence of cracks that cause a loss in stiffness. It can be noted also as the variations in frequency are smaller for higher amount of prestressing; this is due to the effect of prestressing force of reduce the formation of cracking during the load, or close the existing cracks.

Table 39: Natural frequency values for the first mode for 5 different prestressing levels

Cycle	P0		P1		P2	
	f [Hz]	% Decrement	f [Hz]	% Decrement	f [Hz]	% Decrement
0	17,30	100,00%	17,12	100,00%	16,88	100,00%
1	15,25	88,16%	16,00	93,48%	16,19	95,95%
2	9,30	53,77%	9,77	57,04%	10,91	64,63%

Cycle	P3		P4	
	f [Hz]	% Decrement	f [Hz]	% Decrement
0	17,03	100,00%	17,03	100,00%
1	16,15	94,80%	16,31	95,76%
2	11,52	67,65%	12,13	71,21%

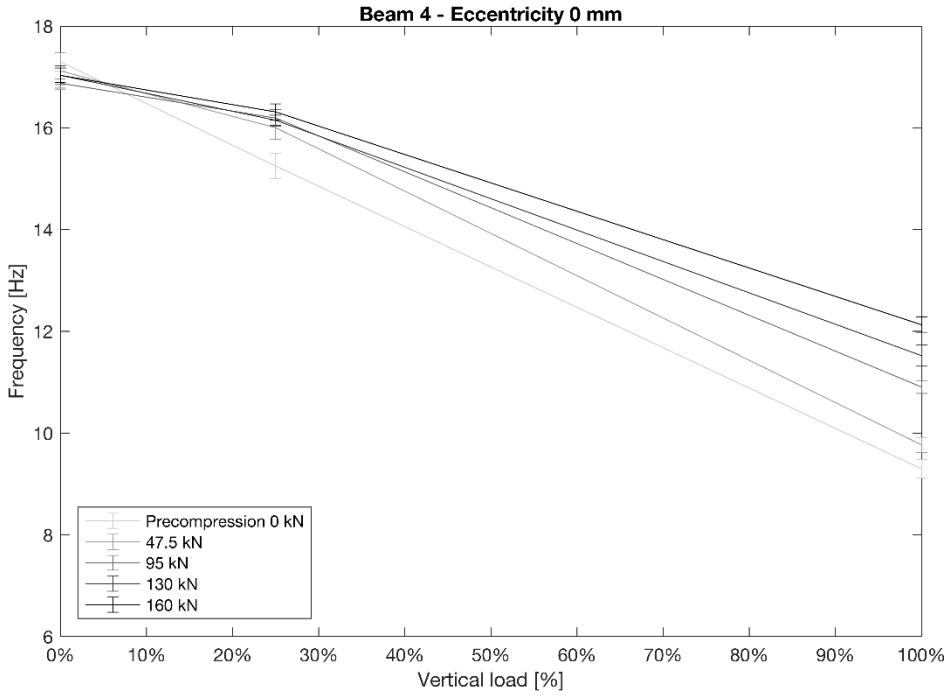

Figure 5.21 Frequency variation as function of the beam load (% with respect to maximum load)

Knowing the frequency values, a fitting procedure was developed in order to identify the damping ratio based on time histories.

In order to improve the results obtained for prestressed beams, the procedure was modified as follows, and involved the following steps:

1. Windowing of the raw signal of the single accelerometer, in order to select only the post-impulse free decay of vibration (Figure 5.22, upper plot);
2. In order to avoid any influence of the procedure in time history, filtering of the signal was not applied;
3. Instead of the filter, two different fitting algorithms were used. The first fitting algorithm was similar to the one used for prestressed beams: peak picking of the time history, in order to build a time series of the maximum amplitudes of the original signal, and fitting of the peaks with an exponential function of the shape:

   $$f(t) = A_0 e^{-\xi \omega t} \qquad (57)$$

   The fitting algorithm was developed in Matlab ® environment, with the parameters A_0 (initial amplitude) and ξ (damping ratio) unknown;
4. Since in almost all the signals there was a clear coupling of the first 2 frequencies (Figure 5.22, lower plot), another fitting algorithm was studied, of the shape:

   $$f(t) = A_{01} e^{-\xi_1 \omega_1 t} \cos(\omega_1 t + \varphi_1) + A_{02} e^{-\xi_2 \omega_2 t} \cos(\omega_2 t + \varphi_2) \qquad (58)$$

   Where A_{01}, ξ_1 and φ_1 are the initial amplitude, damping ratio and phase of the first mode, and A_{02}, ξ_2 and φ_2 are the initial amplitude, damping ratio and phase of the second mode. The result is shown in Figure 5.22, middle plot.

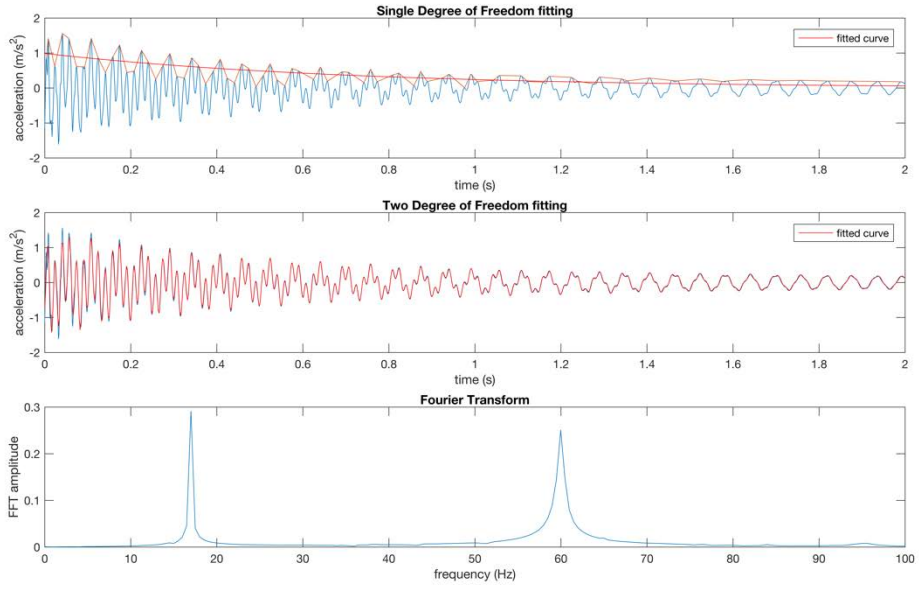

Figure 5.22 Example of free decay of vibration. In red: fitted decay curves

Due to electrical issues of the acquisition system, Beam 4 did not provide reliable results in time domain. Therefore the results in terms of damping are presented only for Beam 5 and Beam 6.

Finally, the following figures show the variation of mode shapes, calculated through EFDD (enhanced frequency domain decomposition) for 4 modes:

1. First transversal mode (1T);
2. First vertical mode (1V);
3. Second transversal mode (2T);
4. Second vertical mode (2V).

The results are represented with respect to the theoretical mode shapes (dashed lines), in the hypothesis of perfect hinge restraints at the bearings.

Every picture represent the 5 prestressing levels for a single damage level. The code FxPy indicates that the measure is taken at damage phase "x" and prestressing level "y".

The modal results are also summarized through the calculation of the MAC (modal assurance criterion), and the results are shown in Figure 5.23.

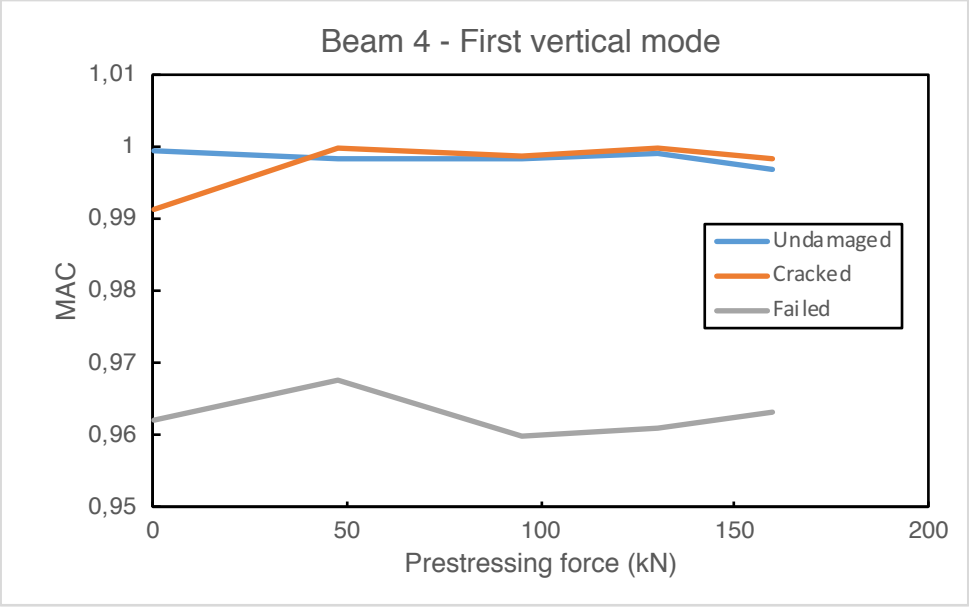

Figure 5.23: Beam 4. Variation of MAC

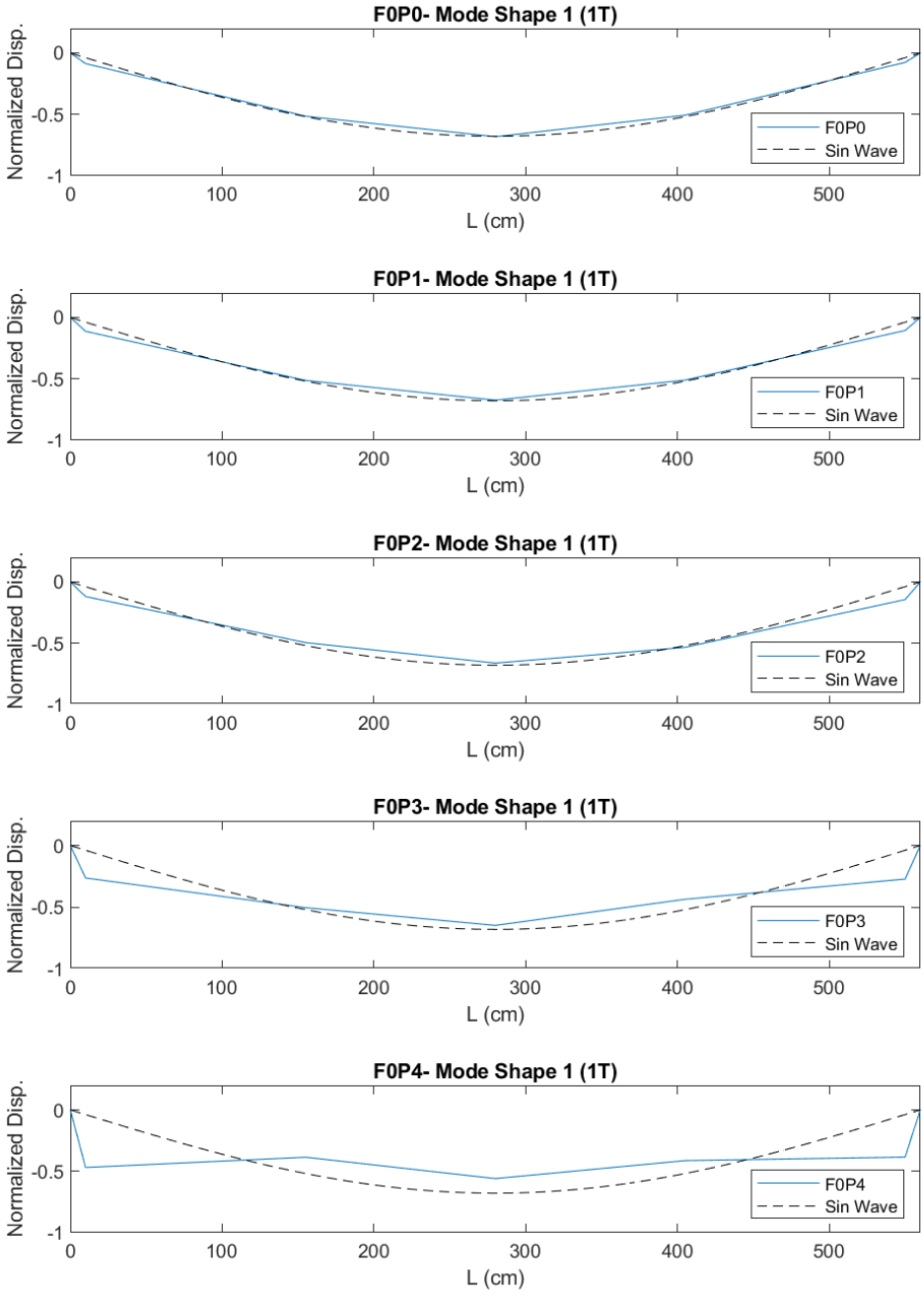

Figure 5.24: Beam 4. Variation of mode shapes for different prestressing levels. Undamaged beam, first transversal mode.

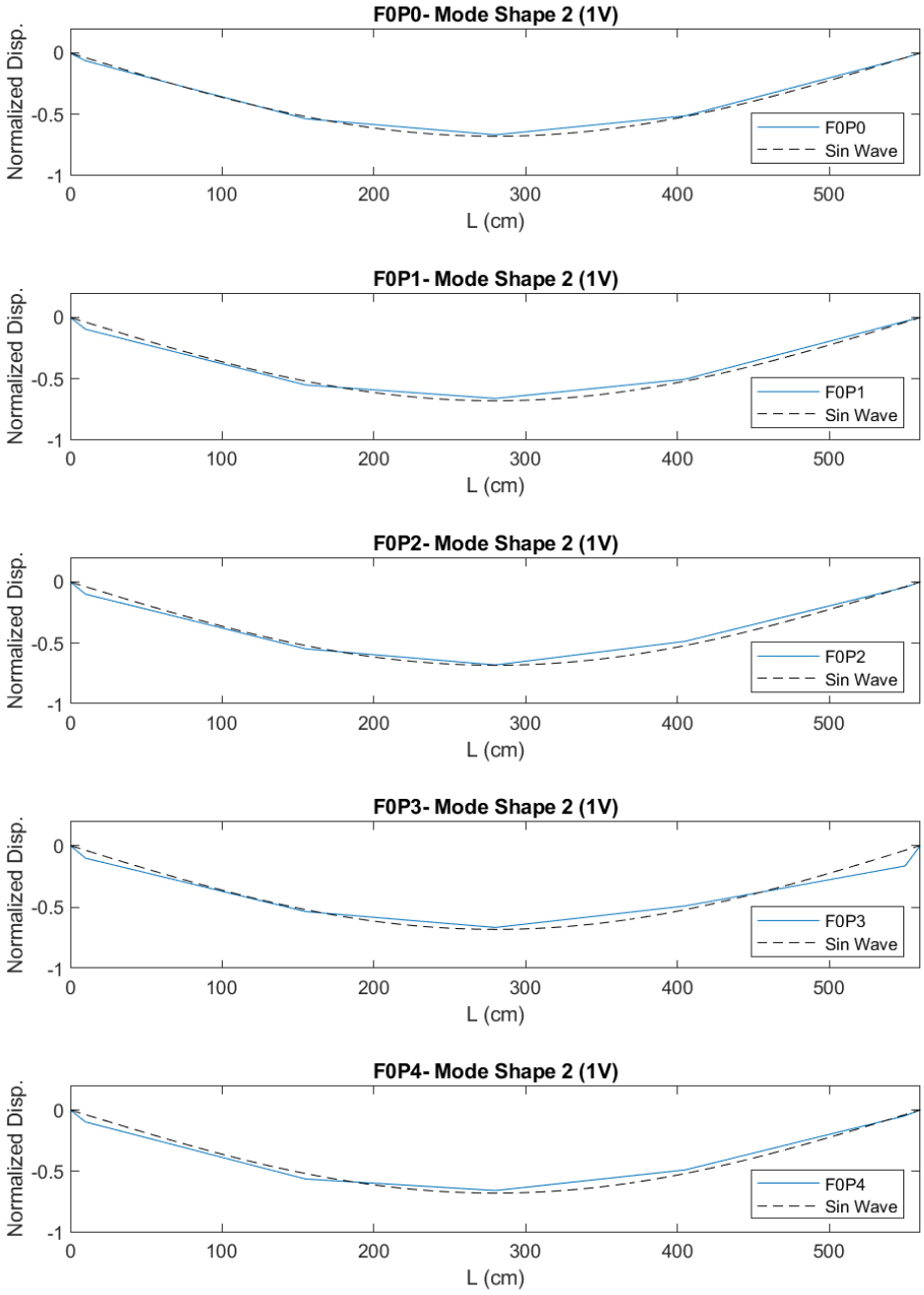

Figure 5.25: Beam 4. Variation of mode shapes for different prestressing levels. Undamaged beam, first vertical mode.

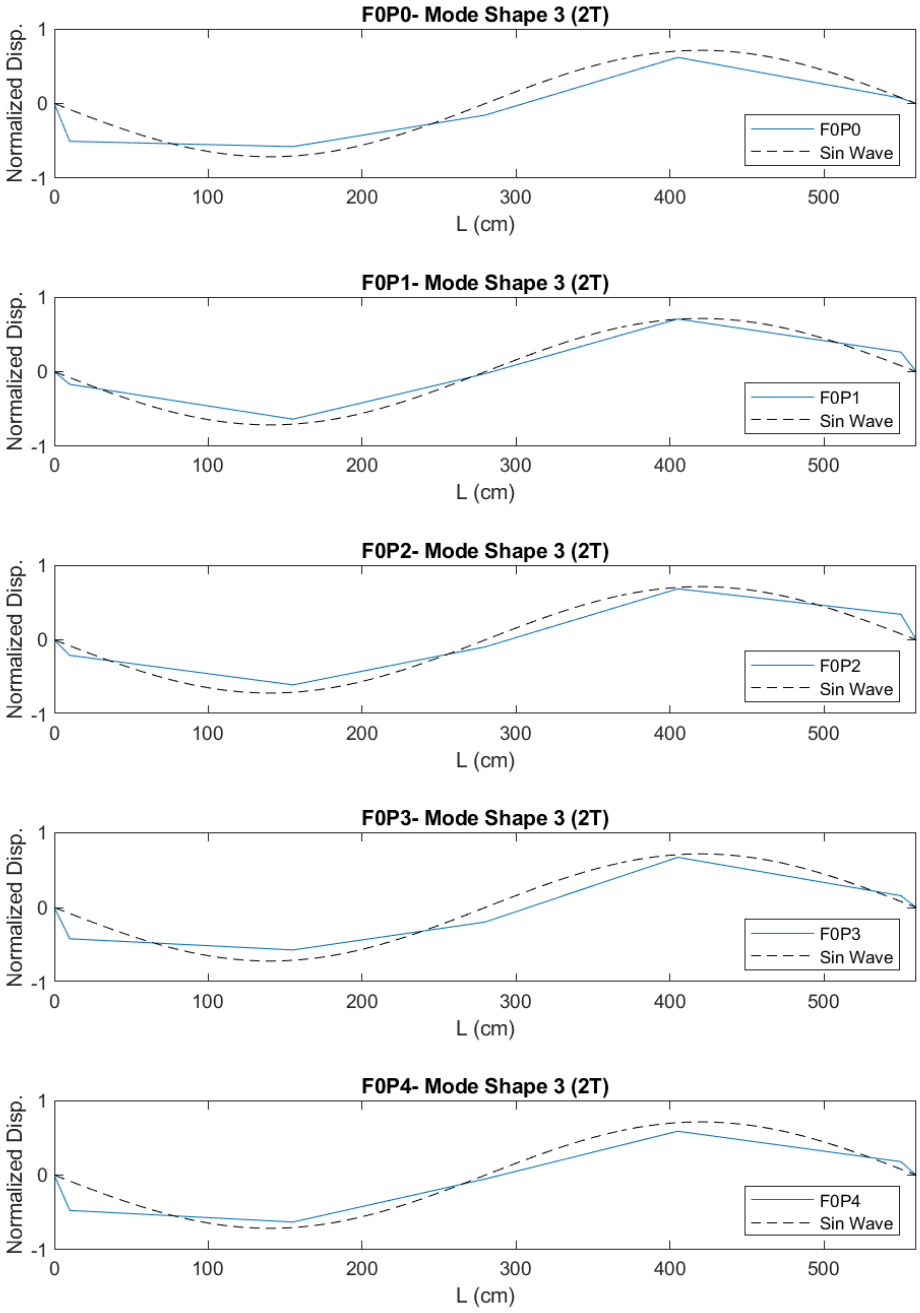

Figure 5.26: Beam 4. Variation of mode shapes for different prestressing levels. Undamaged beam, second transversal mode.

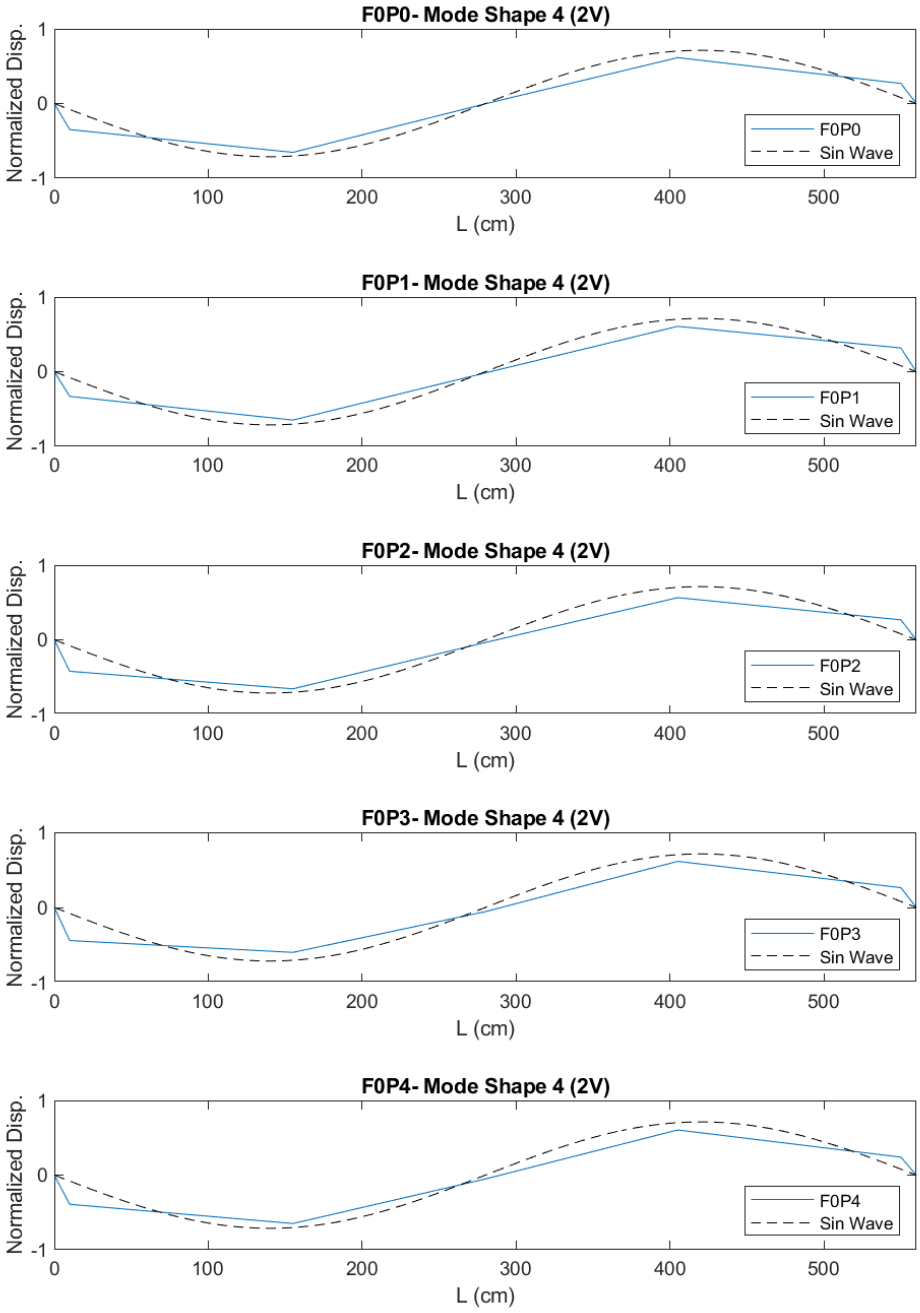

Figure 5.27: Beam 4. Variation of mode shapes for different prestressing levels. Undamaged beam, second vertical mode.

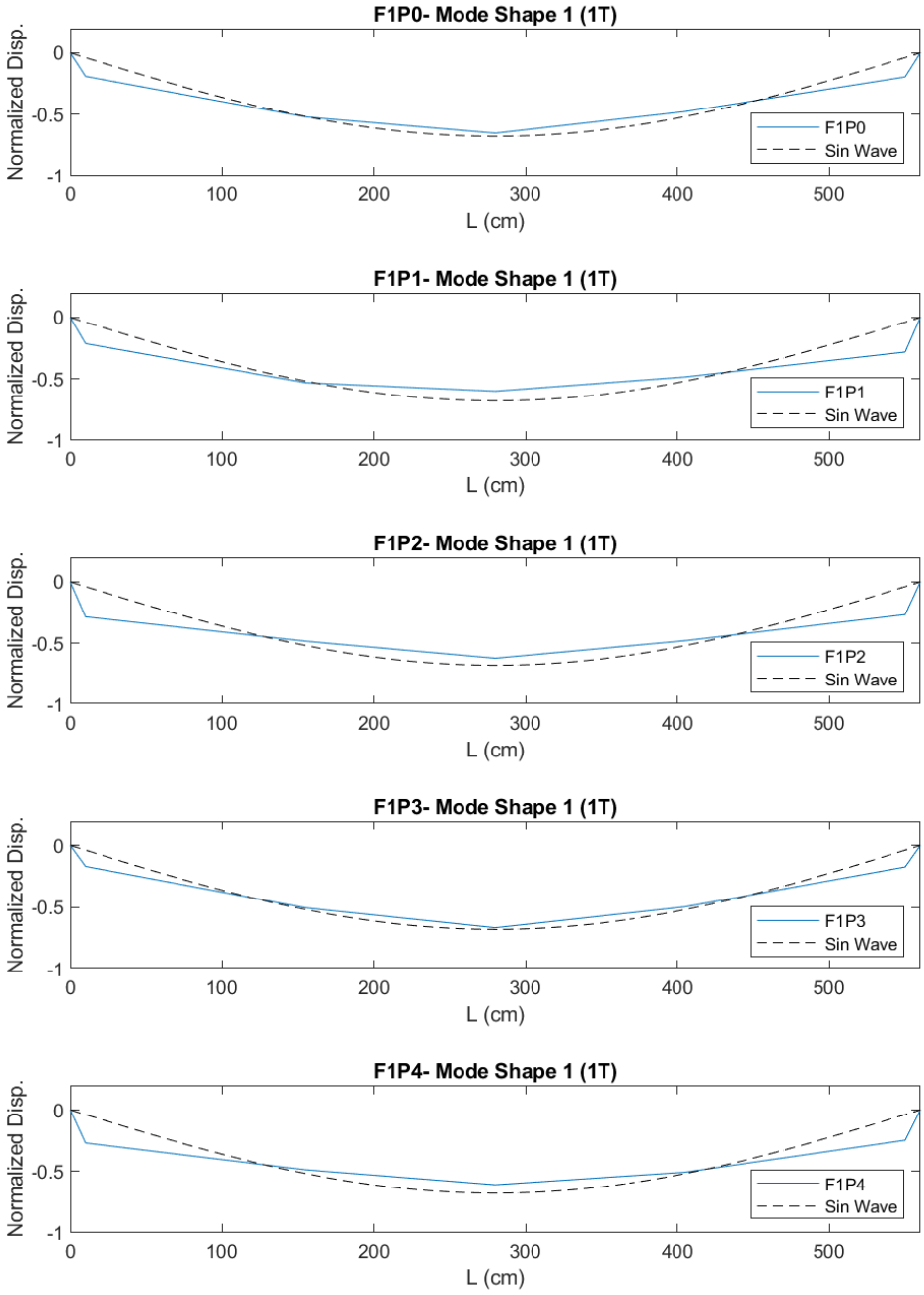

Figure 5.28: Beam 4. Variation of mode shapes for different prestressing levels. Cracked beam, first transversal mode.

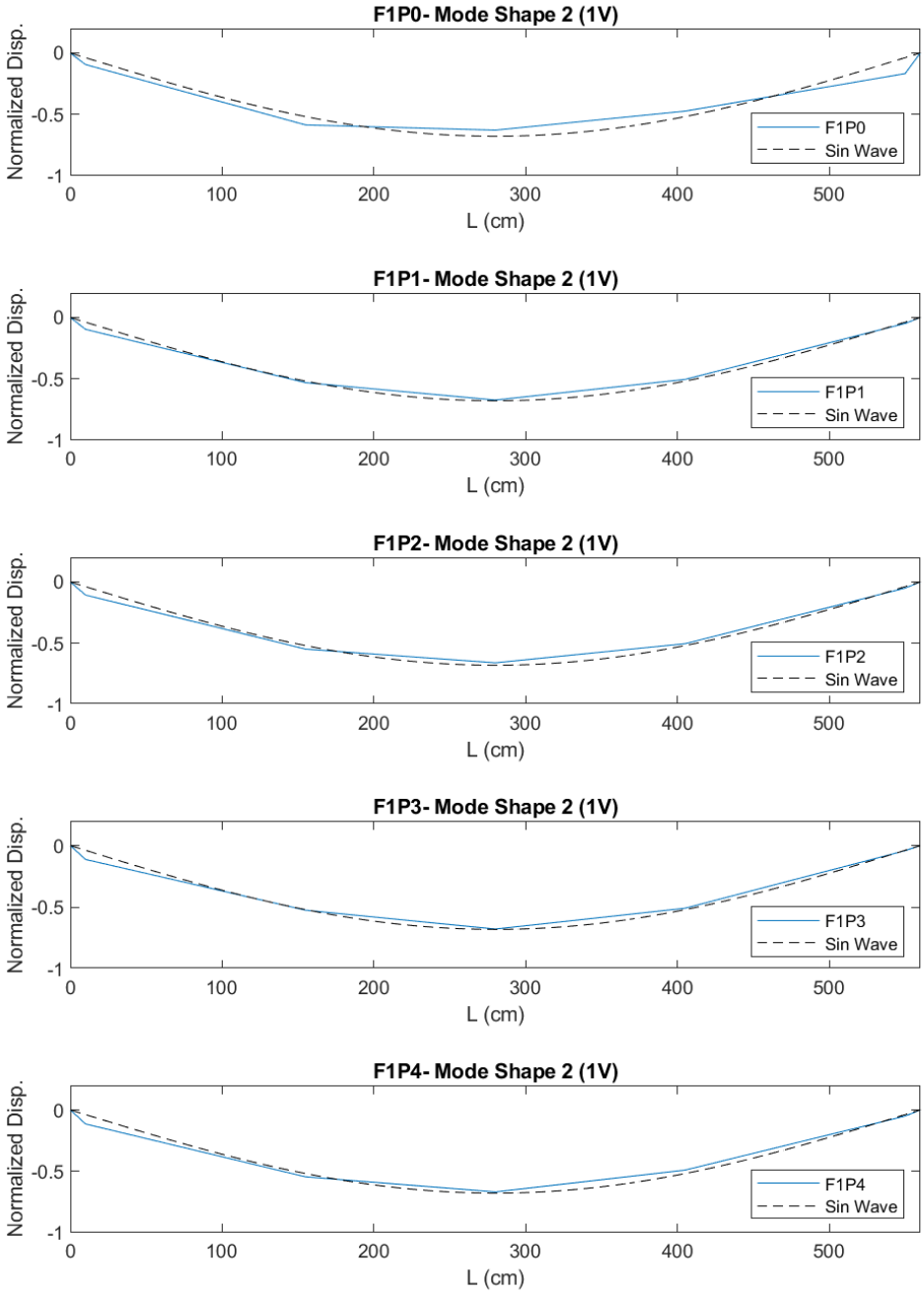

Figure 5.29: Beam 4. Variation of mode shapes for different prestressing levels. Cracked beam, first vertical mode.

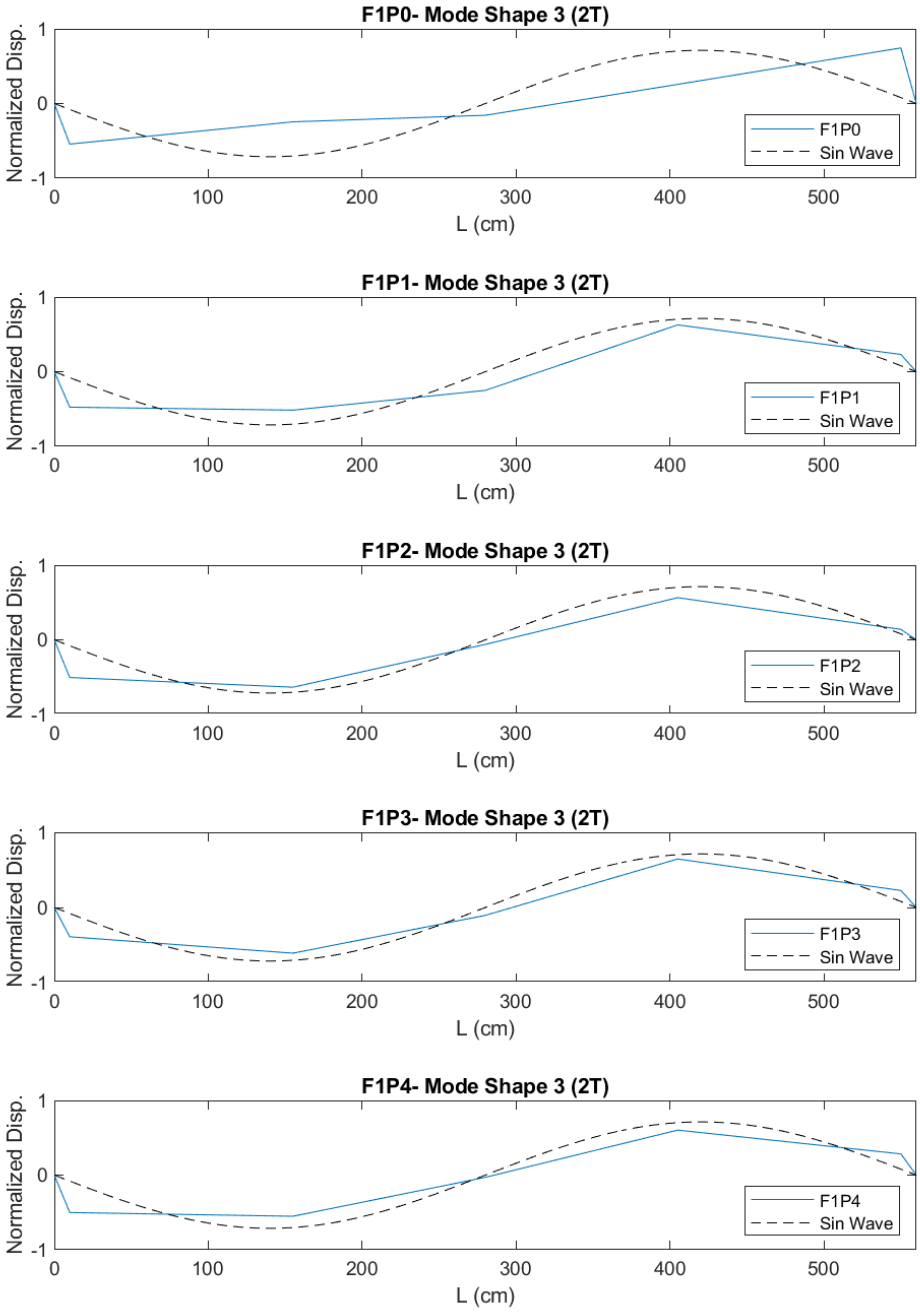

Figure 5.30: Beam 4. Variation of mode shapes for different prestressing levels. Cracked beam, second transversal mode.

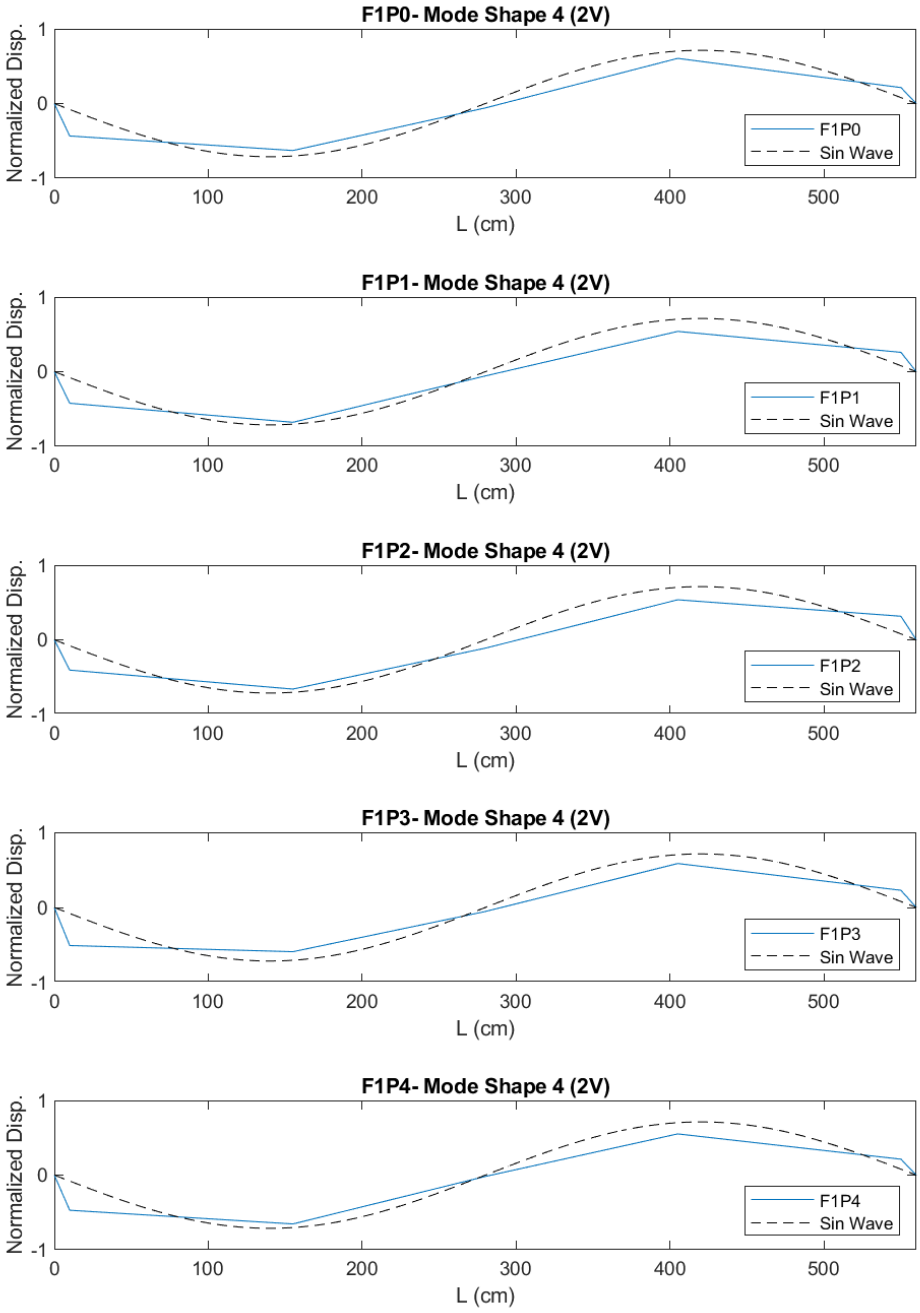

Figure 5.31: Beam 4. Variation of mode shapes for different prestressing levels. Cracked beam, second vertical mode.

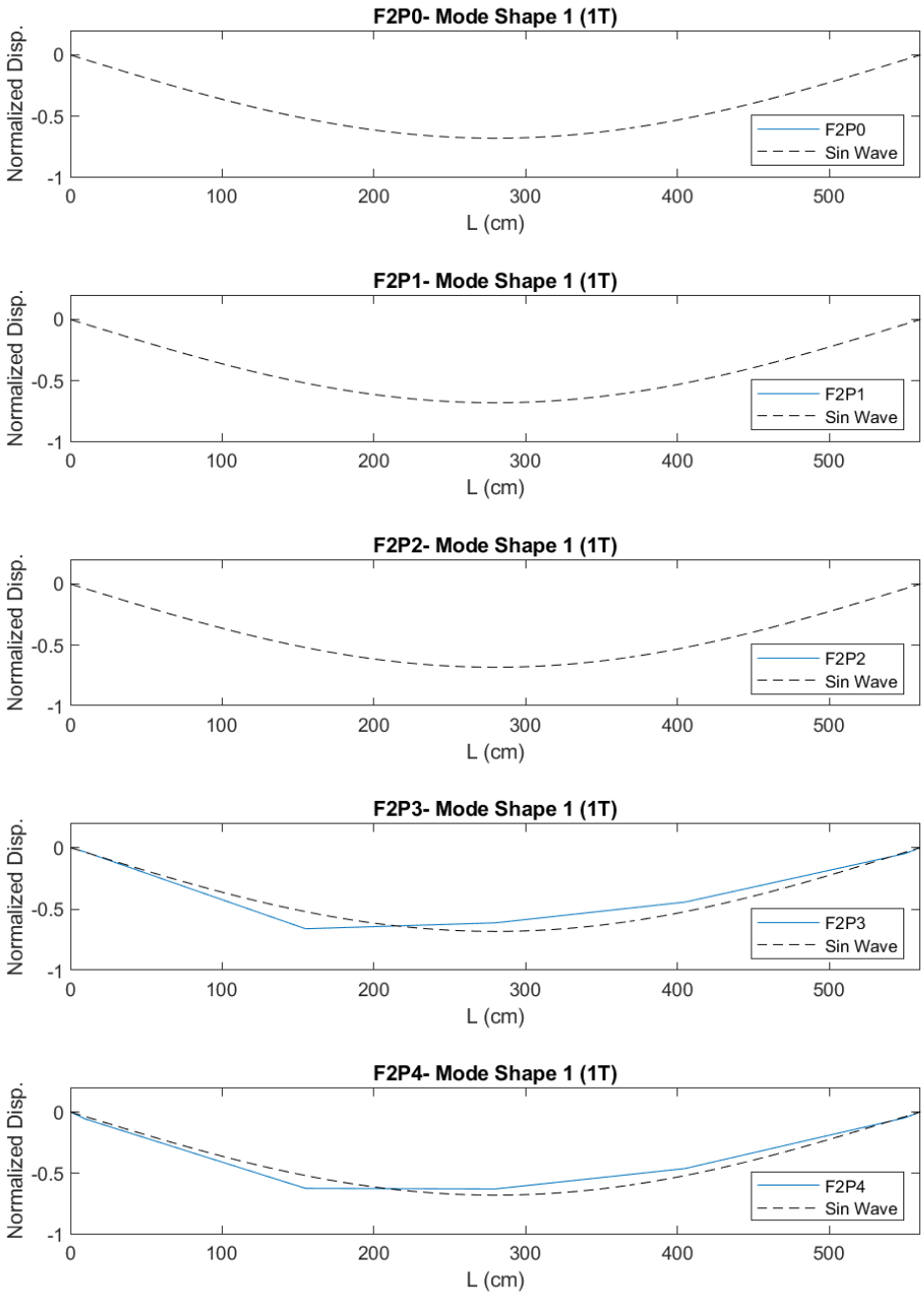

Figure 5.32: Beam 4. Variation of mode shapes for different prestressing levels. Failed beam, first transversal mode.

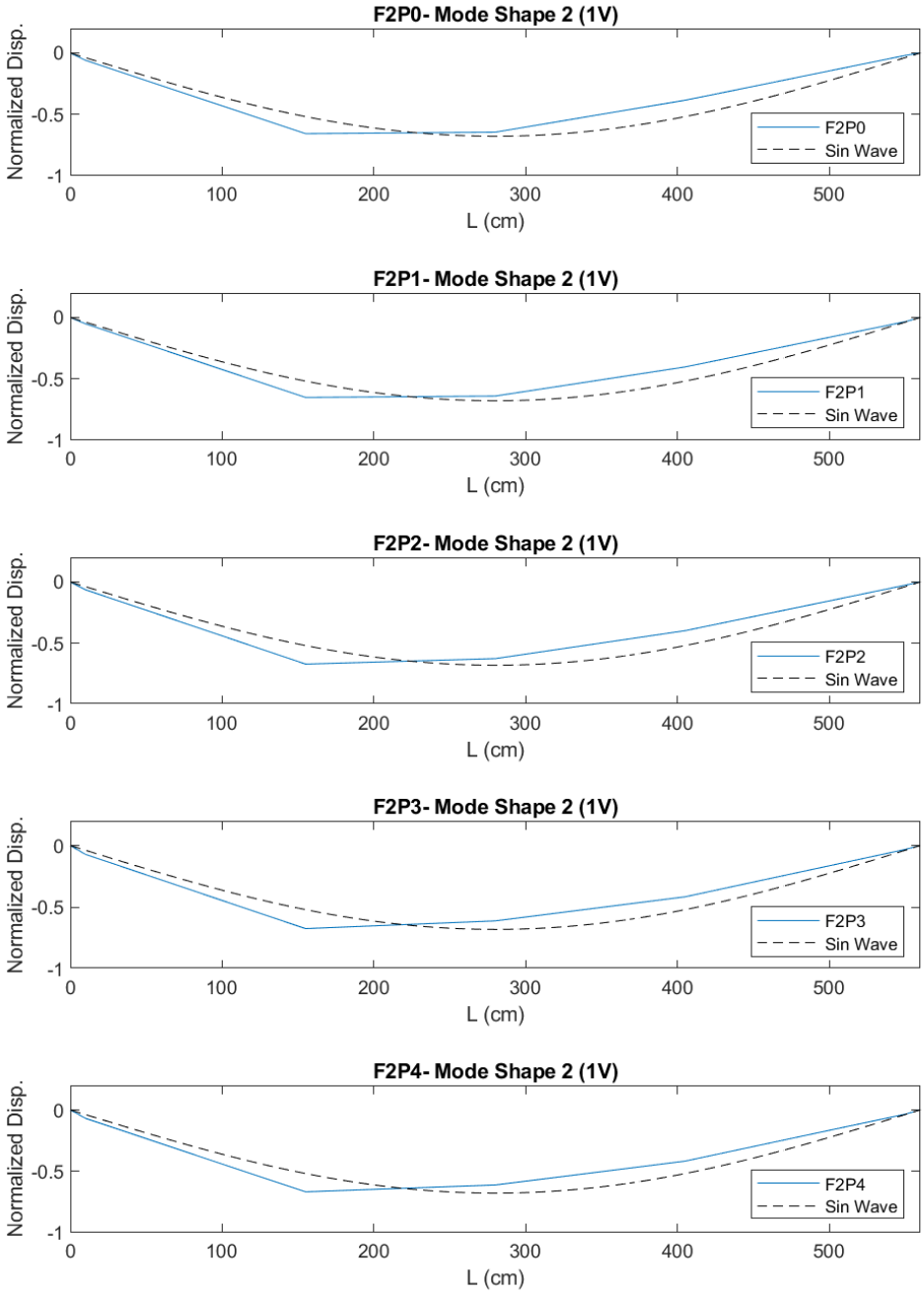

Figure 5.33: Beam 4. Variation of mode shapes for different prestressing levels. Failed beam, first vertical mode.

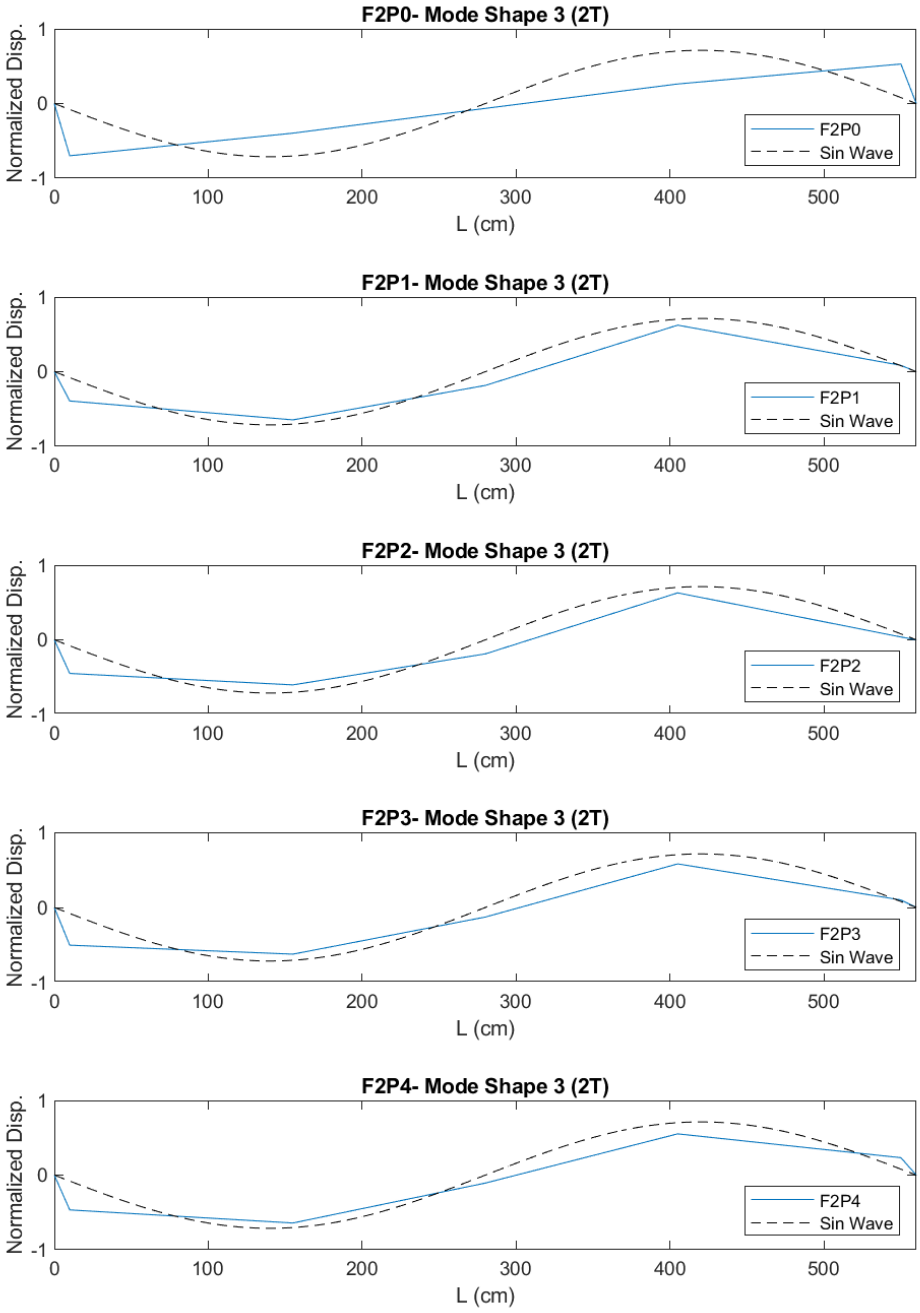

Figure 5.34: Beam 4. Variation of mode shapes for different prestressing levels. Failed beam, second transversal mode.

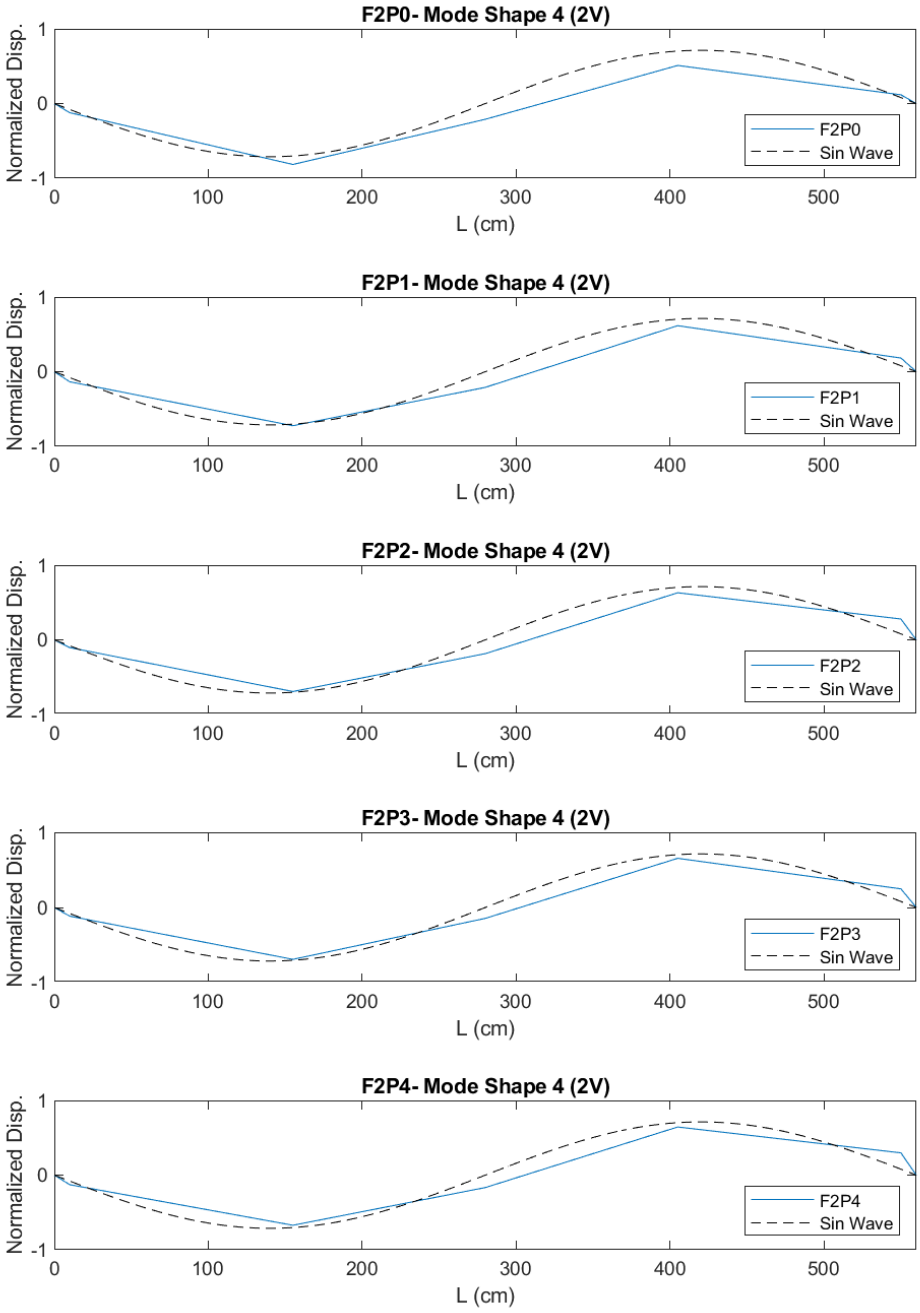

Figure 5.35: Beam 4. Variation of mode shapes for different prestressing levels. Failed beam, second vertical mode.

5.3.3 Beam 5

For each dynamic force applied to the beam, a data set is obtained containing all the responses of the accelerometers and of the hammer, as for the pre-stressed beams.

The calculation of natural frequencies is then made for the most significant impulse points (H4, H5 and H6).

The peaks of the FDD (Frequency Domain Decomposition) have been highlighted in correspondence with the first mode of vibration with the use of the Peak-Picking technique.

The following table shows the mean values of the frequencies for the various cycles which were then inserted into a graph: as expected, the frequency decreases with increasing damage, due to the presence of cracks that cause a loss in stiffness. It can be noted also as the variations in frequency are smaller for higher amount of prestressing; this is due to the effect of prestressing force of reduce the formation of cracking during the load, or close the existing cracks.

Table 40: Natural frequency values for the first mode for 5 different prestressing levels

Cycle	P0		P1		P2	
	f [Hz]	% Decrement	f [Hz]	% Decrement	f [Hz]	% Decrement
0	17,12	100,00%	16,76	100,00%	17,06	100,00%
1	13,79	80,54%	15,62	93,21%	16,23	95,12%
2	9,55	55,80%	10,84	64,70%	11,89	69,67%

Cycle	P3		P4	
	f [Hz]	% Decrement	f [Hz]	% Decrement
0	17,09	100,00%	17,14	100,00%
1	16,25	95,06%	16,30	95,10%
2	12,62	73,82%	14,57	85,00%

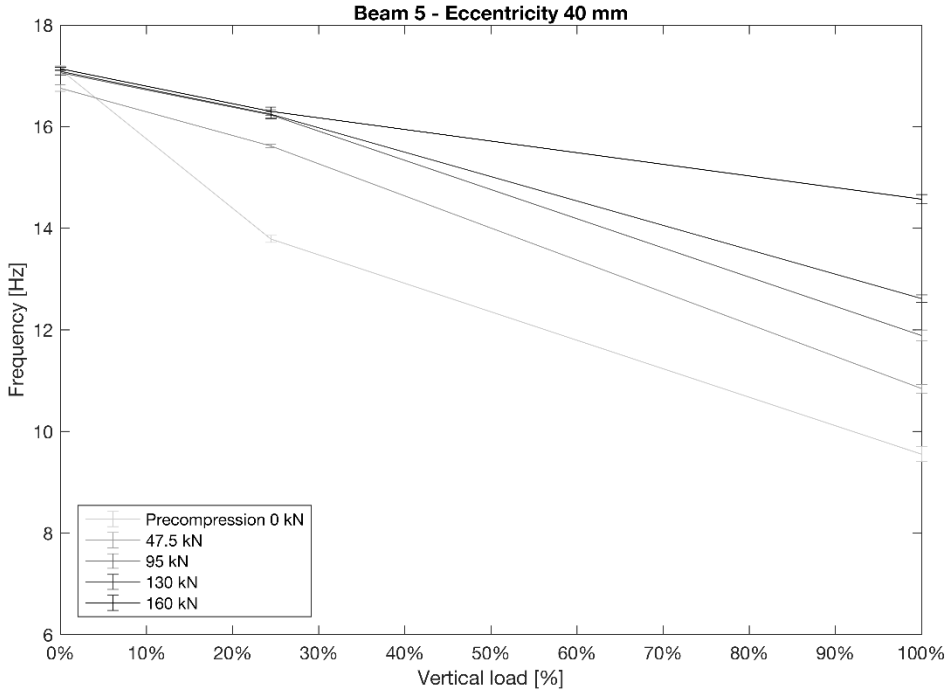

Figure 5.36 Frequency variation as function of the beam load (%)

Knowing the frequency values, a fitting procedure was developed in order to identify the damping ratio based on time histories. The procedure is the same described for Beam 4.

The results, in term of variation of damping ratio, are summarized in the following table e figure. As expected, the damping ratio increases with the increase of damage. Moreover, the variations in frequency are smaller for higher amount of prestressing; as for frequencies, this is due to the effect of prestressing force of reduce the formation of cracking during the load, or close the existing cracks.

Table 41: Beam 5: identified damping ratios

Cycle	P0	P1	P2	P3	P4
	ξ	ξ	ξ	ξ	ξ
0	0,013	0,009	0,014	0,012	0,013
1	0,019	0,011	0,010	0,011	0,018
2	0,085	0,024	0,014	0,012	0,013

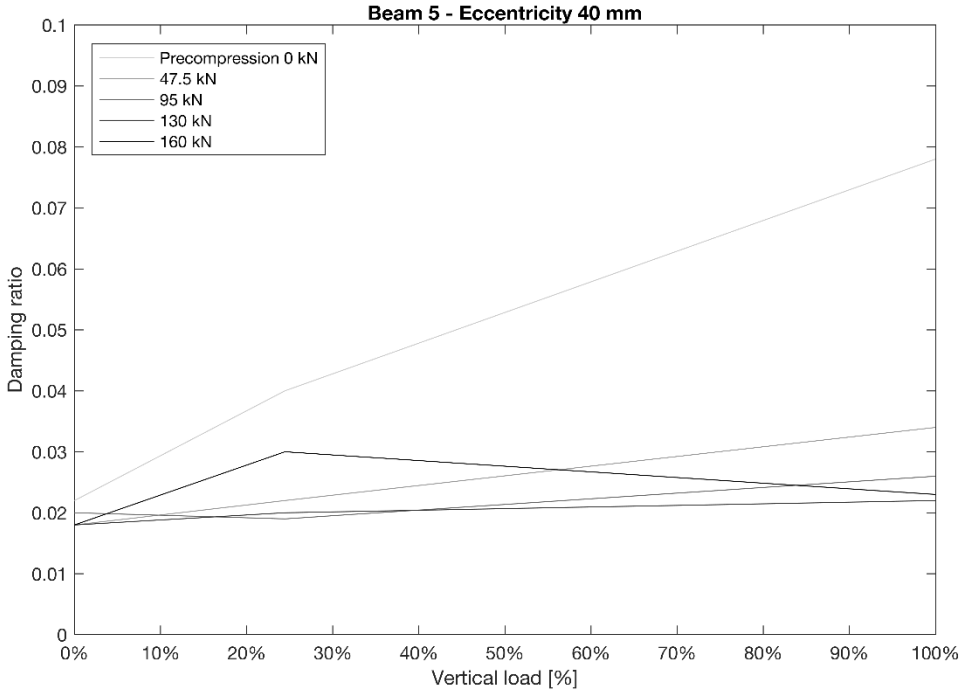

Figure 5.37 Beam 5: variation of damping ratio with increase of damage

Finally, the following figures show the variation of mode shapes, calculated through EFDD (enhanced frequency domain decomposition) for 4 modes:

1. First transversal mode (1T);
2. First vertical mode (1V);
3. Second transversal mode (2T);
4. Second vertical mode (2V).

The results are represented with respect to the theoretical mode shapes (dashed lines), in the hypothesis of perfect hinge restraints at the bearings.

Every picture represent the 5 prestressing levels for a single damage level. The code FxPy indicates that the measure is taken at damage phase “x” and prestressing level “y”.

The modal results are also summarized through the calculation of the MAC (modal assurance criterion), and the results are shown in Figure 5.38.

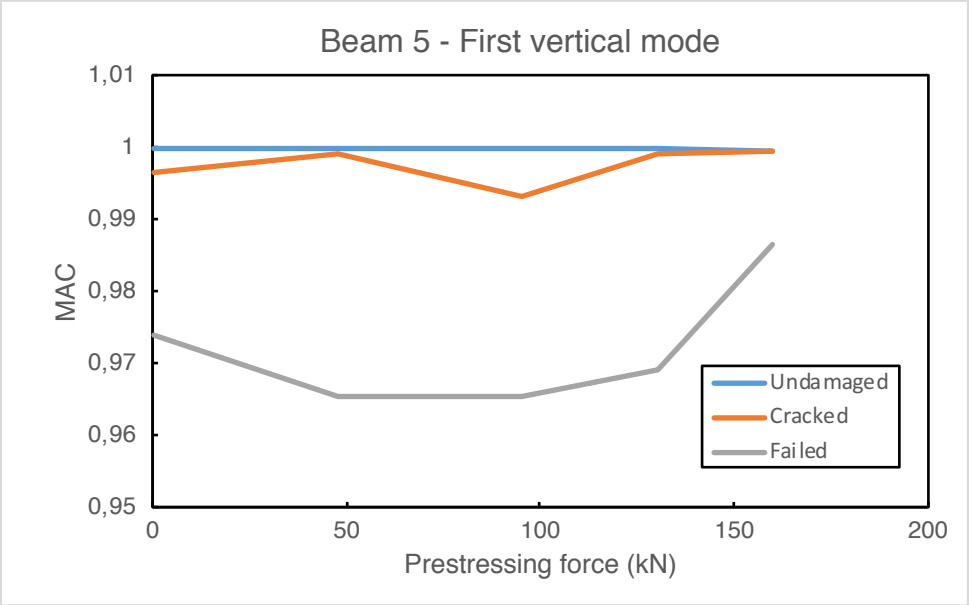

Figure 5.38: Beam 5. Variation of MAC

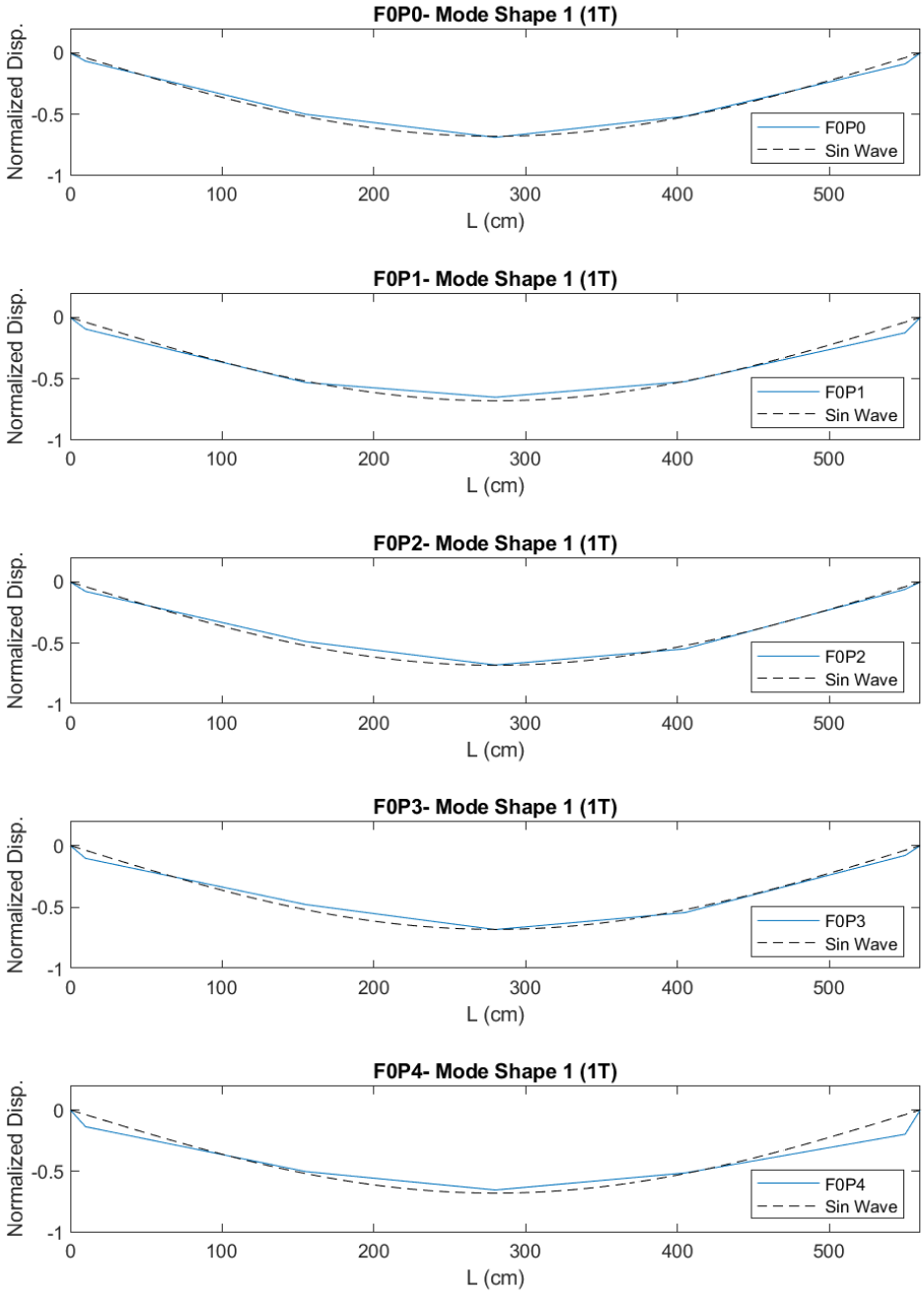

Figure 5.39: Beam 5. Variation of mode shapes for different prestressing levels. Undamaged beam, first transversal mode.

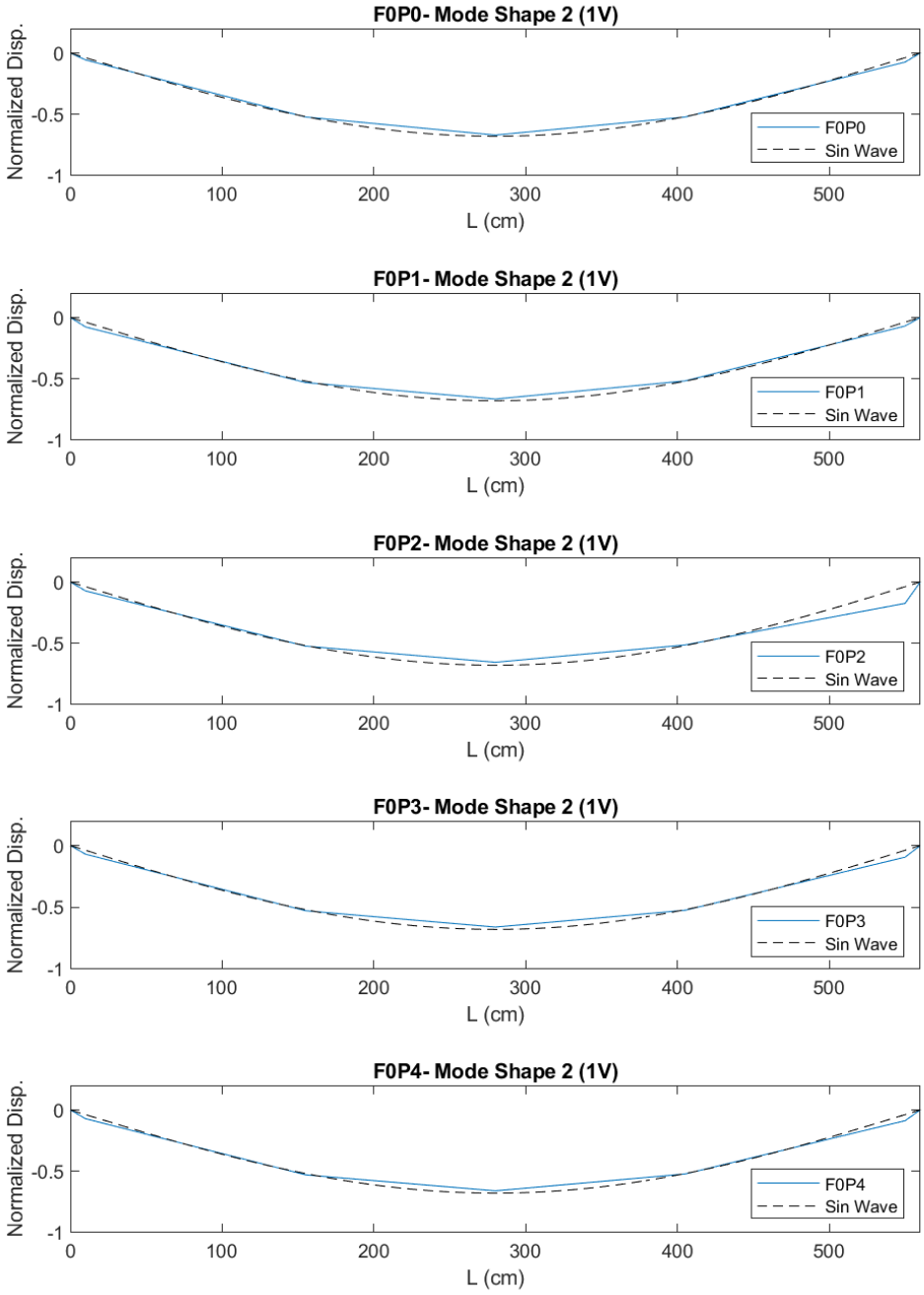

Figure 5.40: Beam 5. Variation of mode shapes for different prestressing levels. Undamaged beam, first vertical mode.

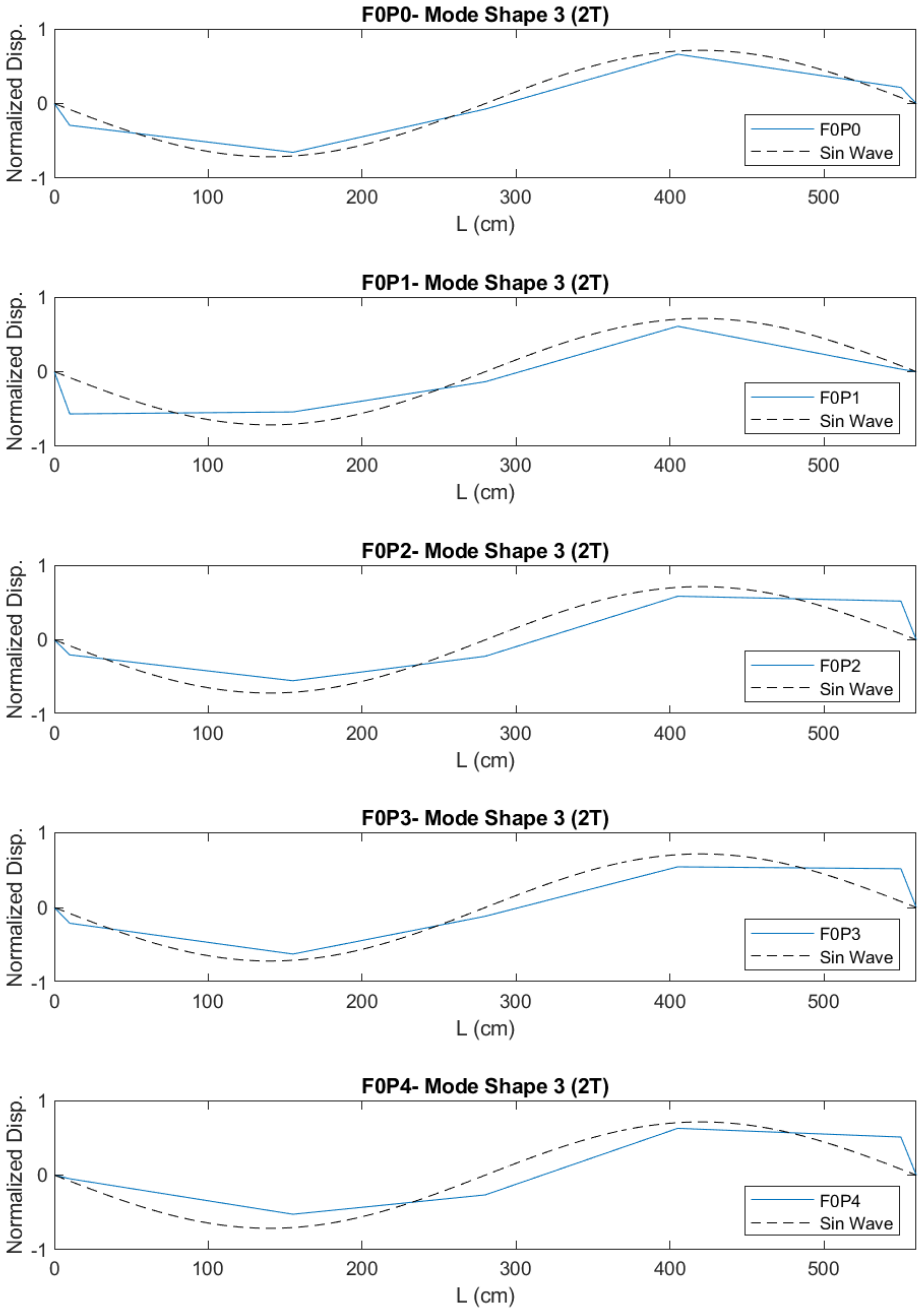

Figure 5.41: Beam 5. Variation of mode shapes for different prestressing levels. Undamaged beam, second transversal mode.

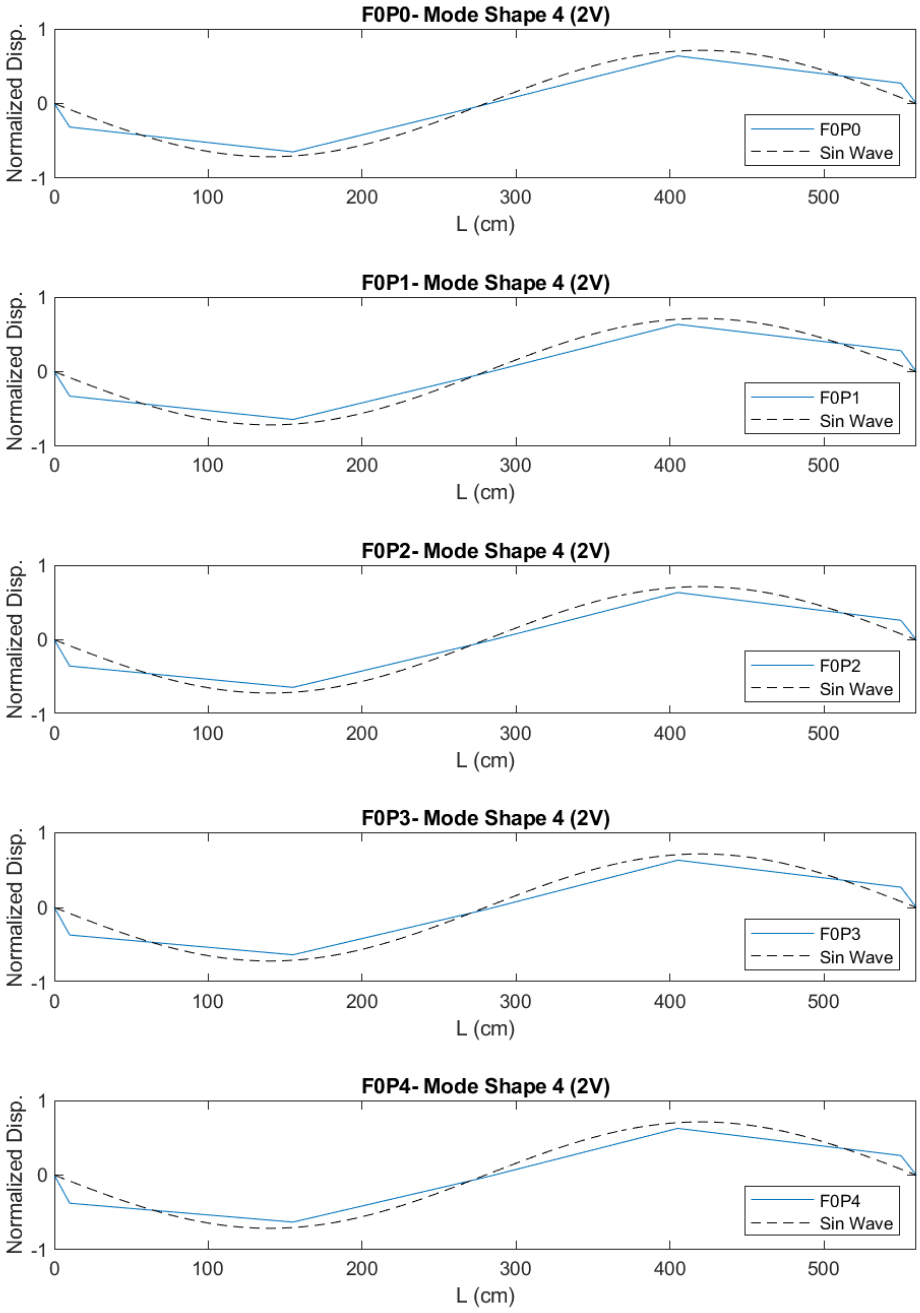

Figure 5.42: Beam 5. Variation of mode shapes for different prestressing levels. Undamaged beam, second vertical mode.

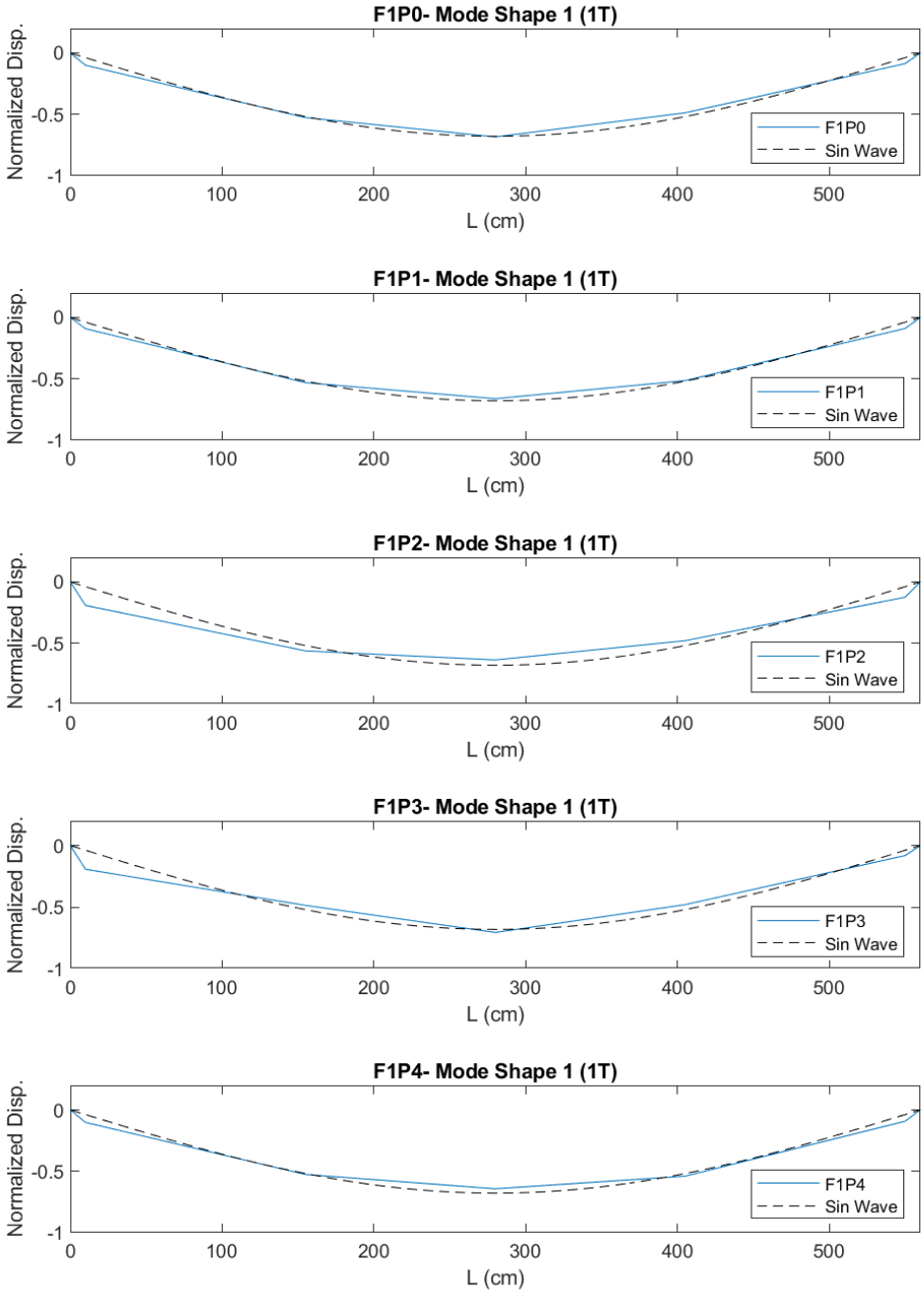

Figure 5.43: Beam 5. Variation of mode shapes for different prestressing levels. Cracked beam, first transversal mode.

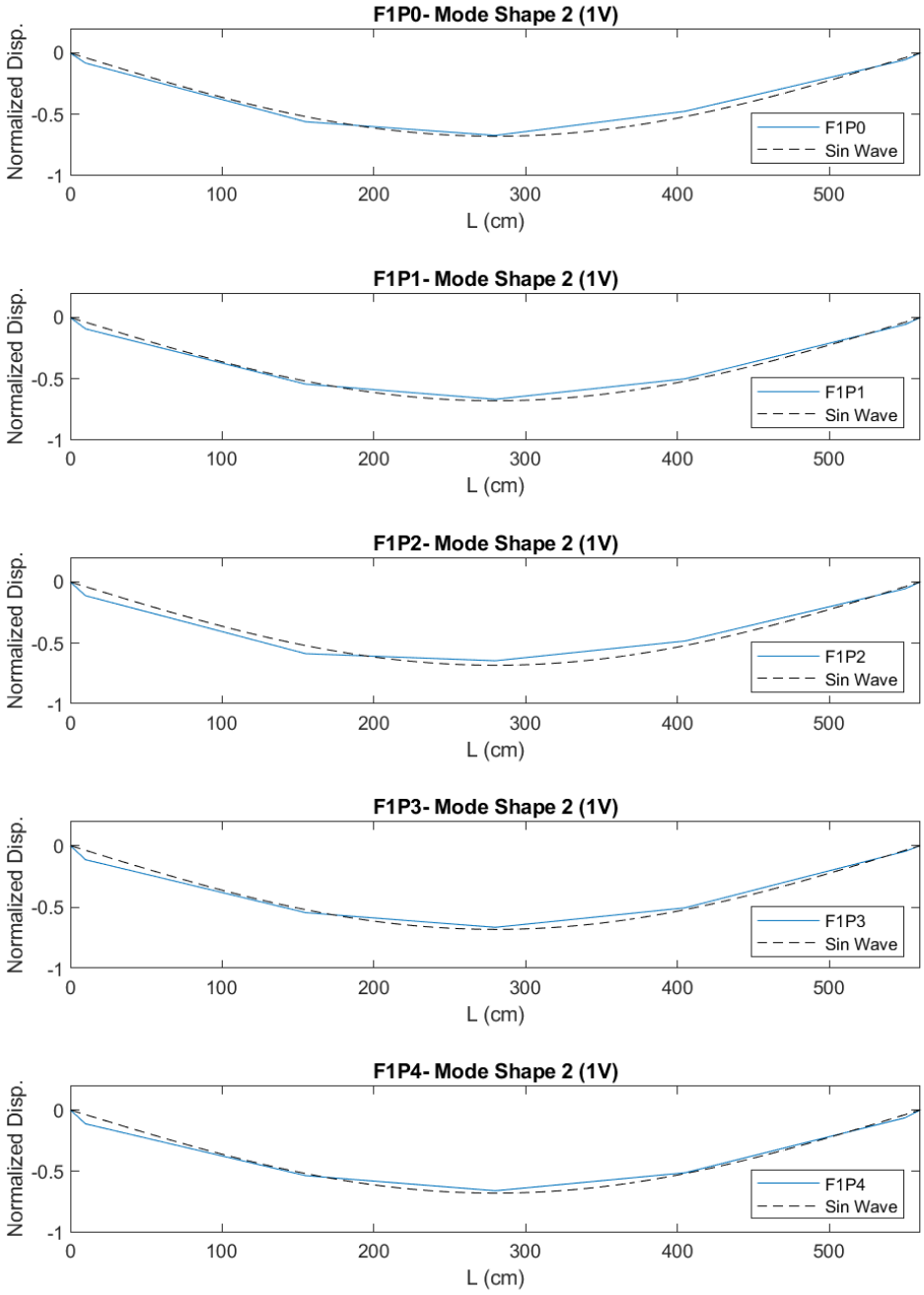

Figure 5.44: Beam 5. Variation of mode shapes for different prestressing levels. Cracked beam, first vertical mode.

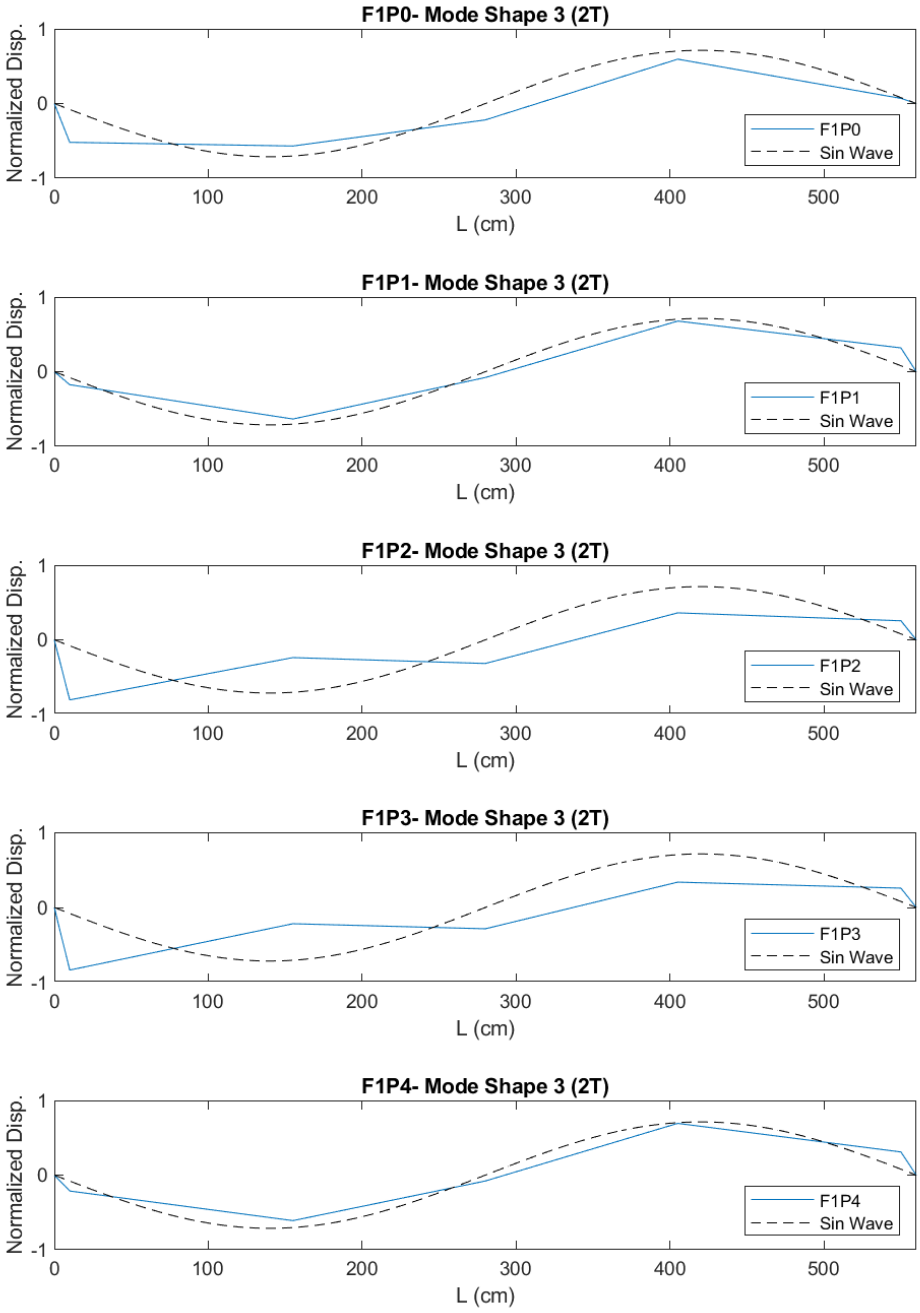

Figure 5.45: Beam 5. Variation of mode shapes for different prestressing levels. Cracked beam, second transversal mode.

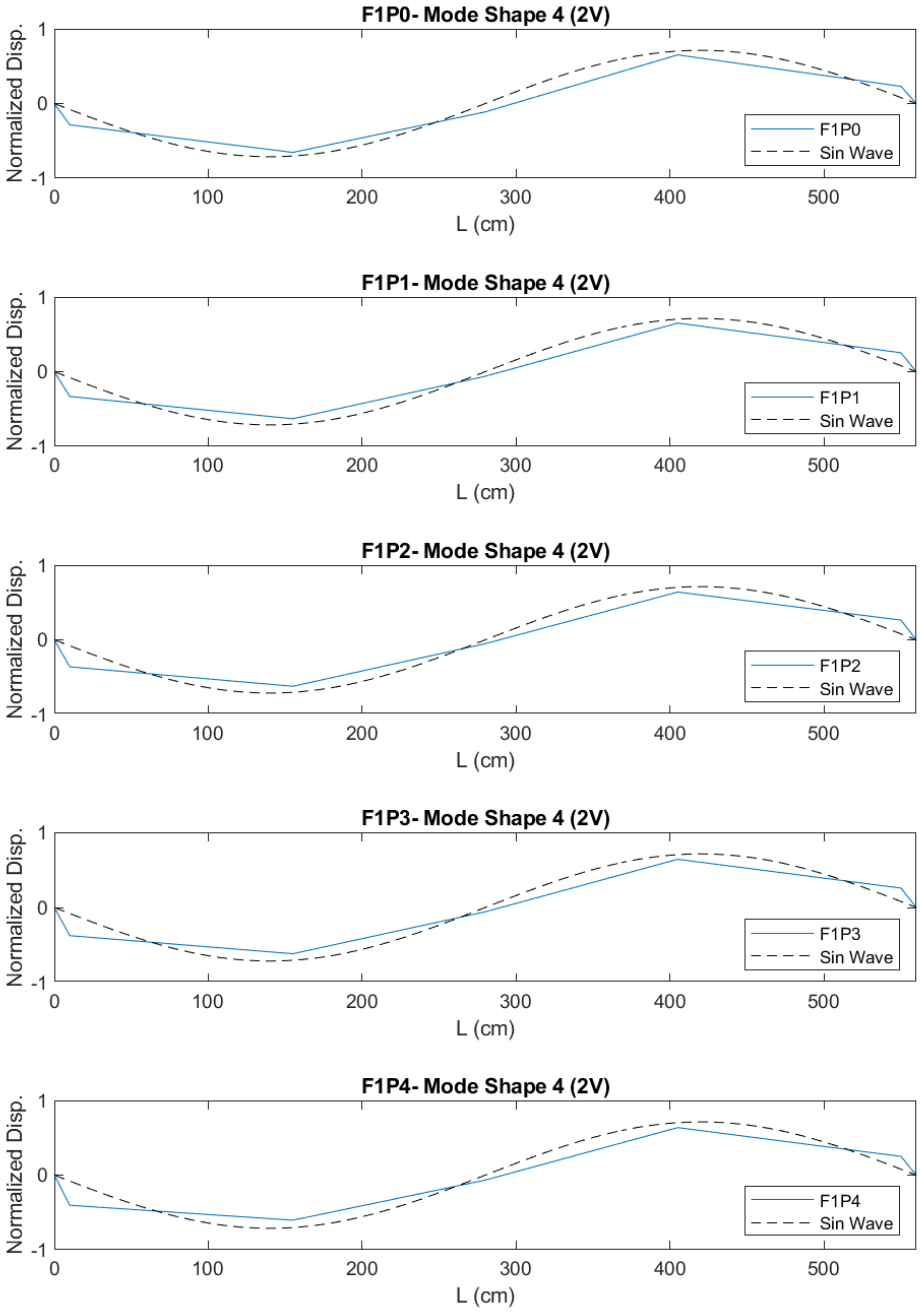

Figure 5.46: Beam 5. Variation of mode shapes for different prestressing levels. Cracked beam, second vertical mode.

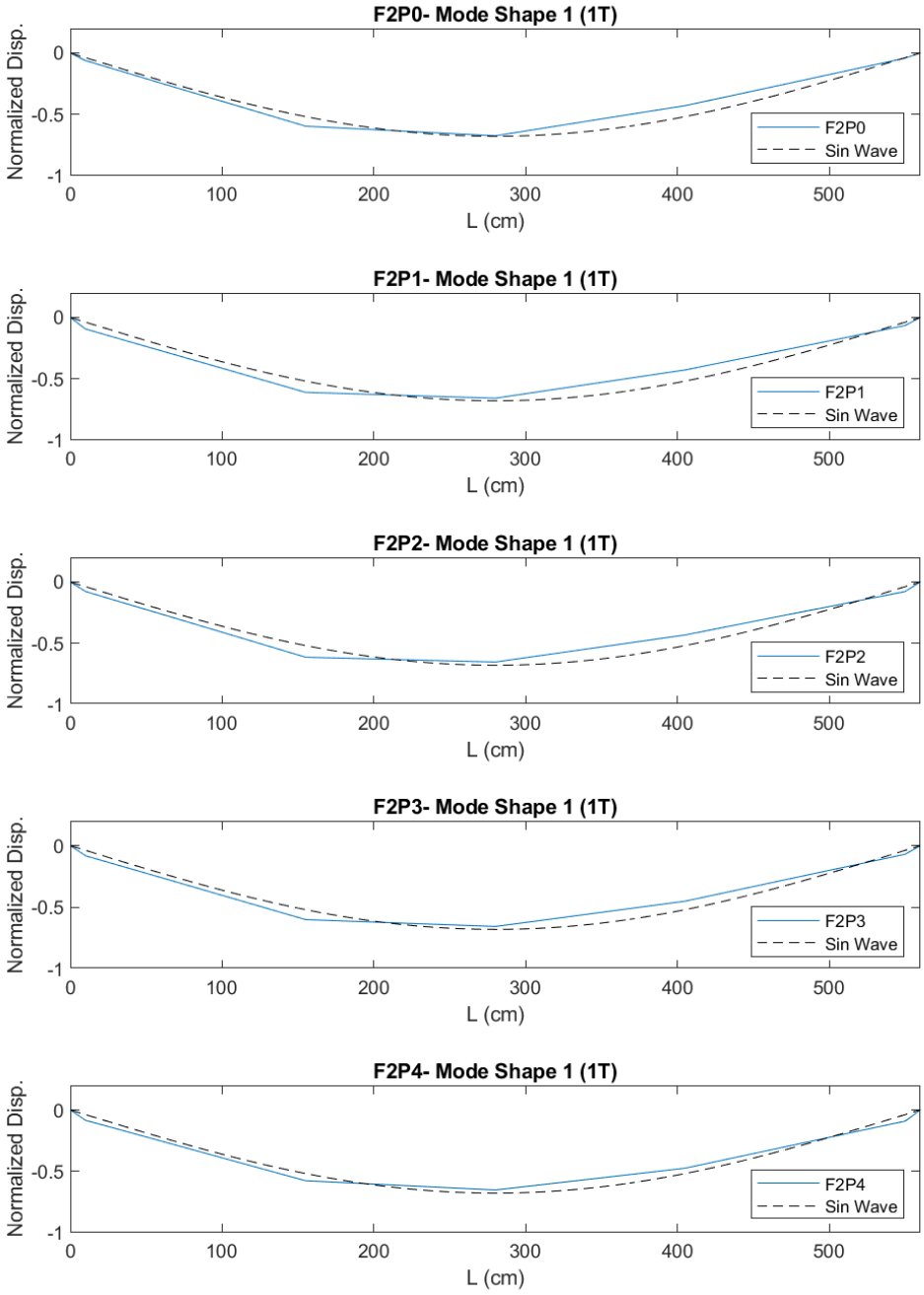

Figure 5.47: Beam 5. Variation of mode shapes for different prestressing levels. Failed beam, first transversal mode.

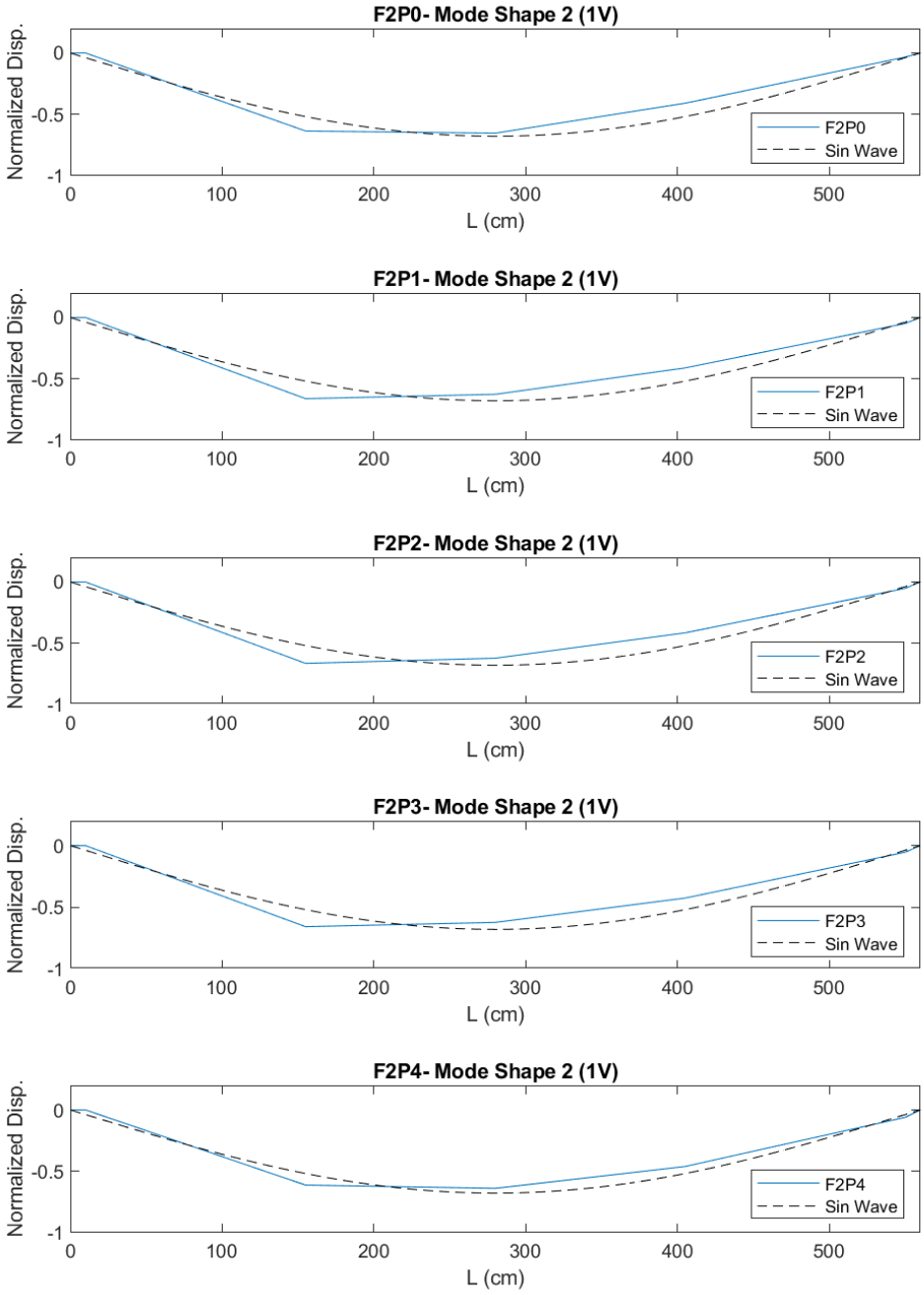

Figure 5.48: Beam 5. Variation of mode shapes for different prestressing levels. Failed beam, first vertical mode.

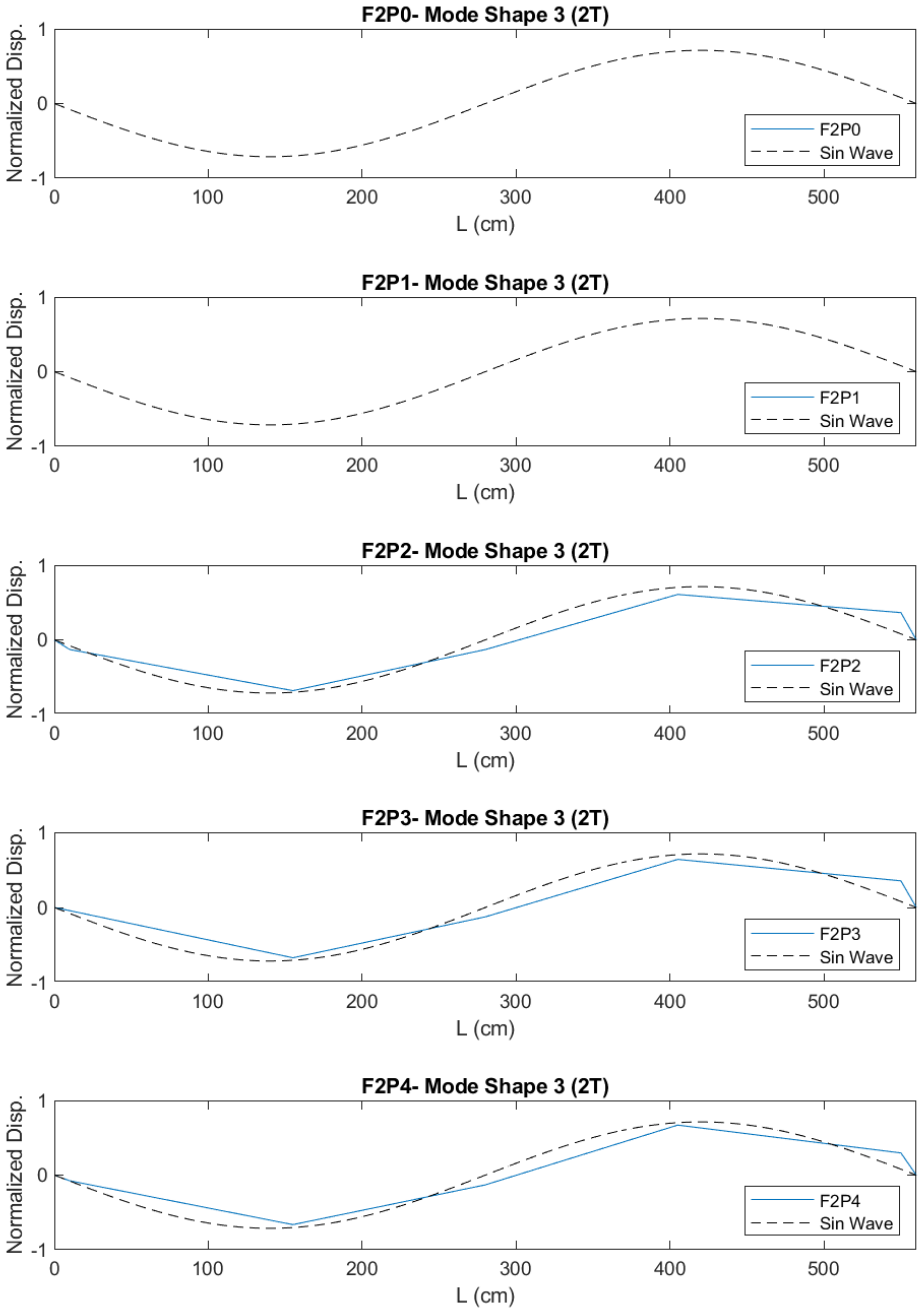

Figure 5.49: Beam 5. Variation of mode shapes for different prestressing levels. Failed beam, second transversal mode.

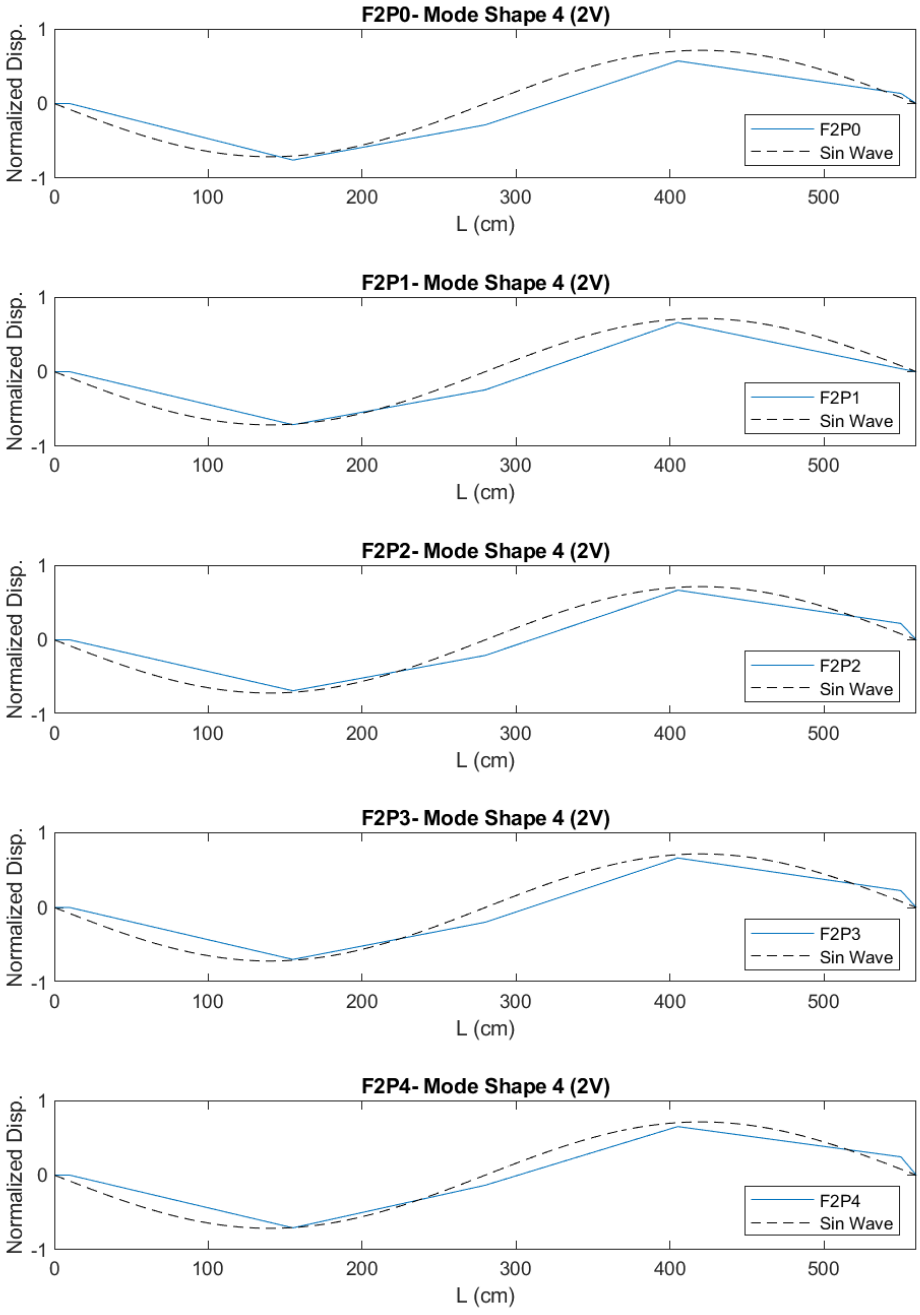

Figure 5.50: Beam 5. Variation of mode shapes for different prestressing levels. Failed beam, second vertical mode.

5.3.4 Beam 6

For each dynamic force applied to the beam, a data set is obtained containing all the responses of the accelerometers and of the hammer, as for the pre-stressed beams.

The calculation of natural frequencies is then made for the most significant impulse points (H4, H5 and H6).

The peaks of the FDD (Frequency Domain Decomposition) have been highlighted in correspondence with the first mode of vibration with the use of the Peak-Picking technique.

The following table shows the mean values of the frequencies for the various cycles which were then inserted into a graph: as expected, the frequency decreases with increasing damage, due to the presence of cracks that cause a loss in stiffness. It can be noted also as the variations in frequency are smaller for higher amount of prestressing; this is due to the effect of prestressing force of reduce the formation of cracking during the load, or close the existing cracks.

Table 42: Natural frequency values for the first mode for 5 different prestressing levels

Cycle	P0		P1		P2	
	f [Hz]	% Decrement	f [Hz]	% Decrement	f [Hz]	% Decrement
0	17,28	100,00%	17,37	100,00%	17,03	100,00%
1	15,54	89,96%	16,27	93,62%	16,66	97,81%
2	9,82	56,84%	10,55	60,73%	12,67	74,41%

Cycle	P3		P4	
	f [Hz]	% Decrement	f [Hz]	% Decrement
0	17,03	100,00%	17,03	100,00%
1	16,78	98,58%	16,86	99,00%
2	14,45	84,86%	14,78	86,75%

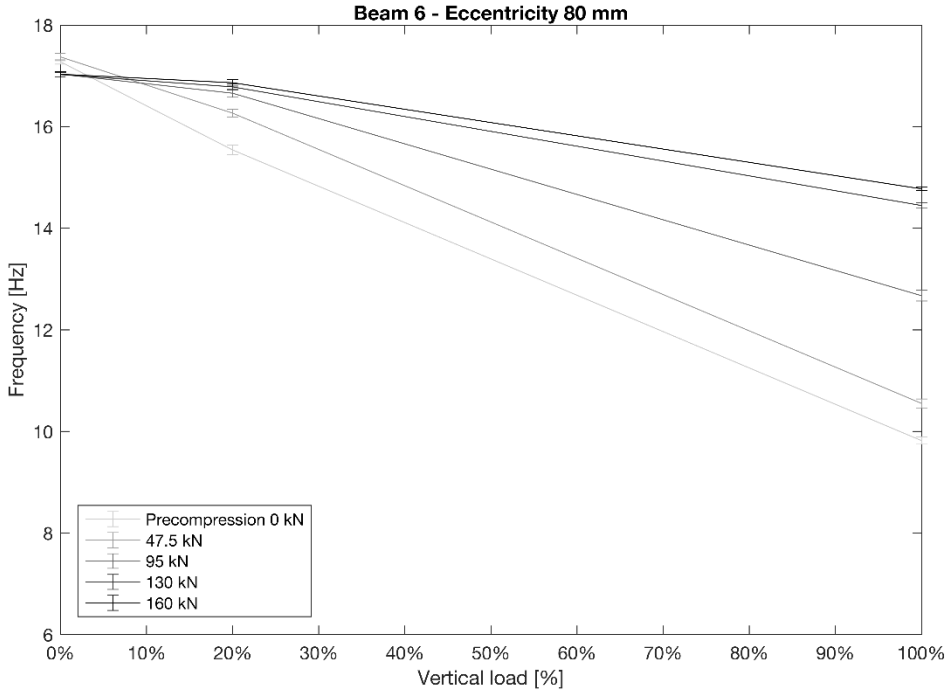

Figure 5.51 Frequency variation as function of the beam load (%)

Knowing the frequency values, a fitting procedure was developed in order to identify the damping ratio based on time histories. The procedure is the same described for Beam 4.

The results, in term of variation of damping ratio, are summarized in the following table e figure. As expected, the damping ratio increases with the increase of damage. Moreover, the variations in frequency are smaller for higher amount of prestressing; as for frequencies, this is due to the effect of prestressing force of reduce the formation of cracking during the load, or close the existing cracks.

Table 43: Beam 6: identified damping ratios

Cycle	P0	P1	P2	P3	P4
	ξ	ξ	ξ	ξ	ξ
0	0,00529	0,00544	0,00419	0,00417	0,00419
1	0,01036	0,00551	0,00445	0,00424	0,00407
2	0,01811	0,01294	0,00800	0,00750	0,00624

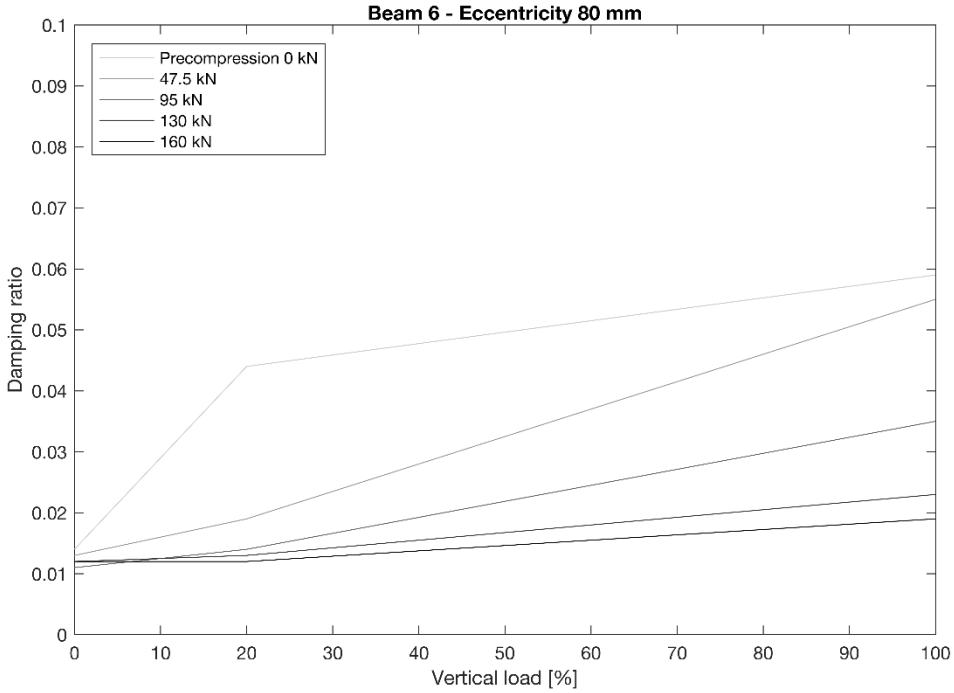

Figure 5.52 Beam 6: variation of damping ratio with increase of damage

Finally, the following figures show the variation of mode shapes, calculated through EFDD (enhanced frequency domain decomposition) for 4 modes:

1. First transversal mode (1T);
2. First vertical mode (1V);
3. Second transversal mode (2T);
4. Second vertical mode (2V).

The results are represented with respect to the theoretical mode shapes (dashed lines), in the hypothesis of perfect hinge restraints at the bearings.

Every picture represent the 5 prestressing levels for a single damage level. The code FxPy indicates that the measure is taken at damage phase “x” and prestressing level “y”.

The modal results are also summarized through the calculation of the MAC (modal assurance criterion), and the results are shown in Figure 5.53.

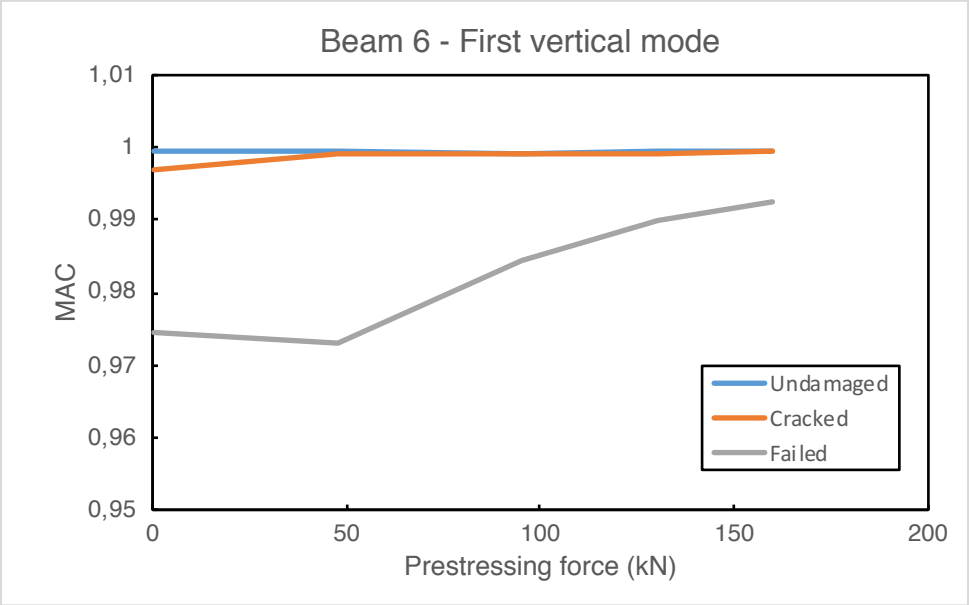

Figure 5.53: Beam 6. Variation of MAC

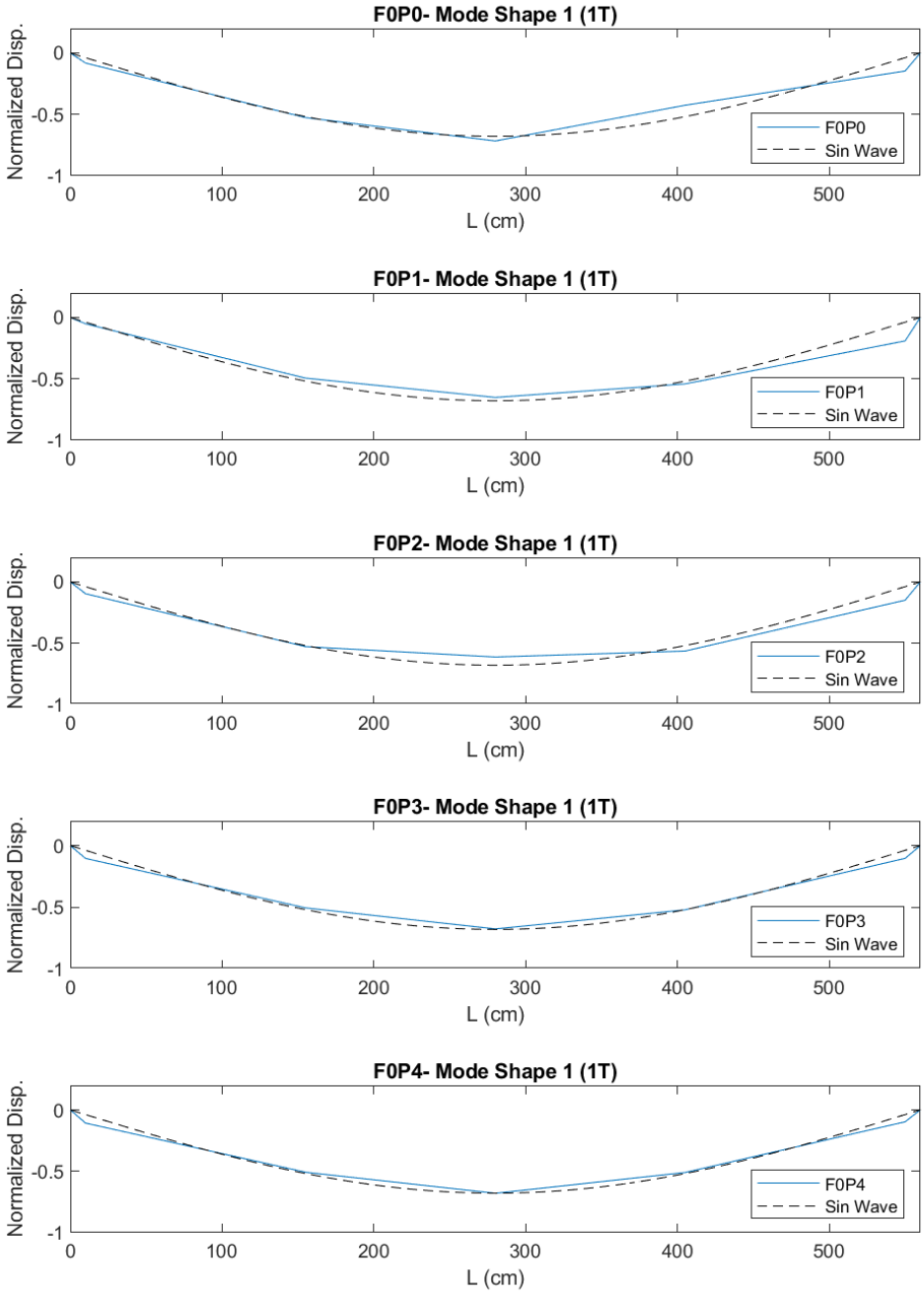

Figure 5.54: Beam 6. Variation of mode shapes for different prestressing levels. Undamaged beam, first transversal mode.

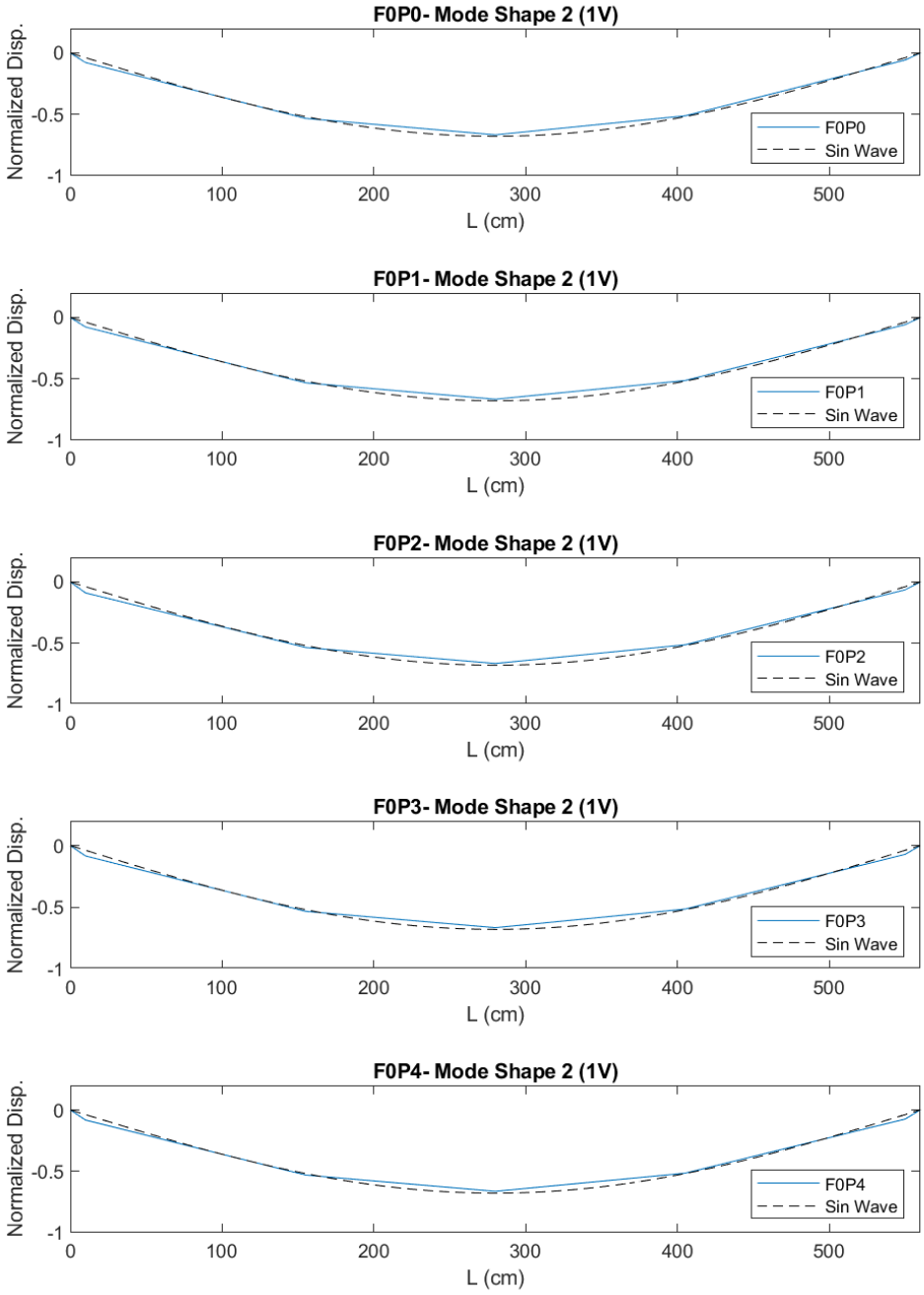

Figure 5.55: Beam 6. Variation of mode shapes for different prestressing levels. Undamaged beam, first vertical mode.

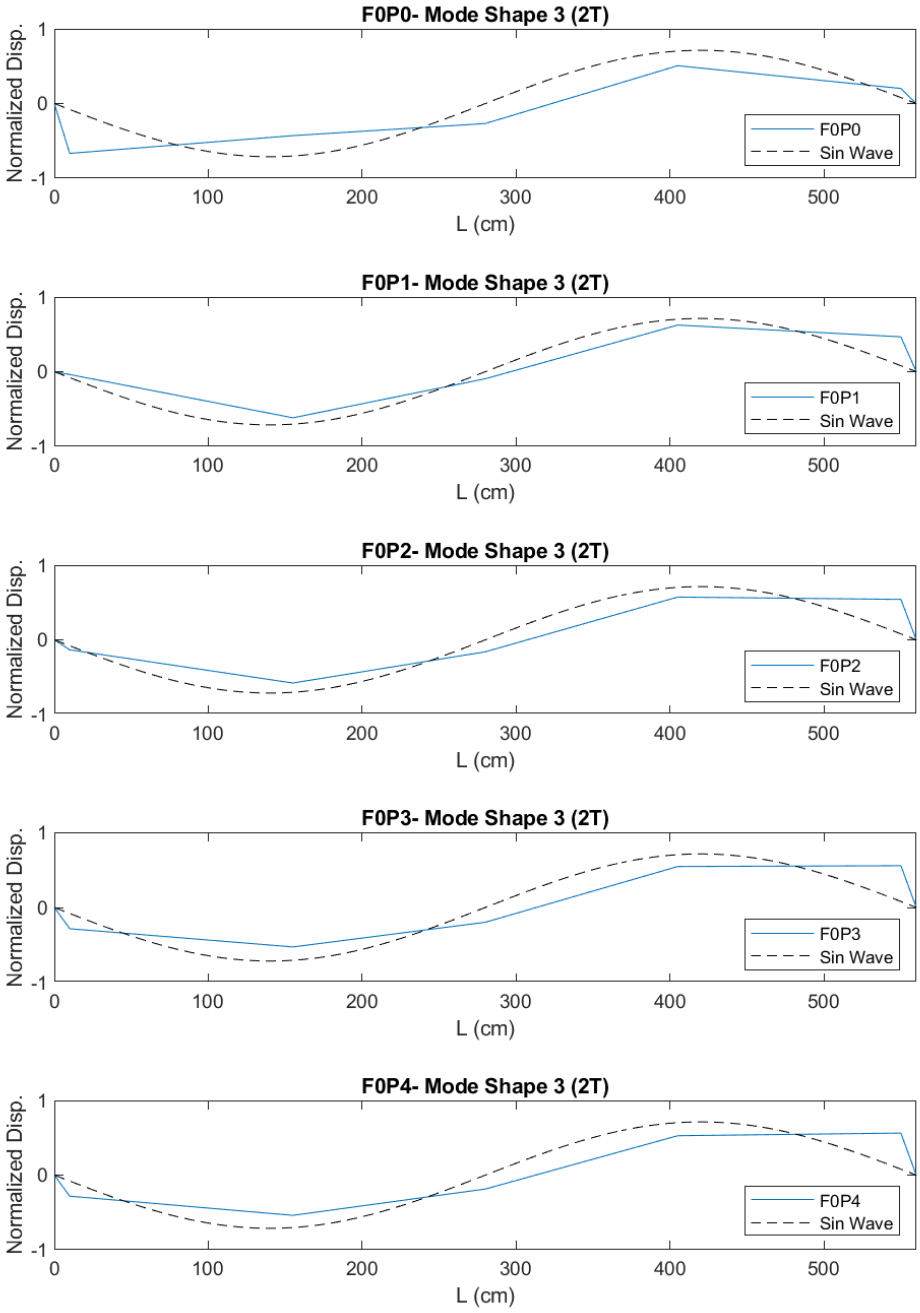

Figure 5.56: Beam 6. Variation of mode shapes for different prestressing levels. Undamaged beam, second transversal mode.

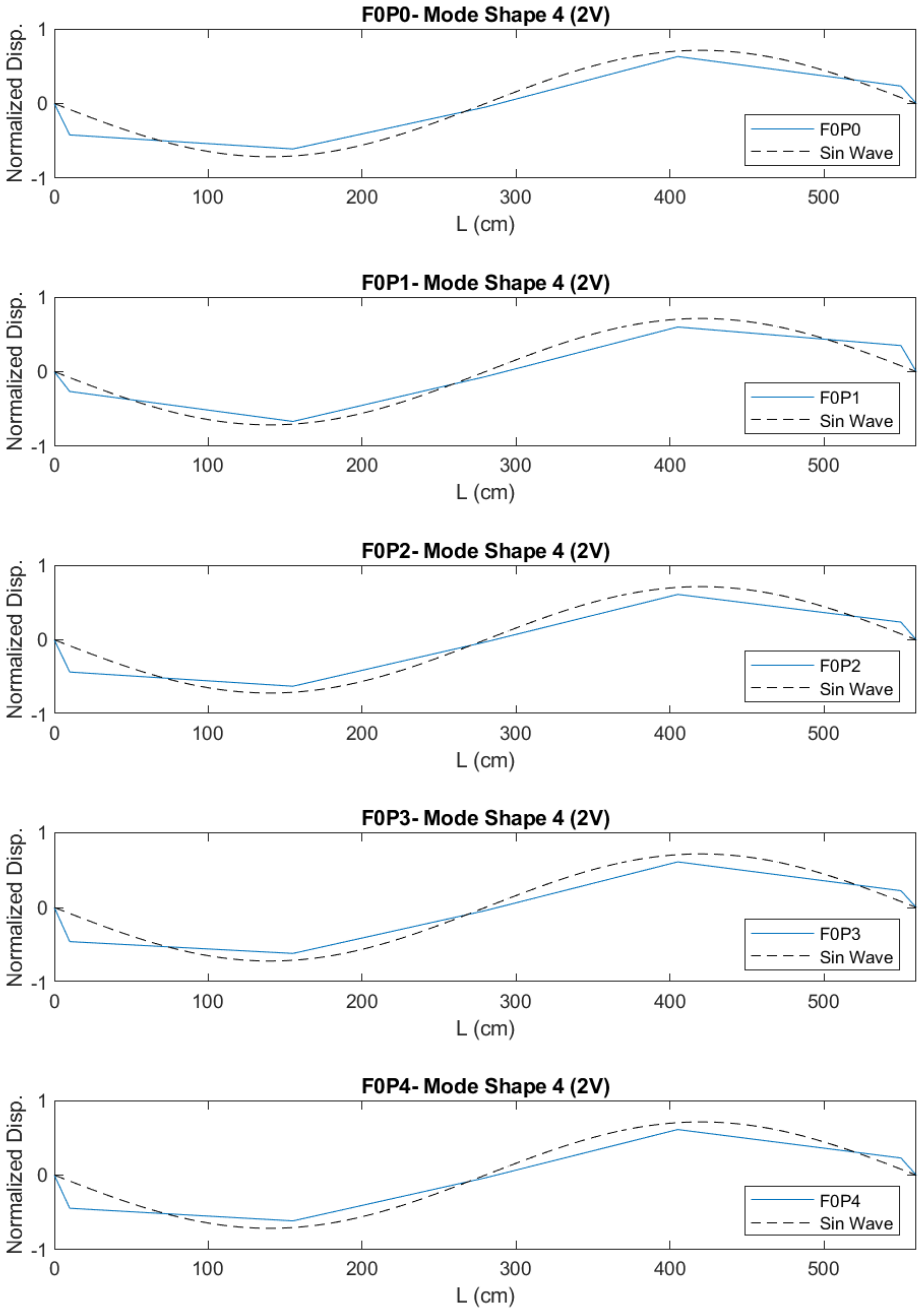

Figure 5.57: Beam 6. Variation of mode shapes for different prestressing levels. Undamaged beam, second vertical mode.

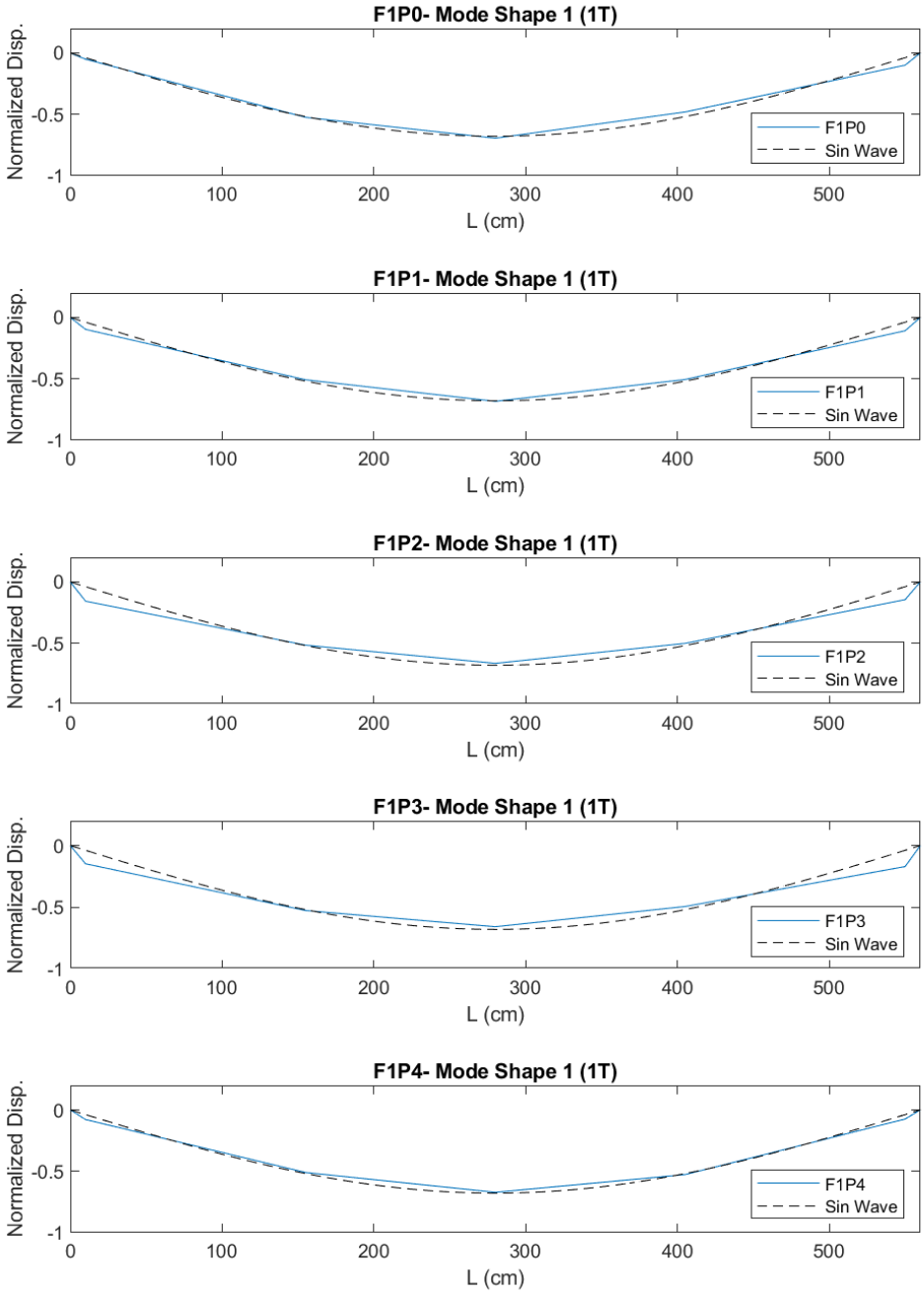

Figure 5.58: Beam 6. Variation of mode shapes for different prestressing levels. Cracked beam, first transversal mode.

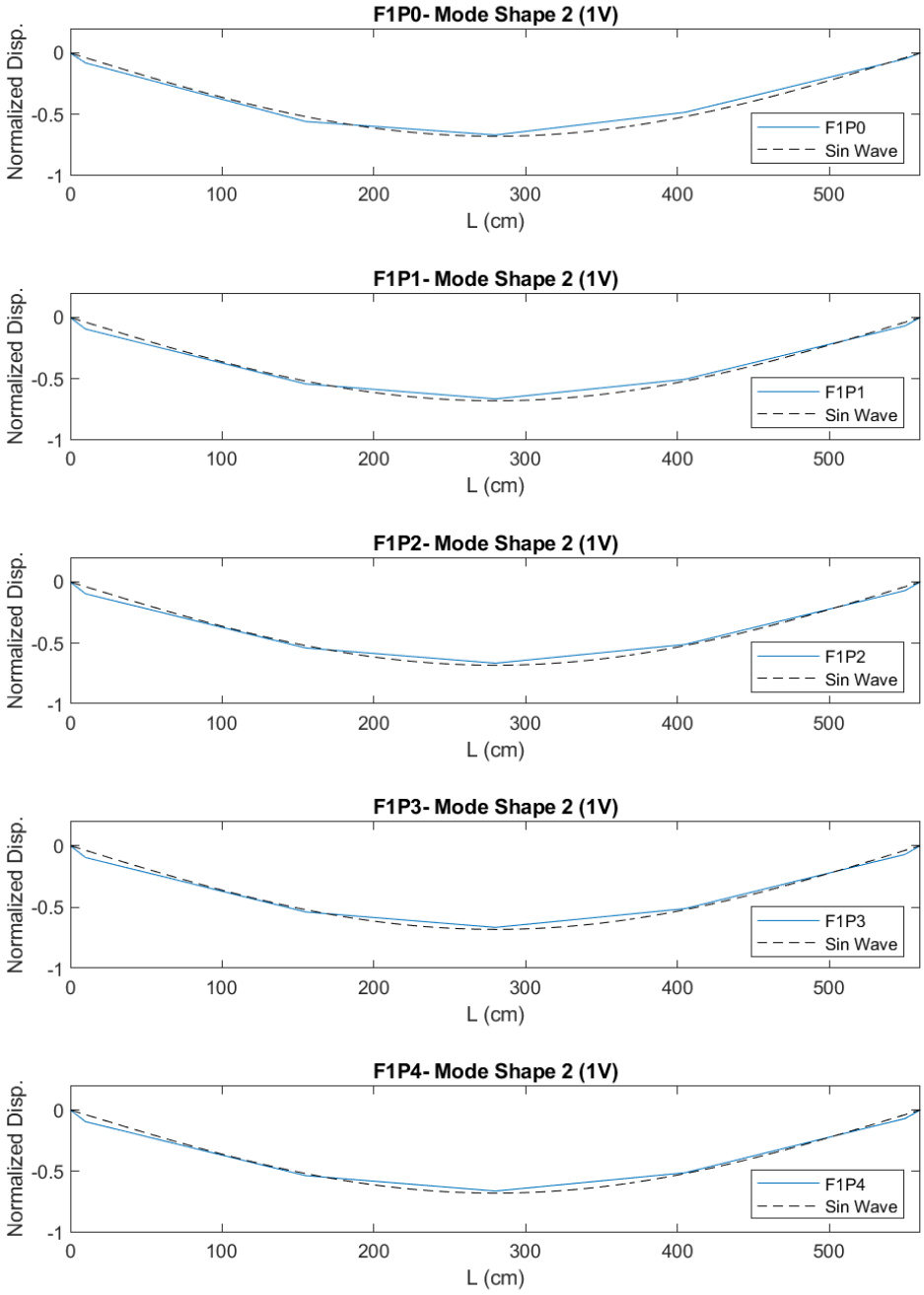

Figure 5.59: Beam 6. Variation of mode shapes for different prestressing levels. Cracked beam, first vertical mode.

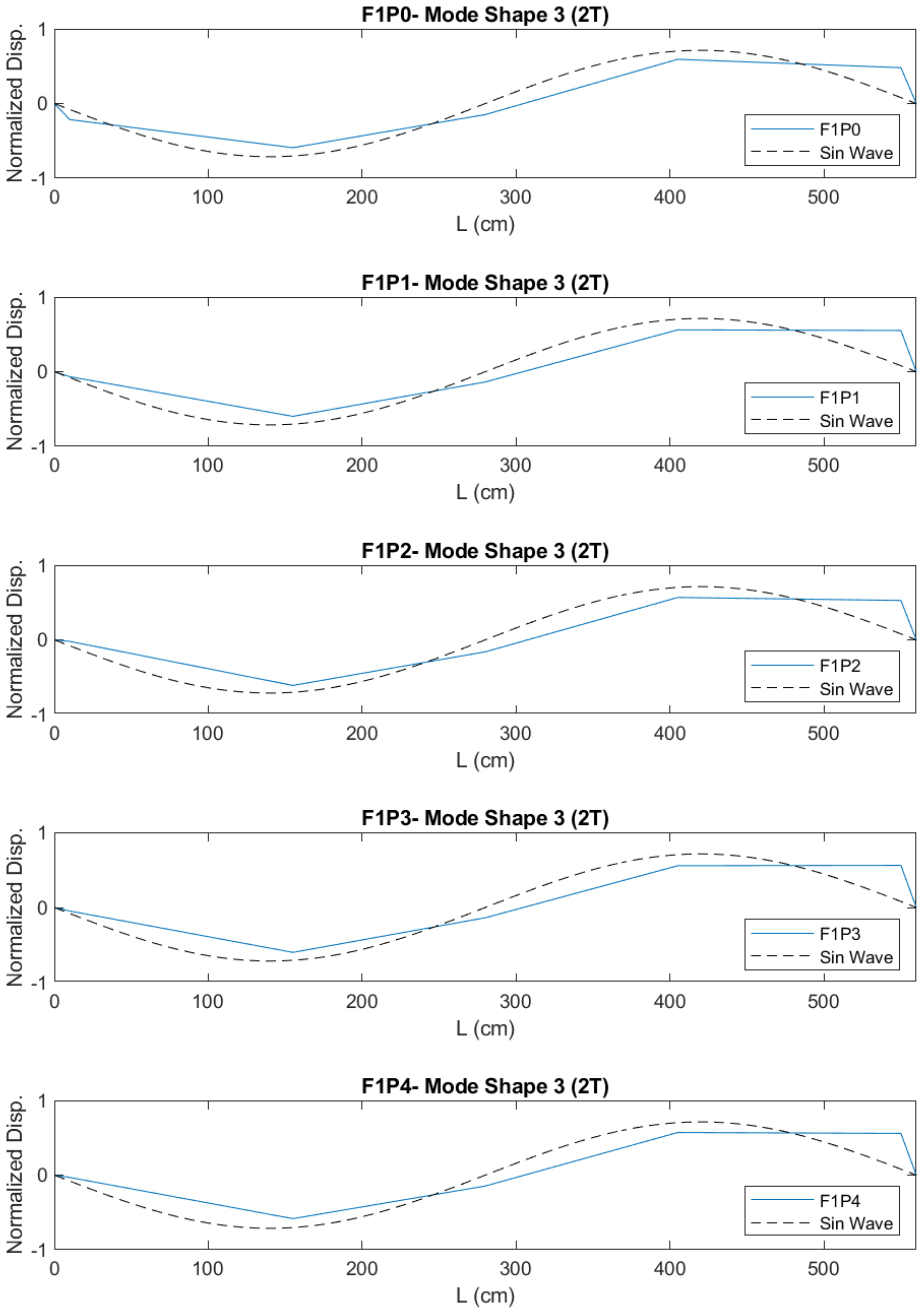

Figure 5.60: Beam 6. Variation of mode shapes for different prestressing levels. Cracked beam, second transversal mode.

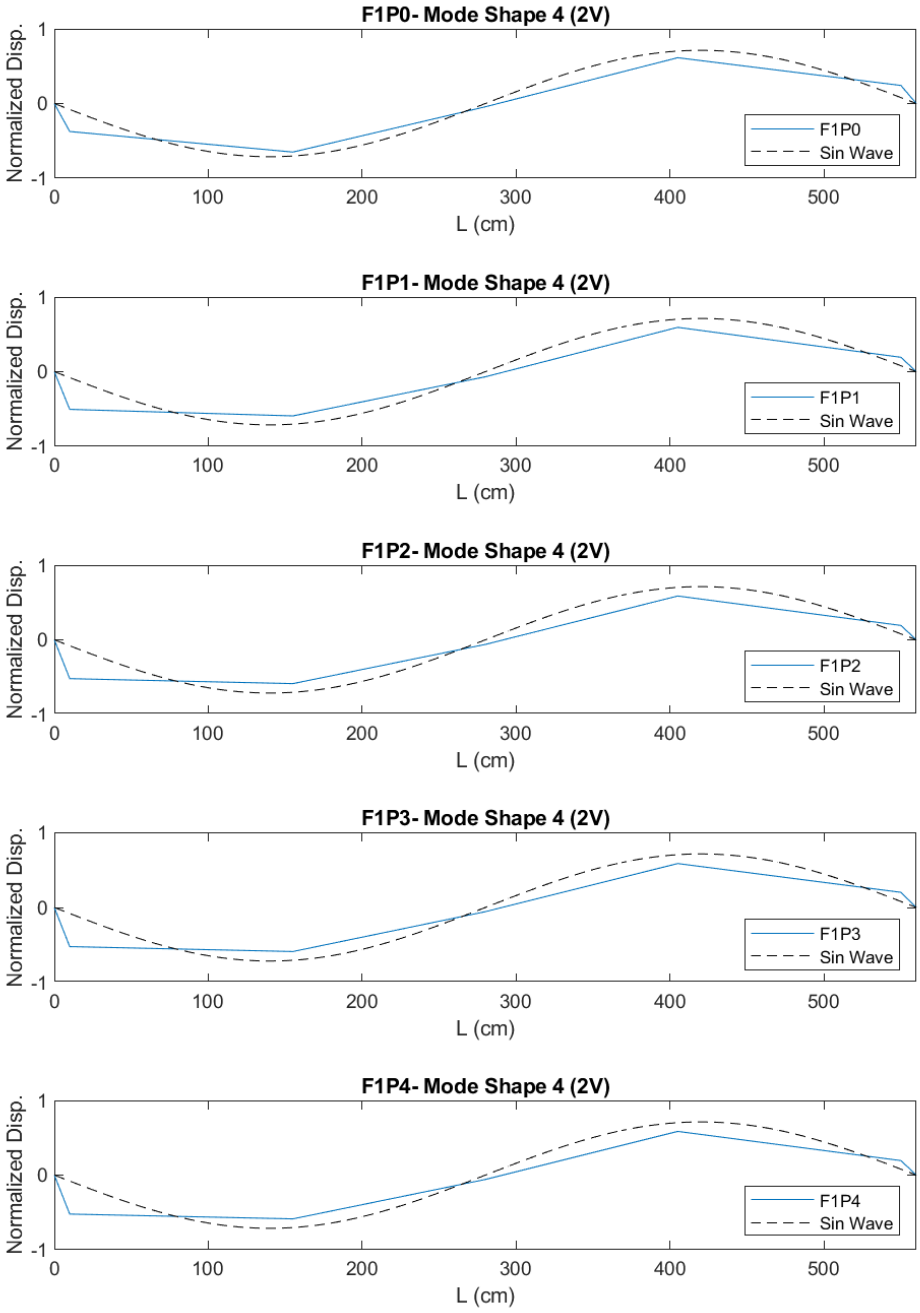

Figure 5.61: Beam 6. Variation of mode shapes for different prestressing levels. Cracked beam, second vertical mode.

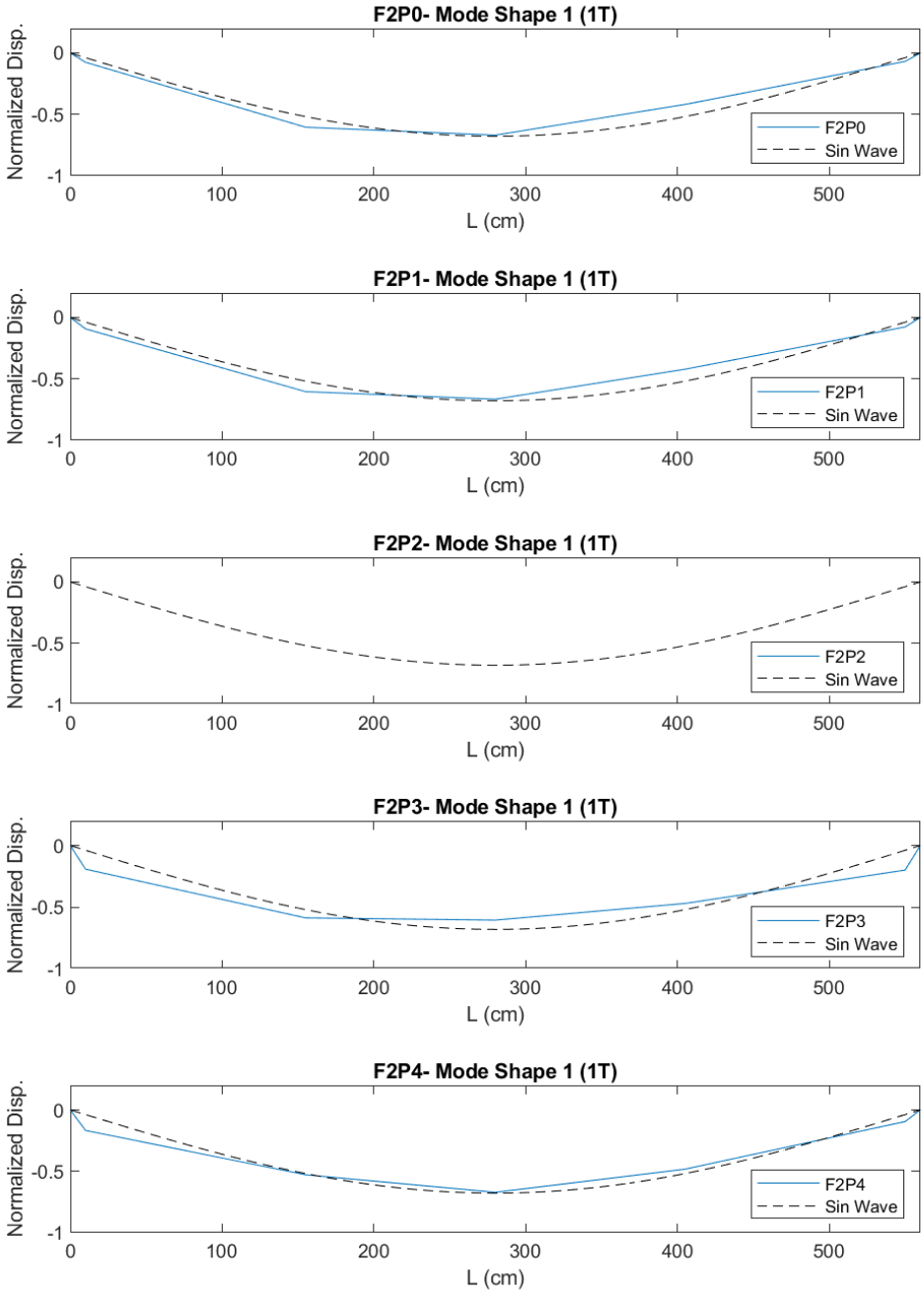

Figure 5.62: Beam 6. Variation of mode shapes for different prestressing levels. Failed beam, first transversal mode.

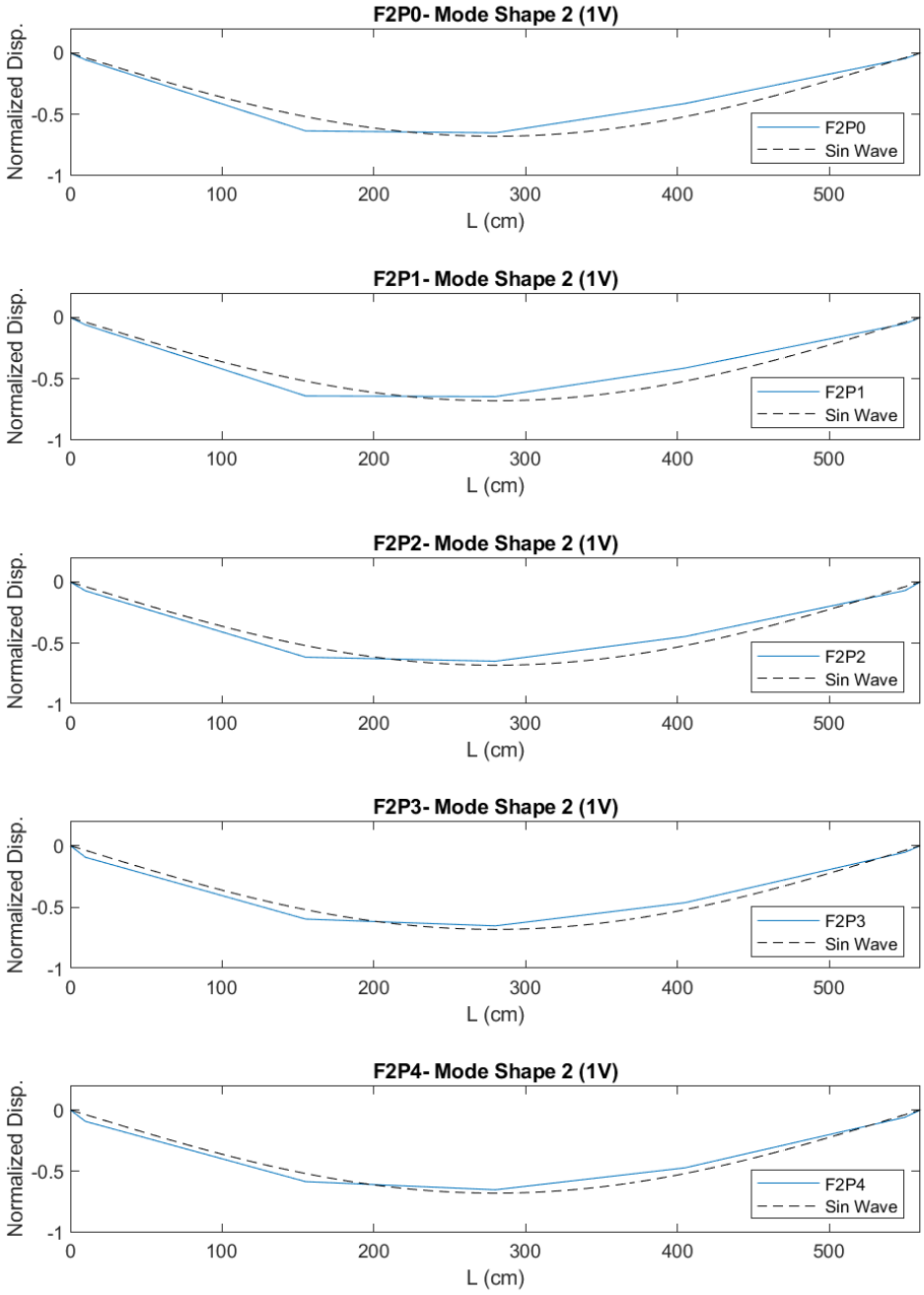

Figure 5.63: Beam 6. Variation of mode shapes for different prestressing levels. Failed beam, first vertical mode.

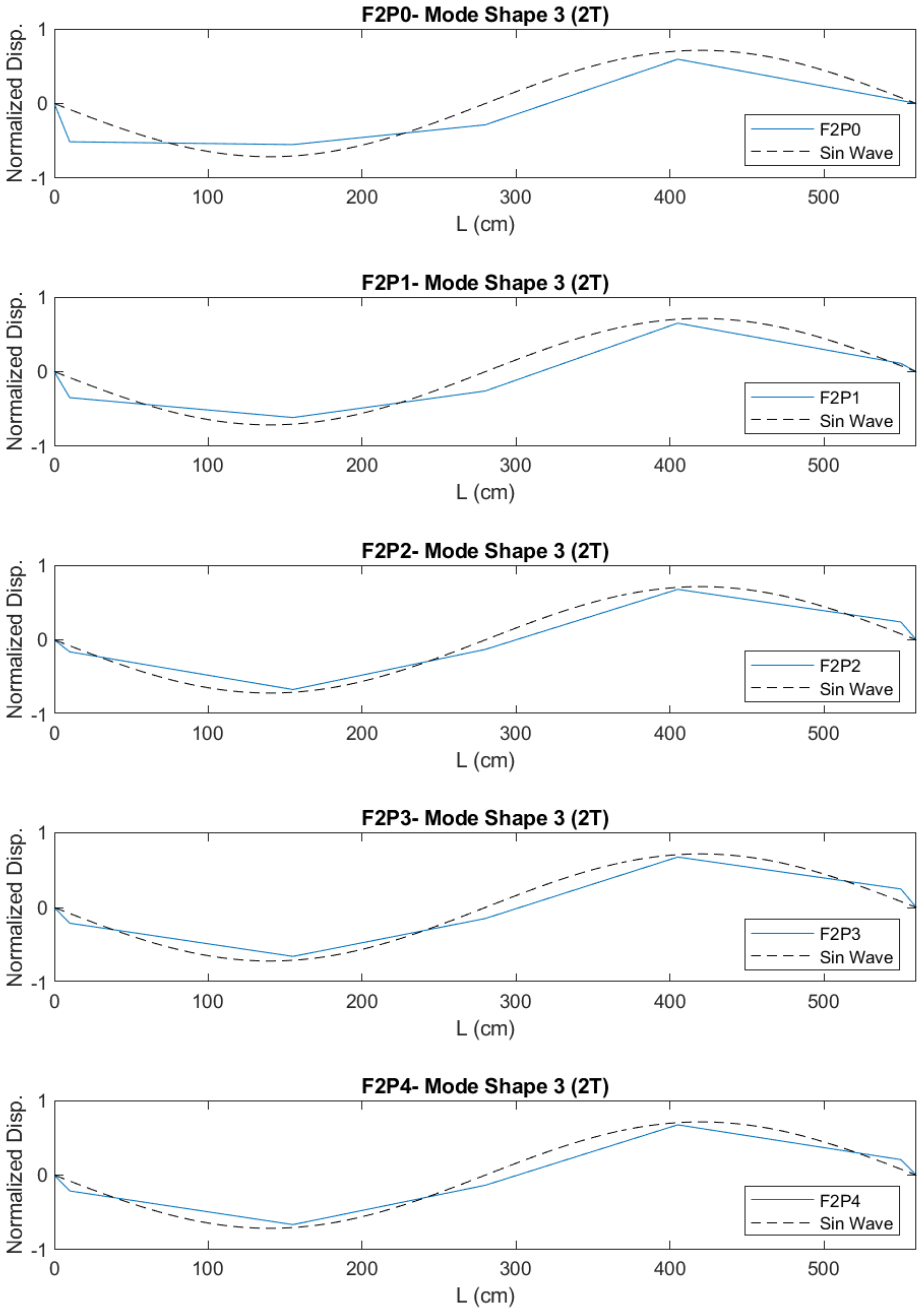

Figure 5.64: Beam 6. Variation of mode shapes for different prestressing levels. Failed beam, second transversal mode.

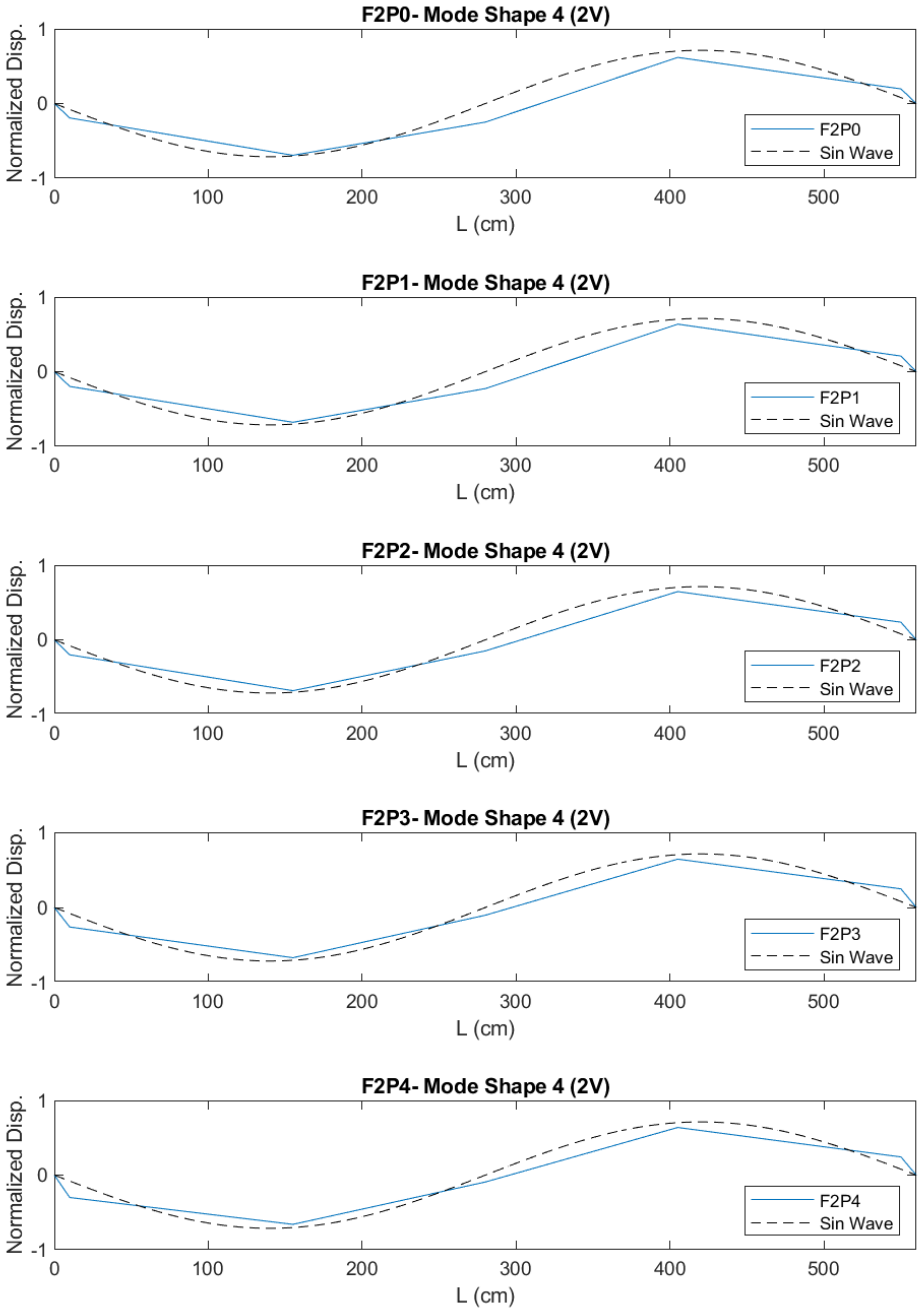

Figure 5.65: Beam 6. Variation of mode shapes for different prestressing levels. Failed beam, second vertical mode.

5.3.5 Variation of damping with prestressing level

Figure 5.66 and Figure 5.67 plot the variation of damping ratio with the prestressing force, respectively for Beams 5 and 6. Beam 4 is not represented for the same reason cited above. In those figures, different colors represent the three (increasing) vertical loading stage used: undamaged beam (blue line), cracked beam (orange line) and failed beam (grey line).

Results show that the values of damping ratio show a general decrease with the increase of prestressing level, while they increase with damage. Moreover, when prestressing force reaches that limit triggering cracks closure, the values of damping drastically fall close to those values characterizing uncracked condition. This tendency seems to confirm the localization of most of the damping phenomena in correspondence to the crack occurrence; the presence of the precompression, in this terms, closes the cracks and reduces the damping. However, this could represent a possible limitation in the use of damping in undamaged or slightly damaged structures, where the change in prestressing could not give a perceptible variation in damping.

Finally, with the increase of damage an increase in data dispersion is observed. Therefore the damping results in the case of widely damaged beams need to be assessed very carefully.

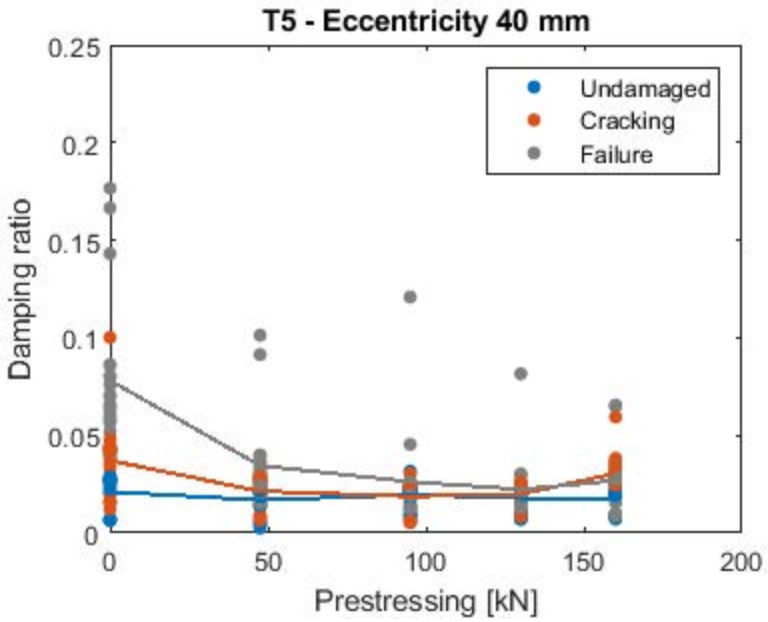

Figure 5.66 Beam 5: variation of damping ratio with prestressing force

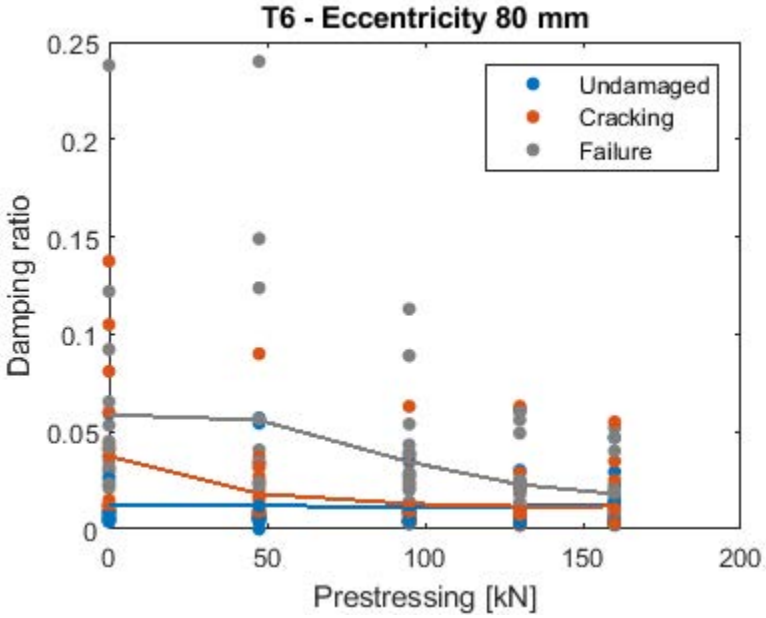

Figure 5.67 Beam 6: variation of damping ratio with prestressing force

6 Considerations regarding residual prestressing identification

The tests conducted on the beams subject to increasing vertical loads (i.e., at different damage conditions) and different level of prestressing force, showed how non-destructive parameters like fundamental frequencies, damping ratio and ultrasonic velocity are influenced by both of the above mentioned parameters. However, while the correlation between damage and fundamental frequency variation is widely recognized in literature, few models can be found that investigate the change in non-destructive parameters with the variation of prestressing force, and most of them do not provide converging results. As discussed in Section 2, vibration-based methods have been criticized for varying reasons, the main is that the variation of such parameters is few perceivable for limited prestressing losses, and this occurs only when concrete cracking is advanced.

For this reason, a procedure is proposed based on the analytical model shown at Eq.2 for the first vibration frequency), that makes use of only NDT results in order to identify the prestressing level of the beams: this approach gives the advantage of being exploitable for practical applications, where static parameters are usually unknown. The procedure can be summarized as it follows:

a) The fundamental frequencies were measured, at each damage level and at each precompression level, with the use of FDD or PSD;
b) The values of the flexural stiffness *EI* utilized in Eq.2 are calculated not in terms of static parameters, but with the use of non-destructive data only. The Young Modulus is calculated through the estimation of the average ultrasonic velocity *v*, for all the signals at the same precompression level, with the well-known formula:

$$E = \frac{(1+\nu)(1-2\nu)}{(1-\nu)}\rho v^2 \qquad (59)$$

where ρ is the density and ν is the Poisson modulus of the concrete material.

c) Regarding the inertia, it was calculated based on theoretical formulas only, i.e. avoiding the use of knowledge on concrete strain obtained with DD1s, and thus on the neutral axis position at each relevant beam section. Hence, with the aim to obtain the global inertia of the section I_g, the portion of the beam subject to cracking was estimated, which was considered as made by partialized reacting sections:

$$I_g = \frac{(L-L_{crack})}{L} I_0 + \frac{L_{crack}}{L} I_C \qquad (60)$$

In the previous Equation,, L_{crack} is the length over which flexural cracking is expected to occur, L is the overall length of the beam, I_o is the inertia of the full reacting (not cracked) section and I_c is the partialized (cracked) section. The ratio L_{crack}/L can be

estimated with a detailed visual inspection of the beam, in order to detect the quantity and distance between existing cracks. Alternatively, the map of the ultrasonic pulse velocity values (or better, using the attenuation of the ultrasonic signal) recorded along the element can be used to estimate where cracking phenomena occur;

d) The theoretical fundamental frequencies are calculated with Eq.2, and compared to the measured frequencies. The amount of prestressing force is then assessed by finding the value that best fits with measured data.

The procedure can be summarized in the following equation, that is equivalent to Eq. 2:

$$f_{estimated} = \frac{\pi}{2L^2}\sqrt{\frac{E_{ultrasonic} I_{visual}}{m}\left(1 - \frac{N}{N_{cr}}\right)} \tag{61}$$

Where $E_{ultrasonic}$ indicates the elastic modulus estimated based on the ultrasonic tests, I_{visual} expresses the cracked inertia based on visual inspection, and $f_{estimated}$ is the estimated frequency.

Figure 6.1 resumes the results for Beams 1, 2 and 3 (prestressed beams) while Figure 6.2, Figure 6.3 and Figure 6.4 show the results of the above described procedure for Beams 4, 5 and 6, respectively.

In Figure 6.1, for prestressed beams, the comparison between experimental frequencies (blue lines) and theoretical frequencies (red lines) are shown. Darker lines represent higher levels of damage. As seen from the picture, the above-described procedure gives a rough estimate of the trend of variation that was expected from experimental results, but some discrepancies are still evident. In particular, the theoretical expression seems to over-estimate the vibrational frequencies for low levels of damage and underestimate them for high levels of damage.

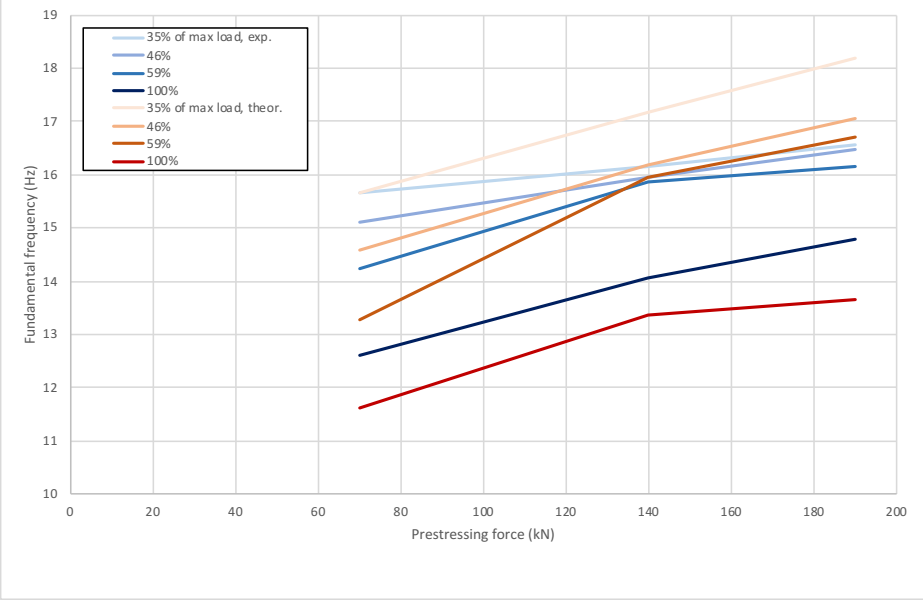

Figure 6.1 Prestressed beams: Variation of fundamental frequency with prestressing force: comparison between experimental (shades of blue) and theoretical (shades of red) results

For post-tensioned beams, the use of post tensioned cables where the prestressing force can be controlled and varied manually during the test, allowed to investigate a higher number of prestressing levels. Concerning the vertical load, for every beam, three levels of damage are studied, that are represented with different colors in the figures: undamaged beam (blue line), cracked beam (orange line) and failed beam (grey line). As it can be seen from the Figure 6.2, Figure 6.3 and Figure 6.4, a good approximation of the model with experimental results was found. In particular the above-described procedure gives a rough estimate of the trend of variation of prestressing force, and it uses NDTs results only, thus being few intrusive for the structure.

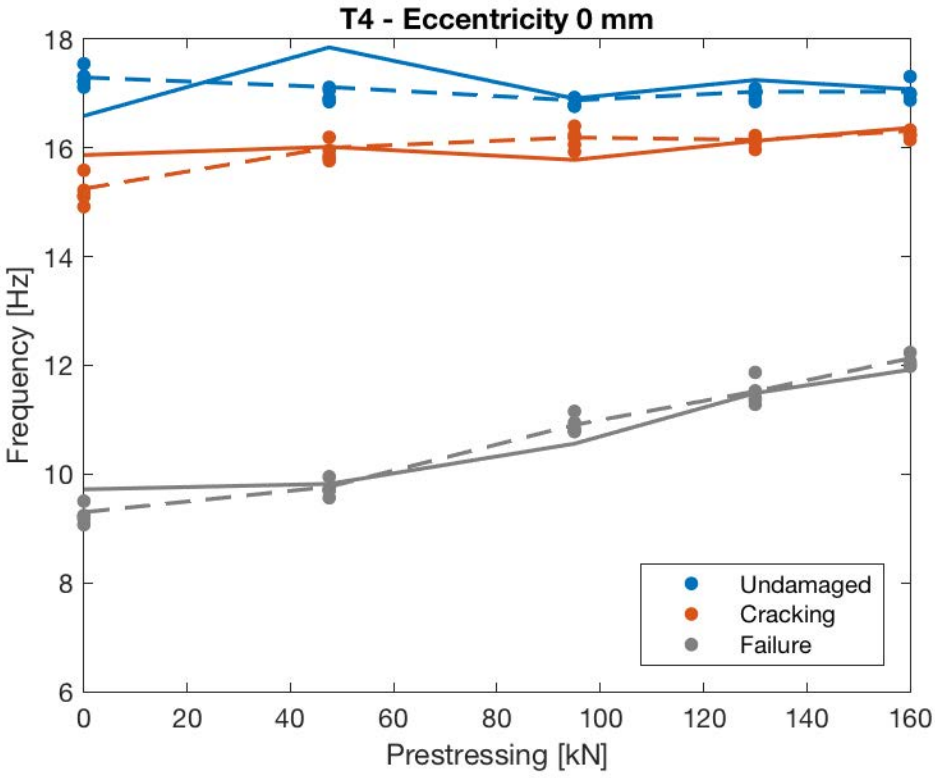

Figure 6.2 Post-tensioned beams: Variation of fundamental frequency with prestressing force: Beam 4. Dashed line: average measured value; solid line: theoretical value.

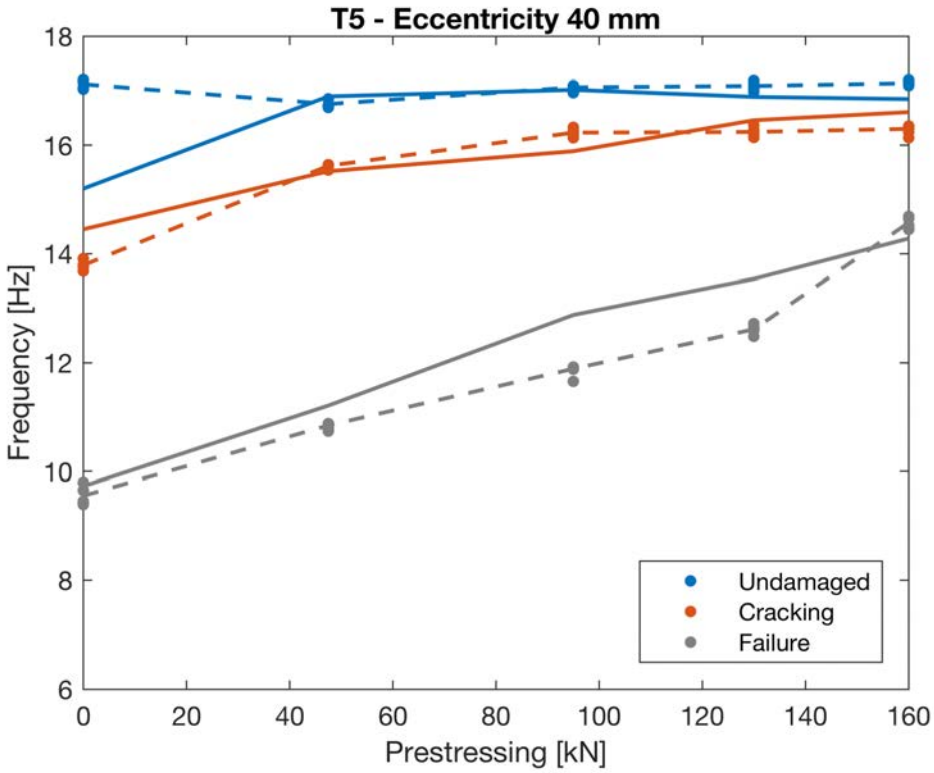

Figure 6.3 Post-tensioned beams: Variation of fundamental frequency with prestressing force: Beam 5. Dashed line: average measured value; solid line: theoretical value.

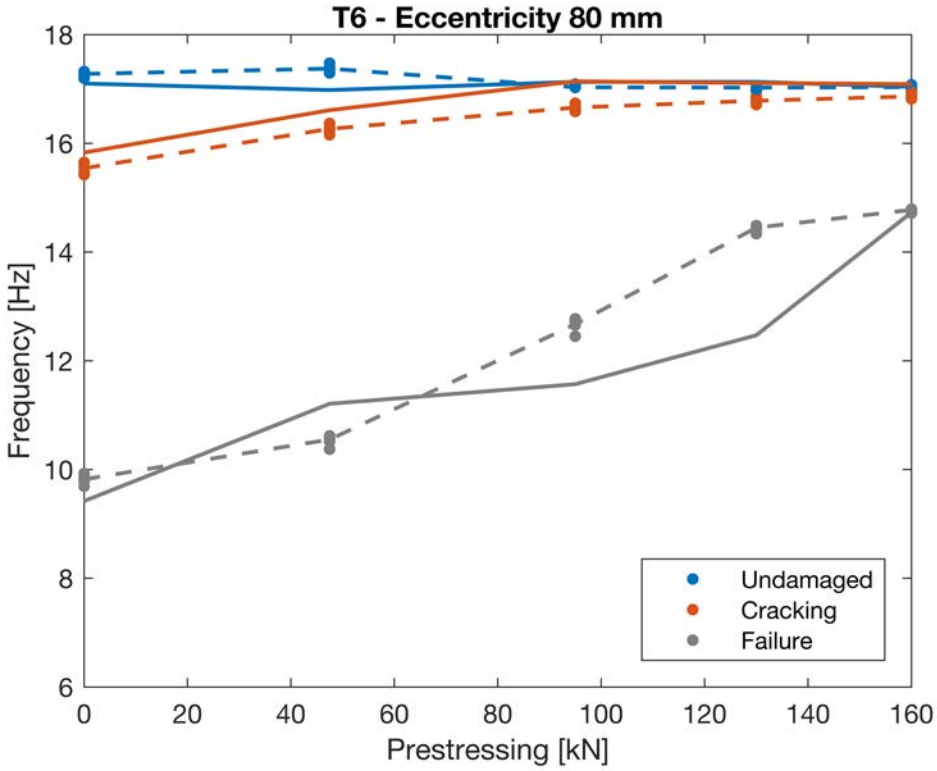

Figure 6.4 Post-tensioned beams: Variation of fundamental frequency with prestressing force: Beam 6. Dashed line: average measured value; solid line: theoretical value.

6.1 Effect of the cable eccentricity

Some considerations were made on the influence of cable eccentricity in the results. As already mentioned, post-tensioned beams are characterized by three different location of the cable, and results highlight that this parameter has some influence in the estimation of natural frequency and beam stiffness. In particular, as seen from Figure 6.2, Figure 6.3 and Figure 6.4, beams with higher cable eccentricity display increasing sensibility in the measured natural frequency variation, when prestressing force is modified. This effect is evident in large damage conditions, and it is probably due to the fact that an higher eccentricity allows cracks to recover more effectively with the increase of prestressing level, with a more significant increase in the value of vibrational frequency. By this point of view, the above exposed theoretical model already takes into account this aspect in the formulation of the inertia (see Eq. 60) since the position of the neutral axis and therefore the entity of cracked inertia depends also on the eccentricity of the cable.

7 Conclusions

In this PhD Thesis, an experimental campaign was carried out on both pre-tensioned and post-tensioned prestressed reinforced concrete (PC) beams and the outcome of the investigation are described and summarized. The research aimed at assessing the influence of varying damage and prestress levels on both static and dynamic structural parameters of the analyzed elements.

Based on the experimental evidences here obtained, some conclusions can be drawn, that are summarized in the following paragraphs, and that contain innovative aspects with respect to the present state of the art in this field of research.

1. One first consideration is made with respect to the comparison of the overall result of the research with the ones reported in §2, and related to the estimation of prestressing loss in literature. The following conclusions can be deducted:
   - In accordance with Saiidi et al. [22], the role of structural stiffness is determinant in the evaluation of the prestressing state with the use of fundamental frequencies;
   - The results of the study are also consistent with respect to the research of Noble et al. [34]. In this paper the authors studied the variation in dynamic properties for uncracked beams, and no significant change was found in the dynamic properties. This seems to be in contrast with the results exposed in this thesis, but it's not: in fact, in the same conditions of the paper from Noble et al. (undamaged beams), also in the present research the fundamental frequency is shown to be almost independent from the variation of prestressing; on the contrary this is not true for increasing amount of damage, where a clear dependence between natural frequency and prestressing amount was found.

2. Fundamental frequencies and damping ratios have shown to depend on the damage level; as expected, frequencies decrease and damping increase with increase of damage.

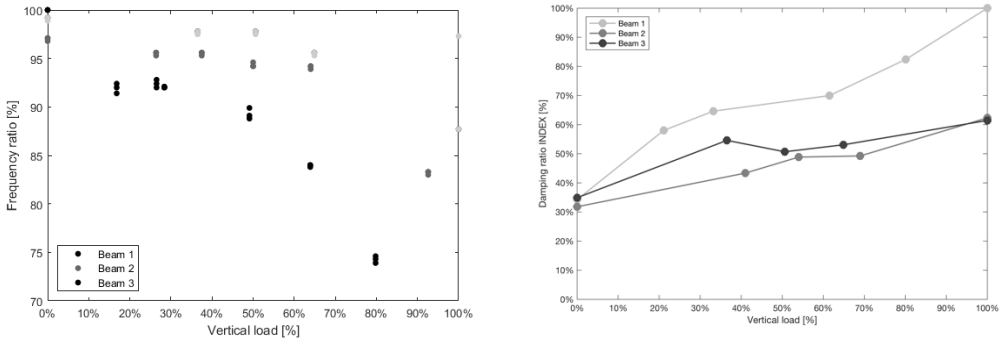

Figure 7.1 Variation of natural frequencies and damping ratio with damage: pre-tensioned beams

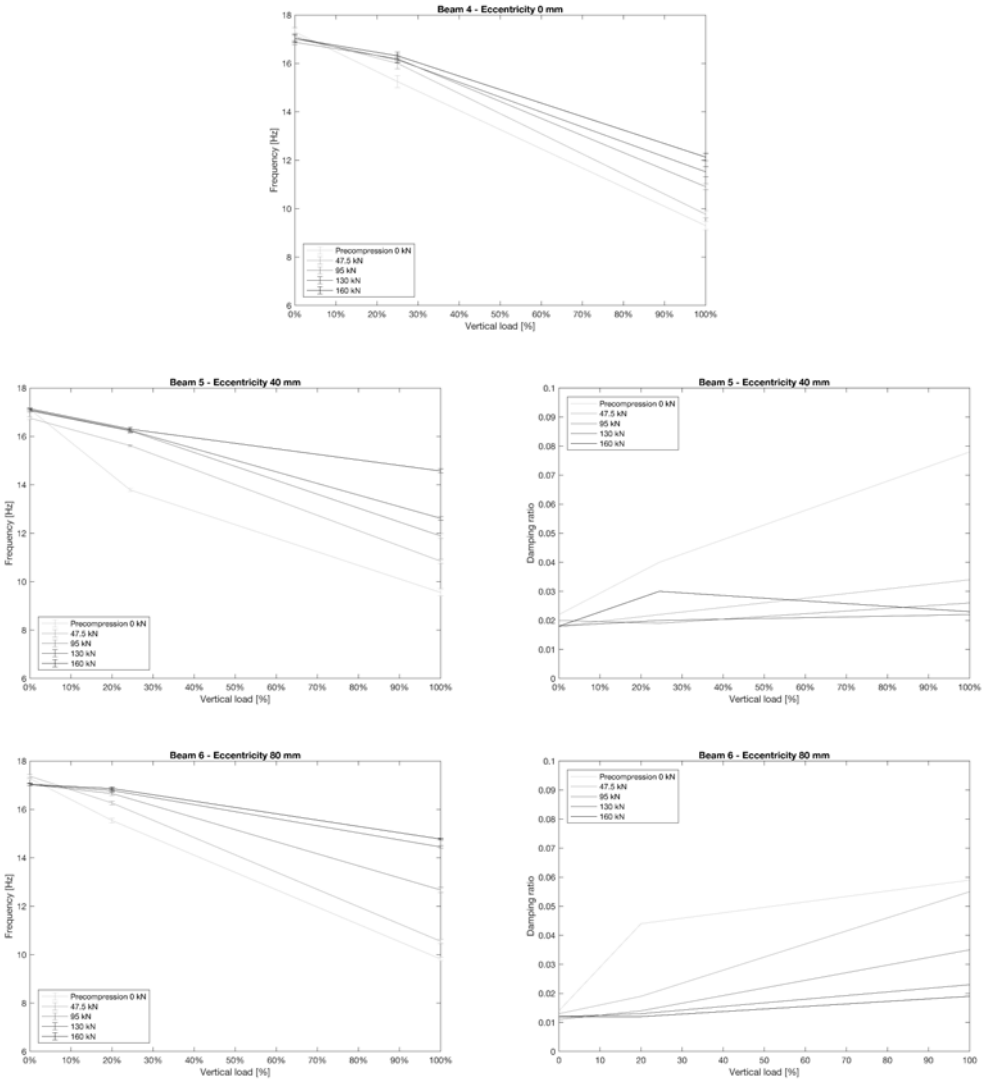

Figure 7.2 Variation of natural frequencies and damping ratio with damage: post-tensioned beams

3. Fundamental frequencies are affected by the precompression level; in particular, for post-tensioned beams, there is a good correspondence between the theoretical formulation and the measured data, but only if the value of flexural stiffness EI is correctly evaluated, accounting for the presence of cracked sections. For pre-tensioned beams, the results are less consistent with the theoretical values, even if the trend is confirmed.

   As already mentioned, the results show that for increasing levels of damage the change in prestressing force corresponds with changing in natural frequency values; on the contrary for low or no damage, the change in natural frequency is small and difficult to detect.

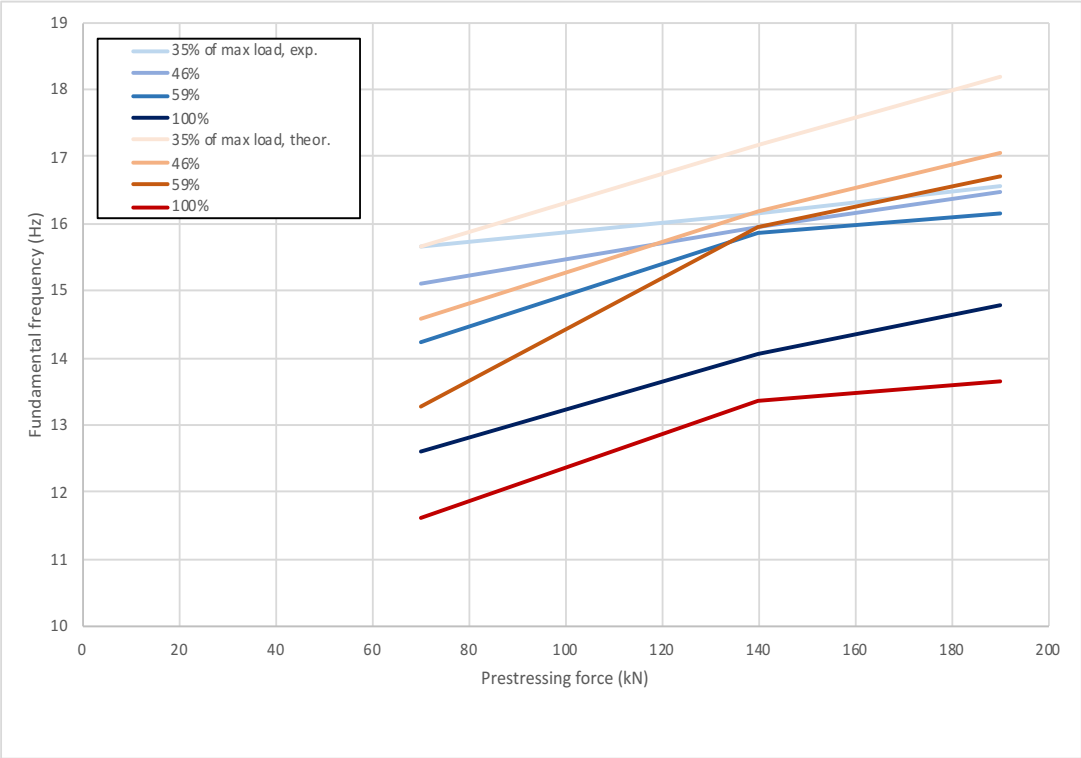

Figure 7.3 Prestressed beams: Variation of fundamental frequency with prestressing force: comparison between experimental (shades of blue) and theoretical (shades of red) results

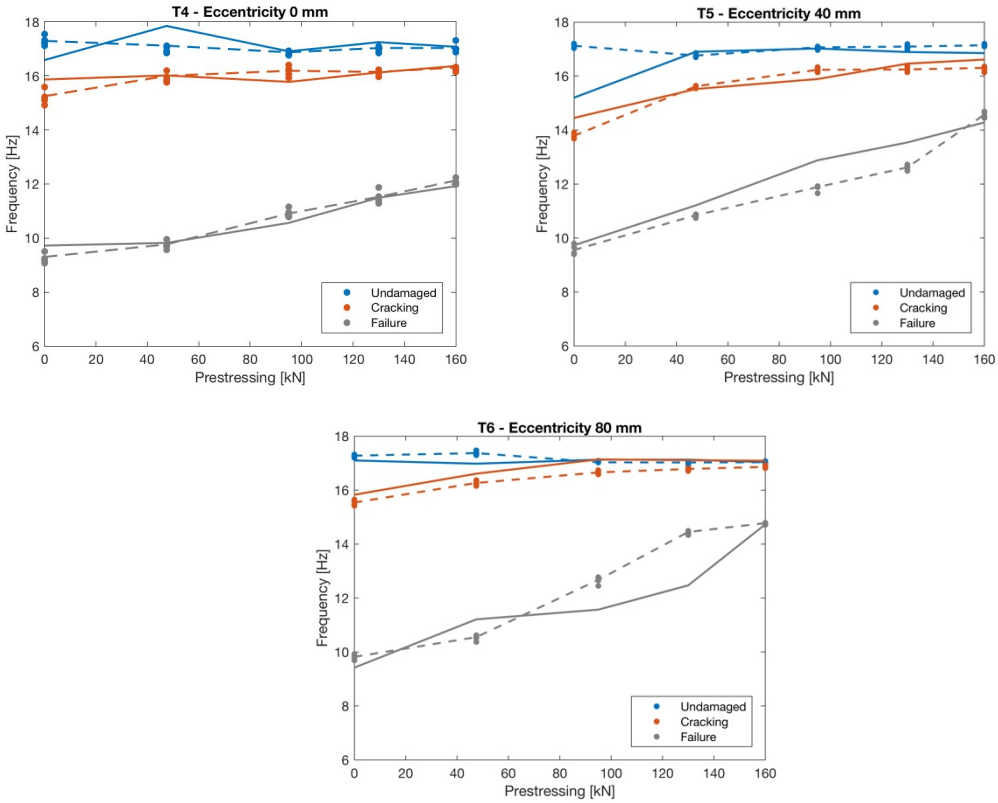

Figure 7.4 Post-tensioned beams: Variation of fundamental frequency with prestressing force. Dashed line: average measured value; solid line: theoretical value.

4. Also dissipation phenomena, like damping ratio and ultrasonic wave attenuation, are subject to variation when prestressing level changes. In particular, the two phenomena appear to be closely related with the presence of cracking phenomena. Their entity is significantly reduced by the presence of precompression, that closes the cracks and reduces the sources of energy dissipation; however, the use of structural damping showed some limitations, due to high dispersion of data for near-failure states and very small changes for low-damage states;

5. Among acoustoelastic methods, is worth recalling that ultrasonic velocity plays important role for proper estimating the flexural stiffness of the element; although, ultrasonic attenuation appears a sufficiently accurate method to well local damage presence (e.g., cracks);

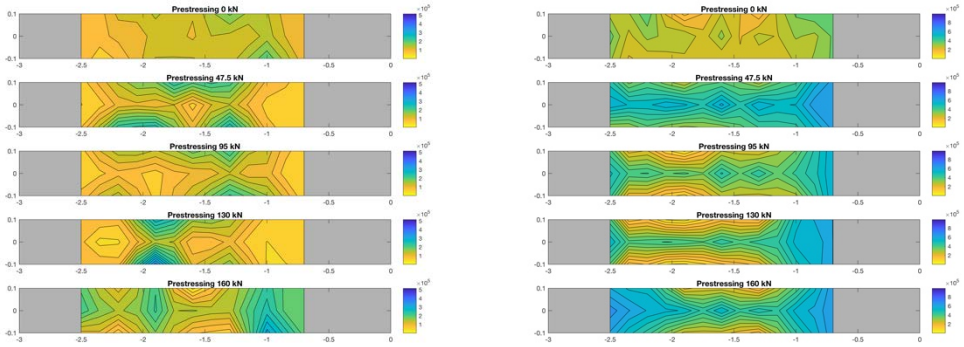

Figure 7.5 Post-tensioned beams: variation of ultrasonic energy attenuation with prestressing force

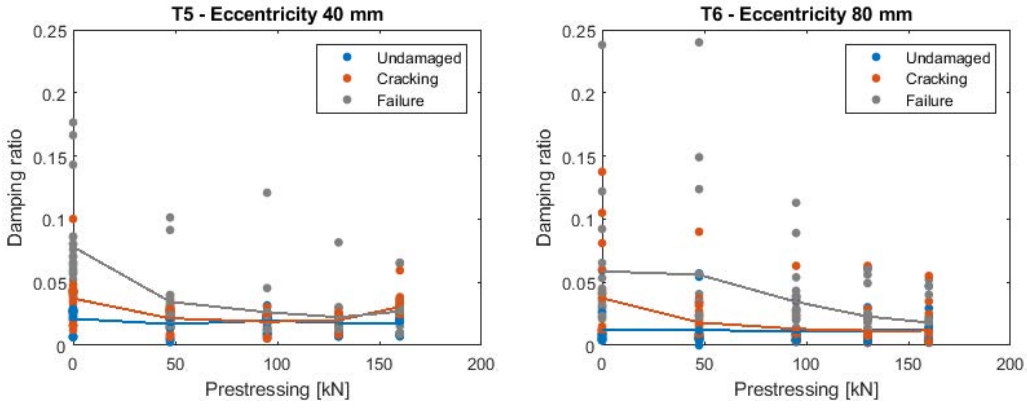

Figure 7.6 Beams 5 and 6: variation of damping ratio with prestressing force

6. Modal parameters depend on damage but do not show dependence on prestressing unless the element is strongly damage. In general, the behavior of modal parameters (like MAC) is similar to the natural frequencies, even if they show less sensitivity to variation of damage.

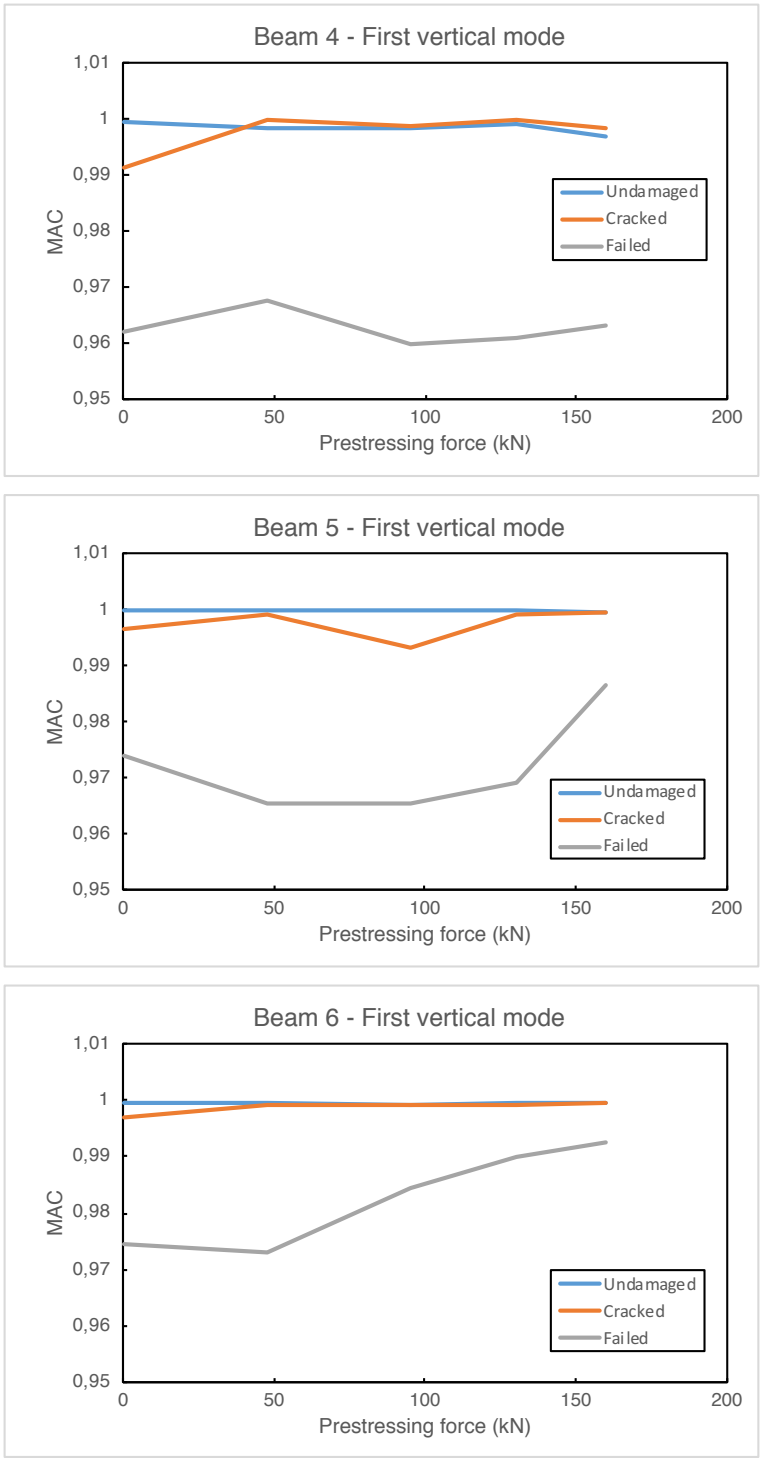

Figure 7.7 Post-tensioned beams: variation of MAC with prestressing

Finally, based on the experimental results obtained here, a procedure for the assessment of the theoretical fundamental frequencies of vibration was tested, that makes use of NDTs parameters only to estimate the level of prestressing in concrete beams. The procedure, applied to the experimental campaign described here, provides an estimation of the trend of the variability of fundamental frequencies, capturing both the effects of changing prestressing level in the elements, and also damage evolution.

The procedure has some advantages by one side and some limitations.

The advantages are linked to the possibility of applying destructive tests in the evaluation of residual prestressing. As exposed, in fact, the procedure makes only use of NDT.

The limitations are instead related to the precision of the results. In fact, as showed by the previous figures, the results for pre-tensioned beams only give a rough estimation of the real prestressing state, while on the other hand the post-tensioned beams show more accurate results.

These discrepancies should be better analyzed in further works, that should consider a sensitivity analysis of the parameters involved in the procedure. Moreover, more tests should be performed both in laboratory and real bridge structures, in order to assess and quantify the limitations of the application in real cases. In this sense, there is the intention to test a procedure similar to the one described here, also coupled by static tests, with the purpose to evaluate the carrying capacity of a small case study bridge.

Indeed, it is believed that, with appropriate calibration, the phenomena investigated in this experimental campaign are valid indicators for damage detection and prestressing loss detection, and the procedure could be therefore potentially applied to a wide number of real structures, where the estimation of the residual amount of prestressing force can be a crucial parameter for the assessing of their health conditions. Also in this case, the procedure has some advantages and some limitations.

The advantages are linked to the possibility of apply the procedure to structures with a large number of repetitive elements, like bridges with a large number of spans of approximately the same length and properties, where a wide campaign of tests is needed to assess the health condition of every beam of every span. In this case, the procedure can be applied with a calibration in few beams. The calibration can be made with the use of destructive or semi-destructive tests, but for all the other spans the tests can be sped up with the proposed procedure. The limitations are linked, as already said, to the precision of the results. In this thesis the tests are performed in controlled conditions, therefore the on-site tests could bring a larger amount of errors (for example due to the kind of dynamic excitation used in the tests). Other errors can arise from the ultrasonic results, where Elastic Modulus depends on the square of the velocity. Therefore, small errors in the measure of velocity, due to presence of passive reinforcement or environmental condition, can lead to larger errors in the evaluation of stiffness. This confirms

the necessity for a deep knowledge of at least one structural element of the series in order to perform a reliable evaluation.

8 References

[1] Faleschini, F., Zanini, M.A., Pellegrino, C. (2018). “Quality control, infrastructure management systems and their implementation in medium-size highway networks.” Proc., eBook for the 8th Workshop Meeting Barcelona, 27th September 2018.

[2] Calvi, G.M., Moratti, M., O'Reilly, G.J., Scattarreggia, N., Monteiro, R., Malomo, D., Calvi, P.M., Pinho, R. (2019). “Once upon a Time in Italy: The Tale of the Morandi Bridge.” Struct. Eng. Int., 29(2), 198-217.

[3] Cawley, P., Adams, R. (1979). “The location of defects in structures from measurements of natural frequencies.” J. Strain Anal., 14(2), 49-57.

[4] Hunt D.L., Weiss S.P., West W.M., Dunlap T.A. and Freemeyer S.R., (1990), Development and Implementation of a Shuttle Modal Inspection System, Sound and Vibration.

[5] Farrar C.R. and Jauregui D.A. (1998a), Comparative Study of Damage Identification Algorithms applied to a bridge: I. Experiment, Smart Mater. Struct., 7, 704-719.

[6] Stubbs N. and Kim J.-T., (1996), Damage Localization in Structures Without Baseline Modal Parameters, AIAA Journal, 34, 8, August.

[7] Doebling S. W., Farrar C.R., Prime M.B. and Shevitz D.W., (1996), Damage Identification and Health Monitoring of Structural and Mechanical Systems from Changes in their Vibration Characteristics: A Literature Review, Los Alamos National Laboratory, report LA-13070-MS.

[8] Zanini, M.A., Faleschini, F., Pellegrino, C. (2017a) Bridge residual service-life prediction through Bayesian visual inspection and data updating.” Struct. Infrastruct. Eng., 13(7), 906-917.

[9] Quirk, L., Matos, J., Murphy, J., Pakrashi, V. (2018). “Visual inspection and bridge management.” Struct. Infrastruct. Eng., 14(3), 320-332.

[10] Osborn, G.P., Barr, P.J., Petty, D.A., Halling, M.W., Brackus, T.R. (2010). “Residual prestress forces and shear capacity of salvaged prestressed concrete bridge girders.” J. Bridge Eng., 10.1061/(ASCE)BE.1943-5592.0000212.

[11] Tu, B., Dong, Y., Fang, Z. (2019). “Time-Dependent Reliability and Redundancy of Corroded Prestressed Concrete Bridges at Material, Component, and System Levels.” J. Bridge Eng., 10.1061/(ASCE)BE.1943-5592.0001461.

[12] Crespo-Minguillón,C., Casas, J.R. (1997). “A comprehensive traffic load model for bridge safety checking.” Struct. Saf., 19(4), 339-359.

[13] Oh, B.H., Yang, I.H. (2000). “Sensitivity analysis of time-dependent behavior in PSC box girder bridges.” J. Struct. Eng., 10.1061/(ASCE)0733-9445(2000)126:2(171).

[14] Modena C., Sonda D. and Zonta D., (1998), Sulla Localizzazione del Danno Strutturale in Elementi di c. a. p., Proc. XII congresso CTE, 293-302.

[15] Modena C., Sonda D. and Zonta D., (1999), Damage Localisation in Reinforced Concrete Structures by using Damping Measurements, Proc. DAMAS99 June 28-30, Dublin, Key Engineering Materials, 167-168, Trans Tech Publications Ltd, 132-141.

[16] Sonda D., (1999), Caratterizzazione dello Stato di Integrità di Strutture e Sottostrutture in c.a. e c.a.p. sulla Base dei Risultati di Prove Dinamiche, PhD Thesis, Università degli Studi G. D’Annunzio, Chieti, Italy.

[17] Zonta D., (2000), Structural Damage Detection and Localization by Using Vibrational Measurements, PhD Thesis, DISTART, Università degli Studi, Bologna, Italy.

[18] Zanini, M.A., Faleschini, F., Pellegrino, C. (2017b). “Probabilistic seismic risk forecasting of aging bridge networks.” Eng. Struct., 136, 219-232.

[19] Bagge, N., Nilimaa, J., Elfgren, L. (2017). “In-situ methods to determine residual prestress forces in concrete bridges.” Eng. Struct., 135, 41-52.

[20] Azizinamini, A., Keeler, B., Rohde, J., Mehrabi, A.B. (1996). “Application of a new nondestructive evaluation technique to a 25-year-old prestressed concrete girder.” PCI J., 41(3), 82-95.

[21] Garber, D.B., Gallardo, J.M., Deschenes, D.J., Bayrak, O. (2015). “Experimental investigation of prestress losses in full-scale bridge girders.” ACI Struct. J., 112(5), 553-564.

[22] Saiidi, M. et al., Prestress Force Effect On Vibration Frequency Of Concrete Bridges (1994). Journal Structural Engineering, 120, pp. 2233-2241.

[23] Abdel-Jaber, H., Glisic, B. (2019). “Monitoring of prestressing forces in prestressed concrete structures - An overview.” Struct. Control. Hlth., e2374.

[24] Kim, J.T., Park, J.H., Hong, D.S., Cho, H.M., Na, W.B., Yi, J.H. (2009). “Vibration and impedance monitoring for prestress-loss prediction in PSC girder bridges.” Smart Struct. Syst., 5(1), 81-94.

[25] Cappello, C., Zonta, D., Ait Laasri, H., Glisic, B., Wang, M. (2018). “Calibration of elasto-magnetic sensors on in-service cable-stayed bridges for stress monitoring.” Sensors, 18(2), 466.

[26] Kim, J., Kim, J. W., Lee, C., Park, S. (2017). “Development of embedded EM sensors for estimating tensile forces of PSC girder bridges.” Sensors, 17(9), 1989.

[27] Hiba, A.J., Branko, G., Monitoring of prestressing forces in prestressed concrete structures - An overview. Struct Control Health Monitoring. 2019;26:e2374.

[28] Park G, Sohn H, Farrar CR, Inman DJ. Overview of piezoelectric impedance-based health monitoring and path forward. The Shock Vib. Digest. (2003); 35(6):451-463. http://svd.sagepub.com/cgi/doi/10.1177/0583102403.

[29] Bertotti G., Hysteresis in magnetism: For physicists, materials scientists, and engineers (1998); Academic Press. http://linkinghub.elsevier.com/retrieve/pii/B9780120932702500714

[30] Hughes DS, Kelly JL. Second-order elastic deformation of solids. Phys Rev. (1953);92(5):1145-1149. http://link.aps.org/doi/10.1103/PhysRev. 92.1145

[31] Tse, F. S., Morse, I. E., and Hinkle, R. T. (1978). Mechanical vibrations, theory and applications. Allyn and Bacon, Inc., Boston, Mass.

[32] Cawley, P. & Adams, R., (1979). The location of defects in structures from measurements of natural frequencies. Journal Of Strain Analysis, 14(2), pp. 49-57.

[33] Dall'Asta, A. & Dezi, L., (1996). Prestress force effect on vibration frequency of concrete bridges-discussion. Journal of Structural Engineering, 122(4), p. 458.

[34] Noble, D., Nogal, M., O'Connor, A. & Vikram, P., (2016). The effect Of Prestress Force Magnitude And Eccentricity On The Natural Bending Frequencies Of Uncracked Prestressed Concrete Beams. Journal of Sound and Vibration,365, pp. 22-44.

[35] Unger, J. F., Teughels, A. & De Roeck, G., (2006). System Identification And Damage Detection Of A Prestressed Concreate Beam. Journal Structural Engineering, 132(11), pp. 1691-1698.

[36] Wang T.H., Wang R., Wang T.-W., (2013). The Variation Of Flexural Rigidity For Post-Tensioned Prestressed Concrete Beams. Journal of Marine Science and Technology, Vol. 21, pp. 300-308.

[37] Toyota, Y., Hirose, T., Ono, S. & Shidara, K., (2016). Experimental Study On Vibration Characteristics Of Prestressed Concrete Beam. Procedia Engineering, 171, pp. 1165-1172.

[38] Lu, Z. & Law, S., (2005). Identification of prestress force from measured structural responses. "Mechanical Systems and Signal Processing. Volume 20, Issue 8, Pages 2186-2199".

[39] Hearn G. and Testa R.B., (1991), Modal Analysis for Damage Detection in Structures, Journal of Structural Engineering, 117, 10, October, 3042-3063.

[40] Stubbs N. and Osegueda R., (1990a), Global Non-destructive Damage Evaluation in Solids, Int. Journal Analytical and Experimental Modal Analysis, 5, 2, 67-79.

[41] Stubbs N. and Osegueda R., (1990b), Global Damage Detection in Solids: Experimental Verification, Int. Journal Analytical and Experimental Modal Analysis, 5, 2, 81-97.

[42] Maia N.M.M., Silva J.M.M., He J., Lieven N., Lin R.-M., Skingle G., To W. and Urgueira A., (1997), Theoretical and Experimental Modal Analysis, Research Studies Press Ltd, Baldock, England.

[43] Ju. F. and Mimovich M., (1986), Modal Frequency Method in Diagnosis of Fracture Damage in Structures, Proceeding of the 4th International Modal Analysis Conference, 1168–1174.

[44] Rizos P.F., Aspragathos N. and Dimarogonas A.D., (1990), Identification of Crack Location and Magnitude in a Cantilever Beam from the Vibration Modes, Journal of Sound and Vibration, 138, 3, 381–388.

[45] Silva J.M.M. and Gomes A.J.M.A., (1994), Crack Identification of Simple Structural Elements Through the use of Natural Frequency Variations: The Inverse Problem, Proceedings of the 12th International Modal Analysis Conference, 1728–1735.

[46] Meneghetti, U. and Maggiore A., (1994), Crack Detection by Sensitivity Analysis, Proceedings of the 12th International Modal Analysis Conference, 1292–1298.

[47] Ewins D. J., (2000), Modal Testing: Theory, Practice and Application, 2nd edition, Research Studies Press Ltd, Baldock, England

[48] Salawu O. S., (1997), Detection of Structural Damage through Changes in Frequency, a Review, Engrg. Struct., 19, 9, 718-723.

[49] Pandey A. K., Biswas M. and Samman M. M., (1991), Damage Detection from Changes in Curvature Mode Shapes, Journal of Structural Engineering, 145, 2, 321-332.

[50] Ko J. M., Wong C. W. and Lam H. F., (1994), Damage Detection in Steel Framed Structures by Vibration Measurement Approach, Proceedings of the 12th International Modal Analysis Conference, 280–286.

[51] Ren W. X. and De Roeck G., (2002a), Structural Damage Identification using Modal Data. I: Simulation Verification, Journal of Structural Engineering, 128, 1, 87-95.

[52] Sampaio R.P.C., Maia N.M.M. and Silva J.M.M., (1999), Damage Detection Using the Frequency-Response-Function Curvature Method, Journal of Sound and Vibration, 226, 5, 1029-1042.

[53] Maia N.M.M., Silva J.M.M., Almas E.A.M. and Sampaio R.P.C., (2003), Damage Detection in Structures: From Mode Shape to Frequency Response Function Methods, Mechanical Systems and Signal Processing, 17, 3, 489-498.

[54] Lee U. and Shin J., (2002), A Frequency-Domain method od Structural Damage Identification Formulated From the Dynamic Stiffness Equation of Motion, Journal of Sound and Vibration, 257, 4, 615-634.

[55] Chouaki A.T., Ladeveze P. and Proslier L., (1998), Updating Structural Dynamic Models with Emphasis on the Damping Properties, AIAA Journal , 36, 6.

[56] Friswell M.I., Inman D.J. and Pilkey D.F., (1998), The Direct Updating of Damping and Stiffness Matrices, AIAA Journal, 36, 3, March, 491-493.

[57] Mahrenholtz O. and Bachmann H., (1991), Appendix C - Damping, Comite Euro-International du Beton - CEB, Lausanne, Switzerland, Bulletin n. 209, 169-180.

[58] Brincker, R.; Zhang, L.; Andersen, P. (2001). "Modal identification of output-only systems using frequency domain decomposition". Smart Materials and Structures. 10 (3): 441. doi:10.1088/0964-1726/10/3/303.

[59] J. David N. Cheeke, Fundamentals and Applications of Ultrasonic Waves. CRC Press (2012).

[60] De Leo, C. & Ferraro, P., s.d. Ispezioni ad ultrasuoni su materiali compositi. Politecnico di Milano, Dipartimento di Ingegneria Aerospaziale

[61] Baronio, E., 2009-2010. Esperienze di laboratorio per la calibrazione di un rilevatore di diffetti digitali ultrasonico. Università degli studi di Parma, Facoltà di Ingegneria, Corso di laurea in Ingegneria Meccanica: Luca Collini.

[62] UNI EN 12504-4: 2005. Testing concrete - Part 4: Determination of ultrasonic pulse velocity (2005).

[63] Blinka J, Sachse W. Application of ultrasonic-pulse-spectroscopy measurements to experimental stress analysis. Exp Mech. 1976;16(12):448-453. http://link.springer.com/10.1007/BF02324101

[64] Allen DR, Sayers CM. The measurement of residual stress in textured steel using an ultrasonic velocity combinations technique. Ultrason. 1984;22(4):179-188. http://linkinghub.elsevier.com/retrieve/pii/0041624X84900349.

[65] Rizzo P, Lanza di Scalea F. Wave propagation in multi-wire strands by wavelet-based laser ultrasound. Exp Mech. 2004;44(4):407-415. http://exm.sagepub.com/cgi/doi/10.1177/0014485104044321

[66] Rizzo P. Ultrasonic wave propagation in progressively loaded multi-wire strands. Exp Mech. 2006;46(3):297-306.

[67] Bianchi G., Sorrentino R., Electronic Filter Simulation & Design, McGraw Hill Professional, 2007.

[68] Espion B., Halleux P., Moment curvature relationship of reinforced concrete sections under combined bending and normal force, Materials and Structures, 1998, 21, 341-351.